รายงานวิจัยฉบับสมบูรณ์

โครงการ การศึกษาพฤติกรรมของท่อที่ฝังลึกในดินทรายเมื่อถูกผลักในทิศทางด้านบนและด้านข้างโดยวิธีคำนวณทางตัวเลข

โดย สยาม ยิ้มศิริ

กรกฎาคม 2548

สัญญาเลขที่ TRG4580098

รายงานวิจัยฉบับสมบูรณ์

โครงการ การศึกษาพฤติกรรมของท่อที่ฝังลึกในดินทรายเมื่อถูกผลักในทิศทางด้านบนและด้านข้าง
โดยวิธีคำนวณทางตัวเลข

ผู้วิจัย

ดร. สยาม ยิ้มศิริ

ภาควิชาวิศวกรรมโยธา คณะวิศวกรรมศาสตร์ มหาวิทยาลัยบูรพา

สนับสนุนโดยสำนักงานกองทุนสนับสนุนการวิจัย

กิตติกรรมประกาศ

หัวหน้าโครงการวิจัยผู้รับทุนขอกราบขอบพระคุณ Dr. Kenichi Soga ที่ได้ให้ความกรุณาทำหน้าที่เป็นนักวิจัยที่ปรึกษาของโครงการวิจัยนี้ โครงการวิจัยนี้สำเร็จลุล่วงด้วยคำแนะนำและความเอาใจใส่ของท่าน อีกทั้งหัวหน้าโครงการก็ยังได้เรียนรู้สิ่งต่างๆมากมายจากท่านตลอดระยะเวลาของโครงการนี้

หัวหน้าโครงการวิจัยผู้รับทุนขอแสดงความขอบพระคุณสำหรับการสนับสนุนทั้งทางด้านเทคนิคและไม่เทคนิคของบุคคลดังต่อไปนี้เป็นพิเศษ ได้แก่ ผศ.ดร. บรรหาญ ลิลา, ผศ.ดร. สัญชัย มิตรเอม, ผศ.ดร. ฐิรวัตร บุญญะฐี, และ ผศ.ดร. ปิยฉัตร ยิ้มศิริ

ขอขอบพระคุณท่านคณบดี ท่านหัวหน้าภาควิชาวิศวกรรมโยธา และ คณาจารย์ ของคณะวิศวกรรมศาสตร์ มหาวิทยาลัยบูรพา ที่ได้ให้การสนับสนุนในด้านต่างๆตลอดระยะเวลาของโครงการนี้

ท้ายที่สุดนี้ขอขอบพระคุณสำนักงานกองทุนสนับสนุนการวิจัยที่ได้กรุณาให้ทุนวิจัยสำหรับโครงการวิจัยนี้

บทคัดย่อ

รหัสโครงการ: TRG4580098

ชื่อโครงการ: การศึกษาพฤติกรรมของท่อที่ฝังลึกในดินทรายเมื่อถูกผลักในทิศทางด้านบนและด้านข้าง
โดยวิธีคำนวณทางตัวเลข

ชื่อนักวิจัย: ดร. สยาม ยิ้มศิริ

Email Address: ysiam@buu.ac.th

ระยะเวลาโครงการ: สิงหาคม 2545 - มิถุนายน 2548

โครงการวิจัยนี้เป็นการศึกษาถึงผลกระทบซึ่งกันและกันระหว่างท่อและดินทราย เมื่อท่อถูกแรงกระทำให้เกิดการเคลื่อนตัวในแนวนอนและเคลื่อนตัวขึ้นในแนวดิ่ง โดยการวิเคราะห์นี้อาศัยวิธีการคำนวณทางตัวเลขที่เรียกว่า Distinct Element Method (DEM) การวิเคราะห์ได้กระทำในกรณีของดินทรายแน่นปานกลางและแน่นที่สัดส่วนระยะการฝังลึกของท่อจนถึงค่า 60 ผลการวิเคราะห์จาก DEM ได้นำไปเปรียบเทียบกับผลการวิเคราะห์จาก Finite Element Method (FEM) ที่ได้กระทำมาก่อนหน้านี้แล้ว โดยจากการเปรียบเทียบพบว่าสำหรับทรายแน่นปานกลางนั้นผลการวิเคราะห์จาก DEM และ FEM ให้ค่าแรงสูงสุดและลักษณะการเปลี่ยนแปลงการวิบัติจากแบบตื้นเป็นแบบลึกที่เหมือนกัน สำหรับทรายแน่นนั้นผลจาก DEM จะให้ลักษณะการเปลี่ยนแปลงการวิบัติจากแบบตื้นเป็นแบบลึกที่ค่อยเป็นค่อยไปกว่าผลที่ได้จาก FEM และผลจาก DEM ยังให้ค่าแรงสูงสุดที่ความลึกมากๆมากกว่าค่าจาก FEM การที่ผลการวิเคราะห์จาก DEM และ FEM มีความแตกต่างกันน่าจะมาจากลักษณะการเคลื่อนตัวของดินรอบๆท่อที่ไม่เหมือนกัน โดย DEM เป็นการวิเคราะห์ที่พิจารณาดินเป็นอนุภาคซึ่งตรงกันข้ามกับ FEM ที่พิจารณาดินเป็นวัสดุเนื้อเดียวต่อเนื่อง ผลการวิเคราะห์จาก FEM ที่ได้นี้จะเป็นการให้ข้อมูลเพิ่มเติมของพฤติกรรมของท่อที่ฝังลึกในดินทราย

คำหลัก: ผลกระทบซึ่งกันและกัยระหว่างท่อและดิน, distinct element analysis, การวิบัติแบบตื้น,
การวิบัติแบบลึก, ทราย

Abstract

Project Code: TRG4580098

Project Title: Numerical study of lateral and upward soil-pipeline interactions in sand at deep embedment conditions

Investigator: Dr. Siam Yimsiri

E-mail Address: ysiam@buu.ac.th

Project Period: August 2002 – June 2005

The soil-pipeline interactions under lateral and upward pipe movements in sand are investigated using Distinct Element Method (DEM) analysis. The simulations are performed for both medium and dense sand conditions at different embedment ratios of up to 60. The comparison of peak dimensionless forces from the DEM and earlier Finite Element Method (FEM) analyses shows that, for medium sand, both methods show similar peak dimensionless forces. For dense sand, the DEM analysis gives more gradual transition of shallow to deep failure mechanisms than the FEM analysis and the peak dimensionless forces at very deep depth are higher in the DEM analysis than in the FEM analysis. The comparison of the deformation mechanism suggests that this is due to the differences in soil movements around the pipe associated with its particulate nature. The DEM analysis provides supplementary data of the soil-pipeline interaction in sand at deep embedment condition.

Keywords: soil-pipeline interaction, distinct element analysis, shallow failure mechanism, deep failure mechanism, sand

Executive Summary

An understanding of pipeline response to vertical and lateral ground movements is essential in pipeline design. Rational design under these conditions requires knowledge of soil forces resulting from the relative soil-pipeline displacement. The design formulations of the load-displacement characteristics for soil-pipeline interactions are given by ASCE's "Guideline for the Seismic Design of Oil and Gas Pipeline System (1984)". This Guideline recommends that the peak dimensionless forces and the displacement at peak forces are functions of the embedment depth of the pipe and soil friction angle, and that the non-linear relationship between the force and displacement is modeled by a rectangular hyperbola. These design values are derived from the database of pipe testing at relatively shallow embedment depths. However, there are situations where the pipe embedment ratios can be deeper than the values given in the guideline. Typical scenarios are the construction of a large embankment over an area with existing pipelines and installation of deep pipelines due to already congested underground space. If the design is based on a linear extrapolation from the ASCE data, the Guideline would overestimate the peak load exerted on the pipe and the stiffness of the soil-pipeline interaction. This overestimation would in turn results in uneconomical design.

The deep embedded pipeline problem has been investigated by Yimsiri et al. (2004). They examined various analytical solutions available for the peak forces onto a pipe and strip anchor and showed that there are large differences in the computed peak dimensionless forces for deep embedment conditions. It was concluded that a linear extrapolation from the ASCE data of shallow depth should not be employed because of the change in failure mechanism from shallow (i.e. ground surface dependent) to deep embedment conditions (i.e. ground surface independent). They performed finite element analysis to examine the transition in both medium and dense sands. Unfortunately, it is not possible to validate their findings because full-scale pipe loading experimental results or any other supplementary data are not available.

This study has been undertaken to provide supplementary data for deep embedded pipes using the Distinct Element Method (DEM). First, DEM analysis was conducted for shallow embedment depth conditions to calibrate the input parameters by comparing the results to the experimental data reported by Trautmann & O'Rourke (1983). The analysis was then

extended to deeper embedment conditions. Due to its discontinuous nature, it is considered that DEM should better simulate the soil movement close to the pipe at large pipe displacements and, hence, may yield more realistic results to the problem compared to the continuum-based finite element analysis.

For medium sand, the comparison of the peak dimensionless forces from the DEM and FEM analysis shows good match between the two. For dense sand, the DEM data show more gradual transition from shallow to deep failure mechanism and have a tendency to give a somewhat larger peak forces at very deep depths. The advantage of DEM over FEM is its ability to simulate large movement of soil around the pipe. Also, the DEM analysis can continue with unlimited pipe movement until it reaches ultimate peak force (or further), whereas the continuum based FEM often stops at some pipe displacements before the peak force can be reached because large distortion of the mesh causes numerical convergence problem. The investigation of the soil displacement patterns computed by DEM shows larger soil mass movement compared to FEM data, especially for dense sand.

The DEM results from this study confirm the findings by Yimsiri et al (2004) that the calculation of the soil-pipeline interaction at deep embedment conditions should not base on a linear extrapolation from the ASCE data of shallower embedment depths. However, the DEM results suggest that (i) there may be a possibility of underestimation of the peak dimensionless force at very deep embedment depths if the design chart proposed by Yimsiri et al. (2004) is employed and (ii) the transition from shallow to deep failure mechanism may proceed more gradually than suggested by Yimsiri et al. (2004). The results from this DEM analysis together with earlier FEM analysis will serve as a Class-A prediction of future full-scale tank tests of this problem.

Table of Contents

Page

1. Introduction

2. Review of ASCE Guideline for pipeline design

3. Review of experimental study

4. Distinct element analysis

5. DEM analyses of pipe under lateral loading

6. DEM analyses of pipe under upward loading

7. Discussion and conclusions

Chapter 1

Introduction

1.1 General

An understanding of pipeline response to vertical and lateral ground movements is essential in pipeline design. Rational design under these conditions requires knowledge of the soil forces resulting from relative soil-pipeline displacement. These movements may arise from offshore slope failures, earthquake-induced faulting, landslide and liquefaction, urban excavation and tunneling, and excessive ground settlement. Under such circumstances, loads are induced in a pipeline by relative motion between the pipeline and surrounding soil. This occurs when the soil restricts the free motion of the pipeline or when the pipeline attempts to resist the motion of the surrounding soil. The amount of restraint or load exerted on the pipeline is a non-linear function of the relative soil-pipeline displacement. Once this relationship is established, the soil-pipeline system can be analyzed approximately by a numerical method, in which the pipe is represented by beam elements and the soil reactions are modeled by spring-slider elements in the vertical, lateral, and axial directions.

The formulations of the load-displacement characteristics for soil-pipeline interactions are given by ASCE in its “Guideline for the Seismic Design of Oil and Gas Pipeline System (1984)”. This Guideline recommends that the peak dimensionless forces and the displacement at peak forces are functions of the embedment depth of the pipe, and that the non-linear relationship between the forces and displacements is modelled by a rectangular hyperbola. These recommendations are derived from the database of research works for the pipe embedment depths of $H_c/D \leq \sim 10$ to 20 for lateral and upward pipe movement, where H_c is the depth to the centerline of the pipe and D is the external diameter of the pipe.

There are some situations where the pipe embedment ratios can be deeper than the values recommended by ASCE. This is due to, for example, the construction of high embankment over the area with existing pipeline and the congestion of the underground structures forcing the new pipeline to go deeper (installed by pipe-jacking). Under this condition, the H_c/D ratio can be as large as 40 to 60, which is well beyond the range of the recommendations given in the ASCE Guideline. If the calculation is based on a linear extrapolation from the ASCE data of shallower embedment depths, it is expected that the

Guideline would overestimate the peak load exerted on the pipe and the stiffness of the soil-pipeline interaction. This overestimation would in turn results in uneconomical design.

This potential problem has been considered by Yimsiri et al. (2004), who performed the numerical analysis by Finite Element Method (FEM) to study the soil-pipeline behavior in sand at deep embedment condition. However, there has not been any full-scale experimental result to exactly confirm this FEM result. Therefore, this research project was undertaken to supplement additional data on the soil-pipeline interaction in sand at deep embedment depths by another approach of numerical analysis.

1.2 Purposes

As mentioned earlier, the ASCE Guideline is based on the research data for $H_c/D \leq \sim 10$ to 20. Most of the published experimental studies of pipeline behavior are performed at depths smaller than the depths of interest in this study (H_c/D up to 60). To the author's knowledge, the largest H_c/D studied is 25 for lateral pipe loading (Audibert & Nyman, 1977) and 13 for upward pipe loading (Trautmann & O'Rourke, 1983). Furthermore, the critical embedment depths (the depth after which the peak dimensionless force becomes constant with embedment ratios) have been reported only for loose sand. Only Dickin & Leung (1983) reported the critical embedment depth for dense sand from their centrifuge tests. Thus, it is necessary to perform a study of pipeline behavior at deep embedment depths to gain more understanding.

In this study, the numerical analysis by Distinct Element Method (DEM) was undertaken to study the behavior of pipeline under lateral and upward loading. Firstly, the experimental results of the pipeline behavior by Trautmann & O'Rourke (1983) at shallow depth were simulated to (i) establish a simulation technique, (ii) obtain input parameters for numerical models, and (iii) examine the accuracy of the analysis. Secondly, the DEM analyses were extended to deeper embedment depths up to H_c/D = 60. Thirdly, the DEM analysis results were compared with the ASCE Guideline and the previous FEM analysis by Yimsiri et al. (2004). Finally, the discussions and conclusions were made.

The specific goals of this study are:-

1. To present the capability of the DEM analysis to simulate the pipeline-soil behavior,

2. To determine the peak forces exerted on a buried pipeline at deep embedment depths for lateral and upward pipe movements,
3. To determine the critical embedment depth, where the deep failure mechanism happens,
4. To assess the consistency of the DEM analysis results with the ASCE Guideline and the previous FEM analysis results, and
5. To investigate deformation pattern of soil particles around pipe, which may be represented more realistically by DEM analysis.

1.3 Layout of the report

Following the introductory chapter, Chapter 2 briefly describes the ASCE Guideline for the design of pipeline subjected to lateral and upward movements. The discussions of the potential problems for an application of this guideline to a pipe at deep embedment depths are made.

Chapter 3 reviews the experimental study of pipeline subjected to lateral and upward loading at shallow embedment depths performed by Trautmann & O'Rourke (1983). These experimental results are used as a benchmark to determine the input parameters and to examine the accuracy of the present DEM simulation.

Chapter 4 explains the details of the DEM analysis employed in this study. The general concepts of the DEM analysis are explained. The numerical analysis procedures are described. The selection of the parameters is eluciadted. The interpretation of the numerical analysis results is mentioned.

Chapter 5 presents the DEM analysis results of a pipe subjected to lateral loading. First, the DEM analysis results are presented for shallow embedment depths and are compared with the experimental results by Trautmann & O'Rourke (1983). The DEM analyses are then performed for deeper embedment depths and the results are compared with the previous published data.

Chapter 6 presents the DEM analysis results of a pipe subjected to upward loading. The structure of this chapter is similar to Chapter 5.

Chapter 7 presents the discussions and conclusions. The determination of the input parameters for the present DEM analysis is discussed. The pipeline-soil behavior under lateral and upward loading is discussed concerning the obtained peak dimensionless forces and the soil displacement pattern with comparison to the previous FE analysis.

Appendix A presents the force-displacement curves of pipe under lateral loading with comparison with the previous experimental results and FE analysis data.

Appendix B presents the force-displacement curves of pipe under upward loading with comparison with the previous experimental results and FE analysis data.

Appendix C presents the displacement patterns of soil around pipe under lateral loading.

Appendix D presents the displacement patterns of soil around pipe under upward loading.

Appendix E presents the contact force patterns around pipe under lateral loading.

Appendix F presents the contact force patterns around pipe under upward loading.

Appendix G presents the parametric study of the effects of various parameters of the DEM analysis on the triaxial test results.

Appendix H presents the parametric study of the DEM analysis for pipe subjected to lateral loading.

Appendix I presents the parametric study of the DEM analysis for pipe subjected to upward loading.

Chapter 2

Review of ASCE Guideline for pipeline design

2.1 General

In 1984, the Committee on the Gas and Liquid Fuel Lifelines of the ASCE Technical Council on Lifeline Earthquake Engineering published the "Guideline for the Seismic Design of Oil and Gas Pipeline Systems". The Guideline proposed the procedures to determine the peak forces and their corresponding pipe displacements for pipeline-soil interaction at various directions and also provided the equations to describe the non-linear force-displacement relationship. These data are essential to define the spring constant in the numerical analyses of a soil-pipeline interaction problem. The design guideline for a pipeline in sand subjected to lateral and upward movements are summarized in the following sections.

2.2 Pipeline in sand subjected to lateral movement

Lateral restraint of a pipeline represents the resistance (or load) offered by the surrounding soils to any lateral movement of the pipeline. Therefore, the lateral soil-pipeline interaction is similar to a vertical anchor plate moving horizontally relative to the surrounding soils. Based on the experiments performed with pipes buried in dry, uniform sand, a relationship between the force per unit length, F_h, and the lateral displacement, δ_h, has been shown to be represented by the following hyperbolic equation (Das & Seeley, 1975; Audibert & Nymann, 1977; Trautmann & O'Rourke, 1983).

$$F_h = \frac{\delta_h}{A' + B'\delta_h} \qquad \text{………………..} \quad (2\text{-}1)$$

where $A' = 0.15\delta_{h,peak}/F_{h,peak}$

$B' = 0.85/F_{h,peak}$

$F_{h,peak} = \bar{\gamma} H_c N_{qh} D$

$$\delta_{h,peak} = \begin{cases} 0.07 \text{ to } 0.10\,(H_c + D/2) & \text{for loose sand} \\ 0.03 \text{ to } 0.05\,(H_c + D/2) & \text{for medium sand} \\ 0.02 \text{ to } 0.03\,(H_c + D/2) & \text{for dense sand} \end{cases}$$

$\bar{\gamma}$ = effective unit weight of soil

H_c = depth to centerline of the pipeline

N_{qh} = horizontal bearing capacity factor

D = external pipeline diameter

In the Guideline, two analytical models are proposed for determining N_{qh}. Fig. 2-1 shows N_{qh} as a function of H_c/D for soil friction angles between 30° and 45° proposed by Trautmann & O'Rourke (1983) based on the model by Oversen (1964). Fig. 2-2 shows N_{qh} as a function of H_c/D for soil friction angle between 20° and 45° based on the analytical solution of laterally loaded pile by Hansen (1961). It is noted that the values of N_{qh} recommended by Hansen are approximately 50% to 100% larger than those by Trautmann & O'Rourke for a given friction angle. This discrepancy is due to the difference in vertical restraint condition of the pipe in each model. Hansen's model assumes full vertical restraint so the interface friction mobilizes fully, whereas Oversen's model assumes that the wall is free to rise with the passive wedge of soil so the mobilized interface friction is less. Audibert & Nyman (1977) showed that the prediction from Hansen's model show good agreement with their experimental data up to H/D of 25. Trautman & O'Rourke (1983) showed that their experimental data gave good agreement with the prediction made by Oversen's model

The Guideline recommends that the values of N_{qh} be chosen after careful evaluation of the soil conditions in the field and the level of conservatism governing the design. Partially saturated, medium to fine sands will have increased shear strength relative to their dry or saturated states under conditions of short term loading. Neither Hansen's nor Oversen's models accounts for this increased strength associated with partial saturation. Thus, the Guideline suggests that Fig. 2-1 should be applicable for dry or saturated sands and gravels, and for partially saturated gravels and coarse sands and that Fig. 2-2 should be used to conservatively estimate lateral soil forces for most condition of pipeline burial in cohesionless sands and gravels.

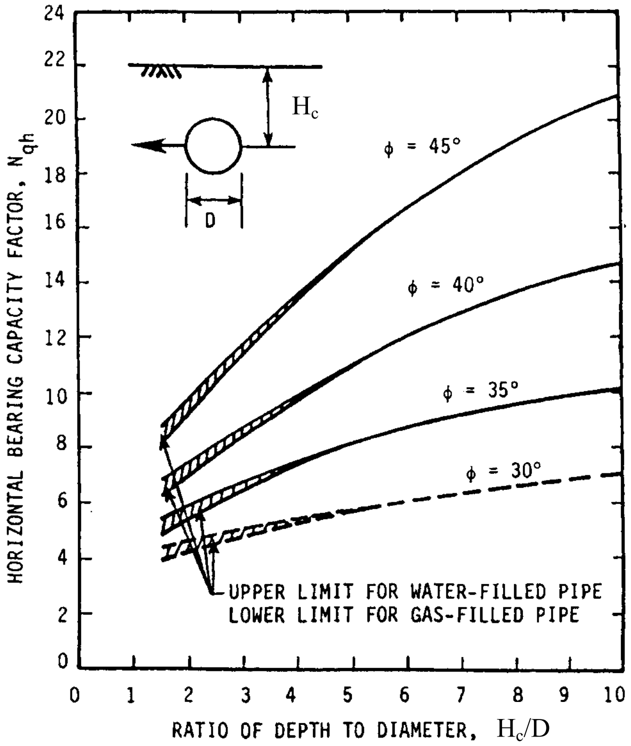

Figure 2-1 Horizontal bearing capacity factor for sand as a function of depth to diameter ratio of buried pipeline (after Trautmann & O'Rourke, 1983)

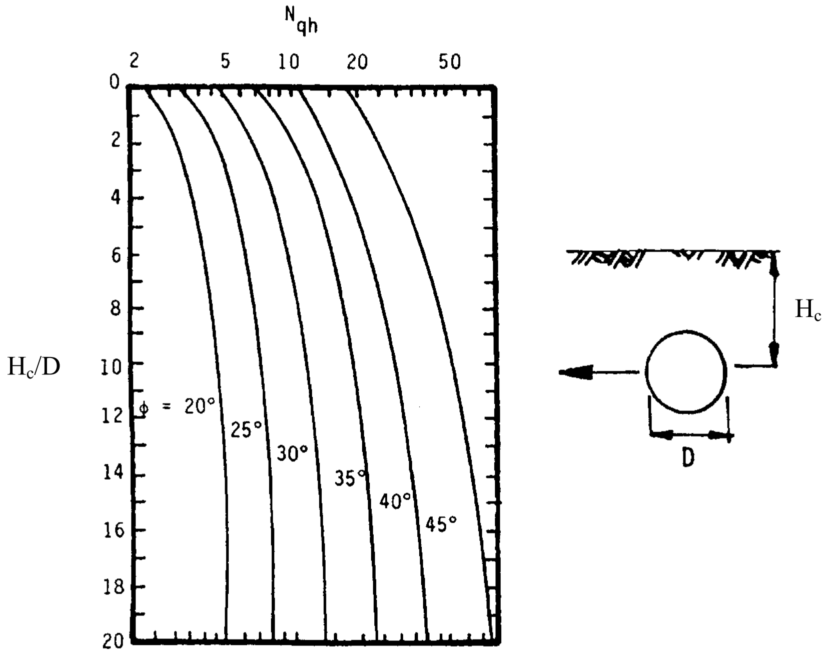

Figure 2-2 Horizontal bearing capacity factors as a function of depth to diameter ratio for pipelines buried in sand (after Hansen, 1961)

2.3 Pipeline in sand subjected to upward movement

Upward restraint of a pipeline represents the resistance offered by the surrounding soils to any upward movement of the pipeline. Therefore, the upward soil-pipeline interaction is also similar to a horizontal anchor plate subjected to upward movement. Based on the tests performed with pipes buried in dry, uniform sand, a relationship between the force per unit length, F_v, and the vertical upward displacement, δ_v, is represented by the following hyperbolic relationship (Trautmann & O'Rourke, 1983).

$$F_v = \frac{\delta_v}{A'' + B''\delta_v} \qquad \text{………………..} \quad (2\text{-}2)$$

where $A'' = 0.07\delta_{v,peak}/F_{v,peak}$

$B'' = 0.93/F_{v,peak}$

$F_{v,peak} = \bar{\gamma} H_c N_{qv} D$

$\delta_{v,peak} = 0.01$ to $0.015H_c$ for dense to loose sand

$\bar{\gamma}$ = effective unit weight of soil

H_c = depth to centerline of the pipeline

N_{qv} = vertical uplift factor

D = external diameter of pipe

Fig. 2-3 summarizes the values of N_{qv} for vertically displaced pipeline in dry or saturated sand as a function of H_c/D and soil friction angle. The plots shown by the solid lines are based on the test results reported by Trautmann & O'Rourke (1983). The plots shown by the dotted lines were derived from the finite element analysis reported by Rowe & Davis (1982) for a horizontal anchor plate lifted under the conditions of no soil dilatancy and no interface friction. In Fig. 2-3, the Rowe & Davis' solutions have been modified to account for the cylindrical shape of the pipe by subtracting the weight of the soil occupying the upper half of the pipeline from the predicted forces. The vertical uplift factors shown in Fig. 2-3 account for the weight of a gas pipeline. For liquid pipelines, the weight of the contents should be added to the force determined from the figure to give the total resistance to uplift.

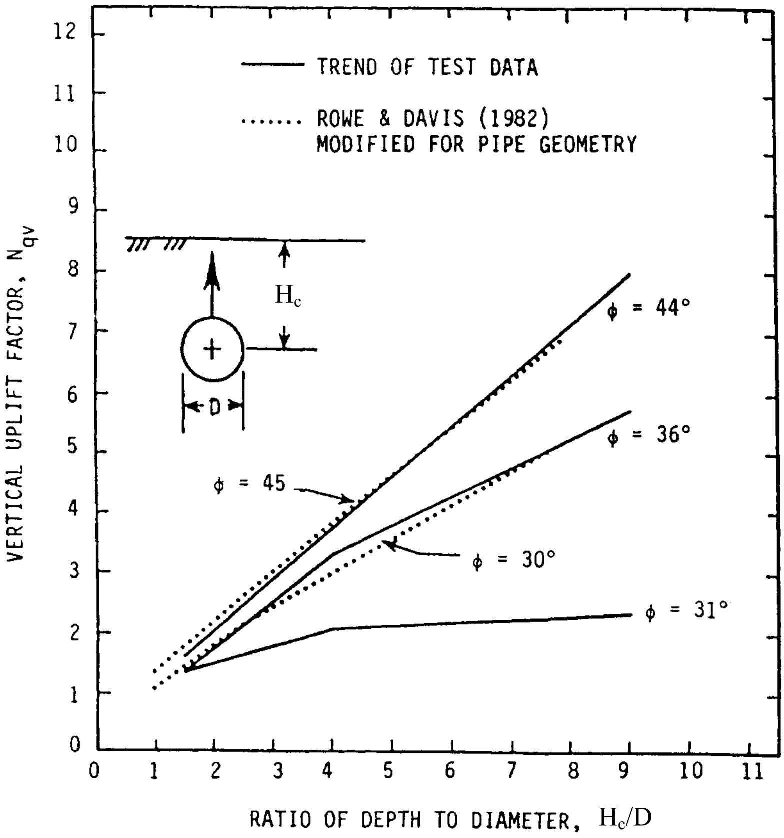

Figure 2-3 Vertical uplift factor for sand as a function of depth to diameter ratio of buried pipelines (after Trautmann & O'Rourke, 1983)

2.4 Discussion

The force-displacement relationships of lateral and upward pipe movements are assumed to be a rectangular hyperbola. The peak dimensionless forces, N_{qh} and N_{qv}, and the corresponding pipe displacements at the peak forces are influenced by the burial depth. The constants N_{qh} and N_{qv} increase with H_c/D. At deeper embedment depths, it is expected that this Guideline would overestimate the peak force and soil stiffness if the calculation is based on a linear extrapolation from the data of shallower embedment depth. This is due to the fact that the failure mechanism at deeper embedment depths is different from that at shallow embedment depths as experimentally shown by several researchers (e.g. Audibert & Nyman, 1977; Akinmusuru, 1978; Dickin & Leung, 1985). At the depths beyond the critical embedment depth, the peak dimensionless force should become constant independent of the embedment ratio. The critical embedment depth has been reported only for loose sand. There is no available data for medium and dense sands.

Chapter 3

Review of experimental study

3.1 General

The experimental results of the pipeline behavior subjected to lateral and upward loadings by Trautmann & O'Rourke (1983) are used as benchmarks to determine the input parameters for the present DEM models and to examine the capability of the DEM analysis technique. Their results of ϕ102 mm pipe in medium and dense sands are of concern in this research because the sand placed around a pipeline is often in the state of medium to dense conditions. In the following, their experimental study is summarized.

3.2 Testing apparatus

The pipe loading tests were performed in a test compartment of 1.2 m (W) × 2.3 m (L) × 1.2 m (D). The steel pipe had outside diameters of 102 mm, wall thicknesses of 6.4 mm, and length of 1.20 m. The schematic diagrams of the test set ups are shown in Figs. 3-1 and 3-2. The value of H is the depth to the base of the pipe and H_c is the depth to the centerline of the pipe.

To ensure uniformity of test conditions, sand was placed in the test compartment with a mechanical spreading hopper suspended from an overhead service crane. The crane also transported an electric vibrator, which was used to compact the sand to obtain medium or dense deposits.

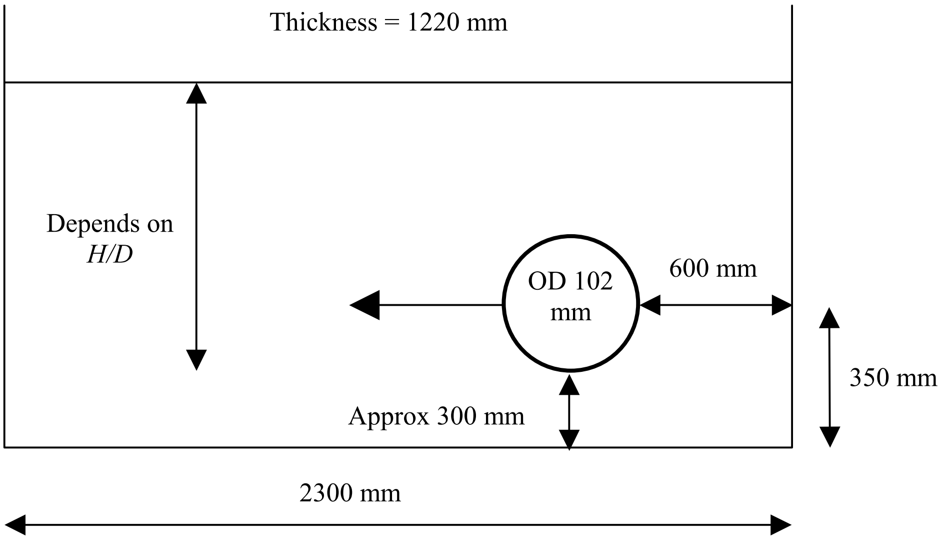

Figure 3-1 Experimental set-up of lateral pipe loading

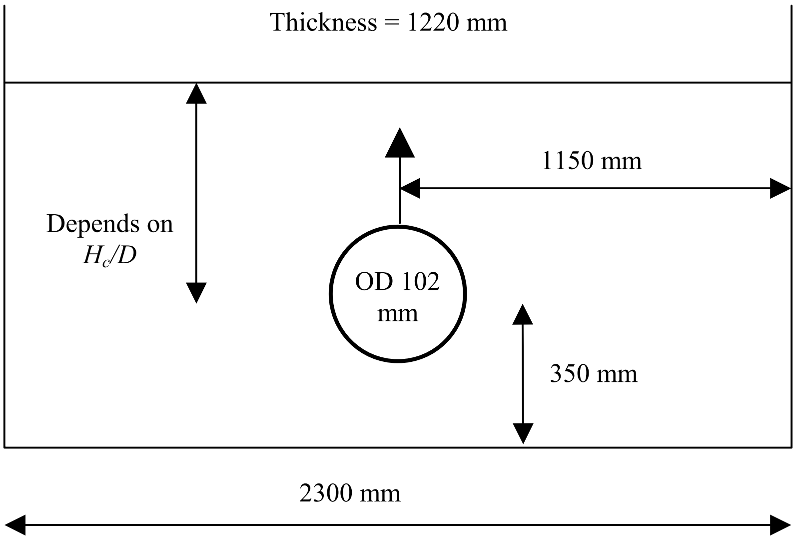

Figure 3-2 Experimental set-up of upward pipe loading

3.3 Testing programme

The testing programme was designed to investigate the effects of embedment depth and density of sand on the pipeline behavior subjected to lateral and upward loadings. The testing programmes are shown in Tables 3-1 and 3-2 for lateral and upward pipe loadings, respectively.

Table 3-1 Summary of experiments of lateral loading of pipe in sand (Trautmann & O'Rourke, 1983)

Test No.	Pipe Diameter (mm)	Density (kN/m^3)	H/D
45	102	16.4	2.0
26	102	16.4	4.0
27	102	16.4	4.0
29	102	16.4	4.0
30	102	16.4	4.0
46	102	16.4	6.0
51	102	16.4	8.5
48	102	16.4	11.5
49	102	16.4	11.5
22	102	17.7	2.0
23	102	17.7	4.0
24	102	17.7	6.0
25	102	17.7	8.5
32	102	17.7	11.5

Table 3-2 Summary of experiments of upward loading of pipe in sand (Trautmann & O'Rourke, 1983)

Test No.	Pipe Diameter (mm)	Density (kN/m^3)	H_c/D
44	102	16.4	1.5
43	102	16.4	4.0
42	102	16.4	8.0
41	102	16.4	13.0
38	102	17.7	1.5
37	102	17.7	4.0
40	102	17.7	8.0
39	102	17.7	13.0
50	102	17.7	4.0

3.4 Properties of tested sand

Cornell filter sand was used for all the tests. This soil is a clean, subangular, fluvioglacial sand, having a coefficient of uniformity C_u of 2.6, and an effective grain size D_{10} of 0.2 mm. It contains 20% quartz, 40% limestone fragments, 20% siltstone fragments, and 10% quartzite fragments in addition to trace quantities of other constituents. Its specific gravity is 2.74 and the minimum and maximum densities, measured in accordance with ASTM standard, are 15.5 and 18.3 kN/m^3, respectively. Uncompacted sand deposits made with the sand spreader, however, had a density of 14.8 kN/m^3, which was lower than the value determined by the ASTM standard procedure. In this study, therefore, the density of 14.8 kN/m^3 obtained with the sand spreader was adopted as the minimum density. The three densities used in the test series were 14.8, 16.4, and 17.7 kN/m^3, which corresponded to 0, 45, and 80% relative density, respectively. According to Lambe & Whitman (1979), their states can be described as “very loose”, “medium”, and “dense”. However, only medium and dense sands are of interest in this research.

The angle of shearing resistance for the sand was measured in a direct shear test device at normal stresses ranging from 2.5-20 kN/m^2, which includes the range of stress encountered during the actual tests. It was shown that the angle of shearing resistance was essentially constant with respect to normal stress over the range of 2.5-20 kN/m^2. Fig. 3-3 shows the relationship between friction angle and initial sand density for a normal stress of 5 kN/m^2. For the test densities of 14.8, 16.4, and 17.7 kN/m^3, the corresponding peak friction angles are 31°, 35°, and 44°, respectively.

The results of the torsional simple shear tests and triaxial tests under drained condition on Cornell filter sand were presented by Turner & Kulhawy (1987). The sand specimens were prepared by air pluviation and tamping was employed to achieve the desired density. The data from the triaxial tests were used for the determination of the input soil parameters. The triaxial test results are presented in Sections 4.5.1.

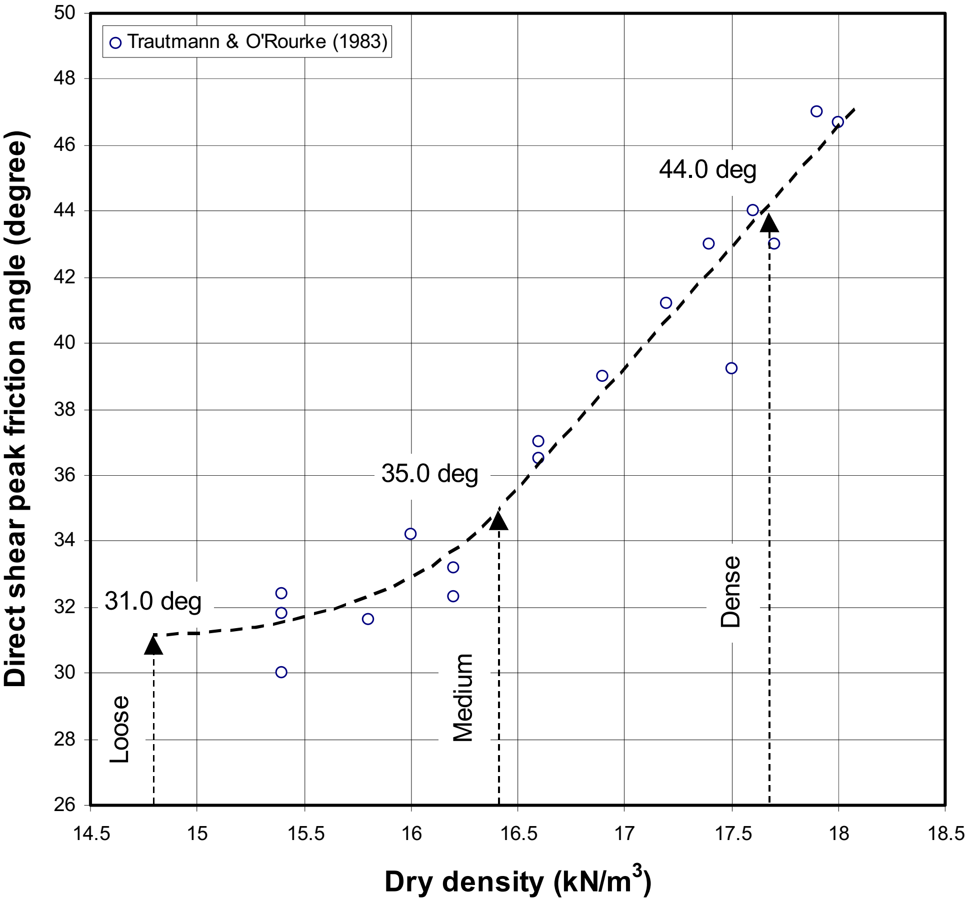

Figure 3-3 Relationship between peak friction angle from direct shear tests and dry density

3.5 Test results

The experimental results by Trautmann & O'Rourke (1983) are presented in terms of force-displacement relationship in comparison with the present DEM analysis results in Appendix A and B.

Chapter 4

Distinct element analysis

4.1 General

The Distinct Element Method (DEM) was employed as a numerical analysis approach in this study. In the following, the concepts of the DEM analysis are briefly explained. The numerical simulation by the distinct element code PFC^{3D} is described. The determination of the input parameters for DEM modelling is explained. The interpretation of the numerical analysis results is mentioned.

4.2 Distinct element method numerical analysis

The Distinct Element Method (DEM) simulates the mechanical behavior of a system comprised of a collection of arbitrary shaped particles which displace independently from one another and interact only at contacts. The analysis allows finite displacements and rotations of discrete bodies, including complete detachment, and recognizes new contacts automatically as the calculation progresses. The method was introduced by Cundall (1971) for analysis of rock mechanics problems and then applied to soils by Cundall & Strack (1979).

In the DEM analysis, the interaction of particles is viewed as a transient problem with the state of equilibrium developing whenever the internal forces balance. The equilibrium of contact forces and displacements of a stressed assembly of particles are found through a series of calculations tracing the movements of the individual particles. These movements are the results of propagation through the medium of disturbance originating at the boundaries. This is a dynamic process in which the speed of propagation depends on the physical properties of the discrete system.

The dynamic behavior is represented numerically by a timestepping algorithm, in which it is assumed that the velocities and accelerations are constant within each timestep. The solution scheme is identical to that used by the explicit finite-difference method for continuum analysis. The timestep is chosen to be very small so that, during a single timestep, disturbance cannot propagate from any particle further than its immediate neighbors. Hence, at all times, the forces acting on any particles are determined exclusively by its interaction with the particles with which it is in contact. The critical timestep can be calculated from the speed at which the disturbance can propagate. The speed is a function of the physical properties of the discrete system (e.g. mass and moment of inertia of the particles, and contact stiffnesses). The use of an explicit, as opposed to an implicit, numerical scheme makes it possible to simulate the non-linear interaction of a large number of particles without excessive memory requirements or the need for an iteration procedure.

The calculation cycles performed in DEM analysis repeatedly alternate between the application of Newton's second law of motion to the particles and a force-displacement law at the contacts as well as the constant updating of the particles and walls position as shown in Fig. 4-1. Newton's second law is used to determine the motion of each particle arising from the contact and body forces acting upon it, while the force-displacement law is used to update the contact forces arising from the relative motion at each contact. The important characteristic of the DEM is an allowance of finite displacements and rotations of discrete bodies, including complete detachment and ability to recognise new contact automatically as the calculation progresses. Thus, the efficient contact detection and revision algorithm is very important for DEM simulation. Further details of the available algorithm can be found in e.g. Cundall (1988a) and Lian et al. (1994).

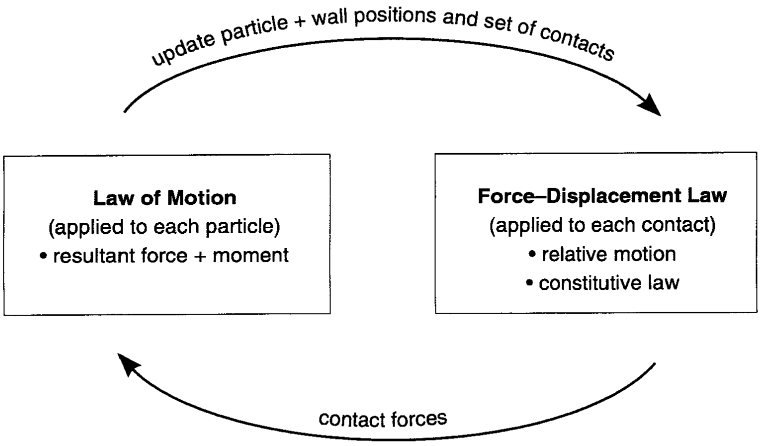

Figure 4-1 Calculation cycle in DEM analysis (Itasca, 1999)

4.3 Distinct element code PFC^{3D}

4.3.1 General assumptions

In this study, DEM numerical analysis is performed by the distinct element code PFC^{3D}, which is commercially available by Itasca Consulting Group. The code PFC^{3D} models the movement and interaction of the stressed assemblies of rigid spherical particles. It can be viewed as a simplified implementation of the DEM because of the restriction to rigid spherical particles: the general DEM can handle deformable polygonal-shaped particles. The code PFC^{3D} performs calculation with the following assumptions;

- Particles are treated as rigid bodies.
- Contacts occur over a vanishing small area (i.e. at a point).
- Behavior at the contacts uses a soft-contact approach, wherein the rigid particles are allowed to overlap to another at contact points.
- The magnitude of the overlap is related to the contact force via the force-displacement law, and all overlaps are small in relation to particle sizes.
- All particles are spherical.

Hereafter, the spherical particle and the rigid boundary wall acting on the particle in PFC^{3D} model are sometimes simply referred to as “ball” and “wall”, respectively.

By default, PFC^{3D} operates in “static” mode – that is, internal damping is applied that causes the system of particles to reach equilibrium in a minimum number of cycles. If the system is physically unstable, then the resulting motion will be damped but not eliminated. The type of damping embodied in PFC^{3D} acts to suppress acceleration motion rather than velocity. In this way, steady motion (e.g. particles in steady flow down a chute) is not prohibited. For situations where accelerations and inertial forces are known to be important, the damping should be reduced to a value that is more reasonable physically. In the present analysis, the static mode was employed. More information concerning the theoretical background of the DEM analysis by PFC^{3D} can be found in the PFC^{3D} manual (Itasca, 1999).

4.3.2 Contact models

DEM analysis requires knowledge of a force-displacement law at particle contacts. Particles interact with other particles and boundary walls through the forces that develop at their contacts. The term “contact” is used here to denote this interaction and each contact corresponds to a physical touching. In PFC^{3D}, every contact involves two entities (either ball-to-ball or ball-to-wall) and occurs at a single point through which the contact force acts.

A contact model describes the physical behavior occurring at a contact. It is common to use an elastic-perfectly plastic relationship between the contact force and relative contact displacement. The normal and tangential contact stiffnesses relate the normal and tangential components of contact forces and relative contact displacements. In PFC^{3D}, the normal components are related by a secant stiffness, while the tangential components are related by a tangent stiffness. Thus, the total normal contact force can be computed at any time if the total normal contact displacement is known, but only the increment of tangential contact force can be computed for a given increment of tangential contact displacement. This means that if the normal contact stiffness is altered during the course of a simulation, there will be an immediate effect upon the entire assembly, but if the tangential contact stiffness is altered during the course of a simulation, it will only affect the new increments of tangential contact force. This fact makes it possible for the PFC^{3D} code to handle arbitrary placement of balls and changes in ball radius after a simulation has begun.

4.3.2.1 Linear elastic contact model

The linear elastic contact model is employed in this study. In the linear elastic contact model, contact forces and relative contact displacements are linearly related by constant contact stiffnesses, which are functions of the intrinsic contact stiffnesses of the two contacting entities. The linear elastic contact model is defined by the normal contact stiffness K_N and tangential contact stiffness k_T (force/displacement) of the two contacting entities (ball-to-ball or ball-to-wall).

K_N and k_T relate contact force and relative contact displacement in the normal and tangential directions via Eqs. (4-1) and (4-2). The normal contact stiffness is a secant stiffness since it relates the total normal contact force f_N to the total normal contact displacement d_N, whereas the tangential contact stiffness is a tangent stiffness since it relates the increment of tangential contact force Δf_T to the increment of tangential contact displacement Δd_T.

$$f_N = K_N\, d_N \qquad \text{..............................} \quad (4\text{-}1)$$

$$\Delta f_T = k_T\, \Delta d_T \qquad \text{..............................} \quad (4\text{-}2)$$

The contact stiffnesses, when two particles interact, are computed assuming that the stiffnesses of the two contacting entities act in series. The secant normal contact stiffness and tangent tangential contact stiffness are, therefore, defined by;

$$K_N = \frac{K_N^A K_N^B}{K_N^A + K_N^B} \qquad \text{...............................} \ (4\text{-}3)$$

$$k_T = \frac{k_T^A k_T^B}{k_T^A + k_T^B} \qquad \text{...............................} \ (4\text{-}4)$$

where the superscripts *A* and *B* denote the entities in contact (ball-to-ball or ball-to-wall).

4.3.2.2 Criteria for particle sliding

Particle sliding occurs when the tangential contact force reaches its maximum allowable value which is taken to be the minimum coefficient of inter-particle friction angle of the two contacting entities multiplied by the magnitude of the normal contact force. Every contact is checked for particle sliding by calculating the maximum allowable tangential contact force;

$$f_{T,max} = \tan \phi_{\mu,min} f_N \qquad \text{...............................} \ (4\text{-}5)$$

where $f_{T,max}$ is the maximum allowable tangential contact force, $\phi_{\mu,min}$ is the minimum inter-particle friction angle of the two contacting entities, and f_N is the normal contact force.

When the particle sliding occurs, the magnitude of the tangential contact force is scaled down to remain at its maximum allowable value.

4.3.3 Micromechanics parameters

During the analysis, several micromechanics quantities can be obtained over spherical volumes (referred to as a “measurement sphere”) positioned at user-selected locations in the model. These quantities include coordination number, porosity, sliding fraction, stress, and strain rate. However, the only micromechanics parameter relevant to this study is the porosity and void ratio.

Porosity *n* is defined as the ratio of the total void volume within the measurement sphere to the measurement sphere volume;

$$n = \frac{V_{void}}{V_{sphere}} = \frac{V_{sphere} - V_{ball}}{V_{sphere}} = 1 - \frac{V_{ball}}{V_{sphere}} \qquad \text{(4-6)}$$

where V_{sphere} and V_{void} are the volumes of the measurement sphere and the void, and V_{ball} is the volume of the measurement sphere occupied by the balls. V_{ball} is computed by;

$$V_{ball} = \sum_{N_p} V_p - V_{overlap} \qquad \text{(4-7)}$$

where N_p is the number of particles that intersect the measurement sphere, V_p is the volume of particle p contained within the measurement sphere, and $V_{overlap}$ is the volume of particle overlap contained within the measurement sphere. Note that both partial volumes of particles that intersect the measurement sphere and particle overlaps arising from normal contact forces are accounted for in this computation.

Once porosity is obtained, the void ratio e can be computed by;

$$e = \frac{n}{1-n} \qquad \text{(4-8)}$$

4.4 DEM analysis by *PFC*^{3D}

4.4.1 Numerical modeling

The experimental set-ups described in Chapter 3 were modeled by PFC^{3D} for the DEM analysis. The modeling strategies are described as follow.

4.4.1.1 Tank and pipe

The tank and pipe were modeled by series of planar wall. The dimensions of the tank were the same as the actual tank for the cases of $H/D < 30$ and $H_c/D < 30$, whereas the width was doubled for the cases of $H/D \geq 30$ and $H_c/D \geq 30$. The pipe cannot be modeled as a cylindrical shape due to the fact that the wall in PFC^{3D} has to be always in plane. Therefore, the circular cross-section of the pipe was approximately modeled by a 16-side polygon (see Fig. 4-2). The tank wall was assumed to be smooth; the tank model has a normal contact stiffness equal to that of the particles but has zero tangential contact stiffness and zero surface friction. The pipe has identical contact stiffness in both normal and tangential directions and equal to that of the particles. The pipe has its surface friction angle equal to half of the inter-particle friction angle of sand. The parametric study (Appendix H and I) shows that the change in the pipe surface friction angle between $\phi_{pipe} = \phi_\mu/2$ and $\phi_{pipe} = \phi_\mu$ has negligible effects on the pipe loading results.

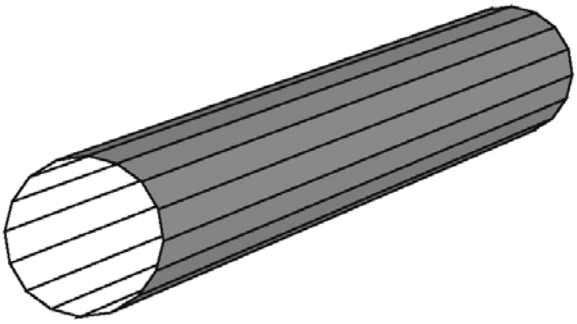

Figure 4-2 DEM model of pipe

4.4.1.2 Sand particles

Sand was modeled as a collection of spherical particles with its size distribution follows normal distribution. Due to computational limitation, it was not possible to model using the actual particle size (D_{10} = 0.2 mm and D_{60} = 0.52 mm) because the number of balls reaches several hundreds thousand. Therefore, the sand particles were modeled by using larger sizes than actual sand with varying sizes in various regions of the model. For the cases of $H/D < 30$ and $H_c/D < 30$, the numerical models are shown in Fig. 4-3 which are identical to the size of experimental tank test by Trautmann & O'Rourke (1983). At the region near the pipe (Region A), the particles are smaller with $r_{average}$ = 12.5 mm and standard deviation = 2.5 mm (25 times larger than actual sand). Further away (Region B), the particles are larger with $r_{average}$ = 25.0 mm and standard deviation = 5.0 mm (50 times larger). When $H/D \geq 17.5$ (for lateral pipe loading) or $H_c/D \geq 17$ (for upward pipe loading), there is Region C with the particle size of $r_{average}$ = 37.5 mm and standard deviation = 7.5 mm (75 times larger). For the cases of $H/D \geq 30$ and $H_c/D \geq 30$, the numerical models are shown in Fig. 4-4 which have their width doubled to reduce boundary interference. At Region D, the particles have $r_{average}$ = 25.0 mm and standard deviation = 5.0 mm (50 times larger than actual sand). Further away (Region E), the particles are larger with $r_{average}$ = 37.5 mm and standard deviation = 7.5 mm (75 times larger). This allowed the number of particles to be less than 180,000 for deepest case. The effects of the extent of the fine particles on the numerical analysis results are also investigated in the parametric study (Appendix H and I). The results show that the extent of fine particles of three time of the diameter of the pipe give acceptable results. The normal and tangential contact stiffnesses of the particles are assumed to be equal ($K_N = k_T$).

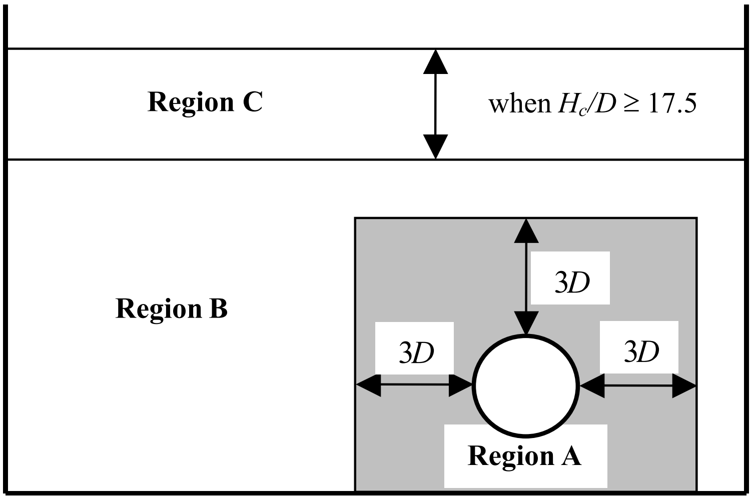

(a) Lateral pipe loading

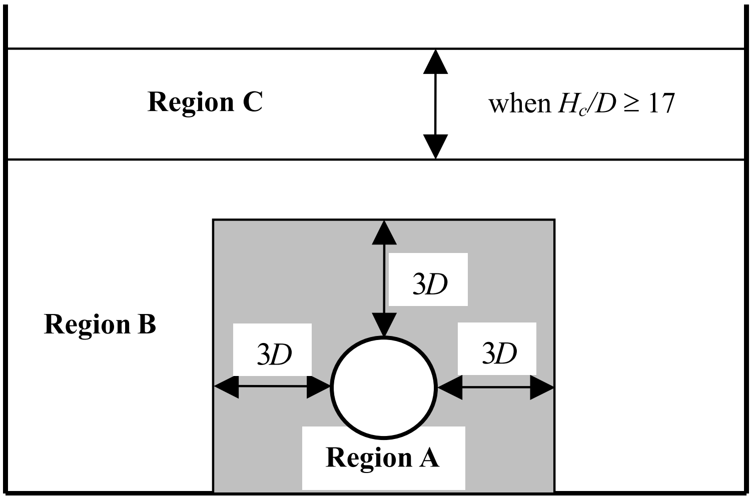

(b) Upward pipe loading

Figure 4-3 Various regions of the DEM model ($H/D < 30$ and $H_c/D < 30$)

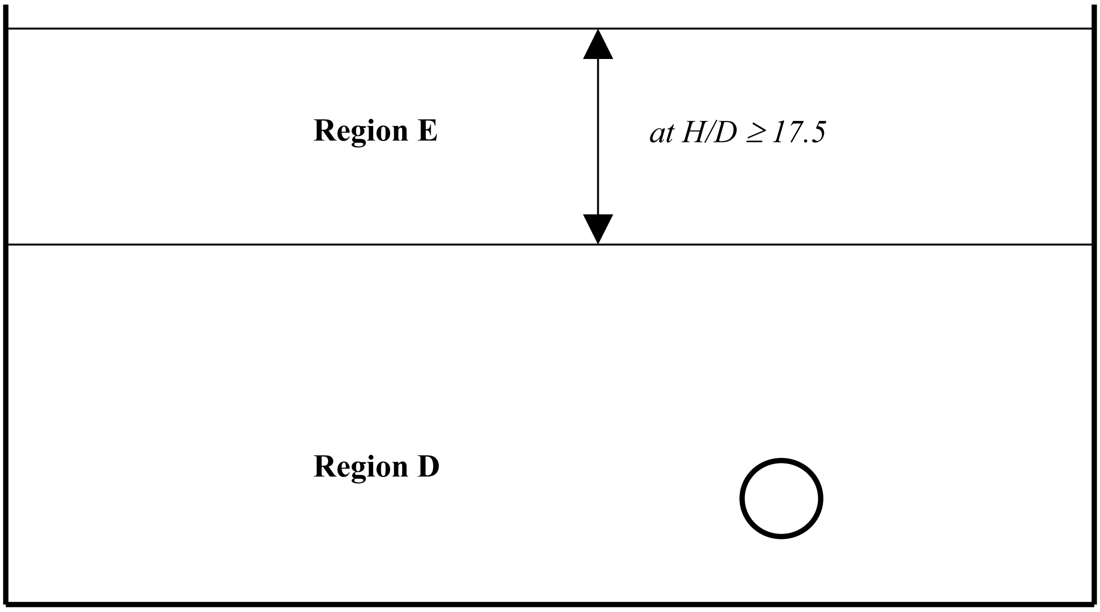

(a) Lateral pipe loading

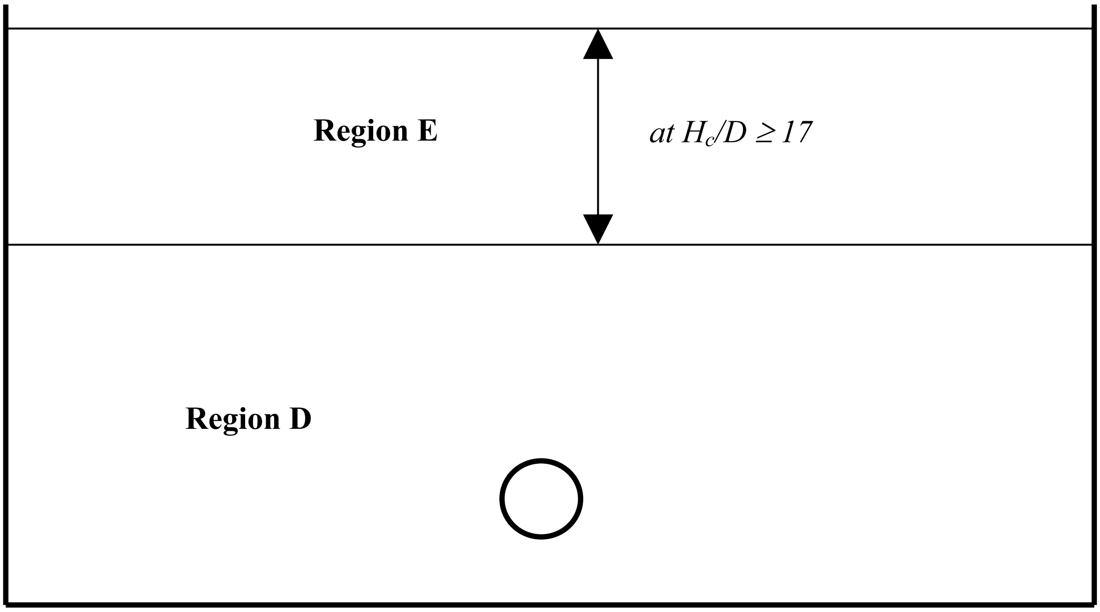

(b) Upward pipe loading

Figure 4-4 Various regions of the DEM model ($H/D \geq 30$ and $H_c/D \geq 30$)

4.4.2 Numerical analysis procedures

The DEM analysis procedures consist of 4 main steps which are explained as follow.

4.4.2.1 Tank set-up

Test tank was numerically prepared by filling the predetermined number of reduce-sized particles into the required cubical space before radius expansion of the spheres to a specified value to obtain predetermined void ratio of the specimen. The specimen preparation method by this radius-expansion has some advantages over the wall-moving method in which the full-sized particles are filled into the cubical space and the positions of the boundary walls are adjusted until the required void ratio is achieved. The radius-expansion method results in more isotropic and uniform specimen, needs less time to reach equilibrium, and preserves the boundary geometry (Itasca, 1999).

4.4.2.2 Initial condition

After set-up, the generated balls were subjected to gravitational force to reach the geostatic condition. During this stage, there were some movement of balls and change in void ratio of the specimen. The initial void ratios of the specimens were adjusted (by trial & error) in order to obtain the required void ratios at the end of the initial condition step. The change of the embedment depth (H or H_c) during this stage was also taken into account (by trial & error).

4.4.2.3 Pipe installation

The pipe was placed into the model by deleting the balls which were located at the desired location before the pipe was installed. The model was then allowed to reach equilibrium again by allowing the pipe to slightly adjust its location by keeping the conditions of $\Sigma F_x = 0$ and $\Sigma F_y = 0$. The examples of the DEM model after pipe installation are shown in Fig. 4-5.

4.4.2.4 Pipe pulling

The pipe was pulled laterally or upwardly by imposing lateral or upward displacement to the pipe. In this manner, the rotation of the pipe was not allowed in the DEM simulation, which is consistent with the experimental set-up and in-situ condition. As reported by Trautmann & O'Rourke (1983) for lateral pipe pulling, the magnitude of the measured torque was negligible with respect to the strength of the pipe in all cases. This means that, in the in-situ condition, the nearby sections of the pipe will restrict the rotation of the laterally loaded section.

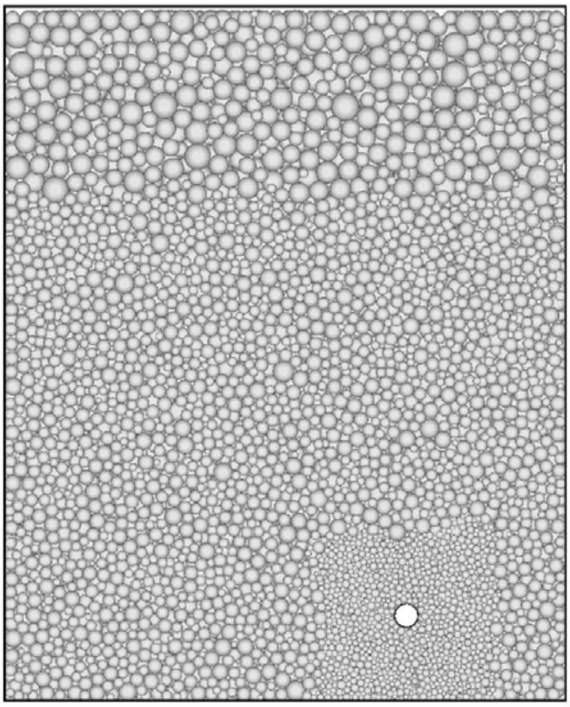

(a) Lateral pipe loading (medium sand, H/D = 25)

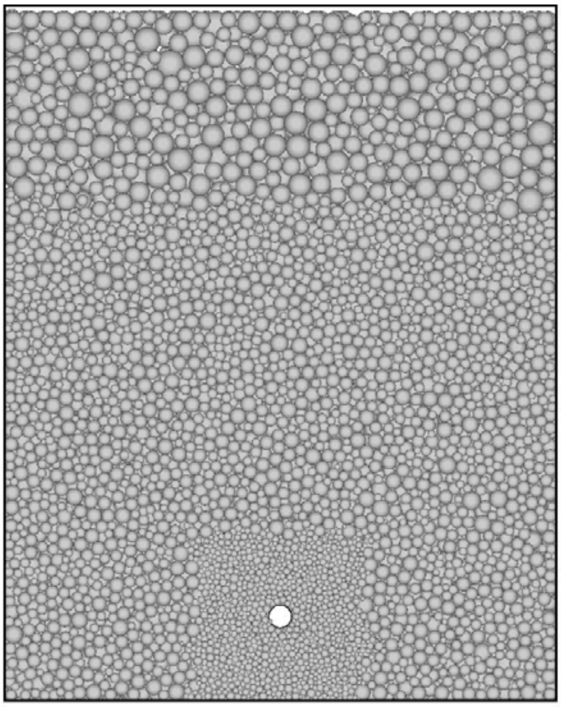

(b) Upward pipe loading (medium sand, H_c/D = 25)

Figure 4-5 Examples of DEM model

4.5 Determination of input parameters

The input parameters for DEM modelling are listed in Table 4-1. These parameters are very difficult to quantify by laboratory tests because the parameters are of micro-scale. Therefore, most parameters are determined from trial&error by calibrating the numerical results with the experimental data of (i) triaxial test results by Turner & Kulhawy (1987) and (ii) pipe loading test results at shallow depth by Trautmann & O'Rourke (1983). In the following, the determination of the input parameters are described.

Table 4-1 Input parameters for DEM analysis

Parameters	Values
Normal contact stiffness of particle, $k_{N,sand}$	From Eqs. (4-10) and (4-11)
Tangent contact stiffness of particle, $k_{T,sand}$	$k_{T,sand} = k_{N,sand}$
Normal contact stiffness of pipe, $k_{N,pipe}$	$k_{N,pipe} = k_{N,sand}$
Tangent contact stiffness of pipe, $k_{T,pipe}$	$k_{T,pipe} = k_{N,pipe}$
Normal contact stiffness of wall, $k_{N,wall}$	$k_{N,wall} = k_{N,sand}$
Tangent contact stiffness of wall, $k_{T,wall}$	$k_{T,wall} = 0$
Inter-particle friction angle, ϕ_μ	$\tan \phi_\mu = 0.5, 1.0, 3.0$
Pipe surface friction angle, ϕ_{pipe}	$\phi_{pipe} = \phi_\mu/2$
Tank wall surface friction angle, ϕ_{wall}	$\phi_{wall} = 0$
Density of particle, ρ (kg/m^3)	2740
Radius of particle, r	Varies in Regions A, B, C, D, E

4.5.1 Triaxial tests

The triaxial test data on Cornell filter sand was simulated by DEM analysis. The selected experimental details are given in Table 4-2. Table 4-3 presents the detail of DEM simulation. Fig. 4-6 shows that the DEM analysis can simulate the stress-strain relationship from triaxial tests by using a high value of inter-particle friction angle. At low values of the inter-particle friction angle, the match cannot be achieved and the value of $\tan \phi_\mu = 3.0$ is the lowest value that can still yield good match. The requirement of high inter-particle friction angle for DEM simulation is due to the use of spherical particles, which allows excessive particle rolling (e.g. Thomas & Bray, 1999). Fig. 4-7 shows the dependency of the contact stiffness on the confining stress. The relationship can be derived as shown in Eq. (4-9). The obtained power value is within the normal value for soil, which is approximately 0.5 (Hardin & Black, 1966). This is due to the fact that the DEM analysis matches both stiffness and strength from triaxial test. It has been shown that the triaxial stiffness (Young's modulus) has a relationship with confining strress in the same manner as the contact stiffness does (Chang & Liao, 1994).

$$k\ (\text{N/m}) = 204340\, p_o'^{\,0.41} \qquad (p_o' \text{ in kPa}) \qquad \ldots\ldots\ldots\ldots\ldots\ldots \quad (4\text{-}9)$$

Table 4-2 Triaxial test programme (after Turner & Kulhawy, 1987)

Test No.	**Test type**	$\gamma_{dry,o}$* **(kN/m^3)** **(after consoln.)**	e_o* **(after consoln.)**	p_o' **(kPa)**
D-1	CIDC	18.66	0.517	40
D-2	CIDC	17.79	0.540	69
D-3	CIDC	18.05	0.517	98

* estimated from the relevant data because they were not exactly stated in Turner & Kulhawy (1987)

Table 4-3 DEM analysis detail

Test No.	e_o **(after consoln.)**	p_o' **(kPa)**	$k_{N,sand} = k_{T,sand}$ **(N/m)**
D-1	0.515	40	1.0×10^6
D-2	0.517	69	1.2×10^6
D-3	0.497	98	1.5×10^6

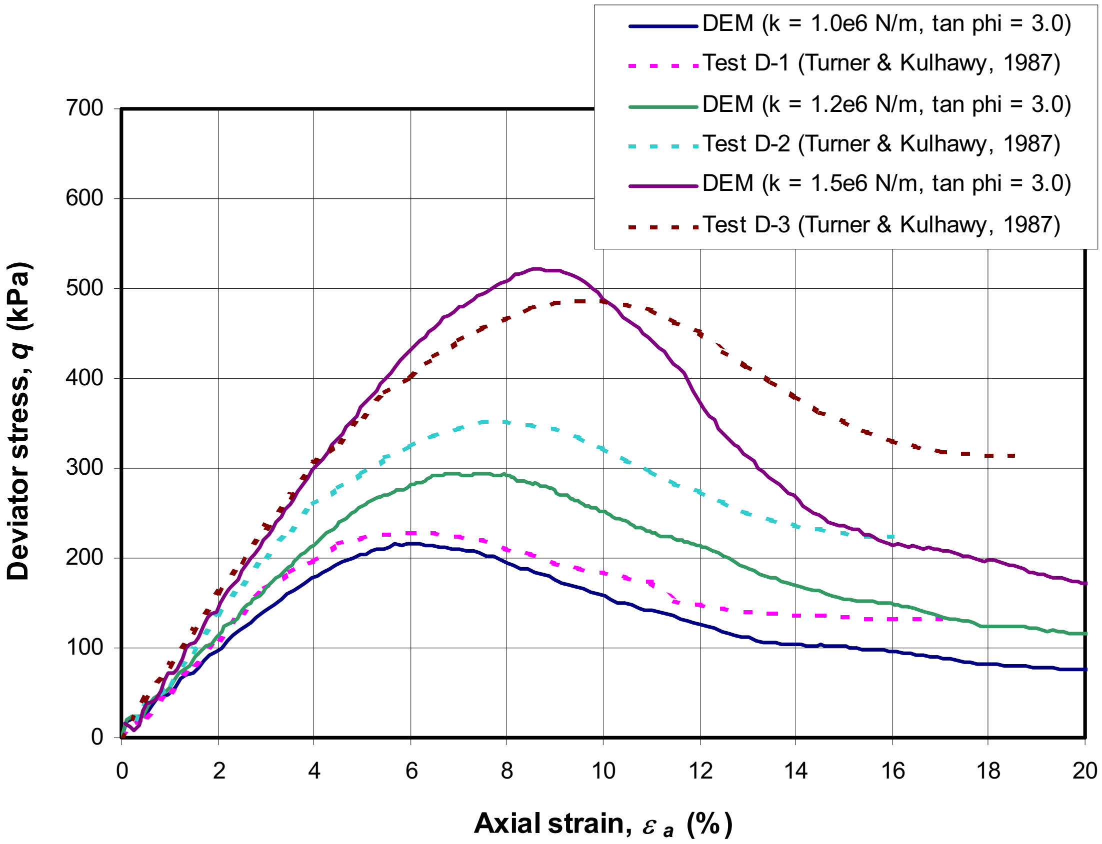

Figure 4-6 Calibration of DEM results against triaxial test data

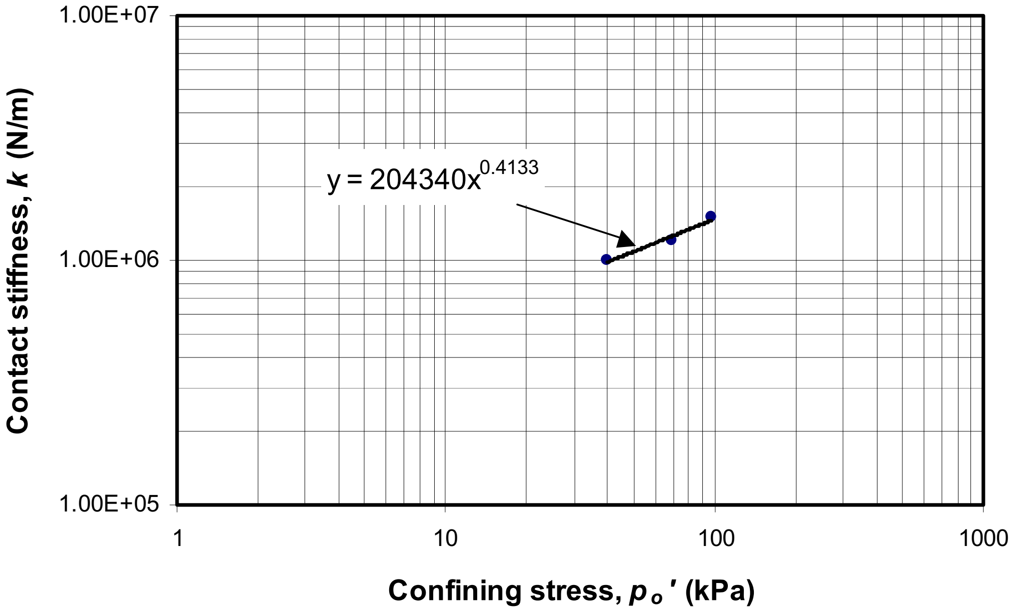

Figure 4-7 Relationship between contact stiffness and confining stress from triaxial simulation

4.5.2 Pipe loading test

It was found that the contact stiffness from Eq. (4-9) could not give a good match when used in the pipe loading simulation. Therefore, the contact stiffness was, instead, derived by fitting the peak forces from the DEM analysis results with the pipe loading data at shallow depths by using tan $\phi_\mu = 0.5, 1.0, 3.0$. It was, at first, intended to use tan $\phi_\mu = 3.0$, which was consistent with the value found from the triaxial simulation. However, it was found that using lower value of the inter-particle friction angles could still achieve good match of the peak forces. The force-displacement curves from the case of lowest tan ϕ_μ (tan $\phi_\mu = 0.5$) yield stiffest results due to the largest contact stiffness used, and vice versa. In lateral and upward pipe loading, the case of tan $\phi_\mu = 0.5$ shows good match with the experimental results at shallow depth (H/D = 2, 4, and 8.5); however, when the embedment depth increases, the case of tan $\phi_\mu = 3.0$ give better match. The resulting force-displacement relationships are presented in Appendix A and B. The obtained relationships between the contact stiffness and the vertical effective stress are shown in Fig. 4-8 and the following relationships are proposed.

<u>Lateral pipe loading</u>

$$\left.\begin{array}{ll} k\,(\text{N/m}) = 2118.095\sigma_c'^{2.201} & \text{for } \tan\phi_\mu = 0.5 \\ k\,(\text{N/m}) = 1576.395\sigma_c'^{1.956} & \text{for } \tan\phi_\mu = 1.0 \\ k\,(\text{N/m}) = 753.261.859\sigma_c'^{1.909} & \text{for } \tan\phi_\mu = 3.0 \end{array}\right\} \text{..................(4-10)}$$

σ_c' (kPa) = vertical effective stress at bottom of pipe

<u>Upward pipe loading</u>

$$\left.\begin{array}{ll} k\,(\text{N/m}) = 6.714\sigma_c'^{3.813} & \text{for } \tan\phi_\mu = 0.5 \\ k\,(\text{N/m}) = 41.072\sigma_c'^{2.761} & \text{for } \tan\phi_\mu = 1.0 \\ k\,(\text{N/m}) = 112.859\sigma_c'^{2.176} & \text{for } \tan\phi_\mu = 3.0 \end{array}\right\} \text{.................. (4-11)}$$

σ_c' (kPa) = vertical effective stress at center of pipe

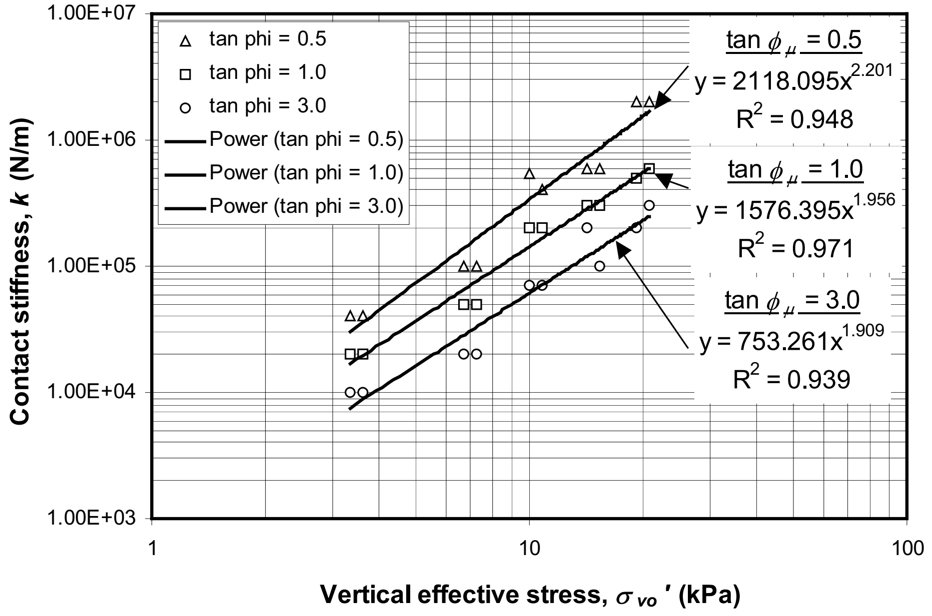

(a) Lateral pipe loading

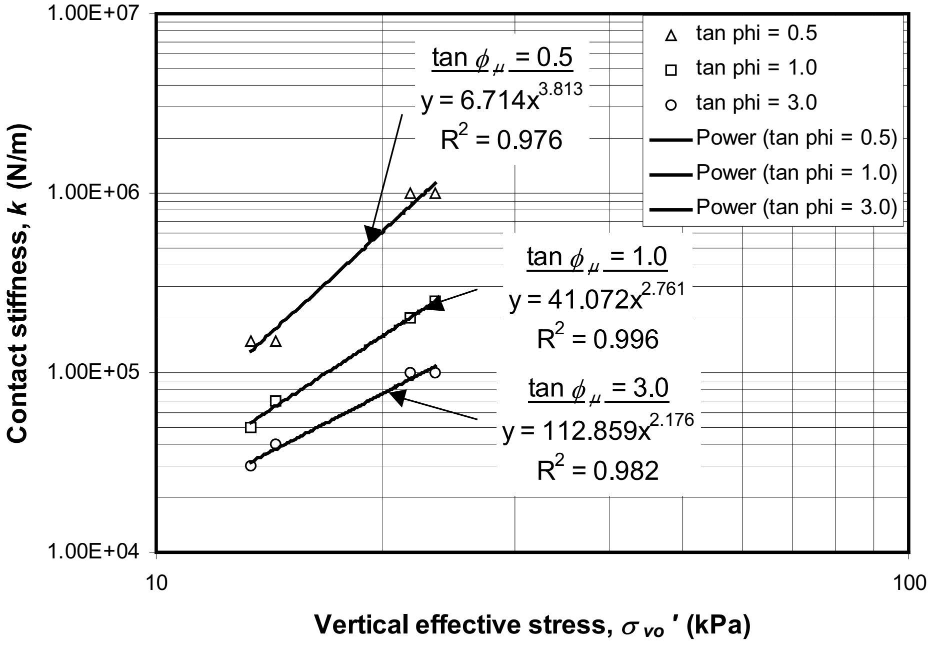

(b) Upward pipe loading

Figure 4-8 Relationship between contact stiffness and confining stress from pipe loading simulation

It is noted that various combinations of the contact stiffness and tan ϕ_μ can yield similar peak forces. With larger tan ϕ_μ, the required contact stiffness is lower. It is interesting to find that the contact stiffness affects the strength (peak force) of pipe loading problem, which is not the case for triaxial problem where the contact stiffness affects only modulus, not strength (see Appendix G). This may be due to the more complex mode of shearing in pipe loading problem. It is also noted that the obtained power value is greater than 0.5 which is the normal value for soil (Hardin & Black, 1966); this may be also due to the complexity of mode of loading. The peak force values employed for fitting is governed by complex pipeline-soil interaction at relatively large strain; however, the contact stiffness is the behavior at very small strain

4.6 Determination of peak force from DEM analysis results

The peak forces from the DEM analysis results were determined by the following criteria:-

(a) The peak force was defined as a largest force of the force-displacement curve or as a force which reaches the constant value with increasing pipe displacement.

(b) When the condition of peak or constant load was not achieved because the analysis could not continue far enough to reach this condition, a rectangular hyperbola was used to fit the data as suggested by Trautmann & O'Rourke (1983).

Using the procedure described by Konder (1963), the force-displacement data for each test were plotted on the transformed axes of δ/F and δ, where δ is the pipe displacement and F is the force exerted on the pipe. A linear regression was then fitted to the data to obtain the slope, b, and the δ/F-axis intercept, a. The force-displacement can then be approximated as;

$$F = \frac{\delta}{a + b\delta} \qquad \text{………………..} (4\text{-}12)$$

where $1/a = \lim_{\delta \to 0}(\partial F / \partial \delta)$ = initial stiffness of force-displacement curve

$1/b = \lim_{\delta \to \infty}(F)$ = peak force

However, as described by Duncan (1980), the hyperbolic model commonly overestimates peak force values. In the instances when an peak force could be determined or reasonably estimated, the hyperbola was found to overpredict the actual ultimate force by an average of 11%. This trend can be characterised by a failure ratio R_f of 0.9. This correction value was then applied to all results, i.e. $F_{peak} = 0.9(1/b)$.

An example of the hyperbolic fitting is shown in Fig. 4-9.

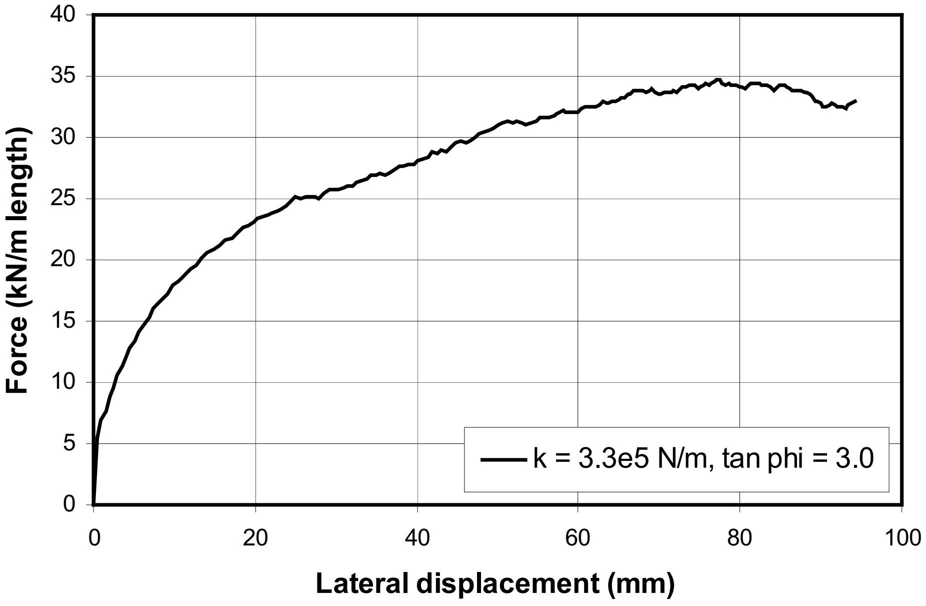

(a) Force-displacement relationship

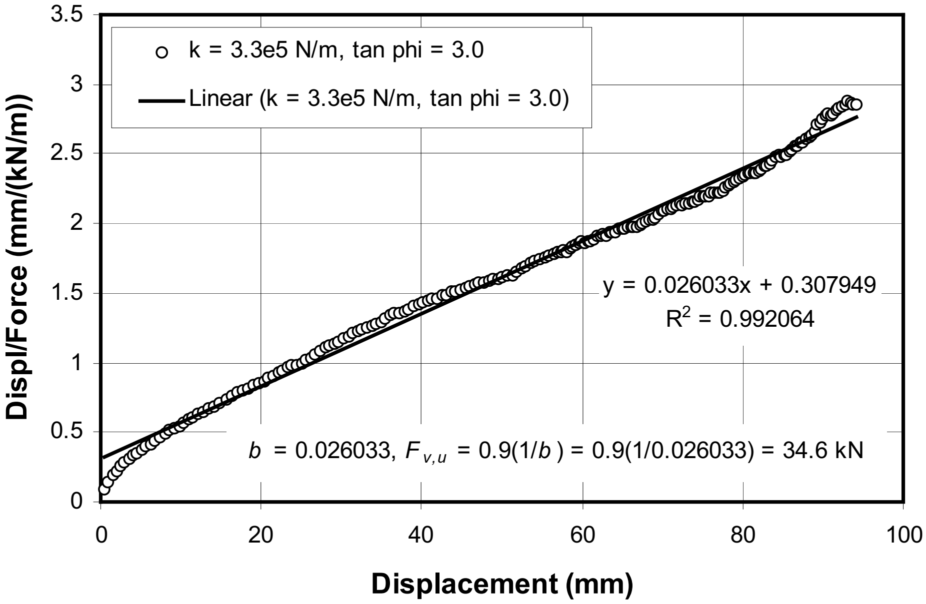

(b) $\delta_v/F_v \sim \delta_v$ relationship

Figure 4-9 Peak force determination by hyperbolic fitting for lateral pipe loading, medium sand, $H/D = 14.5$

Chapter 5

DEM analyses of pipe under lateral loading

5.1 Analysis procedure and program

The geometry of the numerical model was based on the experimental study by Trautmann & O'Rourke (1983). For all cases of medium sand and the cases of dense sand with $H/D < 30$, all dimensions of the numerical model are the same as those of the experimental set-up except that the embedment depth was adjusted to the required value (Fig. 5-1a). For dense sand with $H/D \geq 30$, the width of the model was doubled to reduce the effect of boundary interference. The analyses were performed for medium and dense sands.

The tank and pipe were modelled by series of planar wall. Sand was modelled as a collection of spherical particles and the size distribution follows normal distribution. The tank wall was assumed to be smooth; the tank model has a normal contact stiffness equal to that of the particles but has zero tangential contact stiffness and zero surface friction. The pipe has identical contact stiffness in both normal and tangential directions and equal to that of the particles. The pipe has its surface friction angle equal to half of the inter-particle friction angle of sand. The pipe was pulled laterally by imposing lateral displacement to the pipe. In this manner, the rotation of the pipe was not allowed in the DEM simulation, which is consistent with the experimental set-up and in-situ condition. As reported by Trautmann & O'Rourke (1983), the magnitude of the measured torque was negligible with respect to the strength of the pipe in all cases. This means that, in the in-situ condition, the nearby sections of the pipe will restrict the rotation of the laterally loaded section. The DEM analysis program is shown in Tables 5-1 and 5-2.

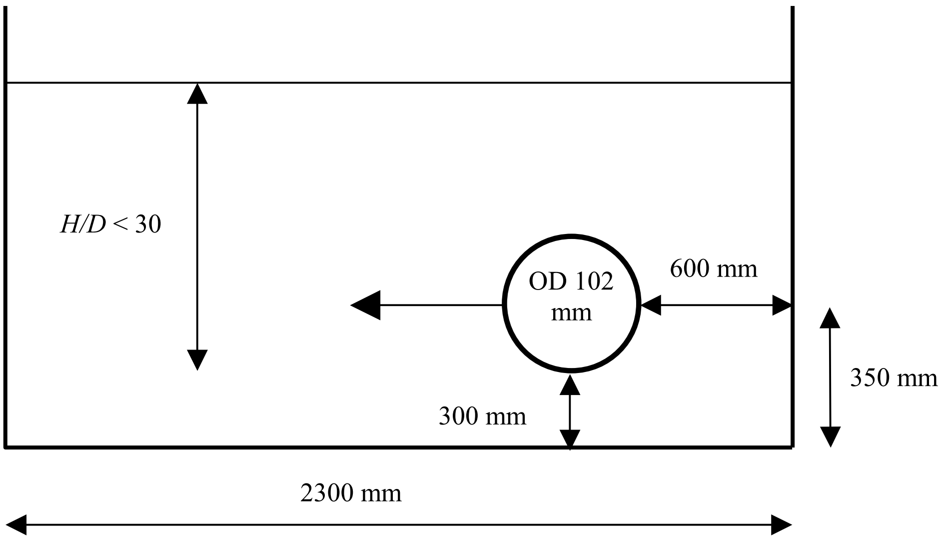

(a) for all cases of medium sand and the cases of dense sand with $H/D < 30$

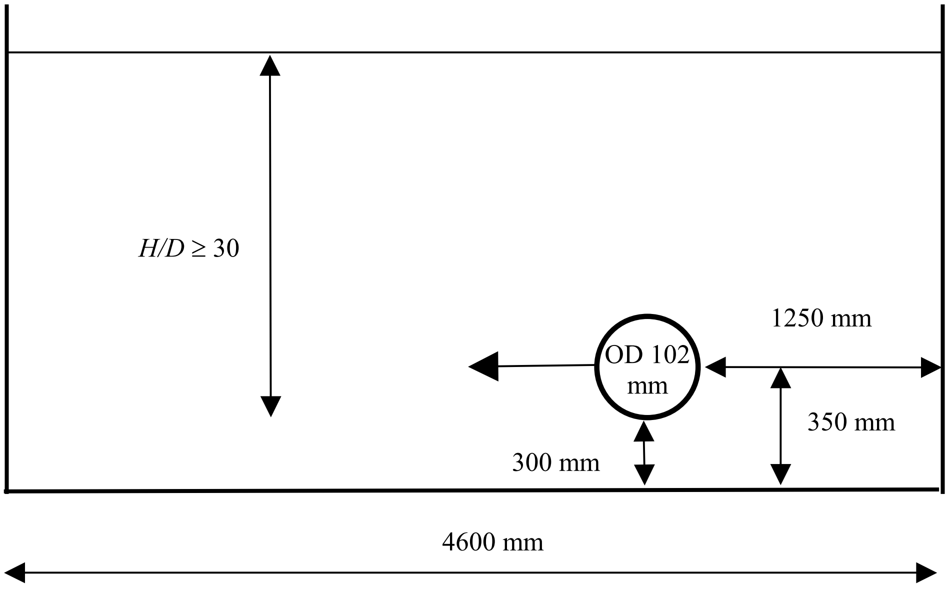

(b) for dense sand with $H/D \geq 30$

Figure 5-1 Geometry of the DEM analyses of lateral pipe loading

Table 5-1 Summary of DEM analysis program and their input parameters: medium sand

Test No.	***H/D***	**Case of tan $\phi_\mu = 0.5$**		**Case of tan $\phi_\mu = 1.0$**		**Case of tan $\phi_\mu = 3.0$**	
		tan ϕ_μ	**$k_{N,sand}$ (N/m)**	**tan ϕ_μ**	**$k_{N,sand}$ (N/m)**	**tan ϕ_μ**	**$k_{N,sand}$ (N/m)**
LMHD2	2	0.5	4.0×10^4	1.0	2.0×10^4	3.0	1.0×10^4
LMHD4	4	0.5	1.0×10^5	1.0	5.0×10^4	3.0	2.0×10^4
LMHD6	6	0.5	5.5×10^5	1.0	2.0×10^5	3.0	7.0×10^4
LMHD85	8.5	0.5	6.0×10^5	1.0	3.0×10^5	3.0	2.0×10^5
LMHD115	11.5	0.5	2.0×10^6	1.0	5.0×10^5	3.0	2.0×10^5
LMHD145	14.5	0.5	2.4×10^6	1.0	8.1×10^5	3.0	3.3×10^5
LMHD175	17.5	0.5	3.6×10^6	1.0	1.2×10^6	3.0	4.8×10^5
LMHD22	22	0.5	5.9×10^6	1.0	1.8×10^6	3.0	7.4×10^5
LMHD25	25	0.5	7.8×10^6	1.0	2.3×10^6	3.0	9.4×10^5
LMHD30	30	0.5	1.2×10^7	1.0	3.3×10^6	3.0	1.3×10^6
LMHD40	40	0.5	2.2×10^7	1.0	5.9×10^6	3.0	2.3×10^6
LMHD60	60	0.5	5.4×10^7	1.0	1.3×10^7	3.0	5.0×10^6

Note: 1. $k_{N,sand} = k_{T,sand} = k_{N,pipe} = k_{T,pipe} = k_{N,wall}$

2. $k_{T,wall} = 0$

3. $\phi_{pipe} = \phi_\mu/2$

4. $\phi_{wall} = 0$

Table 5-2 Summary of DEM analysis program and their input parameters: dense sand

Test No.	***H/D***	**Case of $\tan\phi_\mu = 0.5$**		**Case of $\tan\phi_\mu = 1.0$**		**Case of $\tan\phi_\mu = 3.0$**	
		$\tan\phi_\mu$	**$k_{N,sand}$ (N/m)**	**$\tan\phi_\mu$**	**$k_{N,sand}$ (N/m)**	**$\tan\phi_\mu$**	**$k_{N,sand}$ (N/m)**
LDHD2	2	0.5	4.0×10^4	1.0	2.0×10^4	3.0	1.0×10^4
LDHD4	4	0.5	1.0×10^5	1.0	5.0×10^4	3.0	2.0×10^4
LDHD6	6	0.5	4.0×10^5	1.0	2.0×10^5	3.0	7.0×10^4
LDHD85	8.5	0.5	6.0×10^5	1.0	3.0×10^5	3.0	1.0×10^5
LDHD115	11.5	0.5	2.0×10^6	1.0	6.0×10^5	3.0	3.0×10^5
LDHD145	14.5	0.5	2.8×10^6	1.0	9.4×10^5	3.0	3.8×10^5
LDHD175	17.5	0.5	4.2×10^6	1.0	1.4×10^6	3.0	5.5×10^5
LDHD22	22	0.5	7.0×10^6	1.0	2.1×10^6	3.0	8.5×10^5
LDHD25	25	0.5	9.3×10^6	1.0	2.7×10^6	3.0	1.1×10^6
LDHD30*	30	0.5	1.4×10^7	1.0	3.9×10^6	3.0	1.5×10^6
LDHD40*	40	0.5	2.6×10^7	1.0	6.8×10^6	3.0	2.7×10^6
LDHD60*	60	0.5	6.4×10^7	1.0	1.5×10^7	3.0	5.8×10^6

Note: 1. $k_{N,sand} = k_{T,sand} = k_{N,pipe} = k_{T,pipe} = k_{N,wall}$

2. $k_{T,wall} = 0$

3. $\phi_{pipe} = \phi_\mu/2$

4. $\phi_{wall} = 0$

5. * bigger tank

5.2 Input parameters

The input parameters for DEM models were determined as described in Section 4.5. The input parameters for all DEM analyses are presented in Tables 5-1 and 5-2. For the cases of $2 \le H/D \le 11.5$, the values of $k_{N,sand}$ were derived from fitting peak forces from the DEM analysis with the results of pipe loading experiment (as described in Section 4.5.2). For the cases of $14.5 \leq H/D \leq 60$, the values of $k_{N,sand}$ were derived from the obtained relationships from shallow depths as follow.

$$\left.\begin{array}{ll} k\ (\text{N/m}) = 2118.095\sigma_c'^{2.201} & \text{for } \tan\phi_\mu = 0.5 \\ k\ (\text{N/m}) = 1576.395\sigma_c'^{1.956} & \text{for } \tan\phi_\mu = 1.0 \\ k\ (\text{N/m}) = 753.261.859\sigma_c'^{1.909} & \text{for } \tan\phi_\mu = 3.0 \end{array}\right\} \ldots\ldots\ldots\ldots\ldots\ldots\ldots \quad (5\text{-}1)$$

σ_c' (kPa) = vertical effective stress at bottom of pipe

5.3 DEM analysis results of shallow embedment depths

In this section, the DEM results of shallow embedment depths ($H/D \leq 11.5$) are presented and compared with the experimental results by Trautmann & O'Rourke (1983) to examine the accuracy of the DEM analysis. The results in terms of the hyperbolic force-displacement relationship, the peak forces, and the corresponding pipe displacement are summarized in Tables 5-3 and 5-4.

Table 5-3 DEM analysis results: medium sand

H/D	**tan $\phi_\mu = 0.5$**			**tan $\phi_\mu = 1.0$**			**tan $\phi_\mu = 3.0$**		
	Hyperbolic fit	**$F_{h,peak}$ (kN)**	**$\delta_{h,peak}$ (mm)**	**Hyperbolic fit**	**$F_{h,peak}$ (kN)**	**$\delta_{h,peak}$ (mm)**	**Hyperbolic fit**	**$F_{h,peak}$ (kN)**	**$\delta_{h,peak}$ (mm)**
2	—	2.2	28.0	—	2.2	40.0	—	2.2	46.0
4	—	5.1	33.3	—	5.8	50.6	—	5.6	66.8
6	—	10.5	64.2	—	12.0	69.6	—	11.4	63.7
8.5	$F_h = \frac{\delta_h}{0.0630\delta_h + 0.3813}$	14.3	55.0	$F_h = \frac{\delta_h}{0.0538\delta_h + 0.3347}$	16.7	55.0	$F_h = \frac{\delta_h}{0.0475\delta_h + 0.4190}$	19.0	81.7
11.5	$F_h = \frac{\delta_h}{0.0414\delta_h + 0.2302}$	21.7	49.2	$F_h = \frac{\delta_h}{0.0365\delta_h + 0.2143}$	24.7	53.8	$F_h = \frac{\delta_h}{0.0358\delta_h + 0.3516}$	25.1	87.0
14.5	$F_h = \frac{\delta_h}{0.0372\delta_h + 0.2751}$	24.2	66.7	$F_h = \frac{\delta_h}{0.0282\delta_h + 0.2530}$	31.9	80.4	$F_h = \frac{\delta_h}{0.0260\delta_h + 0.3079}$	34.6	106.1
17.5	$F_h = \frac{\delta_h}{0.0337\delta_h + 0.1726}$	26.7	46.0	$F_h = \frac{\delta_h}{0.0210\delta_h + 0.2133}$	42.9	92.3	$F_h = \frac{\delta_h}{0.0196\delta_h + 0.3286}$	45.9	150.3

22	$F_h = \dfrac{\delta_h}{0.0281\delta_h + 0.1956}$	32.0	62.1	$F_h = \dfrac{\delta_h}{0.0169\delta_h + 0.1339}$	53.2	70.6	$F_h = \dfrac{\delta_h}{0.0162\delta_h + 0.2185}$	55.4	118.1
25	$F_h = \dfrac{\delta_h}{0.0294\delta_h + 0.0955}$	30.6	29.1	$F_h = \dfrac{\delta_h}{0.0205\delta_h + 0.1018}$	44.0	45.7	$F_h = \dfrac{\delta_h}{0.0147\delta_h + 0.1748}$	61.3	108.4
30	$F_h = \dfrac{\delta_h}{0.0226\delta_h + 0.1235}$	39.8	48.9	—	86.7	38.7	$F_h = \dfrac{\delta_h}{0.0114\delta_h + 0.1882}$	78.7	114.1
40	$F_h = \dfrac{\delta_h}{0.0256\delta_h + 0.0612}$	35.1	21.2	$F_h = \dfrac{\delta_h}{0.0158\delta_h + 0.0808}$	57.0	46.3	$F_h = \dfrac{\delta_h}{0.0103\delta_h + 0.1164}$	87.0	97.5
60	$F_h = \dfrac{\delta_h}{0.0209\delta_h + 0.0326}$	43.0	13.8	$F_h = \dfrac{\delta_h}{0.0118\delta_h + 0.0450}$	76.1	33.6	$F_h = \dfrac{\delta_h}{0.0092\delta_h + 0.0544}$	97.7	52.5

Note: F_h is in kN/m length.

δ_h is in mm.

Table 5-4 DEM analysis results: dense sand

H/D	**tan $\phi_\mu = 0.5$**			**tan $\phi_\mu = 1.0$**			**tan $\phi_\mu = 3.0$**		
	Hyperbolic fit	**$F_{h,peak}$ (kN)**	**$\delta_{h,peak}$ (mm)**	**Hyperbolic fit**	**$F_{h,peak}$ (kN)**	**$\delta_{h,peak}$ (mm)**	**Hyperbolic fit**	**$F_{h,peak}$ (kN)**	**$\delta_{h,peak}$ (mm)**
2	—	2.5	10.7	—	2.5	35.9	—	2.5	55.4
4	—	6.2	21.5	—	7.3	35.8	—	6.8	79.0
6	—	13.6	15.7	—	17.0	42.2	—	15.3	79.5
8.5	—	23.2	39.0	—	26.2	64.0	—	21.5	93.6
11.5	—	39.5	29.2	—	44.7	40.1	—	49.7	68.4
14.5	—	49.0	9.6	—	59.7	45.2	—	63.1	75.7
17.5	—	64.3	9.5	$F_h = \dfrac{\delta_h}{0.0121\delta_h + 0.0569}$	74.1	40.8	$F_h = \dfrac{\delta_h}{0.0105\delta_h + 0.1565}$	85.3	127.9
22	—	110.9	8.3	—	107.7	35.7	—	104.8	55.6
25	—	122.5	7.8	—	117.7	27.4	—	126.9	59.7

30	—	170.6	22.5	—	167.6	42.5	$F_h = \dfrac{\delta_h}{0.0056\delta_h + 0.1239}$	161.3	199.8
40	—	300.7	8.0	$F_h = \dfrac{\delta_h}{0.0038\delta_h + 0.0285}$	234.8	67.0	$F_h = \dfrac{\delta_h}{0.0032\delta_h + 0.0727}$	278.6	202.6
60	—	852.9	10.0	$F_h = \dfrac{\delta_h}{0.0016\delta_h + 0.0077}$	417.8	63.5	$F_h = \dfrac{\delta_h}{0.0020\delta_h + 0.0390}$	449.6	175.4

Note: F_h is in kN/m length.

δ_h is in mm.

The comparison of the force-displacement curves from the DEM analyses with the experimental results is shown in Appendix A. The peak forces from DEM results were forced to match the experimental results by adjusting the values of contact stiffness by trial & error. For medium sand, the force-displacement curves from DEM match the experimental results well. However, for dense sand, the force-displacement curves from DEM show little difference from the experimental results and the difference is more for the case of tan ϕ_μ = 3.0.

Fig. 5-2 presents the peak dimensionless forces plotted against *H/D*. The results show that the DEM analysis can simulate the problem of soil-pipeline interaction reasonably well.

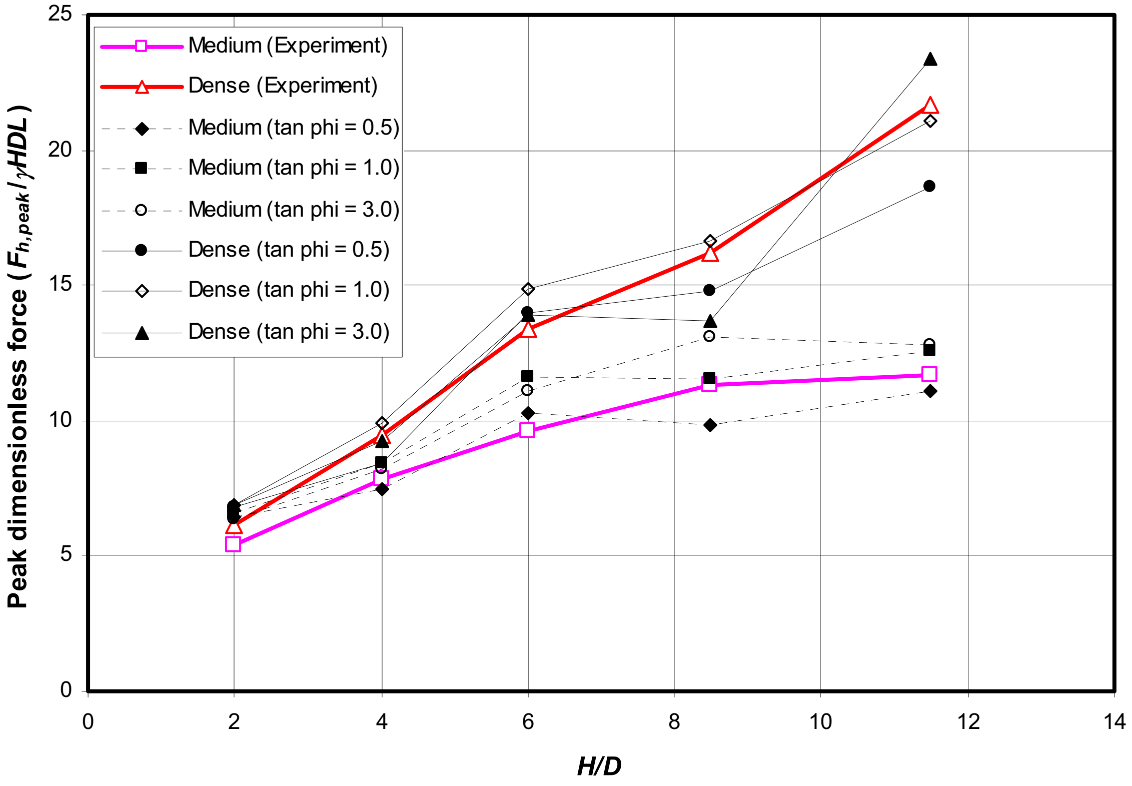

Figure 5-2 Plots of peak dimensionless force against *H/D*

Fig 5-3 shows the normalized peak displacements (pipe displacement at peak force normalized by embedment depth) at different *H/D*s. The data found in the experiments by Trautmann & O'Rourke (1983) are also included in the figure. At 2 ≤ *H/D* ≤ 6, the dimensionless peak displacements from the DEM analysis are larger than those from the experiment, whereas, at *H/D* = 8.5 and 11.5, these two results become more consistent. The dimensionless peak displacement shows the trend to decrease with *H/D*, which is opposite to the experimental results reported by Dickin & Leung (1983).

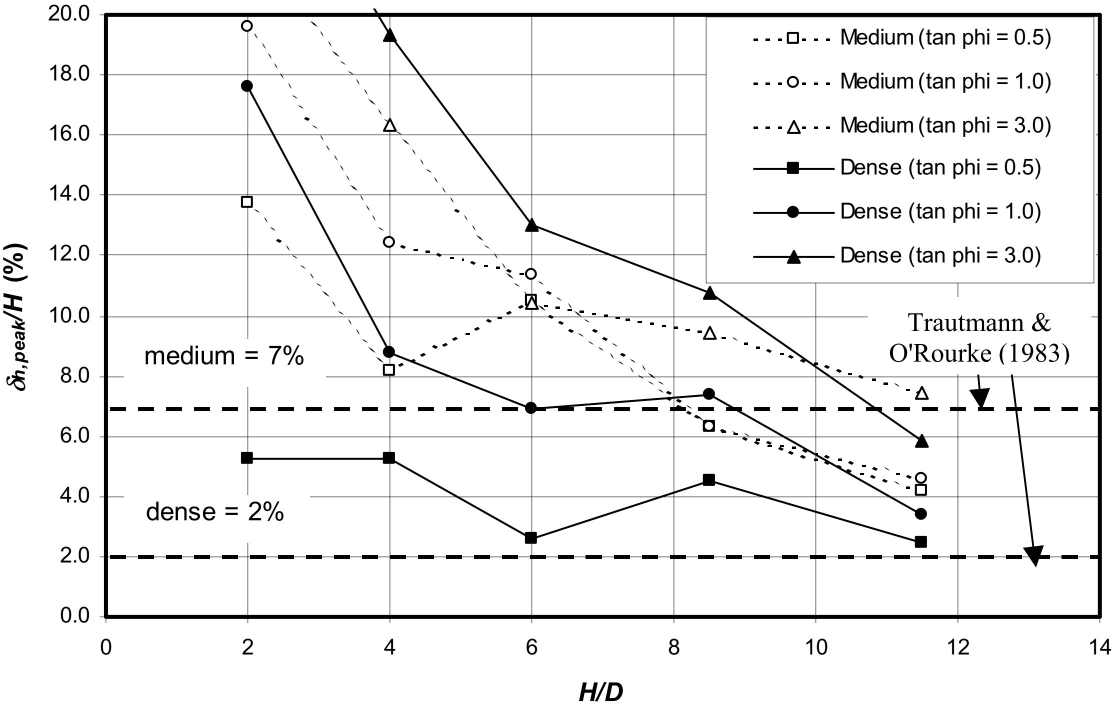

Figure 5-3 Plots of dimensionless peak pipe displacement against *H/D*

5.4 DEM analysis results of deep embedment depth

The results of DEM analysis for deep embedment depths in terms of the hyperbolic force-displacement relationships, the peak forces, and the corresponding pipe displacements at peak forces are summarized in Tables 5-3 and 5-4.

For medium sand, the force-displacement curves from DEM analysis follow the same trend as those from FE analysis for all embedment depths. For dense sand, the force-displacement curves from DEM analysis show some difference from those of FE analysis, especially at deep depth. The results from the case of tan $\phi_\mu = 0.5$ (highest contact stiffness used) show stiffest behavior, whereas the results from the case of tan $\phi_\mu = 3.0$ (lowest contact stiffness used) show softest behavior, which is more consistent with the FE results.

Fig. 5-4 presents the peak dimensionless forces plotted against *H/D* of up to 60. For medium sand, the peak dimensionless forces from the cases of tan ϕ_μ = 1.0 and 3.0 yield similar values with the FE results for the whole range of the *H/D* of interest (*H/D* = 2 to 60), whereas the results from the case of tan ϕ_μ = 0.5 show smaller values. The peak dimensionless forces increase approximately linearly with *H/D* at shallow depths and reach their maximum values at some depths after which the maximum dimensionless forces become approximately constant with *H/D*. The depth when this transition occurs is termed "critical embedment depth" (e.g. Dickin & Leung, 1985) and it indicates a deep failure mechanism. The DEM results show that the critical embedment depth for medium sand is 12 with the peak dimensionless force of 15, which is consistent with the results obtained from FE analysis. For dense sand, the DEM results for the cases of tan ϕ_μ = 1.0, 3.0 yield closest results with the FE analysis with somewhat larger peak dimensionless forces at very deep embedment depth (*H/D* ≥ 40) and more gradual transition from shallow to deep failure mechanism. However, the results from the case of tan ϕ_μ = 0.5 (highest contact stiffness used) show the largest overestimation and does not show any transition from shallow to deep failure mechanism.

Fig 5-5 shows the dimensionless peak displacement plotted against *H/D*. The recommended values from ASCE Guideline are also included in the figure. The dimensionless peak displacement decreases with depth. The stiffest behavior (smallest dimensionless peak displacement) is from tan ϕ_μ = 0.5 which is consistent with the case of largest contact stiffness. The dimensionless peak displacements from the DEM analyses are quite different from those recommended by the ASCE Guideline. At shallow depth, the dimensionless peak displacements from DEM are larger than the ASCE Guideline; however, their values decrease with embedment depth and become smaller than the ASCE Guideline at large depth.

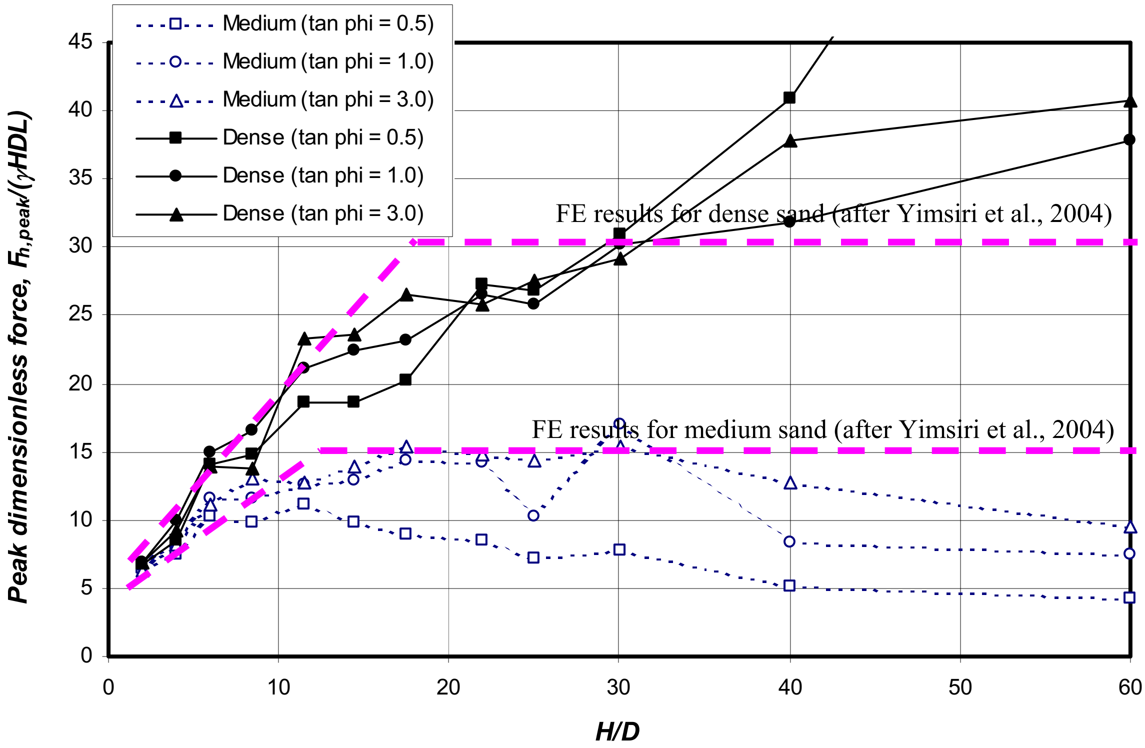

Figure 5-4 Relationship between peak dimensionless force and *H/D*

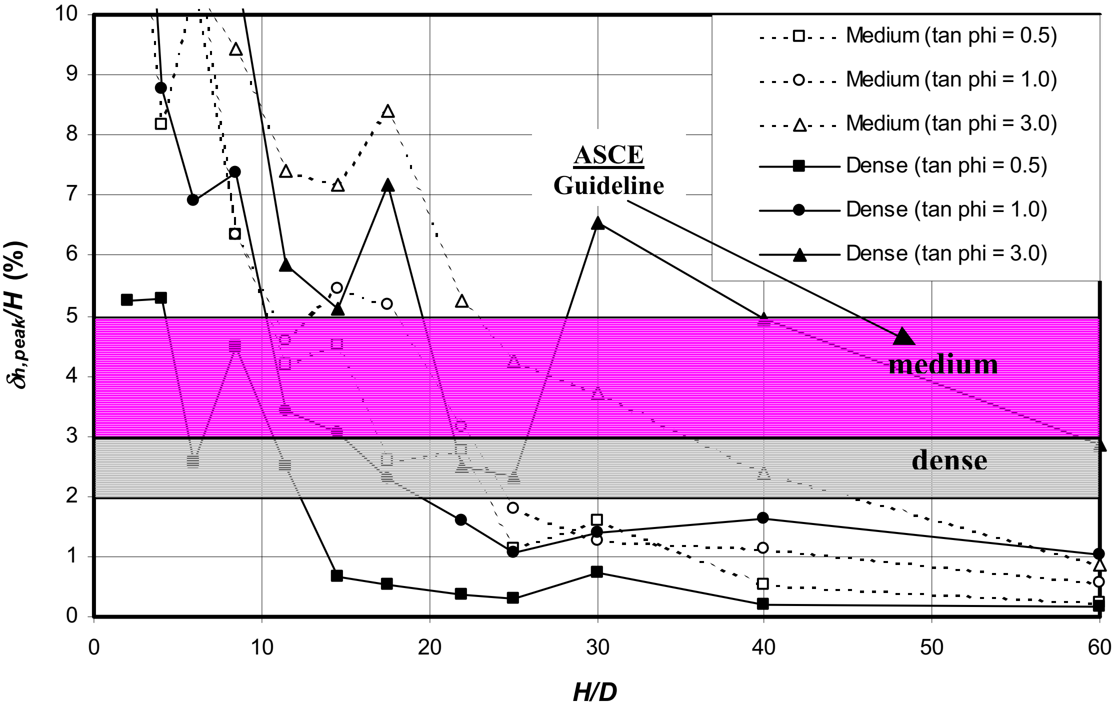

Figure 5-5 Relationship between dimensionless ultimate displacement and *H/D*

The normalized hyperbolic force-displacement relationship of pipe under lateral loading is proposed by ASCE as shown in Eq. (5-2). This is compared with the DEM analysis results in Figs. 5-6 and 5-7 for medium and dense sands, respectively.

$$\frac{F_h}{F_{h,peak}} = \frac{\delta_h / \delta_{h,peak}}{0.15 + 0.85\delta_h / \delta_{h,peak}} \qquad \ldots\ldots\ldots\ldots\ldots\ldots.. \quad (5\text{-}2)$$

For medium sand, the relationship recommended by ASCE reasonably matches the DEM analysis results for the case of tan $\phi_\mu = 3.0$, whereas it forms a lower boundary for the cases of tan $\phi_\mu = 0.5$, 1.0. For dense sand, the relationship recommended by ASCE reasonably matches the DEM analysis results for the cases of tan $\phi_\mu = 1.0$, 3.0; however, this relationship cannot yield good match with the case of tan $\phi_\mu = 0.5$ due to the large scatter of the DEM results themselves.

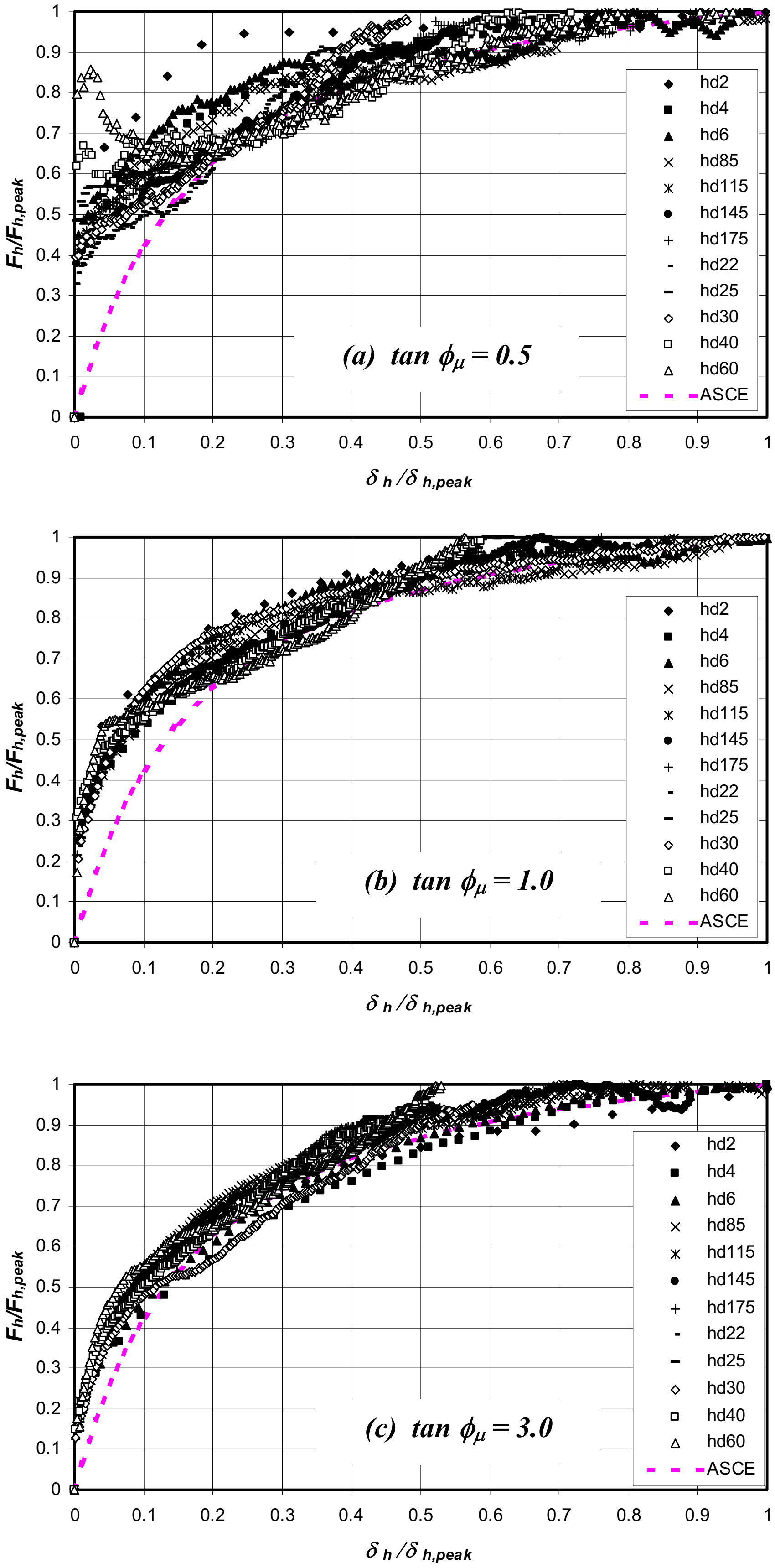

Figure 5-6 Normalized force-displacement relationship: medium sand

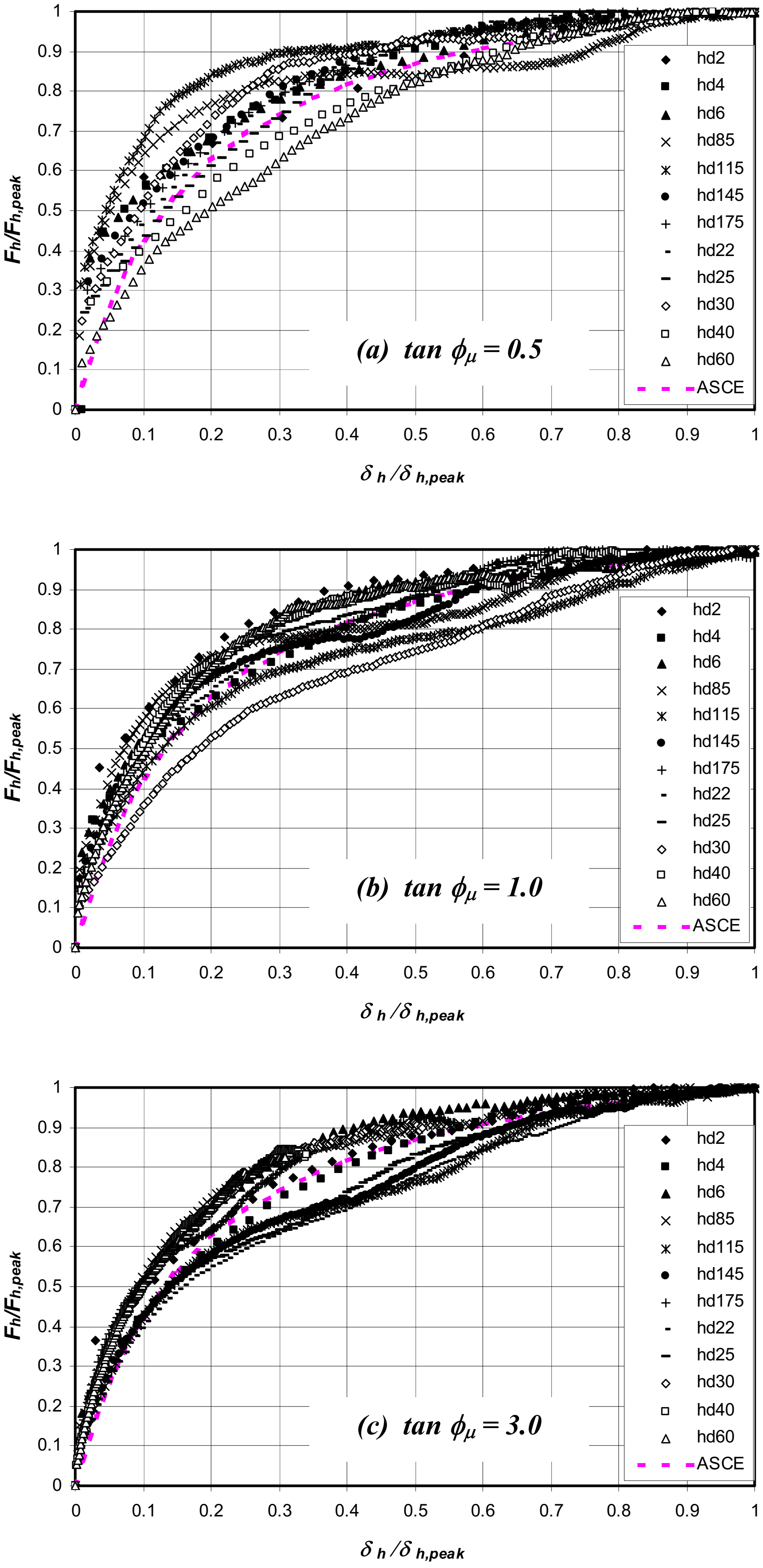

Figure 5-7 Normalized force-displacement relationship: dense sand

5.5 Summary

The DEM analysis is used to simulate the pipeline-soil interaction under lateral loading at deep embedment condition by using the input parameters from the calibration of the analysis with the experimental results at shallow depth. At shallow depth, the force-displacement relationships from the DEM analysis show that the results for medium sand match the experimental data well for all cases of tan ϕ_μ, whereas the results for dense sand match the experimental data well only for the cases of tan $\phi_\mu = 0.5$ and 1.0 with too soft behavior for the case of tan $\phi_\mu = 3.0$. At deep depth, the DEM results of medium sand in term of the peak dimensionless force and force-displacement relationship match the FE results well for all cases. The DEM results for medium sand show deep failure mechanism with the critical embedment depth of 12 and the critical peak dimensionless force of 13 which is consistent with the FE results. For dense sand, the DEM results from the cases of tan ϕ_μ = 1.0, 3.0 yield closest results with the FE analysis with gradual transition from shallow to deep failure mechanism and a tendency of overestimation of the peak dimensionless at very deep depth ($H/D \geq 40$). However, the DEM results for the case of tan $\phi_\mu = 0.5$ show considerably overestimation and do not show any transition from shallow to deep failure mechanism.

The obtained dimensionless peak displacements from DEM do not match the recommendation by Trautmann & O'Rourke (1983) and ASCE Guideline. They show a tendency to decrease as the embedment depth increases. The obtained normalized hyperbolic force-displacement relationship from DEM analysis match the recommendation by ASCE Guideline well for the cases of tan $\phi_\mu = 3.0$ (medium sand) and tan ϕ_μ = 1.0, 3.0 (dense sand).

Chapter 6

DEM analyses of pipe under upward loading

6.1 Analysis procedure and program

The geometry of the numerical model was based on the experimental study by Trautmann & O'Rourke (1983). For all cases of medium sand and the cases of dense sand with $H_c/D < 30$, all dimensions of the numerical model are the same as those of the experimental set-up except that the embedment depth was adjusted to the required value (Fig. 6-1a). For dense sand with $H_c/D \geq 30$, the width of the model was doubled to reduce the effect of boundary interference (Fig 6-1b). The analyses were performed for medium and dense sands.

The tank and pipe were modelled by series of planar wall. Sand was modelled as a collection of spherical particles and the size distribution follows normal distribution. The tank wall was assumed to be smooth; the tank model has a normal contact stiffness equal to that of the particles but has zero tangential contact stiffness and zero surface friction. The pipe has identical contact stiffness in both normal and tangential directions and equal to that of the particles. The pipe has its surface friction angle equal to half of the inter-particle friction angle of sand. The pipe was pulled vertically by imposing upward displacement to the pipe. The DEM analysis programme is shown in Tables 6-1 and 6-2.

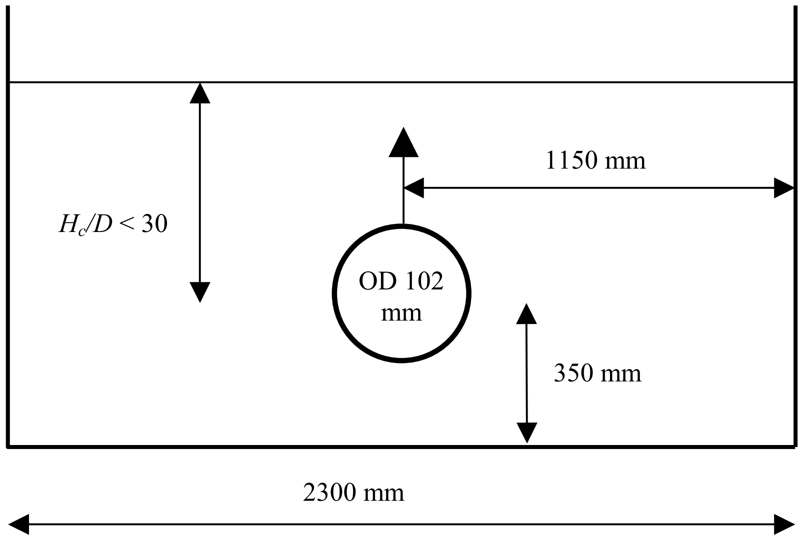

(a) for all cases of medium sand and the cases of dense sand with $H_c/D < 30$

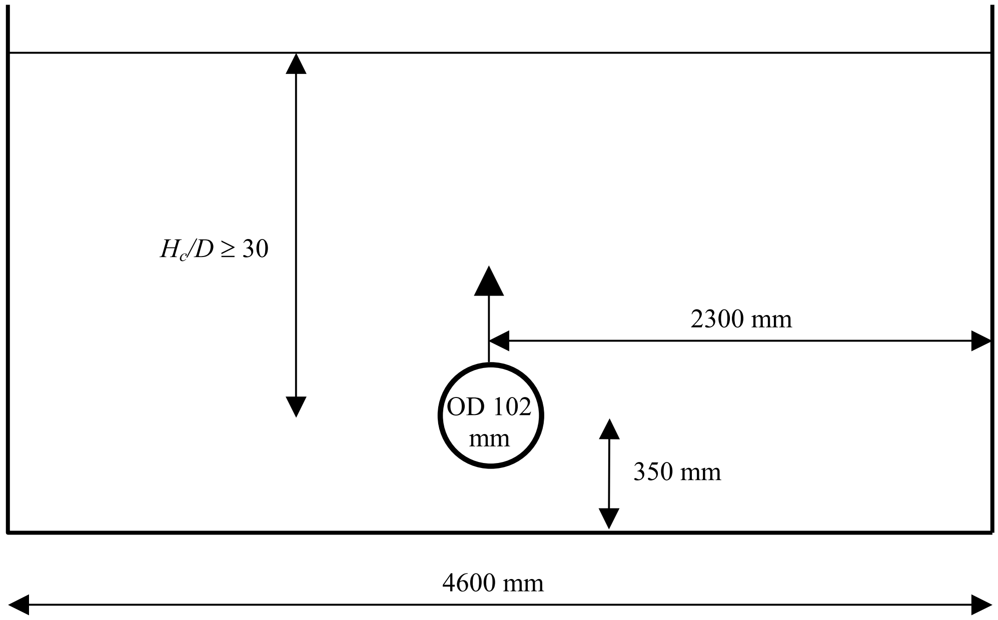

(b) for dense sand with $H_c/D \geq 30$

Figure 6-1 Geometry of the DEM analyses of upward pipe loading

Table 6-1 Summary of DEM analysis program and their input parameters: medium sand

Test No.	**H_c/D**	**Case of $\tan\phi_\mu = 0.5$**		**Case of $\tan\phi_\mu = 1.0$**		**Case of $\tan\phi_\mu = 3.0$**	
		$\tan\phi_\mu$	**$k_{N,sand}$ (N/m)**	**$\tan\phi_\mu$**	**$k_{N,sand}$ (N/m)**	**$\tan\phi_\mu$**	**$k_{N,sand}$ (N/m)**
UMHcD15	1.5	0.5	—	1.0	—	3.0	—
UMHcD4	4	0.5	—	1.0	—	3.0	—
UMHcD8	8	0.5	1.5×10^5	1.0	5.0×10^4	3.0	3.0×10^4
UMHcD13	13	0.5	1.0×10^6	1.0	2.0×10^5	3.0	1.0×10^5
UMHcD17	17	0.5	2.4×10^6	1.0	4.2×10^5	3.0	1.7×10^5
UMHcD21	21	0.5	5.3×10^6	1.0	7.6×10^5	3.0	2.6×10^5
UMHcD25	25	0.5	1.0×10^7	1.0	1.2×10^6	3.0	3.8×10^5
UMHcD30	30	0.5	2.1×10^7	1.0	2.0×10^6	3.0	5.7×10^5
UMHcD40	40	0.5	6.1×10^7	1.0	4.5×10^6	3.0	1.1×10^6
UMHcD60	60	0.5	2.9×10^8	1.0	1.4×10^7	3.0	2.6×10^6

Note: 1. $k_{N,sand} = k_{T,sand} = k_{N,pipe} = k_{T,pipe} = k_{N,wall}$

2. $k_{T,wall} = 0$

3. $\phi_{pipe} = \phi_\mu/2$

4. $\phi_{wall} = 0$

Table 6-2 Summary of DEM analysis program and their input parameters: dense sand

Test No.	**H_c/D**	**Case of $\tan \phi_\mu = 0.5$**		**Case of $\tan \phi_\mu = 1.0$**		**Case of $\tan \phi_\mu = 3.0$**	
		$\tan \phi_\mu$	**$k_{N,sand}$ (N/m)**	**$\tan \phi_\mu$**	**$k_{N,sand}$ (N/m)**	**$\tan \phi_\mu$**	**$k_{N,sand}$ (N/m)**
UDHcD15	1.5	0.5	—	1.0	—	3.0	—
UDHcD4	4	0.5	2.5×10^4	1.0	1.5×10^4	3.0	1.0×10^4
UDHcD8	8	0.5	1.5×10^5	1.0	7.0×10^4	3.0	4.0×10^4
UDHcD13	13	0.5	1.0×10^6	1.0	2.5×10^5	3.0	1.0×10^5
UDHcD17	17	0.5	3.1×10^6	1.0	5.2×10^5	3.0	1.9×10^5
UDHcD21	21	0.5	7.0×10^6	1.0	9.4×10^5	3.0	3.1×10^5
UDHcD25	25	0.5	1.4×10^7	1.0	1.5×10^6	3.0	4.5×10^5
UDHcD30*	30	0.5	2.7×10^7	1.0	2.5×10^6	3.0	6.7×10^5
UDHcD40*	40	0.5	8.2×10^7	1.0	5.6×10^6	3.0	1.3×10^6
UDHcD60*	60	0.5	3.9×10^8	1.0	1.7×10^7	3.0	3.0×10^6

Note: 1. $k_{N,sand} = k_{T,sand} = k_{N,pipe} = k_{T,pipe} = k_{N,wall}$

2. $k_{T,wall} = 0$

3. $\phi_{pipe} = \phi_\mu/2$

4. $\phi_{wall} = 0$

5. * bigger tank

6.2 Input parameters for soil models

The input parameters for DEM models were determined as described in Section 4.5. The input parameters for all DEM analyses are presented in Tables 6-1 and 6-2. For the cases of $1.5 \leq H_c/D \leq 13$, the values of $k_{N,sand}$ were derived from fitting peak forces from the DEM analysis with the pipe loading experiment (as described in Section 4.5.2). For the cases of $17 \leq H_c/D \leq 60$, the values of $k_{N,sand}$ were derived from the obtained relationships from shallow depths as follow.

$$\left.\begin{aligned} &k\ (\text{N/m}) = 6.714\sigma_c'^{3.813} && \text{for } \tan\phi_\mu = 0.5 \\ &k\ (\text{N/m}) = 41.072\sigma_c'^{2.761} && \text{for } \tan\phi_\mu = 1.0 \\ &k\ (\text{N/m}) = 112.859\sigma_c'^{2.176} && \text{for } \tan\phi_\mu = 3.0 \end{aligned}\right\} \ldots\ldots\ldots\ldots\ldots\ldots \quad (6\text{-}1)$$

σ_c' (kPa) = vertical effective stress at center of pipe

6.3 DEM analysis results of shallow embedment depths

In this section, the DEM results of shallow embedment depths ($H_c/D \leq 13$) are presented and compared with the experimental results by Trautmann & O'Rourke (1983) to examine the accuracy of the DEM analysis. The results in terms of the hyperbolic force-displacement relationship, the peak forces, and the corresponding pipe displacement are summarized in Tables 6-3 and 6-4. The cases of very shallow depth (H_c/D = 1.5 and 4) could not be modelled due to instability of model set-up, especially for medium sand.

Table 6-3 DEM analysis results: medium sand

H_c/D	$\tan\phi_\mu = 0.5$			$\tan\phi_\mu = 1.0$			$\tan\phi_\mu = 3.0$		
	Hyperbolic fit	$F_{v,peak}$ **(kN)**	$\delta_{v,peak}$ **(mm)**	**Hyperbolic fit**	$F_{v,peak}$ **(kN)**	$\delta_{v,peak}$ **(mm)**	**Hyperbolic fit**	$F_{v,peak}$ **(kN)**	$\delta_{v,peak}$ **(mm)**
1.5	—	—	—	—	—	—	—	—	—
4	—	—	—	—	—	—	—	—	—
8	—	8.2	21.7	—	7.1	45.1	—	7.2	47.9
13	—	18.9	62.0	—	19.3	61.0	—	18.2	69.3
17	$F_v = \frac{\delta_v}{0.0339\delta_v + 0.2019}$	26.6	54.7	$F_v = \frac{\delta_v}{0.0356\delta_v + 0.1829}$	25.3	46.6	$F_v = \frac{\delta_v}{0.0347\delta_v + 0.2562}$	26.0	68.1
21	$F_v = \frac{\delta_v}{0.0241\delta_v + 0.0948}$	37.4	35.9	$F_v = \frac{\delta_v}{0.0264\delta_v + 0.2964}$	34.1	101.3	$F_v = \frac{\delta_v}{0.0243\delta_v + 0.2874}$	37.1	108.3
25	$F_v = \frac{\delta_v}{0.0214\delta_v + 0.0449}$	42.1	19.1	$F_v = \frac{\delta_v}{0.0195\delta_v + 0.2013}$	46.2	93.8	$F_v = \frac{\delta_v}{0.0191\delta_v + 0.2597}$	47.2	124.5
30	$F_v = \frac{\delta_v}{0.0219\delta_v + 0.0679}$	41.2	28.6	$F_v = \frac{\delta_v}{0.0163\delta_v + 0.1590}$	55.1	86.0	$F_v = \frac{\delta_v}{0.0146\delta_v + 0.2098}$	61.8	132.7

40	—	—	—	$F_v = \dfrac{\delta_v}{0.0126\delta_v + 0.1130}$	71.2	78.2	$F_v = \dfrac{\delta_v}{0.0116\delta_v + 0.1596}$	77.4	120.9
60	—	—	—	$F_v = \dfrac{\delta_v}{0.0100\delta_v + 0.0273}$	89.6	23.5	$F_v = \dfrac{\delta_v}{0.0070\delta_v + 0.0811}$	128.4	102.9

Note: F_v is in kN/m length.

δ_v is in mm.

Table 6-4 DEM analysis results: dense sand

H_c/D	$\tan \phi_\mu = 0.5$			$\tan \phi_\mu = 1.0$			$\tan \phi_\mu = 3.0$		
	Hyperbolic fit	$F_{v,peak}$ (kN)	$\delta_{v,peak}$ (mm)	**Hyperbolic fit**	$F_{v,peak}$ (kN)	$\delta_{v,peak}$ (mm)	**Hyperbolic fit**	$F_{v,peak}$ (kN)	$\delta_{v,peak}$ (mm)
1.5	—	—	—	—	—	—	—	—	—
4	—	3.2	30.4	—	2.9	36.5	—	3.0	36.9
8	—	11.1	23.6	—	10.3	44.6	—	10.0	57.0
13	—	29.3	24.0	—	28.3	47.9	—	23.6	54.4
17	—	53.5	10.3	—	41.9	51.6	$F_v = \frac{\delta_v}{0.0237\delta_v + 0.2770}$	37.9	103.2
21	—	84.4	6.7	—	63.6	37.2	$F_v = \frac{\delta_v}{0.0156\delta_v + 0.1944}$	57.5	108.5
25	—	174.0	5.8	—	83.2	24.1	$F_v = \frac{\delta_v}{0.0105\delta_v + 0.1390}$	85.6	117.6
30	$F_v = \frac{\delta_v}{0.0040\delta_v + 0.0243}$	225.2	54.8	—	107.3	60.0	—	113.4	80.1

40	—	498.9	6.5	—	200.1	29.0	—	169.6	76.8
60	—	1685.2	4.1	—	330.5	22.9	—	303.3	50.8

Note: F_v is in kN/m length.

δ_v is in mm.

The comparison of the force-displacement curves from the DEM analyses with the experimental results is shown in Appendix B. The peak forces from DEM results were forced to match the experimental results by adjusting the values of contact stiffness by trial & error. The force-displacement curves from DEM show little difference from experimental results and the match is best for the case of tan $\phi_\mu = 0.5$.

Fig. 6-2 presents the peak dimensionless forces plotted against H_c/D. The results show that the DEM analysis can simulate the upward pipe loading behavior reasonably well.

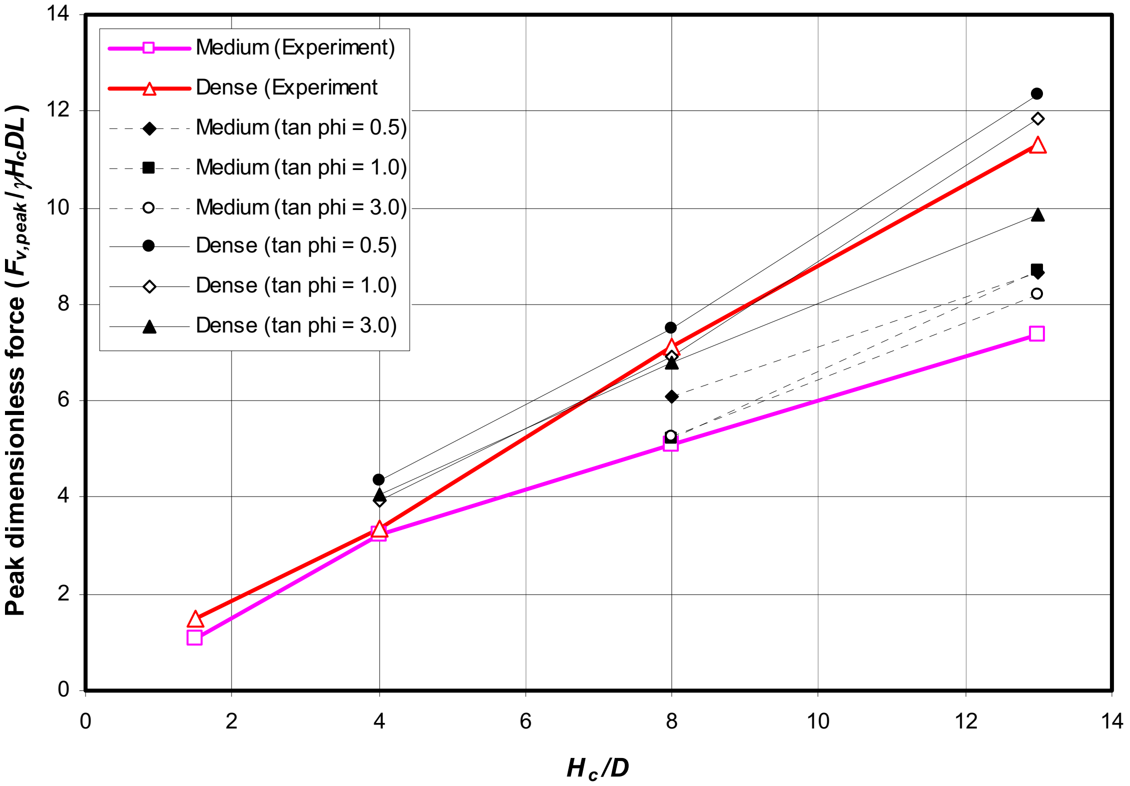

Figure 6-2 Plots of peak dimensionless force against H_c/D

Fig 6-3 shows the normalized peak displacement (pipe displacement at the peak force normalized by embedment depth) at different H_c/Ds. The typical values found in the experiments by Trautmann & O'Rourke (1983) are also included in the figure. The dimensionless peak displacements from the DEM analysis are much larger than the experimental data. The dimensionless peak displacements show a tendency to decrease with H_c/D, which is opposite to the experimental results by Murrey & Geddes (1987) and Dickin (1994).

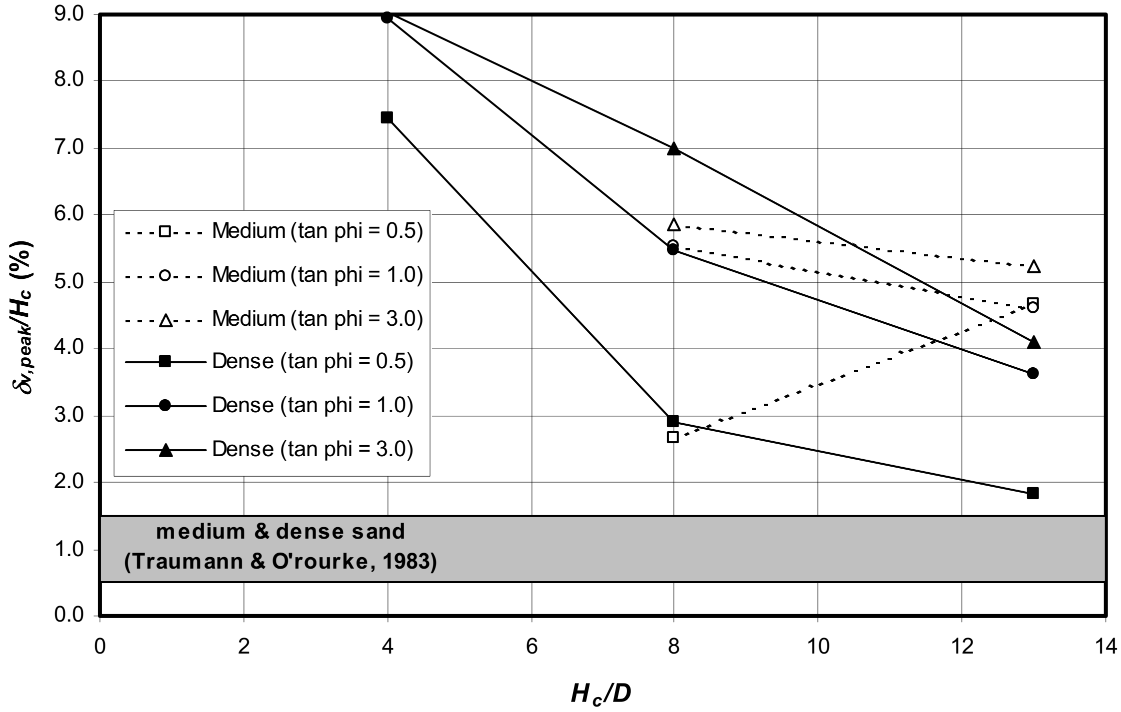

Figure 6-3 Plots of dimensionless peak pipe displacement against H_c/D

6.4 DEM analysis results of deep embedment depths

The DEM analyses were performed for deep embedment depth cases for medium and dense sands. The computed hyperbolic force-displacement relationships, the peak forces, and the corresponding pipe displacements are summarized in Tables 6-3 and 6-4.

The force-displacement curves from the DEM analysis are compared with those from the previous FE analysis as shown in Appendix B. In case of medium sand, the results from DEM at all embedment depths are consistent with the FE results, except for the case of tan ϕ_μ = 0.5 at very large depth ($H_c/D \geq 40$). In case of dense sand, the force-displacement curves from DEM analysis show more different trend from those of FE analysis when the embedment depth increases. The results from the case of tan ϕ_μ = 0.5 (highest contact stiffness used) show stiffest behavior, whereas the results from the case of tan ϕ_μ = 3.0 (lowest contact stiffness used) show softest behaviour which is more consistent to the FE results. When $H_c/D \geq 17$, the DEM results for the case of tan ϕ_μ = 0.5 become considerably different from the FE analysis by showing considerably larger peak force.

Fig. 6-4 presents the peak dimensionless force plotted against H_c/D of up to 60. For medium sand, the peak dimensionless forces from the cases of tan ϕ_μ = 1.0 and 3.0 yield consistent results with the FE results for the whole range of the H_c/D of interest (H_c/D = 1.5 to 60), whereas the results from the case of tan ϕ_μ = 0.5 show a tendency to give smaller values at deep depth. The peak dimensionless forces show deep failure mechanism by increasing approximately linearly with H_c/D at shallow depths and reaching their critical dimensionless force of 13 at the critical embedment depth of 25. This is consistent with the results from the FE analysis. For dense sand, the peak dimensionless forces from DEM are consistent with the FE analysis only for the case of tan ϕ_μ = 1.0, 3.0 which show a tendency to give larger peak dimensionless force at very deep depth ($H_c/D \geq 60$) and more gradual transition from shallow to deep failure mechanism. The case of tan ϕ_μ = 0.5 shows considerably higher peak dimensionless force and does not consistent with the rest of the data.

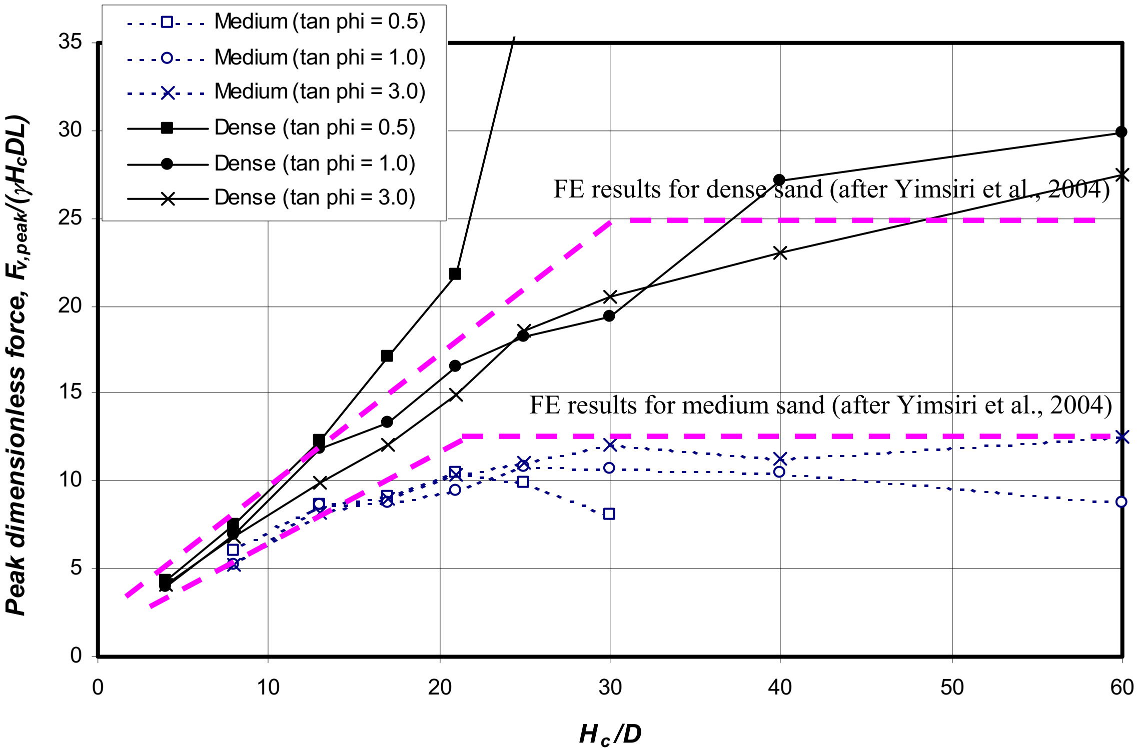

Figure 6-4 Relationship between peak dimensionless force and H_c/D

Fig 6-5 shows the dimensionless peak displacement plotted against H_c/D. The recommended values from ASCE Guideline are also included in the figure. The dimensionless peak displacement show a tendency to decrease as the H_c/D increases. The stiffest behavior (smallest dimensionless peak displacement) is from tan ϕ_μ = 0.5 which is consistent with the case of largest contact stiffness. The dimensionless peak displacements from the DEM analyses are quite different from those recommended by ASCE Guideline. At shallow depth, the dimensionless peak displacements from DEM are larger than the ASCE Guideline; however, their values decrease with embedment depth and become smaller than the ASCE Guideline at large depth.

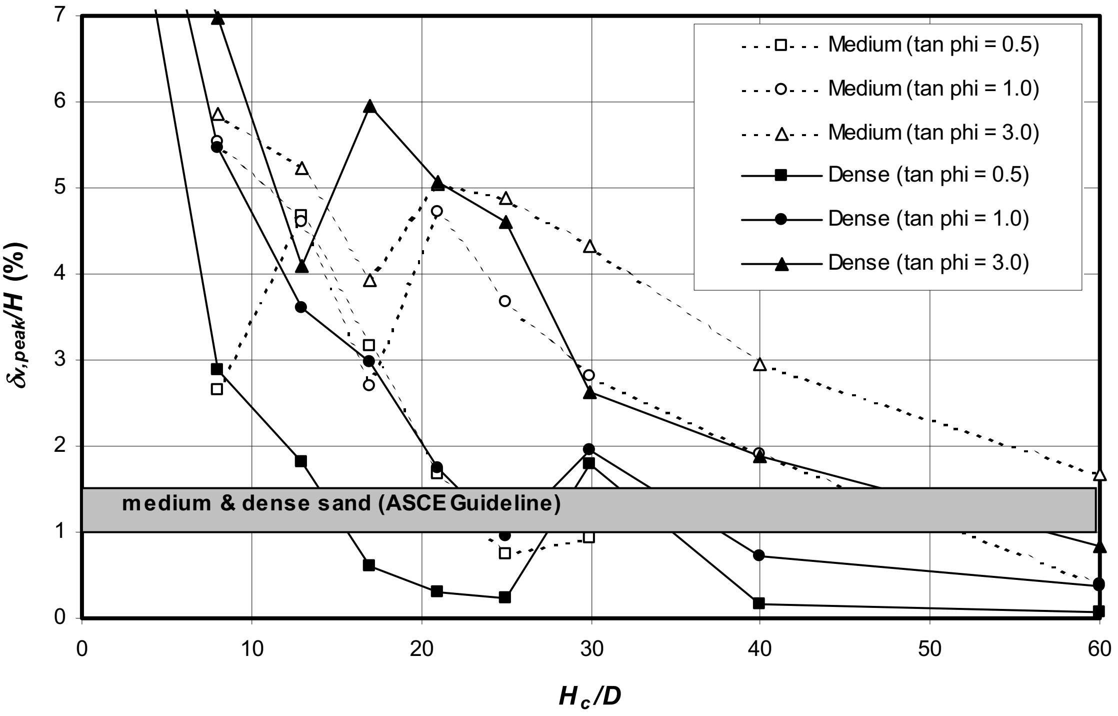

Figure 6-5 Relationship between dimensionless peak displacement against H_c/D

The normalized hyperbolic relationship between force and displacement under upward loading proposed by ASCE, as shown in Eq. (6-2), is compared with the DEM analysis results in Figs. 6-6 and 6-7 for medium and dense sands, respectively.

$$\frac{F_v}{F_{v,peak}} = \frac{\delta_v / \delta_{v,peak}}{0.07 + 0.93\delta_v / \delta_{v,peak}} \qquad \text{………………..} \quad (6\text{-}2)$$

The relationship recommended by ASCE reasonably matches the DEM analysis results for the case of medium sand but forms an upper boundary for the case of dense sand.

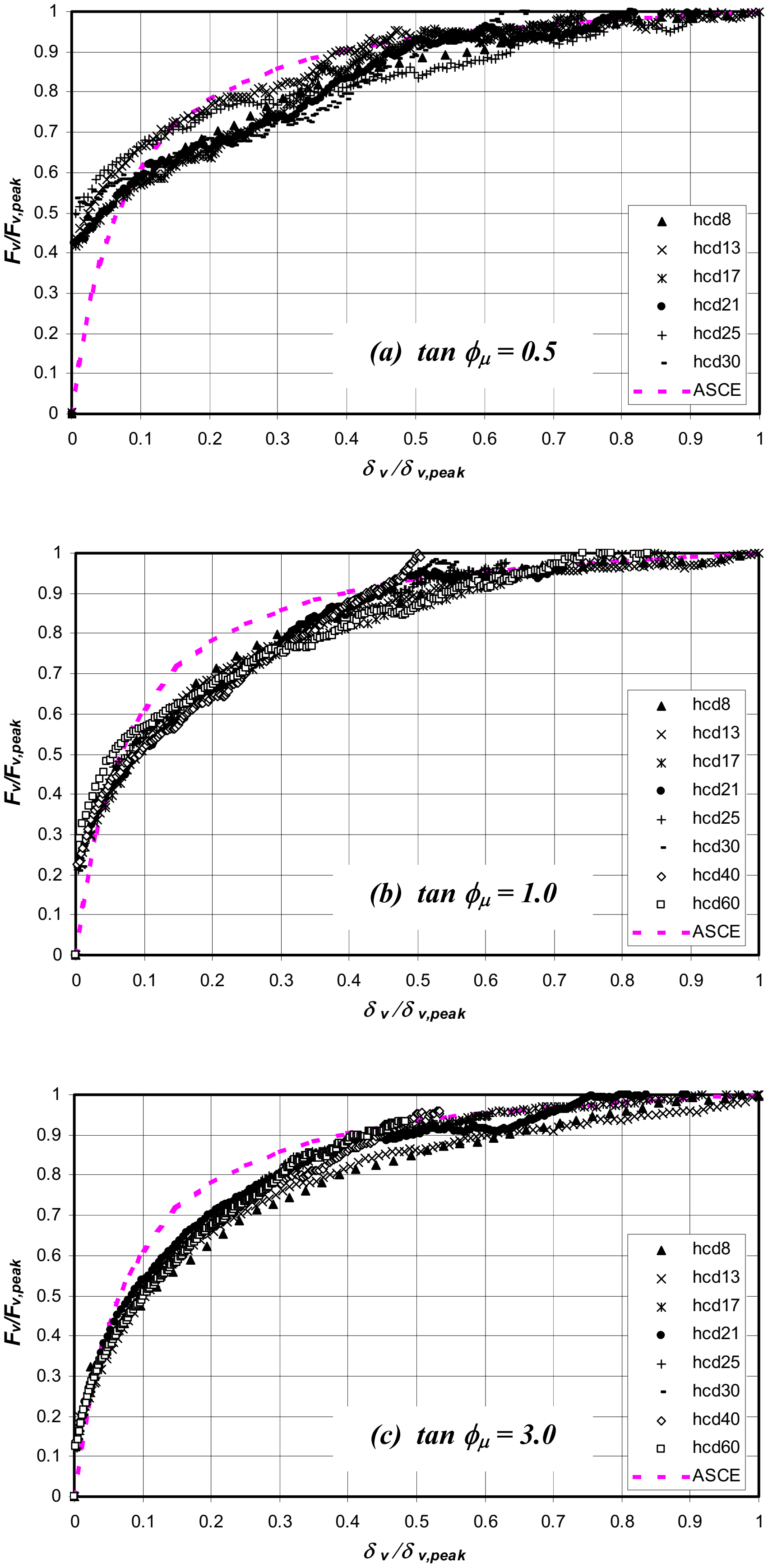

Figure 6-6 Normalized force-displacement relationship: medium sand

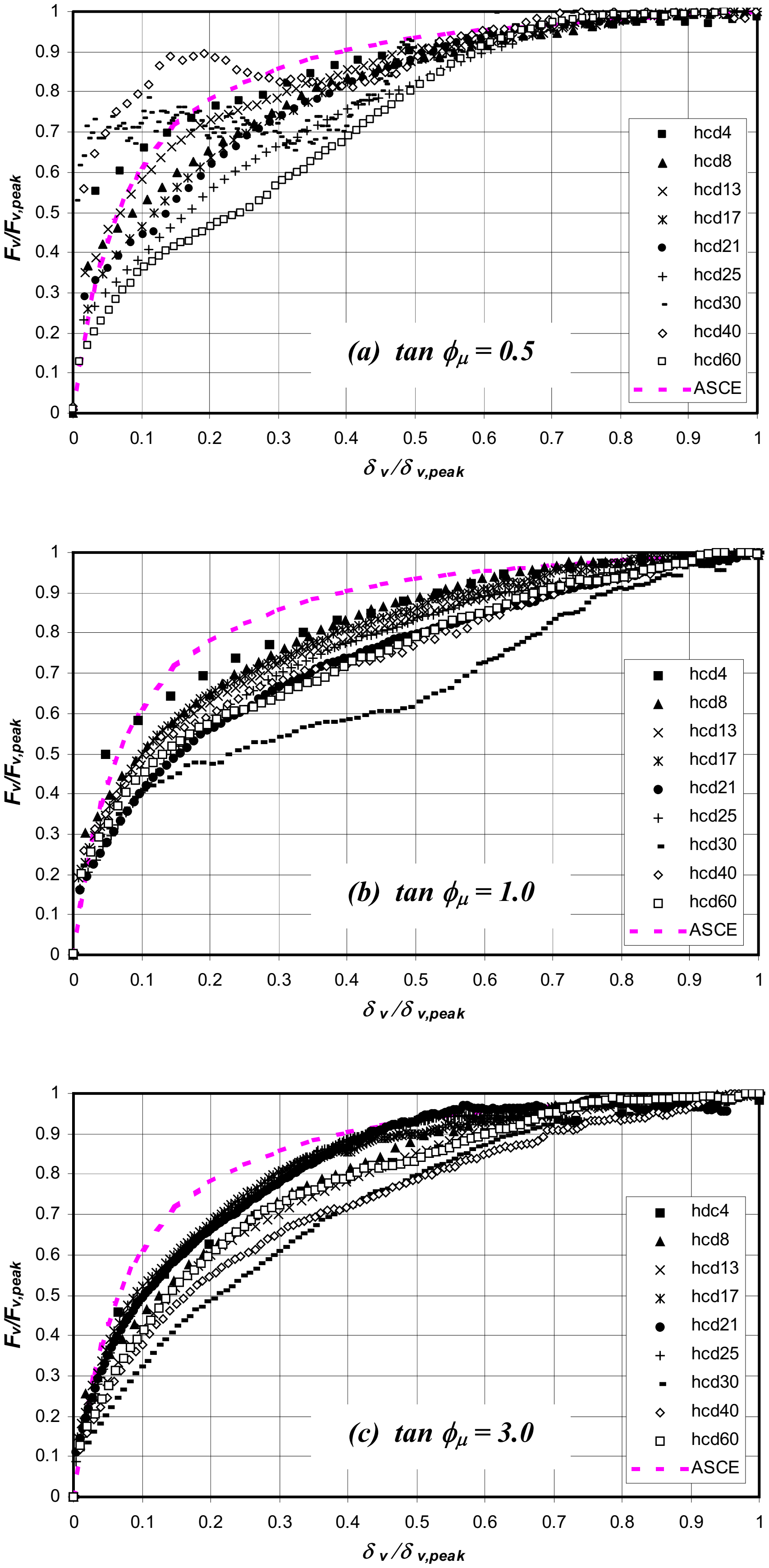

Figure 6-7 Normalized force-displacement relationship: dense sand

6.5 Summary

The DEM analysis is used to simulate the pipeline-soil interaction under lateral loading at deep embedment condition by using the input parameters from the calibration of the analysis with the experimental results at shallow depth. At shallow depth, the force-displacement relationships from the DEM analysis show that the results for medium sand match the experimental data well for all cases of tan ϕ_μ, whereas the results for dense sand match the experimental data well only for the cases of tan $\phi_\mu = 0.5$ and 1.0 with too soft behavior for the case of tan $\phi_\mu = 3.0$. At deep depth, the DEM results of medium sand in term of the peak dimensionless force and force-displacement relationship match the FE results well for all cases. The DEM results for medium sand show deep failure mechanism with the critical embedment depth of 25 and the critical peak dimensionless force of 13, which is consistent with the FE results. For dense sand, the DEM results from the cases of tan ϕ_μ = 1.0, 3.0 yield closest results with the FE analysis with gradual transition from shallow to deep failure mechanism and a tendency of overestimation of the peak dimensionless at very deep depth ($H/D \geq 60$). However, the DEM results for the case of tan $\phi_\mu = 0.5$ shows considerably overestimation and do not show any transition from shallow to deep failure mechanism.

The obtained dimensionless peak displacements from DEM do not match the recommendation by Trautmann & O'Rourke (1983) and ASCE Guideline. They show a tendency to decrease as the embedment depth increases. The obtained normalized hyperbolic force-displacement relationship from DEM analysis match the recommendation by ASCE Guideline well for the cases of medium sand and form an upper boundary for the case of dense sand.

Chapter 7

Discussion and conclusions

7.1 Selection of input parameters

There may be some arguments about the determination of the input parameters and their validity in the present DEM analysis because some parameters may seem to be unrealistic. The use of a high value of the inter-particle friction angle is due to the use of spherical particles which allows excessive particle rolling (e.g. Thomas & Bray, 1999). The obtained power value from triaxial simulation is 0.41, which is within the normal value for soil, which is approximately 0.5 (Hardin & Black, 1966). This is due to the fact that the DEM analysis matches both stiffness and strength from triaxial test. It was shown that the triaxial stiffness (Young's modulus) has a relationship with confining stress in the same manner as the contact stiffness does (Chang & Liao, 1994). However, the obtained power value from pipe loading simulation is much greater than the normal value for soil; this may be due to the complexity of mode of shearing in pipe loading problem. The peak force values employed for fitting is governed by complex deformation at relatively large strain; however, the contact stiffness is the behavior at very small strain.

It is also noted that various combinations of the contact stiffness and tan ϕ_μ can yield similar peak forces. With larger tan ϕ_μ, the required contact stiffness is lower. It is interesting to find that the contact stiffness affects the strength (peak force) for this problem, which is not the case for triaxial problem where the contact stiffness affects only modulus, not strength (see Appendix G). This may also be due to the more complex mode of shearing in pipe loading problem.

7.2 Pipeline behavior under lateral loading

Fig. 7-1 shows that, at shallow depth, the force-displacement relationships from the DEM analysis for medium sand match the experimental data well for all cases of tan ϕ_μ, whereas the results for dense sand match the experimental data well only for the cases of tan ϕ_μ = 0.5 and 1.0 with too soft behavior for the case of tan ϕ_μ = 3.0. Fig. 7-2 shows that, at deep depth, the force-displacement relationships from medium sand still match the FE results well for all cases of tan ϕ_μ, whereas the results for dense sand show that the case of tan ϕ_μ =

3.0 yield closest results with the FE analysis and a tendency of overestimation of the peak dimensionless force for the case of tan $\phi_\mu = 0.5$.

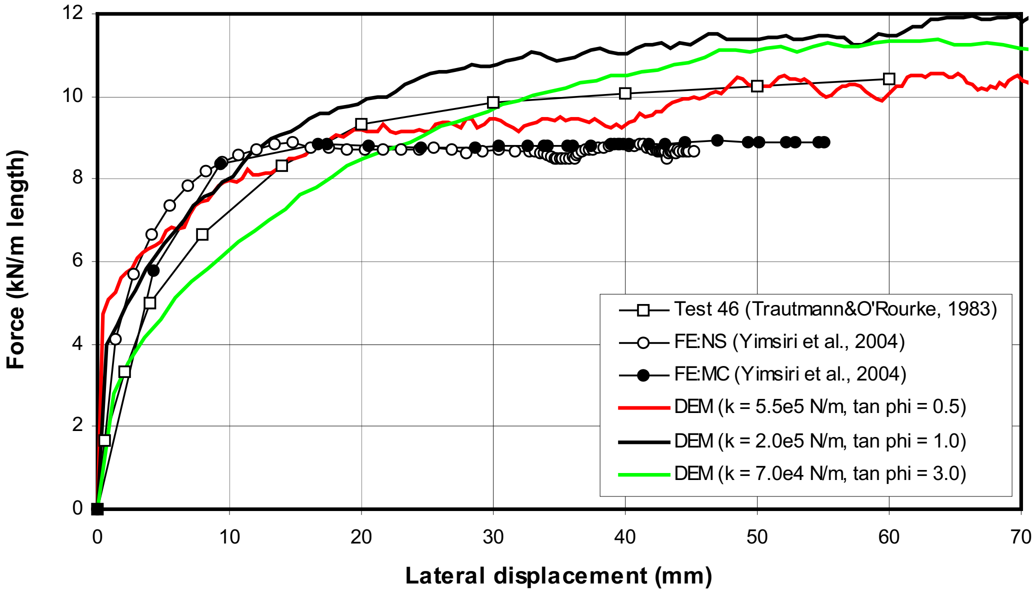

(a) H/D = 6, Medium sand

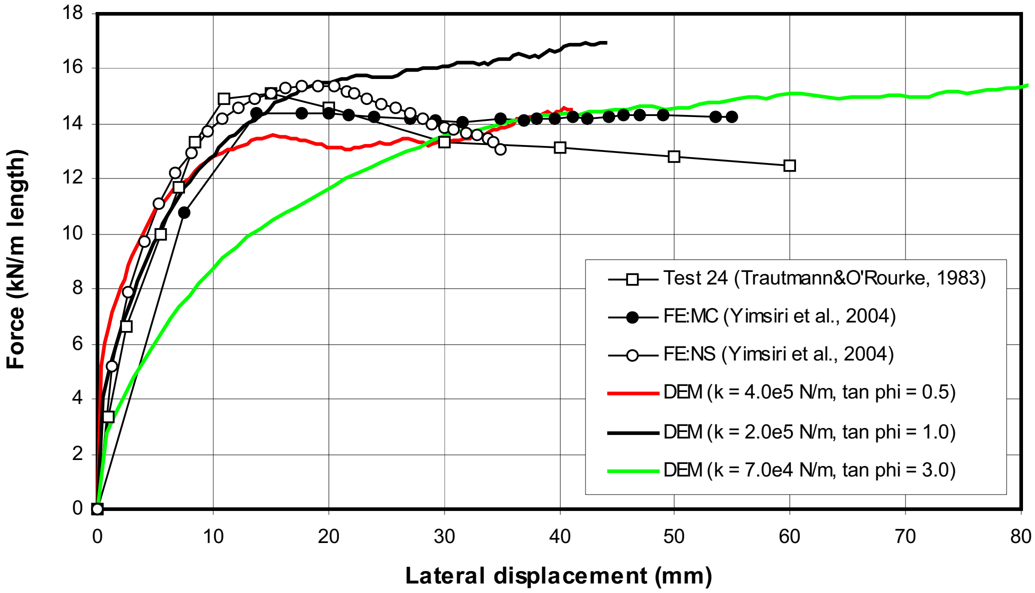

(b) H/D = 6, Dense sand

Figure 7-1 Force-displacement relationships at shallow embedment depth of lateral pipe loading

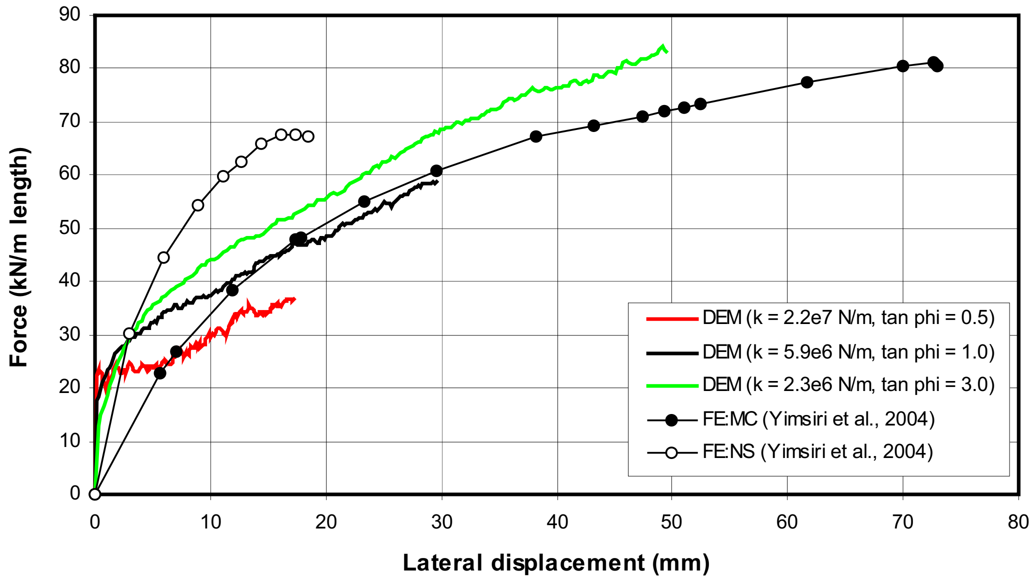

(a) H/D = 40, Medium sand

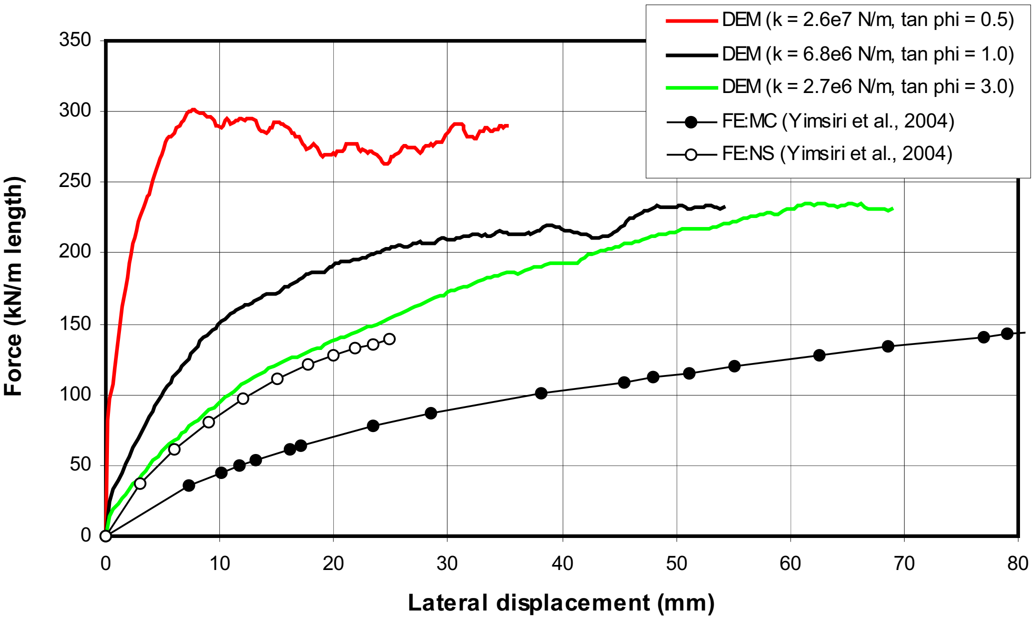

(b) H/D = 40, Dense sand

Figure 7-2 Force-displacement relationships at deep embedment depth of lateral pipe loading

The comparison of peak dimensionless forces from the DEM and FEM analyses is shown in Fig. 7-3. For medium sand, the DEM results match the FE results well for all cases. The DEM results for medium sand show deep failure mechanism with the critical embedment depth of 12 and the critical peak dimensionless force of 13, which is consistent with the FE results. For dense sand, the DEM results from the cases of tan ϕ_μ = 1.0, 3.0 yield closest results with the FE analysis with gradual transition from shallow to deep failure mechanism and a tendency of overestimation of the peak dimensionless at very deep depth ($H/D \geq 40$). However, the DEM results for the case of tan ϕ_μ = 0.5 show considerably overestimation and do not show any transition from shallow to deep failure mechanism.

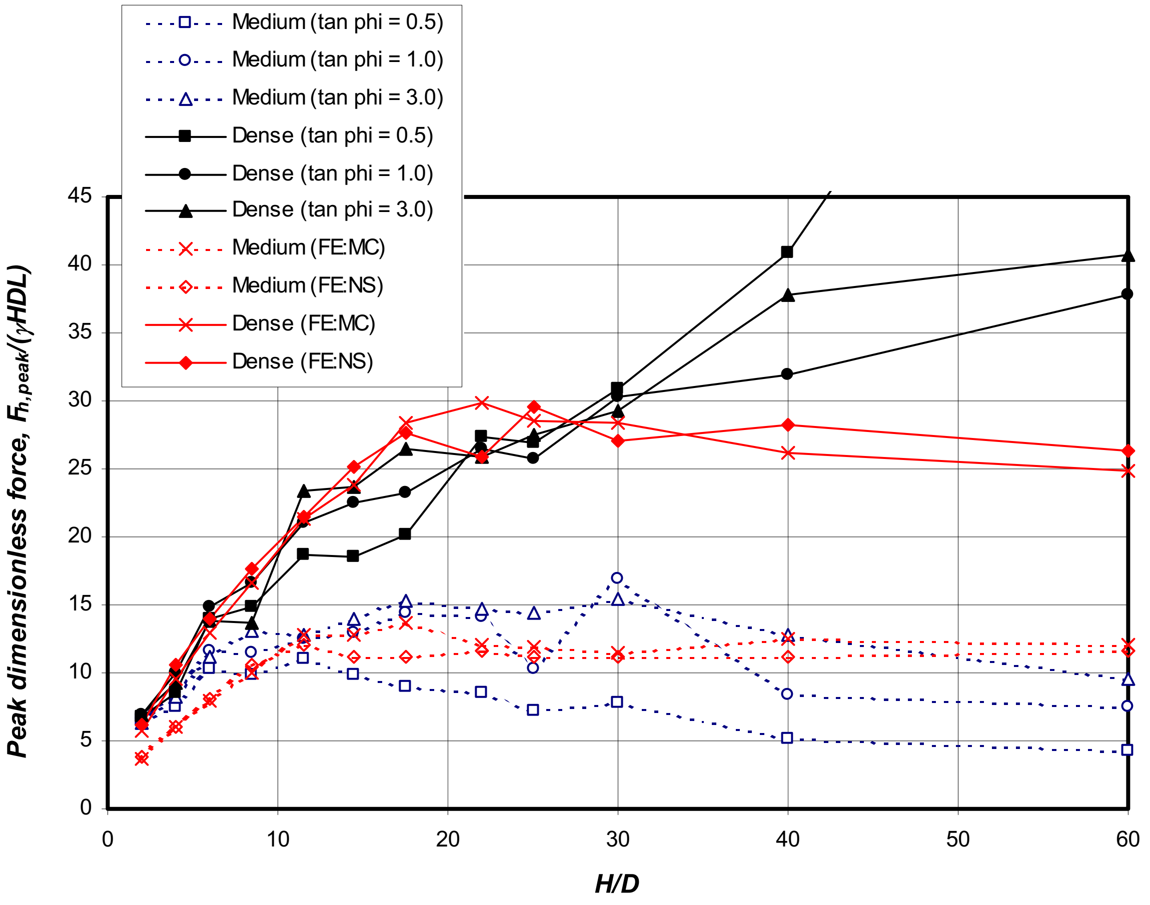

Figure 7-3 Comparison of peak dimensionless force of lateral pipe loading from DEM and FEM

Fig. 7-4 shows that displacement pattern from the experimental tank test of medium sand at H/D = 11.5, which can be compared to those from FEM and DEM (tan ϕ_μ = 3.0) analyses shown in Fig. 7-5. Similarly, Fig. 7-6 shows that displacement pattern from the experimental tank test of dense sand at H/D = 11.5, which can be compared to those from FEM and DEM (tan ϕ_μ = 3.0) analyses shown in Fig. 7-7. It can be seen that the results from DEM better represent the displacement of sand around the pipe; however, the results from DEM involve larger soil mass compared with FEM, especially for dense sand. Fig. 7-8 shows the displacement pattern from DEM analysis at deep embedment depth. The results from medium sand show deep failure mechanism whereby the upward soil deformation does not extend to the ground surface. However, the results from dense sand still show shallow failure mechanism by which the ground surface still shows upward soil deformation. This is consistent with the peak dimensionless force data in Fig. 7-3, which shows that, at H/D = 30, the medium sand case has well reached deep failure mechanism, whereas the dense sand case is still in the transition state. The extent of soil mass involved in the deformation pattern increases as the contact stiffness used increases (or the inter-particle friction angle decreases). This makes the extent of soil deformation of dense sand at deep depth reaches the model boundary for the case of tan ϕ_μ = 0.5 (although the width of the testing compartment was already doubled to avoid or lessen the interference of boundary walls). This is consistent with the peak dimensionless force data in Fig. 7-3, which shows that the results for the case of tan ϕ_μ = 0.5 does not show deep failure mechanism due probably to this boundary effect. Fig. 7-9 presents the contact force chain pattern from DEM analysis. The results also show that the force chain involves large soil mass especially for dense sand.

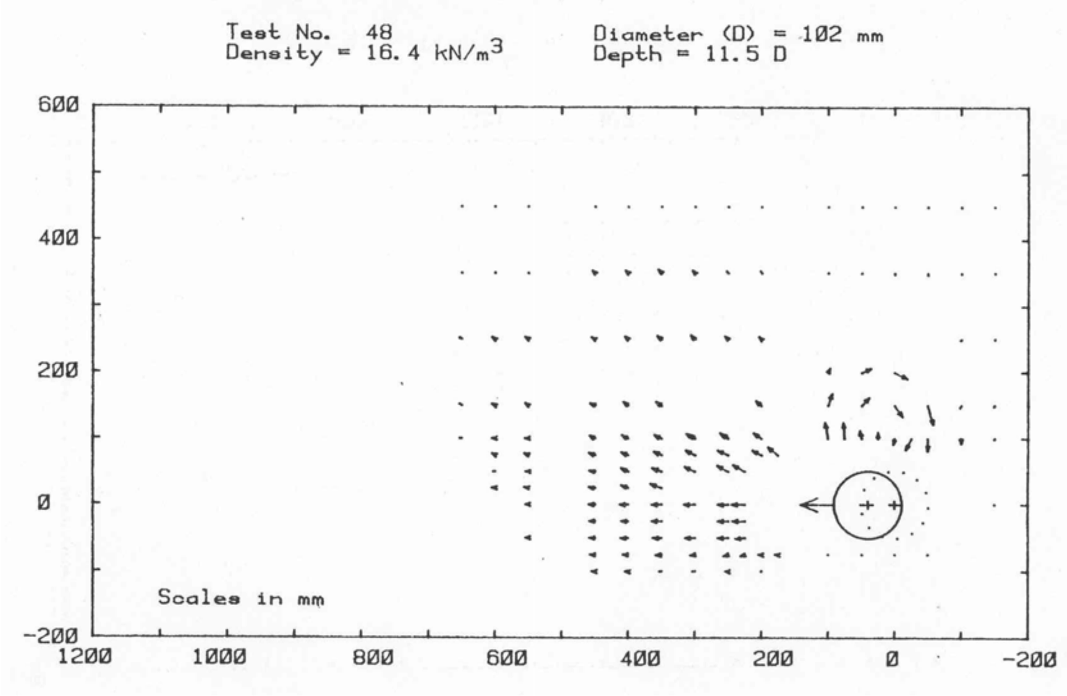

Figure 7-4 Displacement pattern of lateral pipe loading from experimental tank test (*H/D* = 11.5, Medium sand) (Trautmann & O'Rourke, 1983)

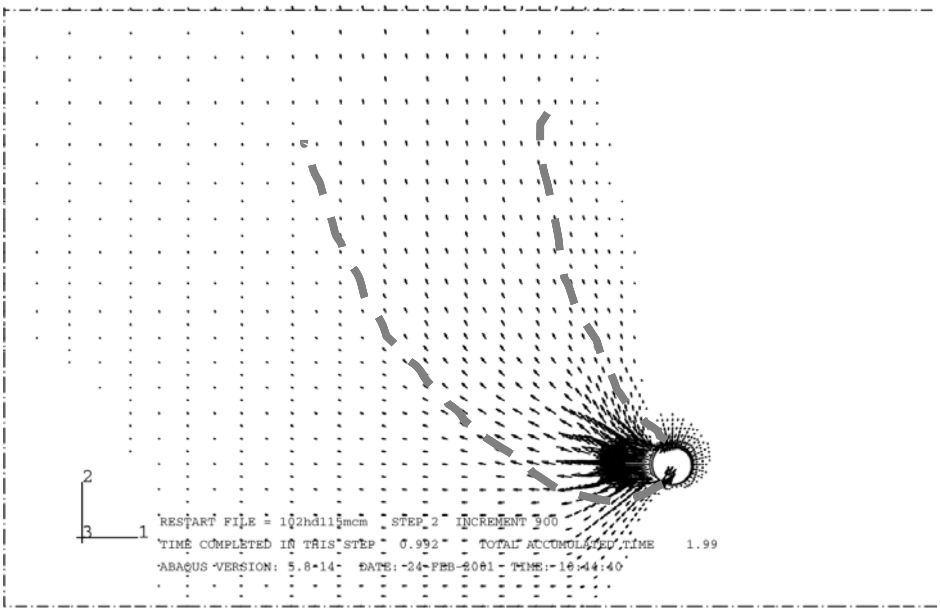

(a) FEM results

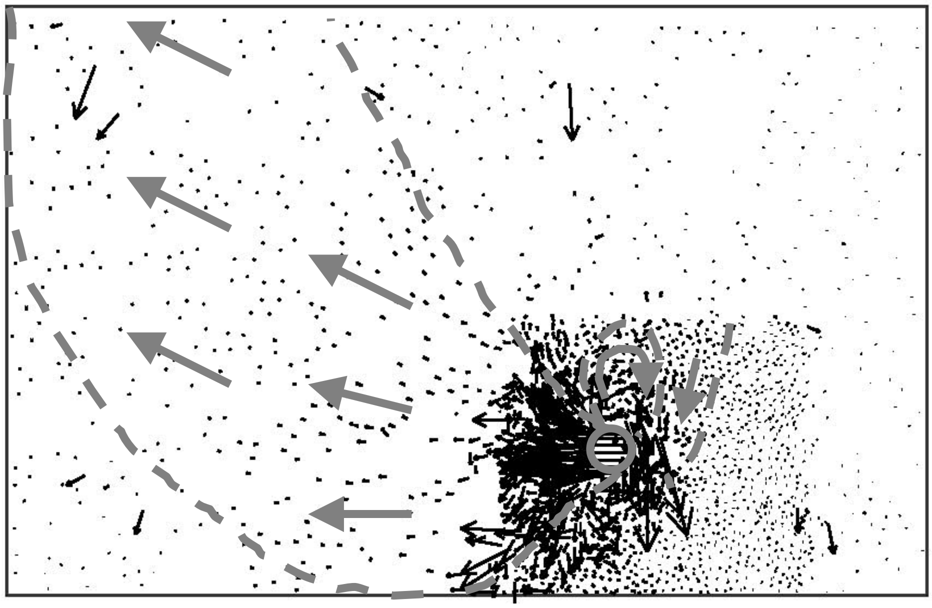

(b) DEM results, tan ϕ_μ = 3.0

Figure 7-5 Comparison of displacement pattern of lateral pipe loading from DEM and FEM (*H/D* = 11.5, Medium sand)

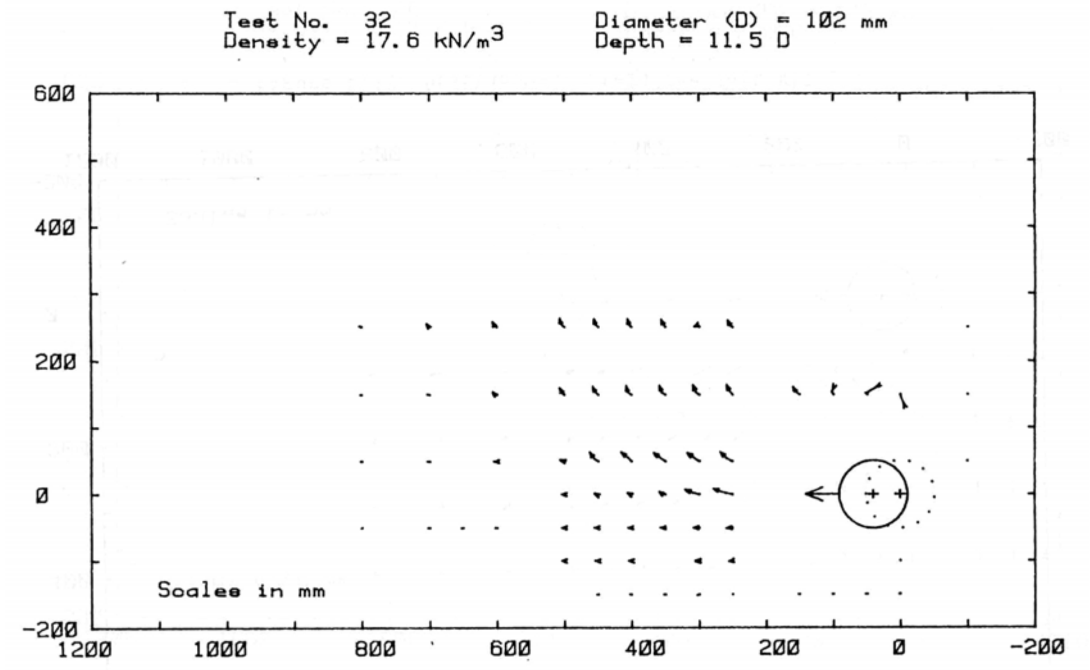

Figure 7-6 Displacement pattern of lateral pipe loading from experimental tank test (*H/D* = 11.5, Dense sand) (Trautmann & O'Rourke, 1983)

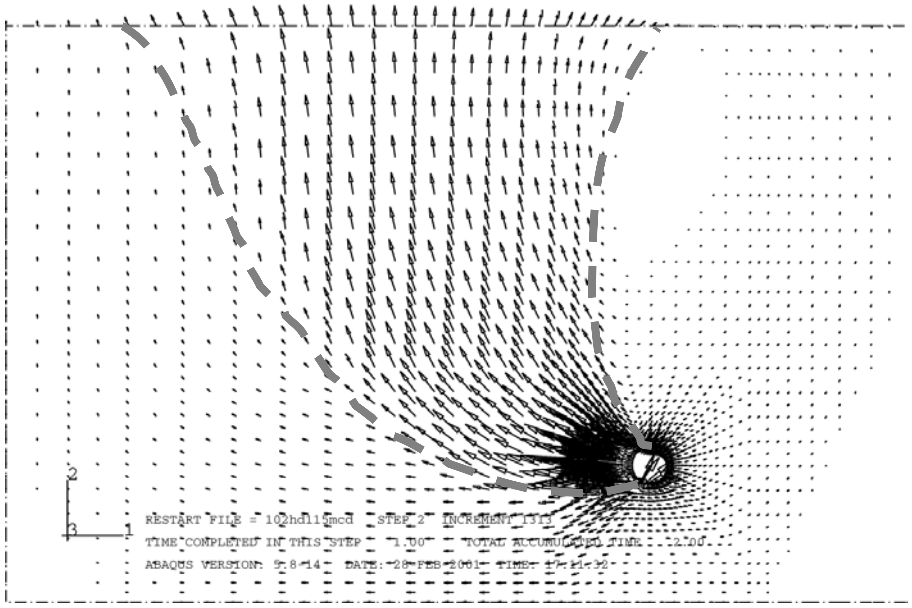

(a) FEM results

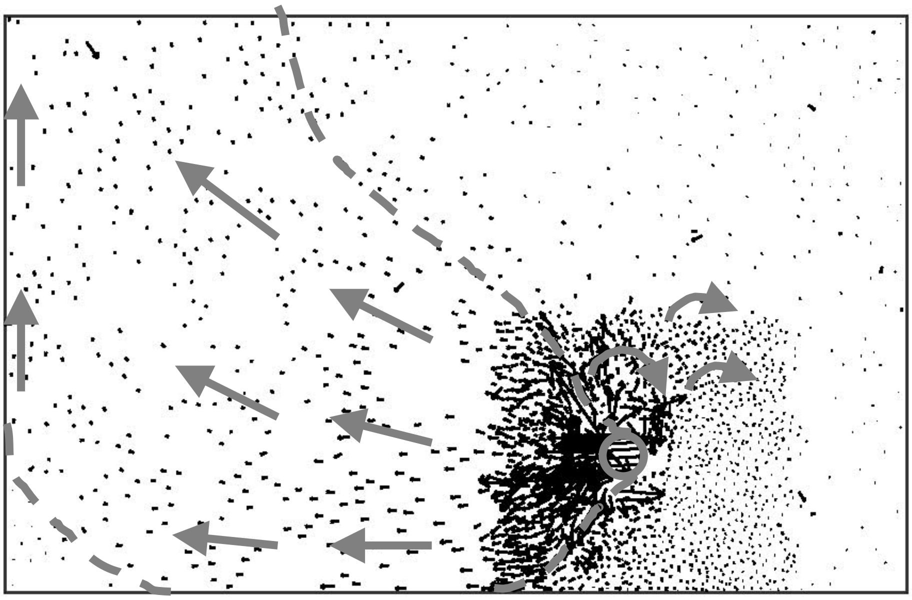

(b) DEM results, tan ϕ_μ = 3.0

Figure 7-7 Comparison of displacement pattern of lateral pipe loading from DEM and FEM (*H/D* = 11.5, Dense sand)

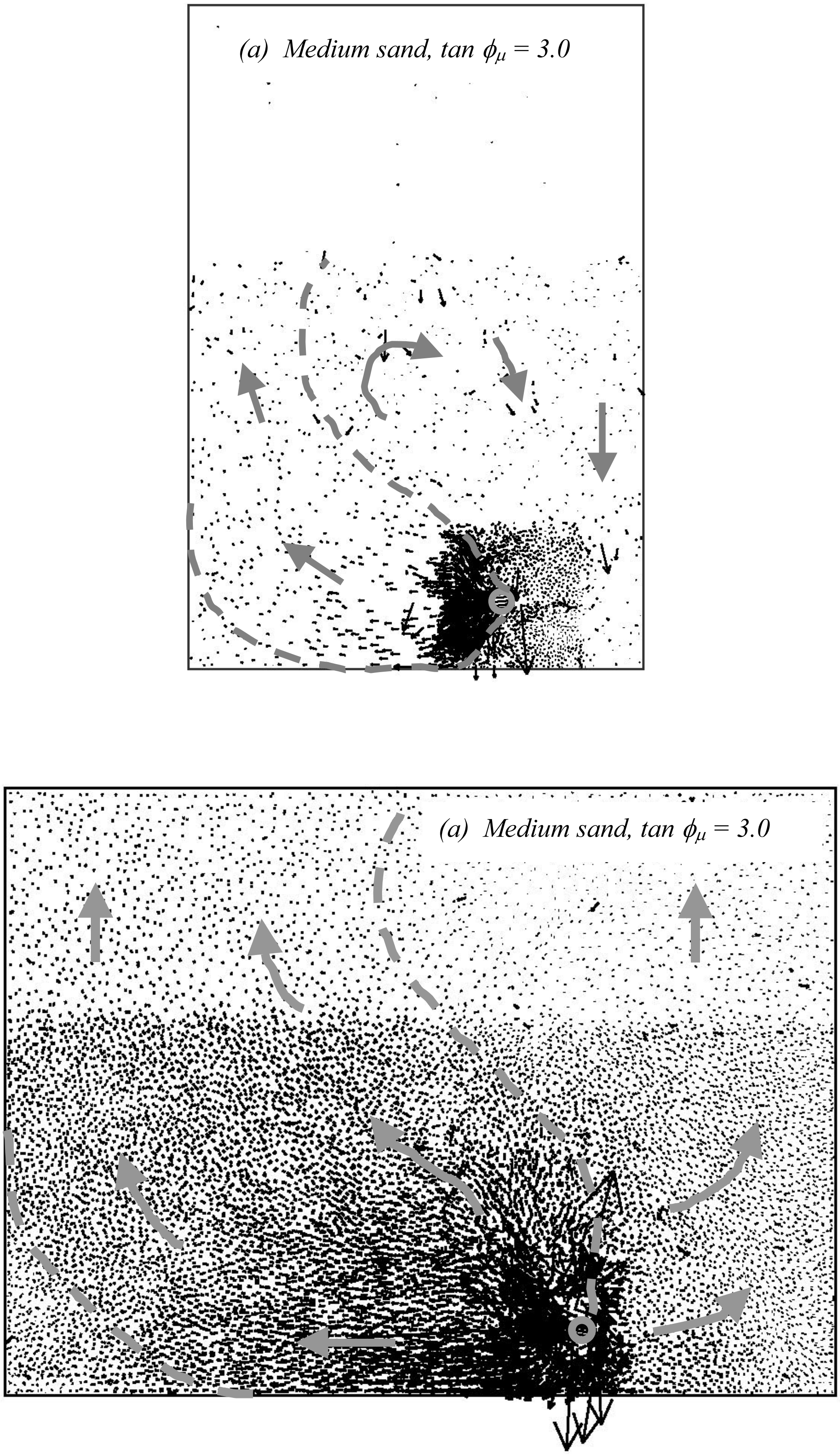

Figure 7-8 Displacement pattern from DEM of lateral pipe loading (*H/D* = 30)

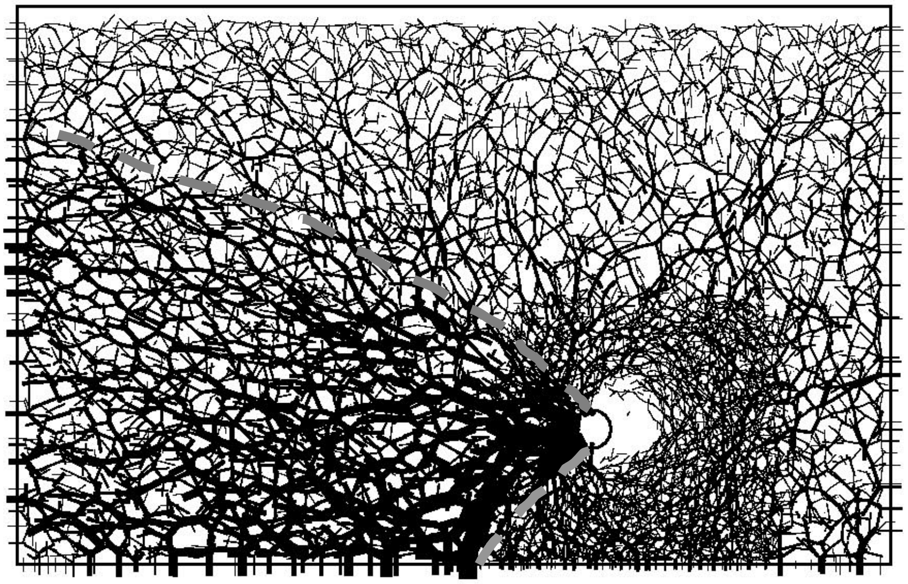

(a) Medium sand, tan $\phi_\mu = 3.0$

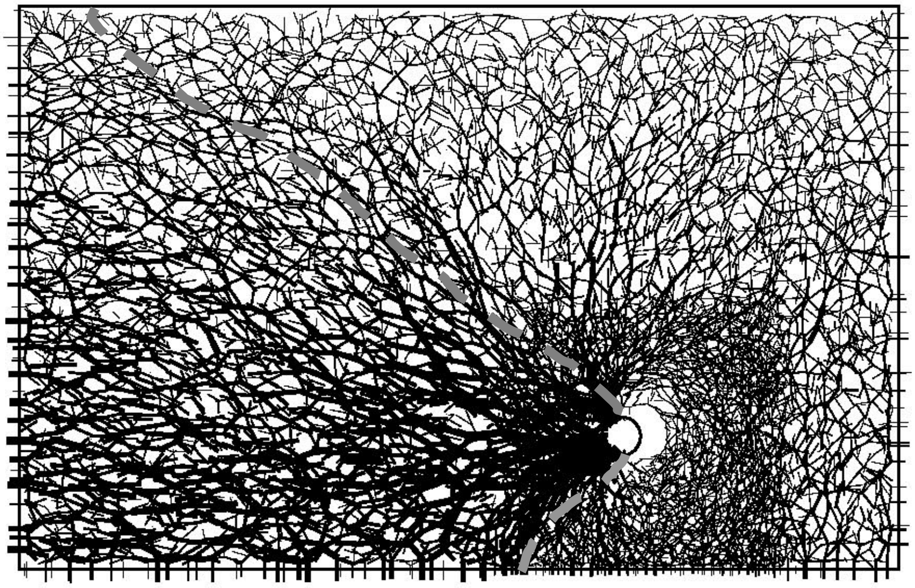

(b) Dense sand, tan $\phi_\mu = 3.0$

Figure 7-9 Contact force chain pattern from DEM of lateral pipe loading ($H/D = 11.5$)

7.3 Pipeline behavior under upward loading

Fig. 7-8 shows that, at shallow depth, the force-displacement relationships from the DEM analysis for medium sand match the experimental data well for all cases of tan ϕ_μ, whereas the results for dense sand match the experimental data well only for the cases of tan $\phi_\mu = 0.5$ and 1.0 with too soft behavior for the case of tan $\phi_\mu = 3.0$. Fig. 7-9 shows that, at deep depth, the force-displacement relationships from medium sand still match the FE results well for all cases of tan ϕ_μ, whereas the results for dense sand show that the cases of tan $\phi_\mu =$ 1.0, 3.0 yield closest results with the FE analysis and a tendency of overestimation of the peak dimensionless force for the case of tan $\phi_\mu = 0.5$.

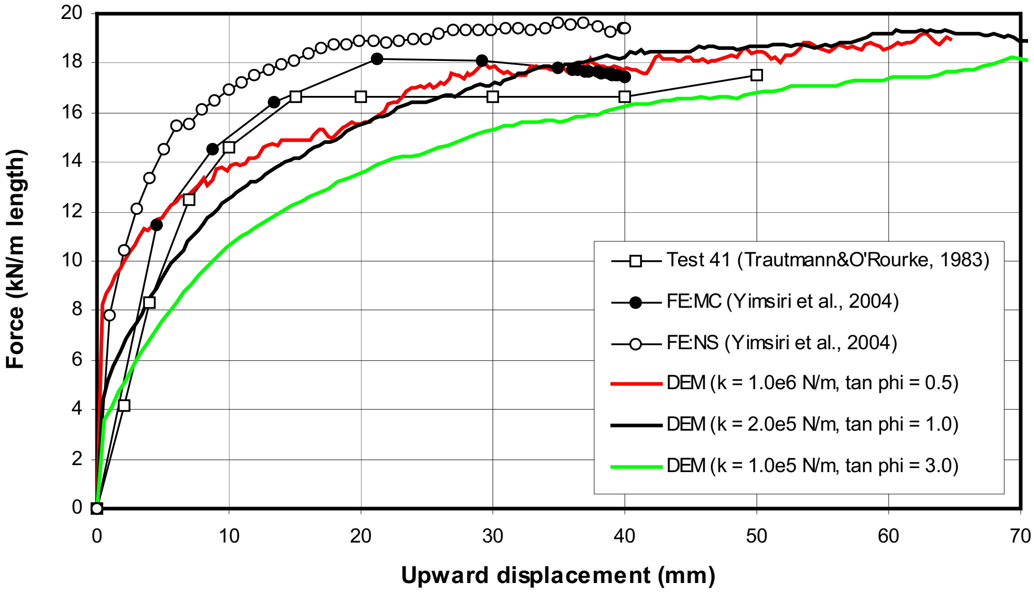

(a) H_c/D = 13, Medium sand

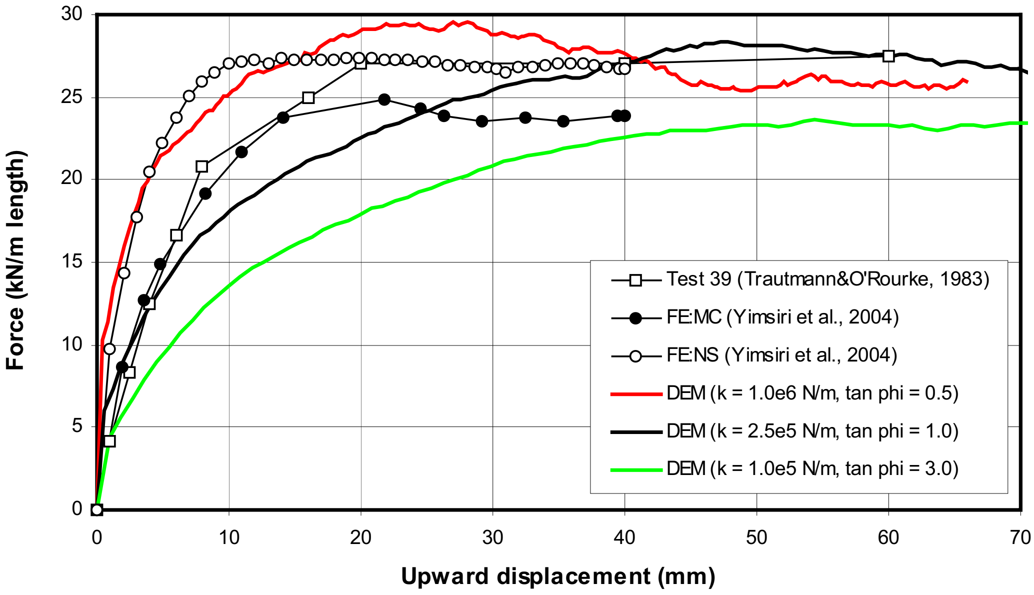

(b) H_c/D = 13, Dense sand

Figure 7-10 Force-displacement relationships at shallow embedment depth of upward pipe loading

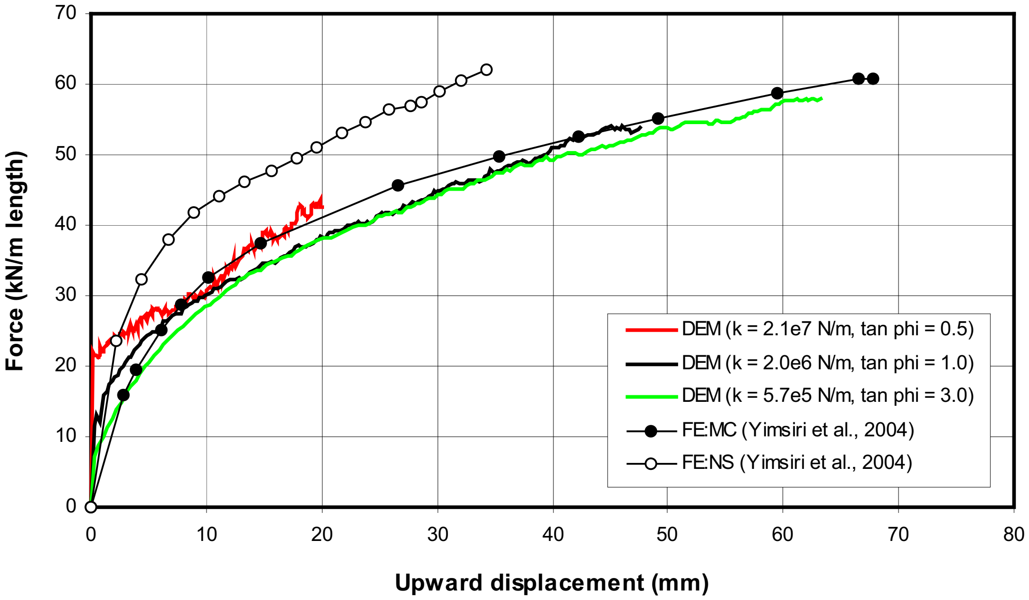

(a) $H_c/D = 30$, Medium sand

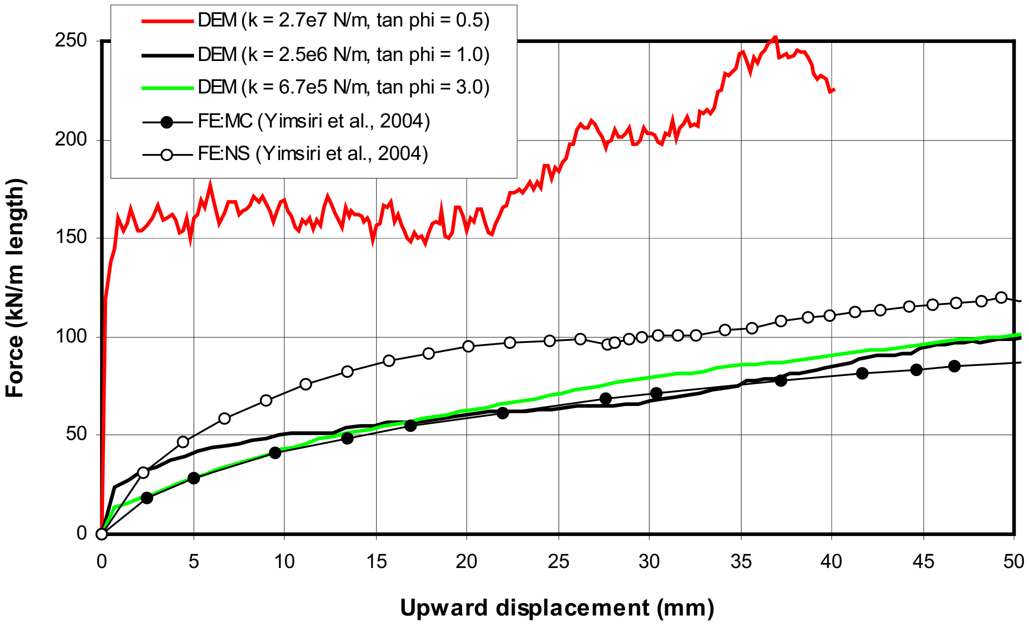

(b) $H_c/D = 30$, Dense sand

Figure 7-11 Force-displacement relationships at deep embedment depth of upward pipe loading

The comparison of the peak dimensionless forces from the DEM and FEM analysis is shown in Fig. 7-10. For medium sand, the DEM results match the FE results well for all cases. The DEM results for medium sand show deep failure mechanism with the critical embedment depth of 25 and the critical peak dimensionless force of 13, which is consistent with the FE results. For dense sand, the DEM results from the cases of tan $\phi_\mu = 1.0$, 3.0 yield closest results with the FE analysis with gradual transition from shallow to deep failure mechanism and a tendency of overestimation of the peak dimensionless at very deep depth ($H_c/D \geq 60$). However, the DEM results for the case of tan $\phi_\mu = 0.5$ show considerably overestimation and do not show any transition from shallow to deep failure mechanism.

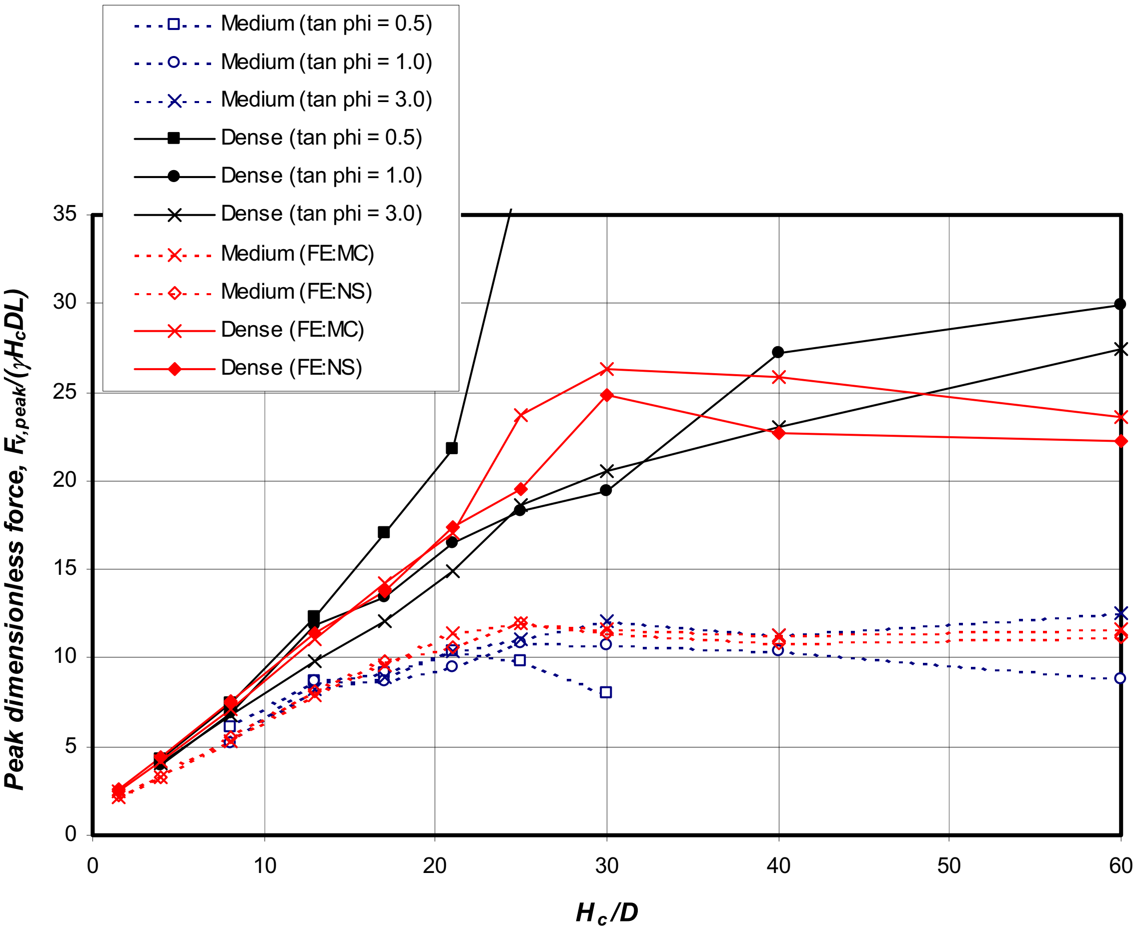

Figure 7-12 Comparison of peak dimensionless force of upward pipe loading from DEM and FEM

Fig. 7-13 shows that displacement pattern from the experimental tank test of medium sand at H_c/D = 13, which can be compared to those from FEM and DEM (tan ϕ_μ = 3.0) analyses shown in Fig. 7-14. Similarly, Fig. 7-15 shows that displacement pattern from the experimental tank test of dense sand at H_c/D = 13, which can be compared to those from FEM and DEM (tan ϕ_μ = 3.0) analyses shown in Fig. 7-16. It can be seen that the results from DEM better represent the displacement of sand around the pipe; however, the results from DEM involve larger soil mass compared with FEM, especially for dense sand. Fig. 7-17 shows the displacement pattern from DEM analysis at deep embedment depth. The results from both medium and dense sands show deep failure mechanism whereby the upward soil deformation does not extend to the ground surface. For medium sand case, this is consistent with the peak dimensionless force data in Fig. 7-12, which shows that a deep failure mechanism has been reached at H_c/D = 30. However, the dense sand case also shows a deep failure mechanism, although, at H_c/D = 30, it is still in the transition state. The extent of soil mass involved in the deformation pattern increases as the contact stiffness used increases (or the inter-particle friction angle used decreases). This makes the extent of soil deformation of dense sand at deep depth reaches the model boundary for the case of tan ϕ_μ = 0.5 (although the width of the testing compartment was already doubled to avoid or lessen the interference of boundary walls). This is consistent with the peak dimensionless force data in Fig. 7-12, which shows that the results for the case of tan ϕ_μ = 0.5 does not show deep failure mechanism due probably to this boundary effect. Fig. 7-18 presents the contact force chain pattern from DEM analysis. The results also show that the force chain involves large soil mass especially for dense sand.

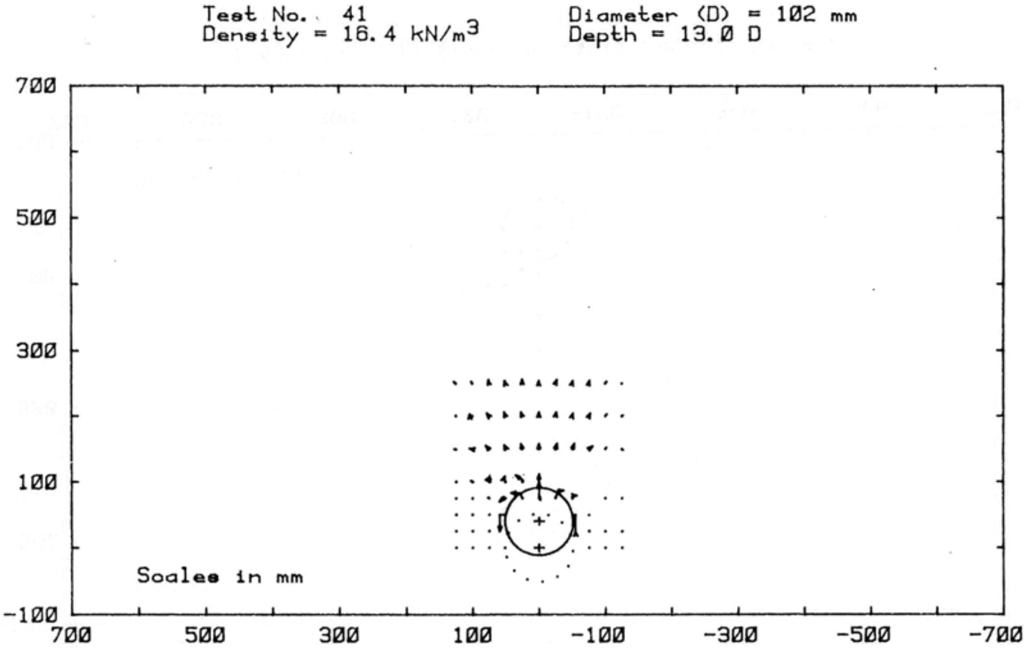

Figure 7-13 Displacement pattern of upward pipe loading from experimental tank test (H_c/D = 13, Medium sand) (Trautmann & O'Rourke, 1983)

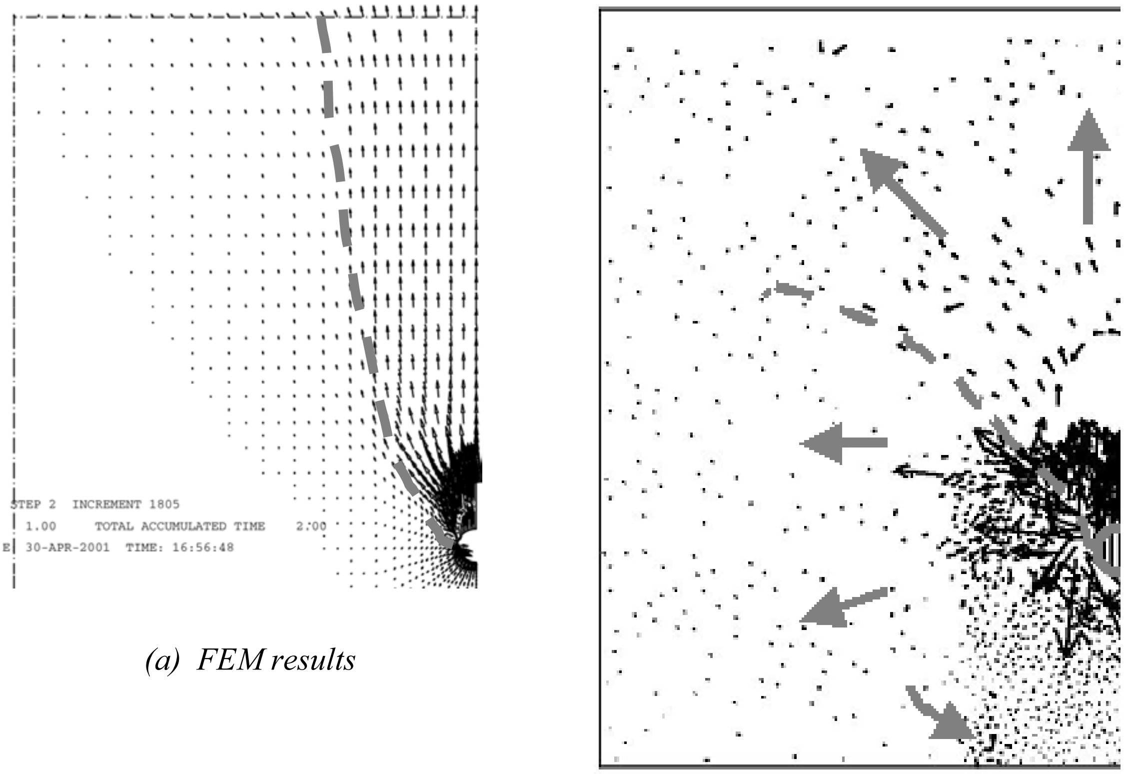

(a) FEM results

(b) DEM results (tan ϕ_μ = 3.0)

Figure 7-14 Comparison of displacement pattern of upward pipe loading from DEM and FEM (H_c/D = 13, Medium sand)

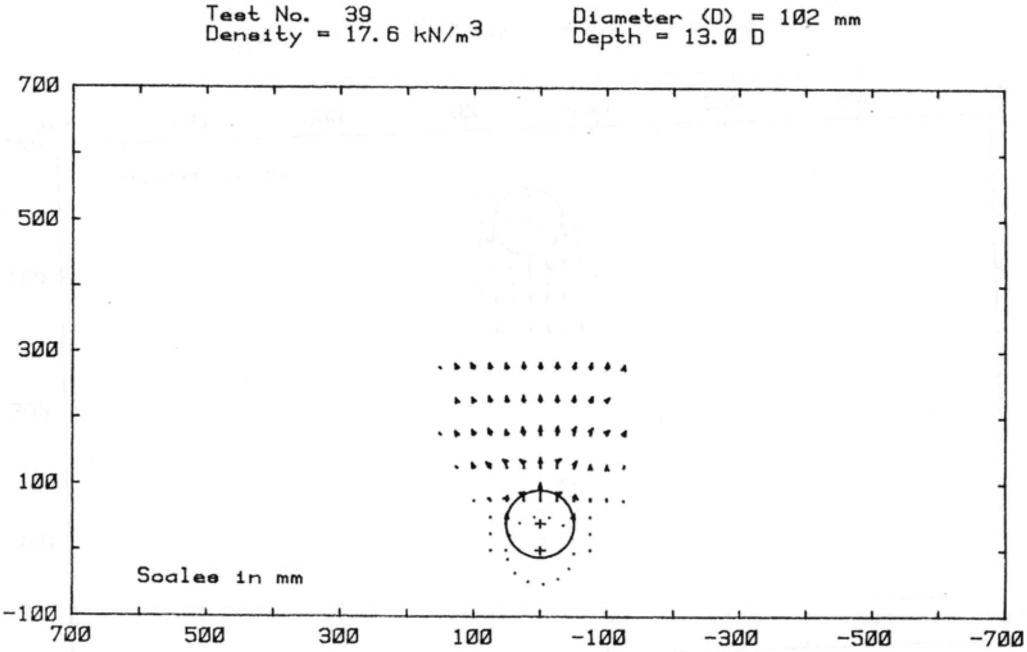

Figure 7-15 Displacement pattern of upward pipe loading from experimental tank test (H_c/D = 13, Dense sand) (Trautmann & O'Rourke, 1983)

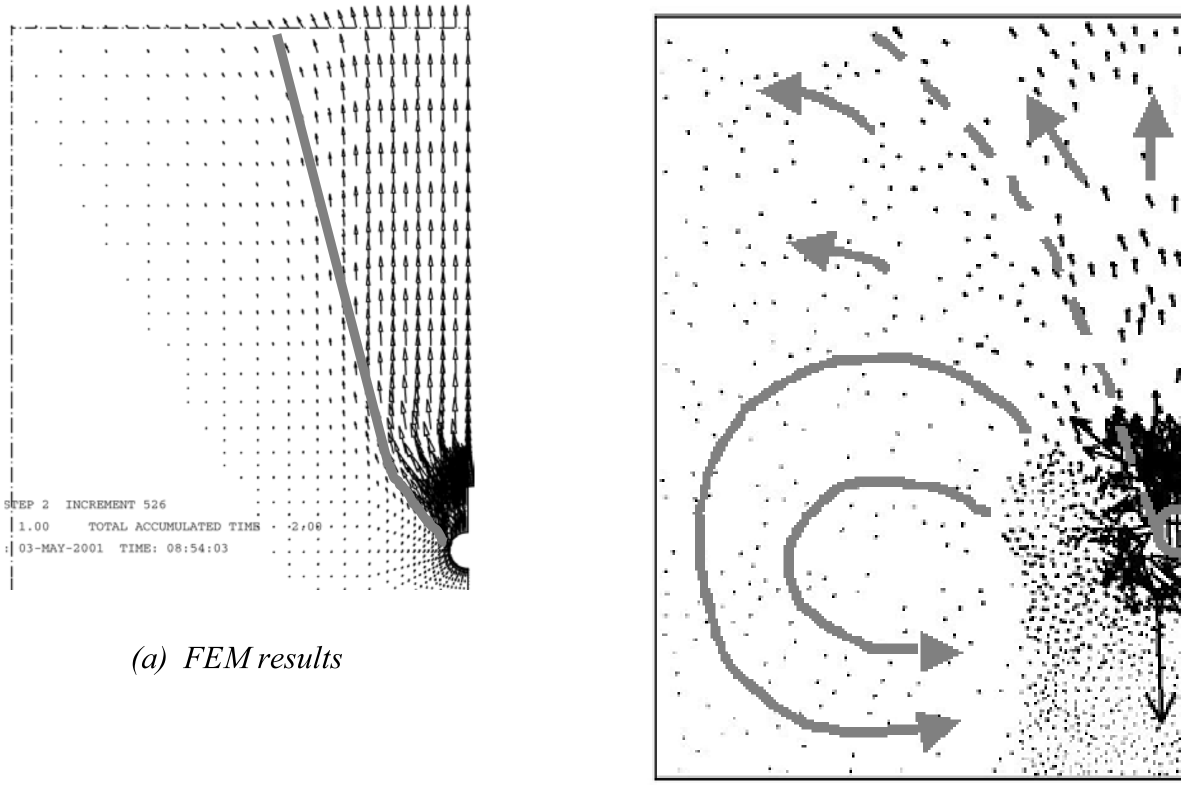

(a) FEM results

(b) DEM results (tan $\phi_\mu = 3.0$)

Figure 7-16 Comparison of displacement pattern of upward pipe loading from DEM and FEM (H_c/D = 13, Dense sand)

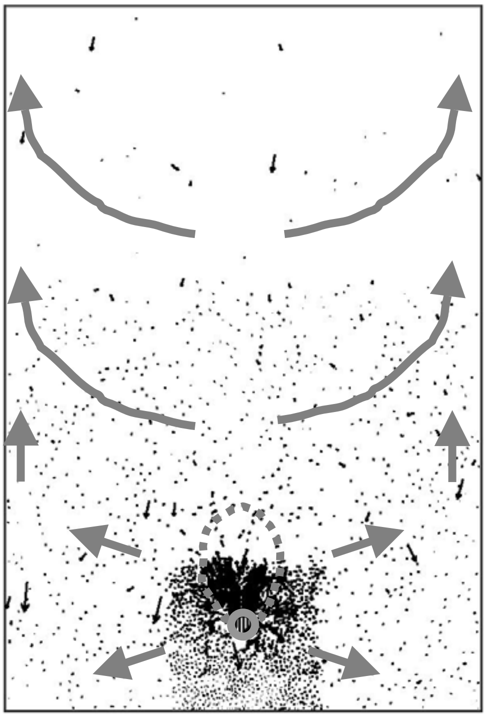

(a) Medium sand, tan ϕ_μ = 3.0

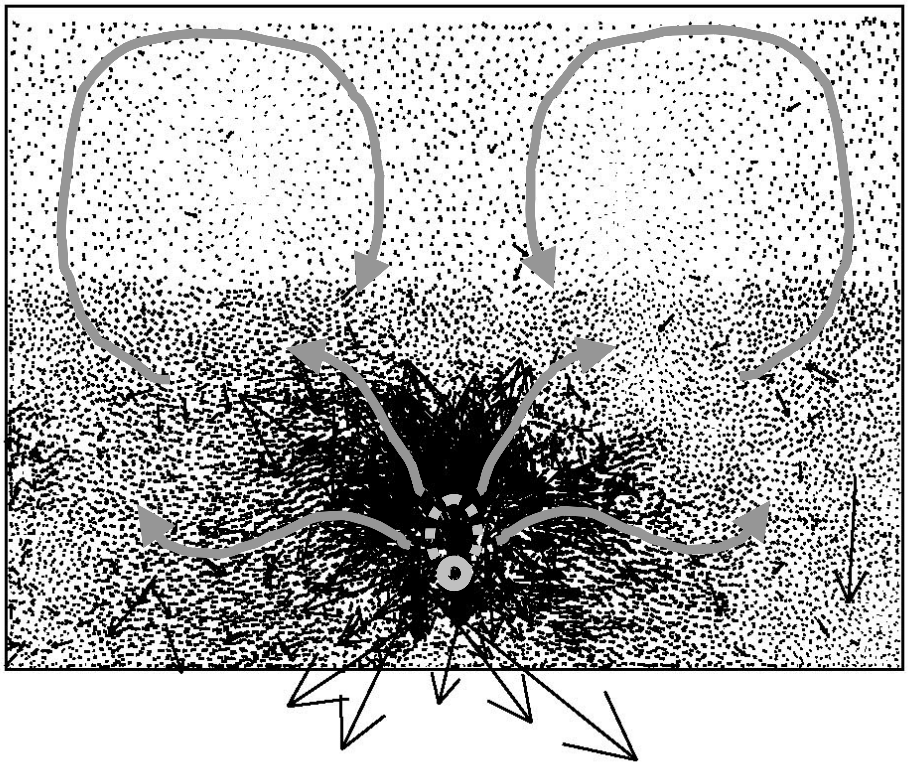

(b) Dense sand, tan ϕ_μ = 3.0

Figure 7-17 Displacement pattern from DEM of upward pipe loading (H_c/D = 30)

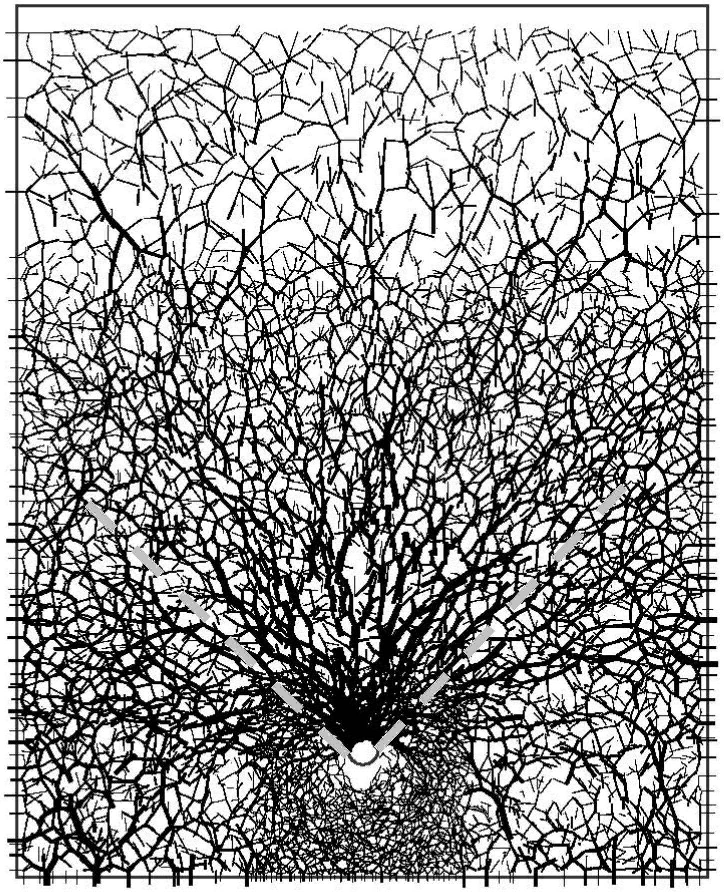

(a) Medium sand, tan ϕ_{μ} = 3.0

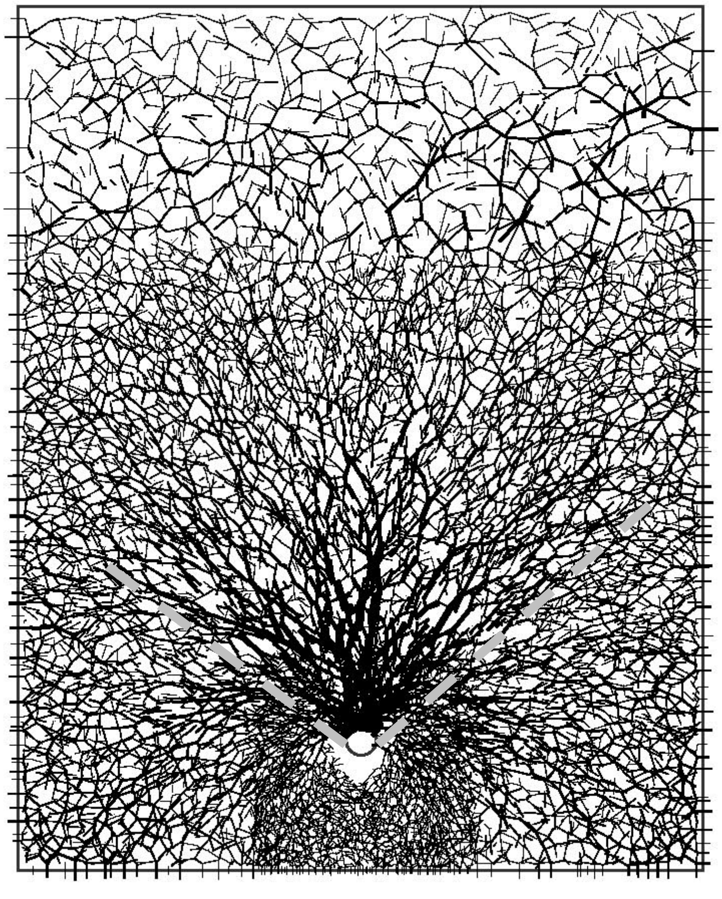

(b) Dense sand, tan ϕ_{μ} = 3.0

Figure 7-18 Contact force chain pattern from DEM of upward pipe loading (H_c/D = 25)

7.4 Conclusions

The soil-pipeline interactions under later and upward pipe movements in sand were investigated using DEM analysis. The simulations were performed for both medium and dense sand conditions at different embedment ratios of up to H/D = 60 and H_c/D = 60. At shallow depth, the force-displacement relationships from the DEM analysis for medium sand match the experimental data well for all cases of tan ϕ_μ, whereas the results for dense sand match the experimental data well only for the cases of tan ϕ_μ = 0.5 and 1.0 with too soft behavior for the case of tan ϕ_μ = 3.0. At deep depth, the force-displacement relationships from medium sand still match the FE results well for all cases of tan ϕ_μ; however, the results for dense sand show that the case of tan ϕ_μ = 3.0 yield closest results with the FE analysis and a tendency of overestimation of the peak dimensionless force for the case of tan ϕ_μ = 0.5.

The comparison of peak dimensionless forces from the DEM and FEM analysis shows that, for medium sand, the DEM results show deep failure mechanism and the results match the FE results well for all cases of tan ϕ_μ. For dense sand, the DEM results from the cases of tan ϕ_μ = 1.0, 3.0 yield closest results with the FE analysis with gradual transition from shallow to deep failure mechanism and a tendency of overestimation of the peak dimensionless at very deep depth. However, the DEM results for the case of tan ϕ_μ = 0.5 show considerably overestimation and do not show any transition from shallow to deep failure mechanism which is due probably to model boundary interference.

The investigation on the displacement patterns shows that the results from DEM analysis, especially for dense sand, involve larger soil mass compared with FEM results.

The results from this DEM analysis together with earlier FEM analysis will serve as a Class-A prediction of the future full-scale tank test of this problem.

Appendix A

Force-Displacement Curves of Pipe under Lateral Loading

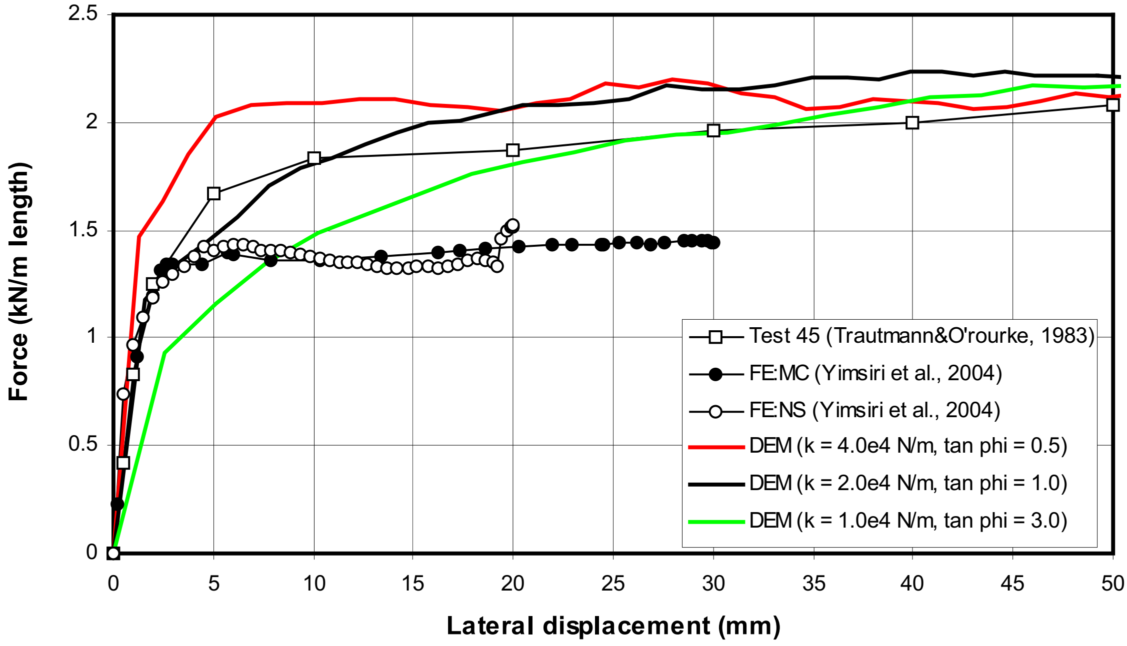

Figure A-1 *H/D* = 2: Medium sand

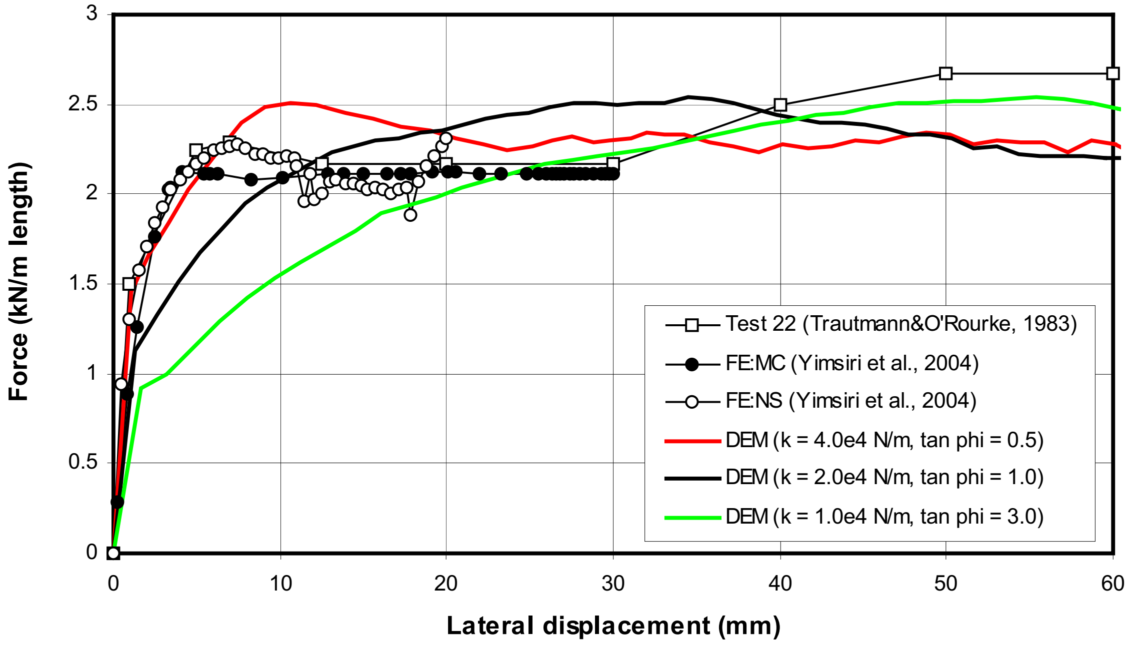

Figure A-2 *H/D* = 2: Dense sand

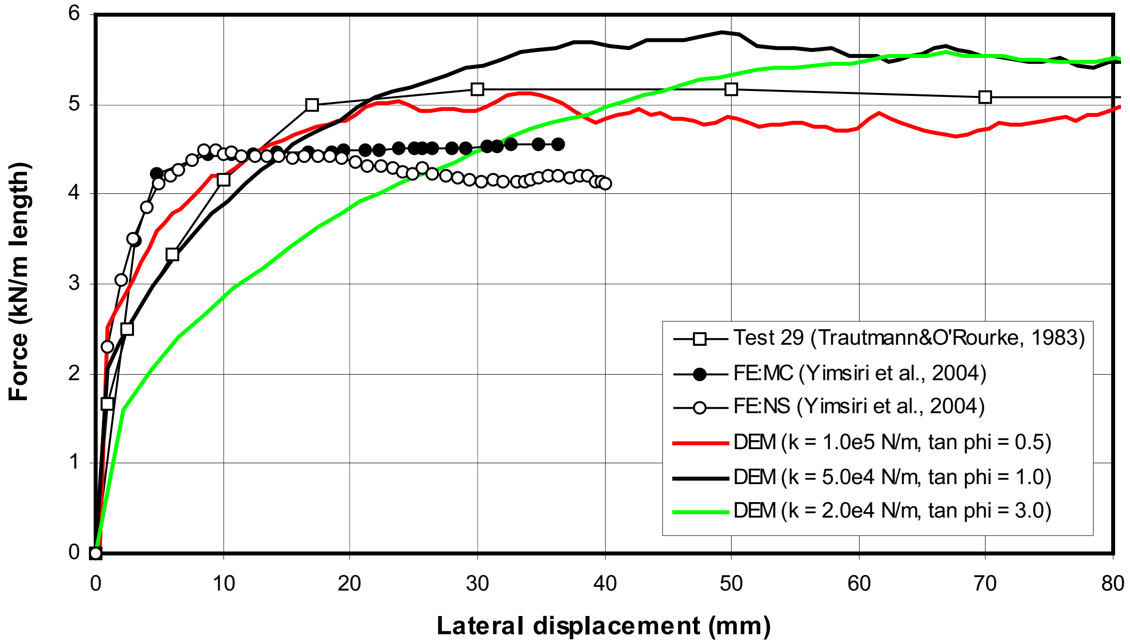

Figure A-3 *H/D* = 4: Medium sand

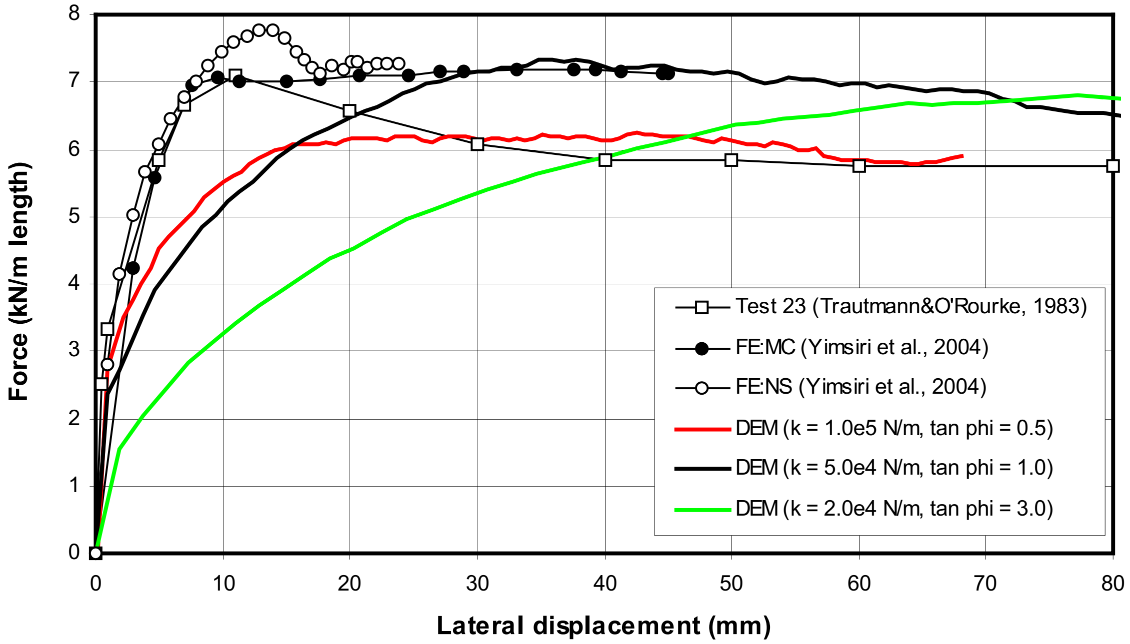

Figure A-4 *H/D* = 4: Dense sand

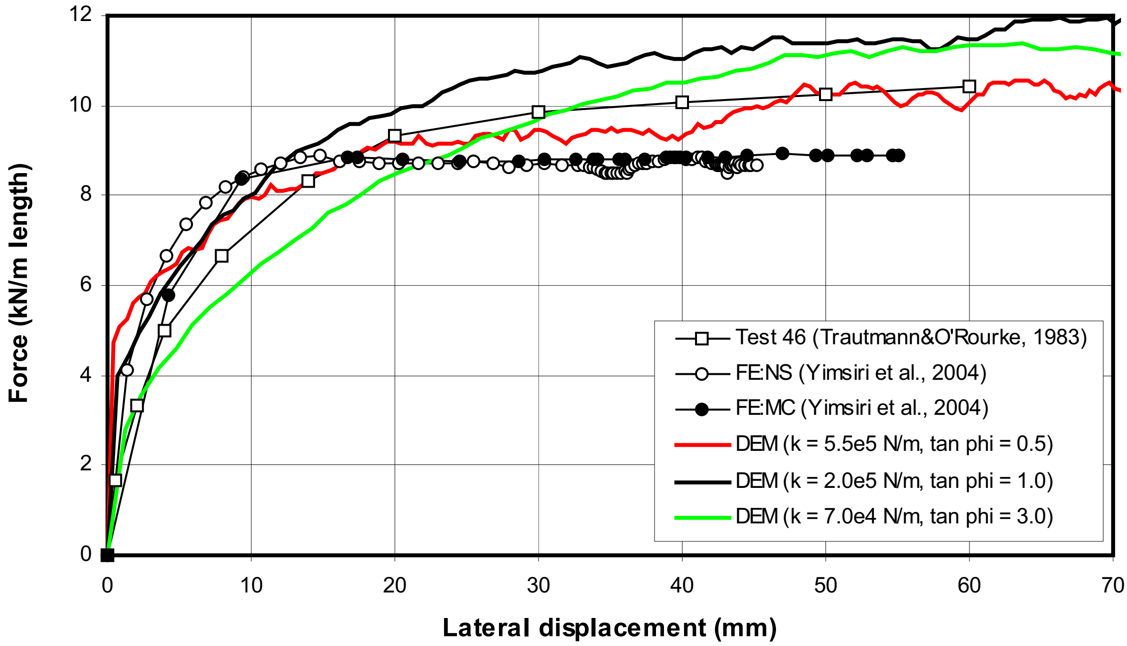

Figure A-5 *H/D* = 6: Medium sand

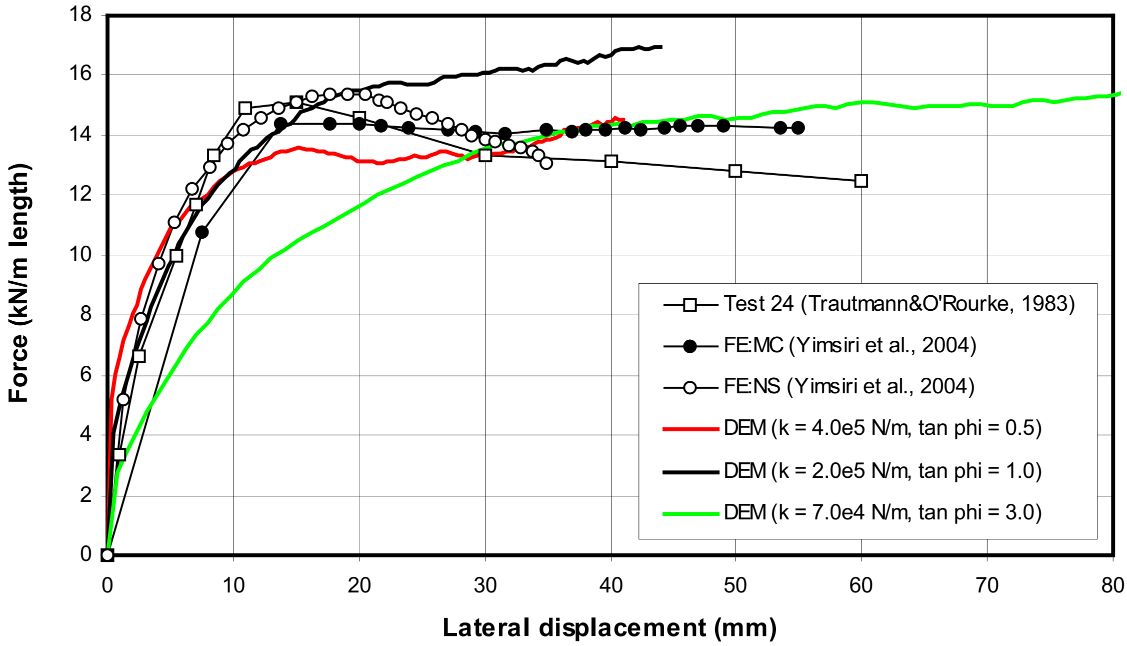

Figure A-6 *H/D* = 6: Dense sand

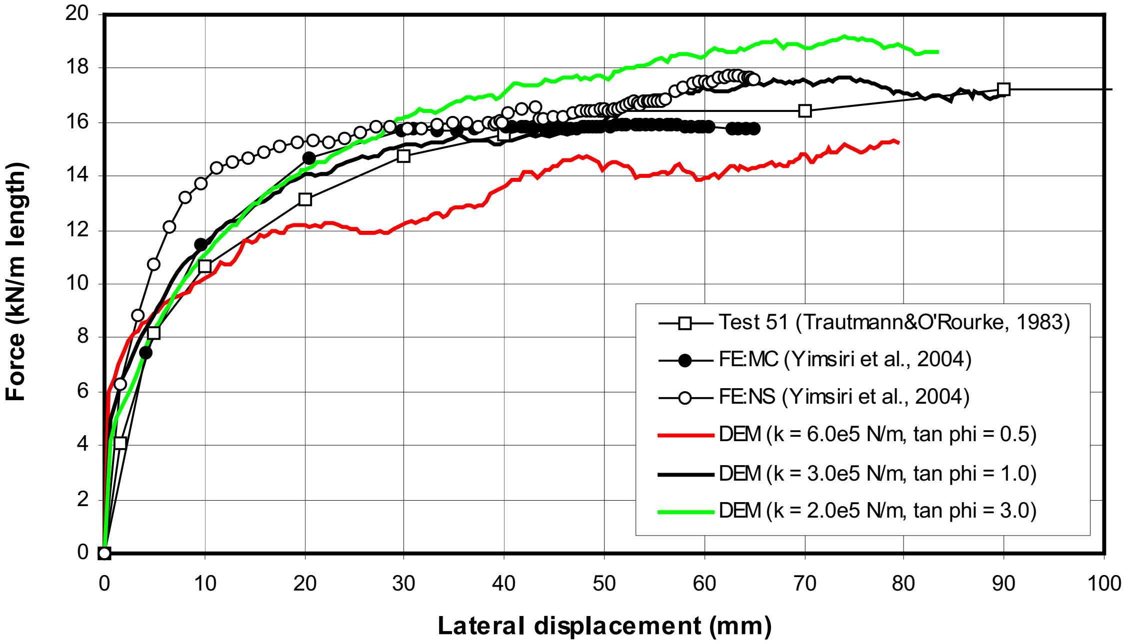

Figure A-7 *H/D* = 8.5: Medium sand

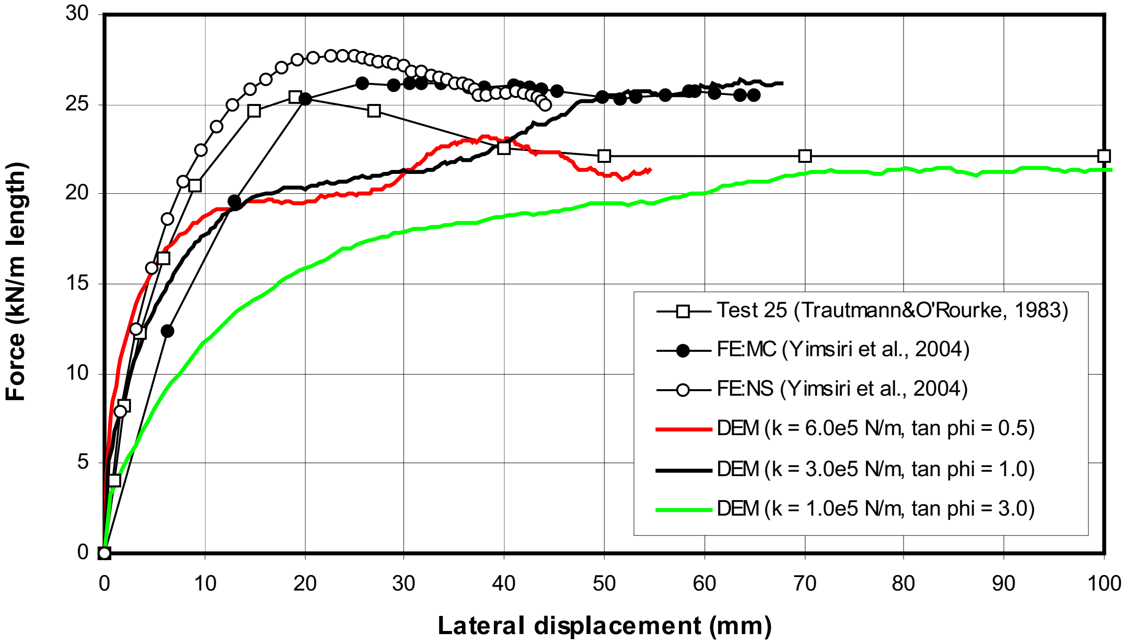

Figure A-8 *H/D* = 8.5: Dense sand

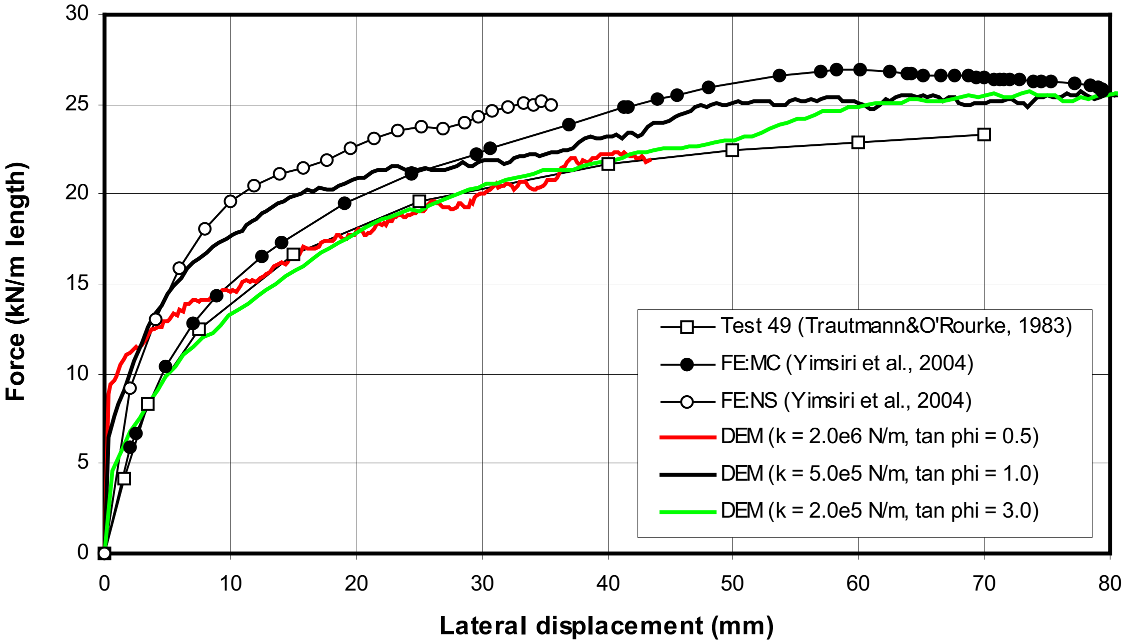

Figure A-9 *H/D* = 11.5: Medium sand

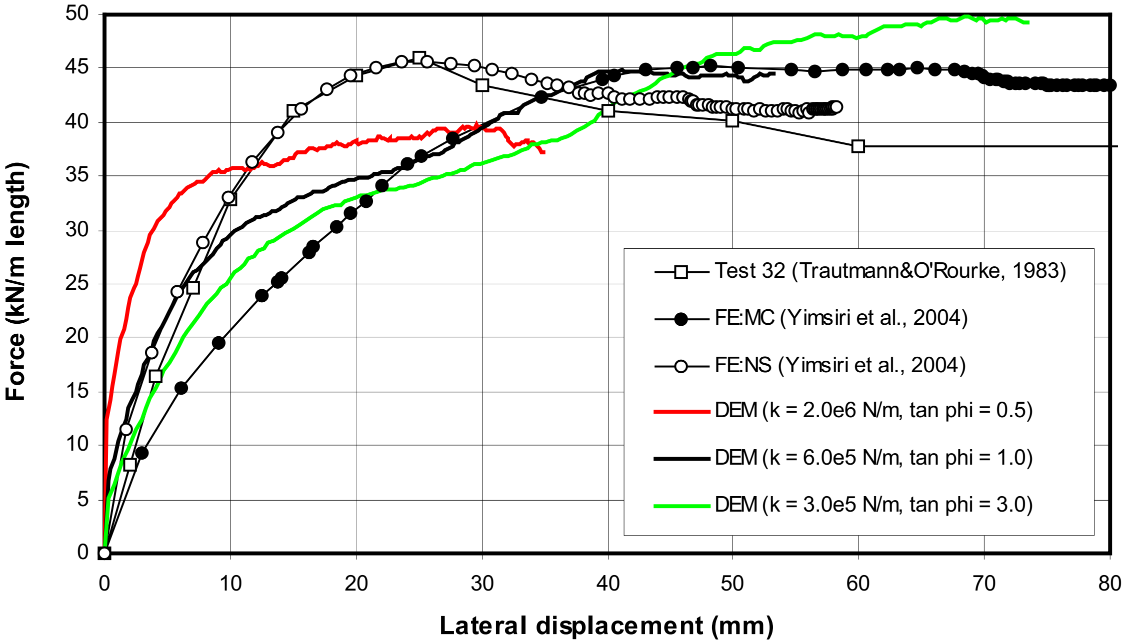

Figure A-10 *H/D* = 11.5: Dense sand

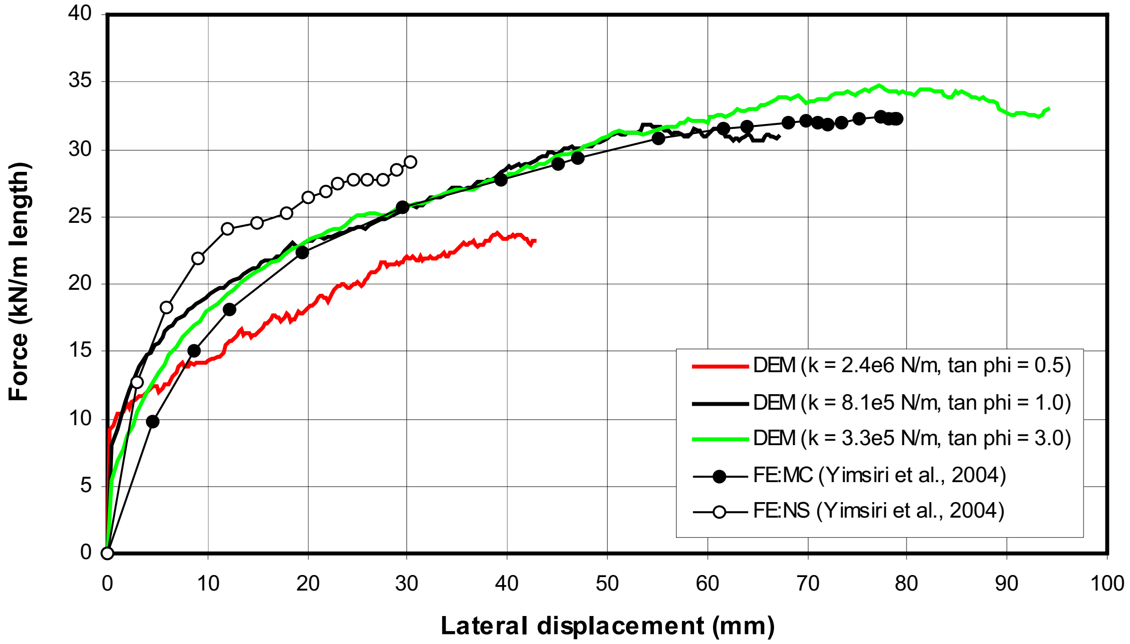

Figure A-19 *H/D* = 14.5, Medium sand

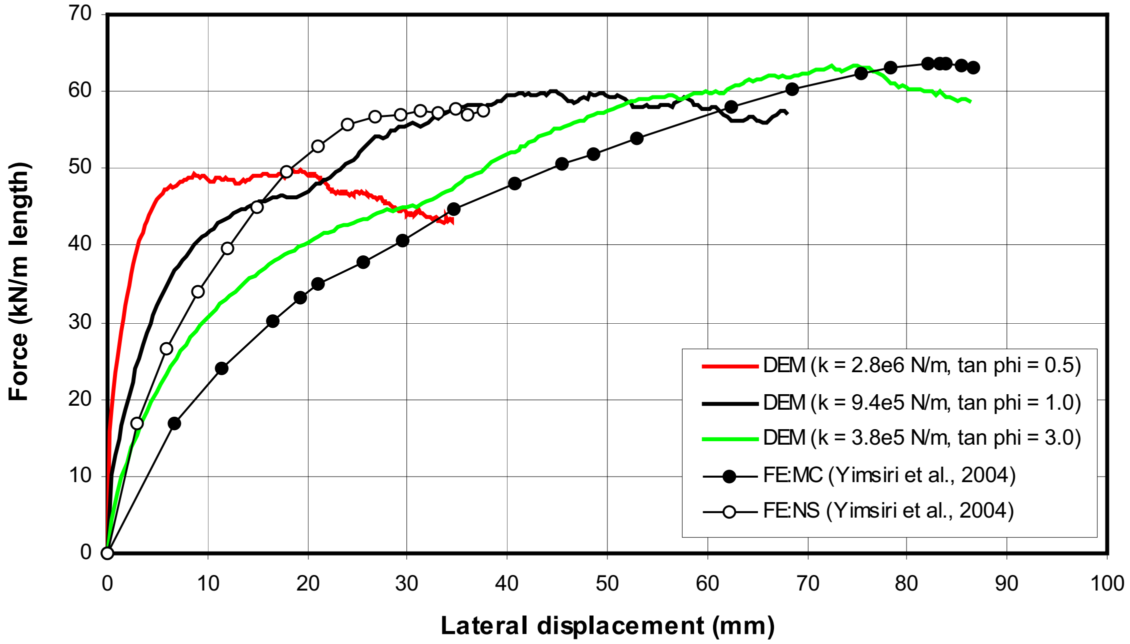

Figure A-20 *H/D* = 14.5, Dense sand

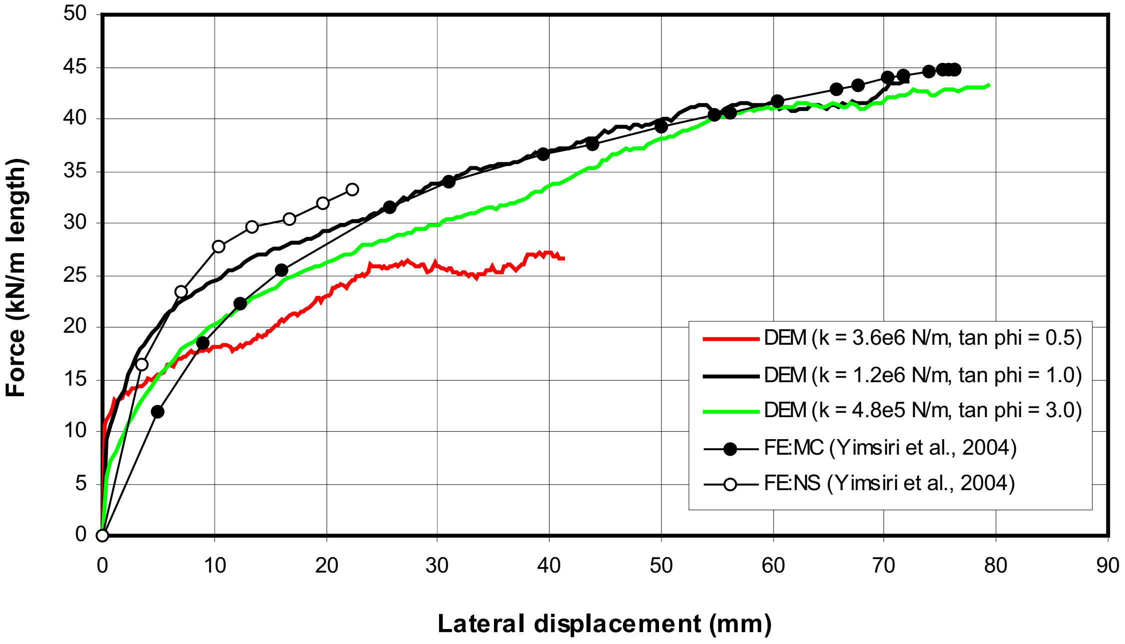

Figure A-21 *H/D* = 17.5, Medium sand

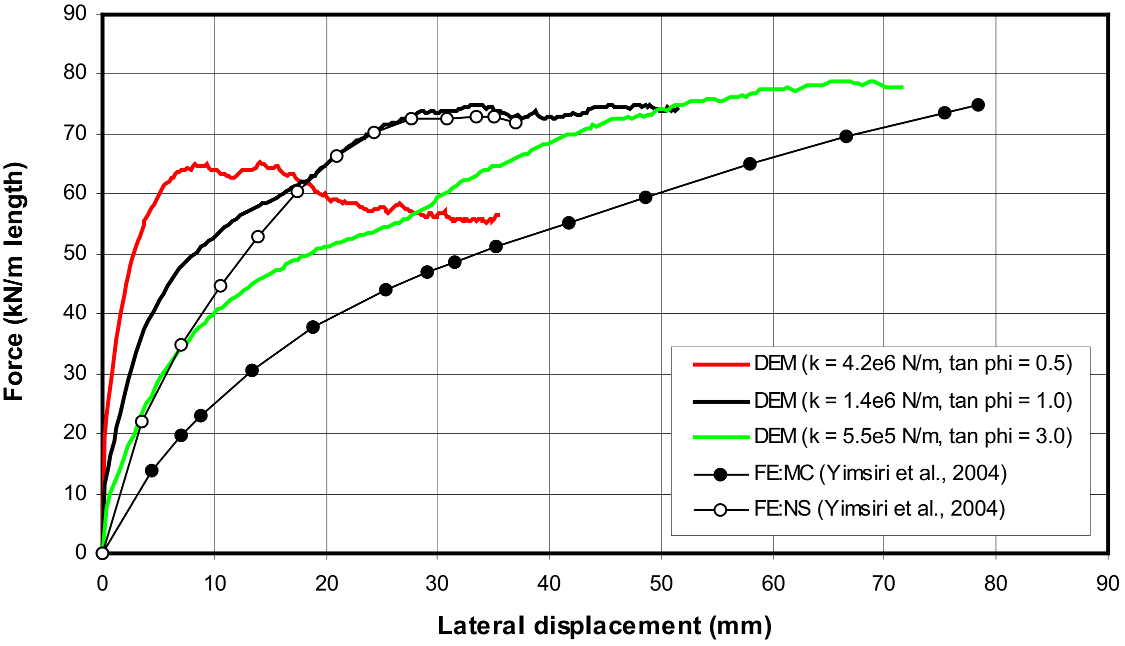

Figure A-22 *H/D* = 17.5, Dense sand

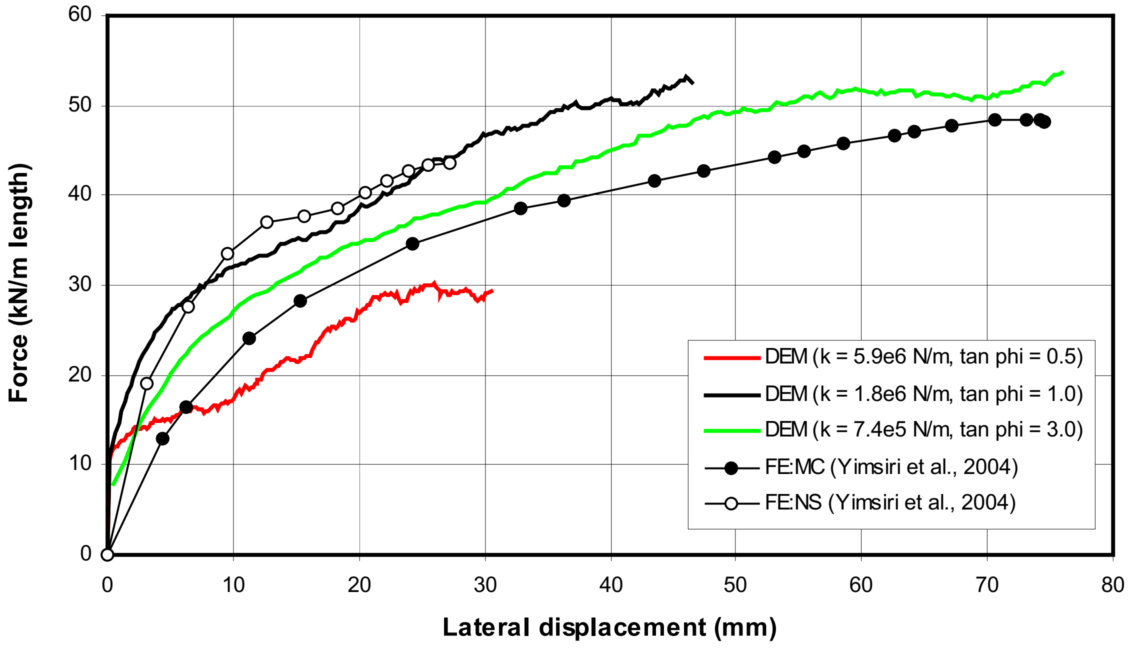

Figure A-23   *H/D* = 22, Medium sand

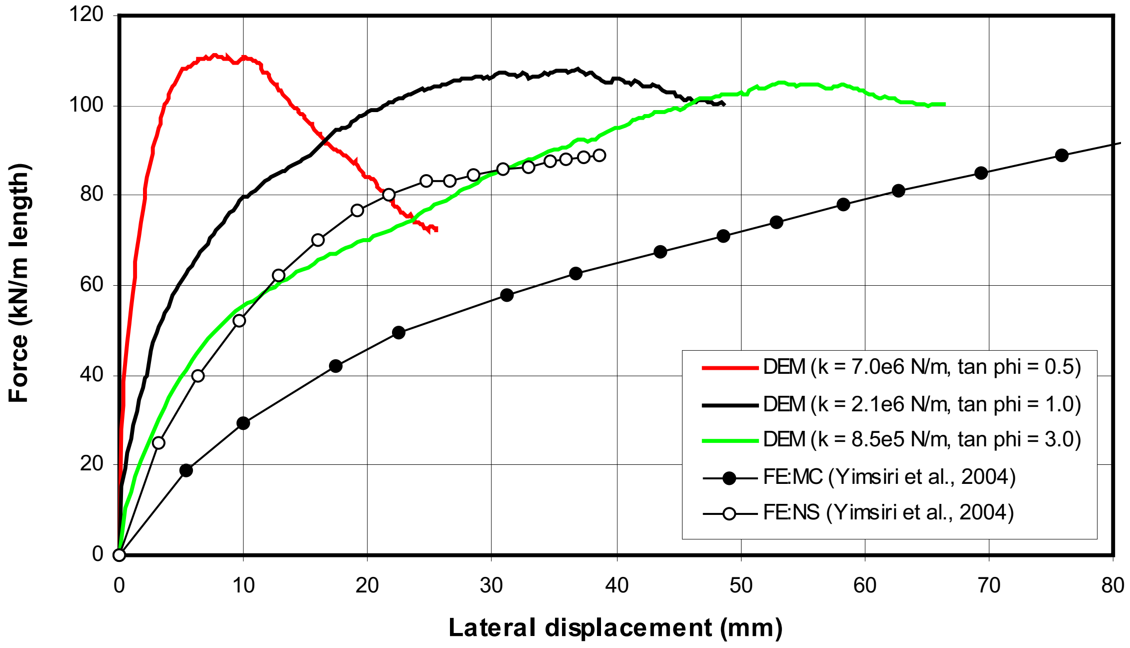

Figure A-24   *H/D* = 22, Dense sand

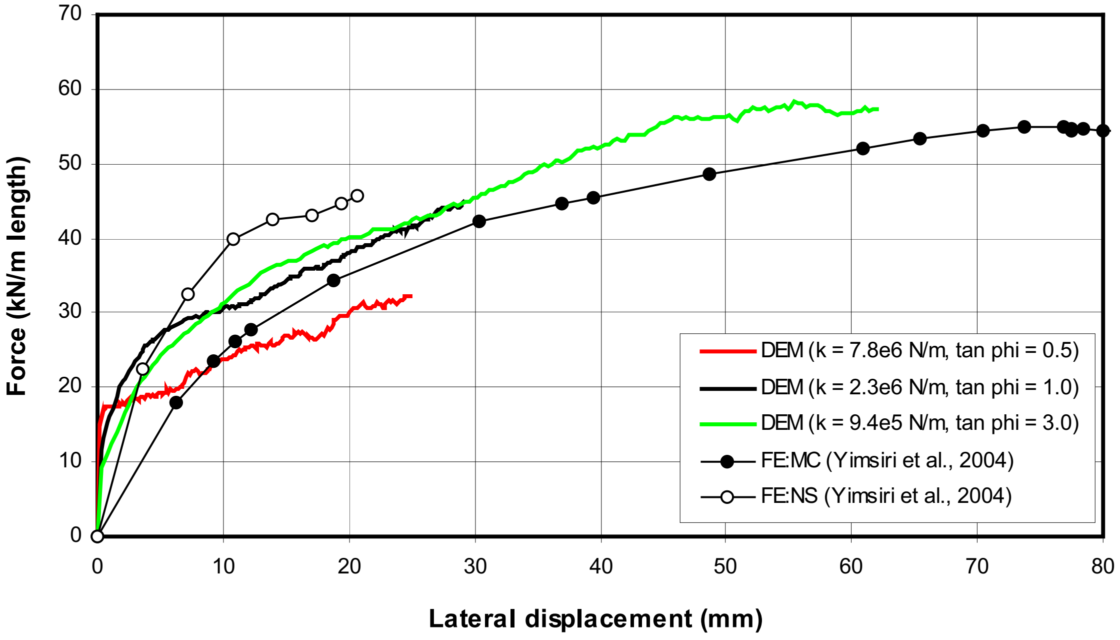

Figure A-25 *H/D* = 25, Medium sand

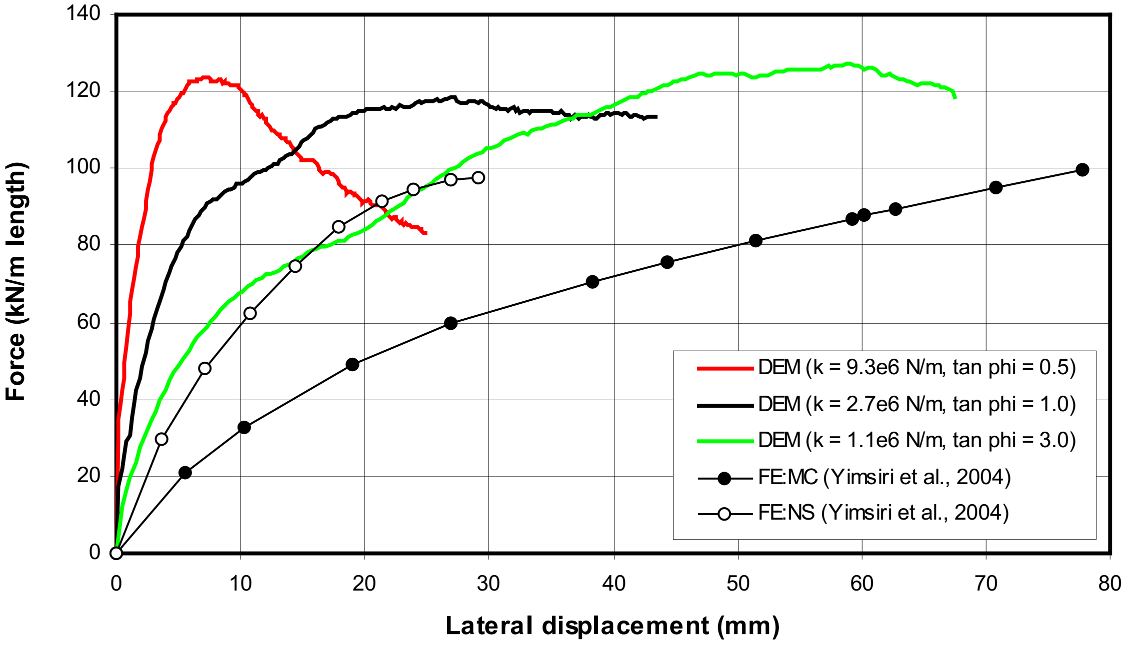

Figure A-26 *H/D* = 25, Dense sand

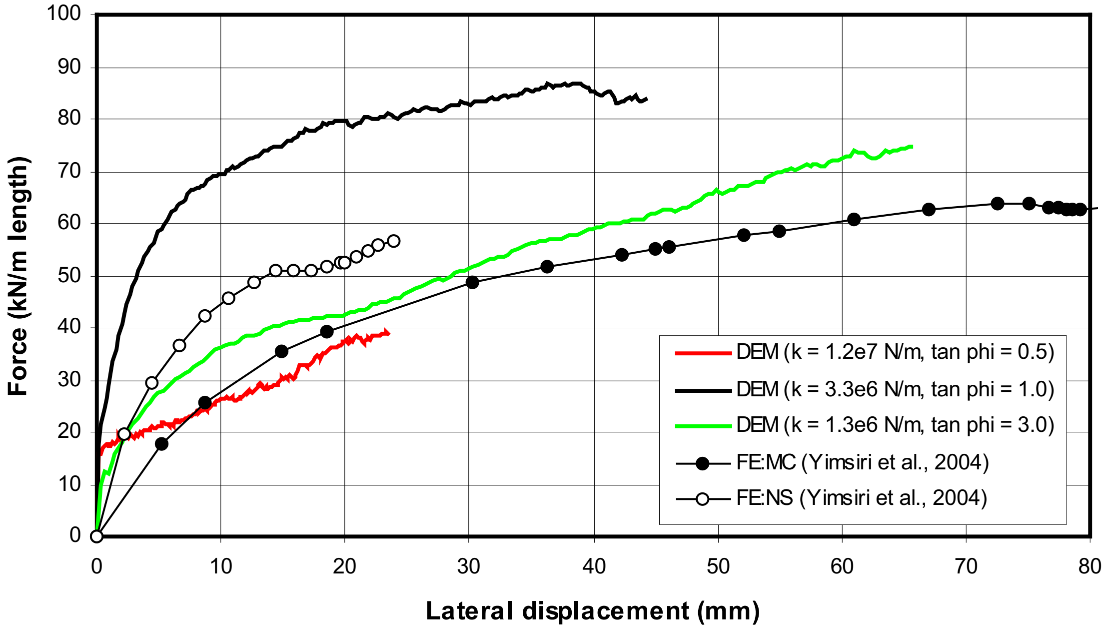

Figure A-27 *H/D* = 30, Medium sand

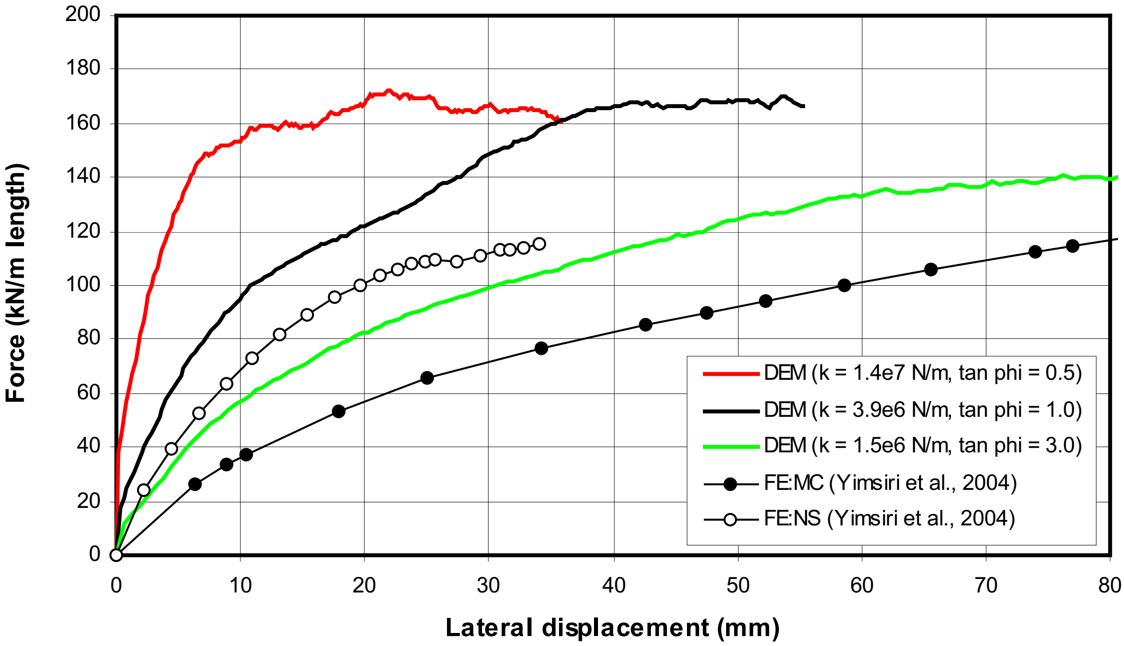

Figure A-28 *H/D* = 30, Dense sand

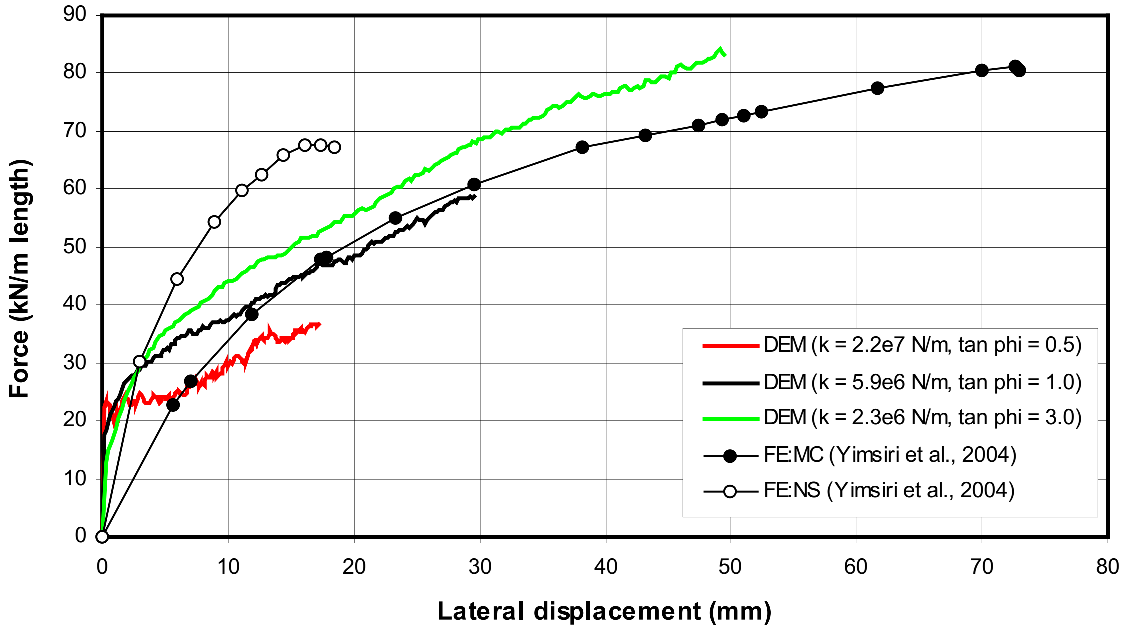

Figure A-29 *H/D* = 40, Medium sand

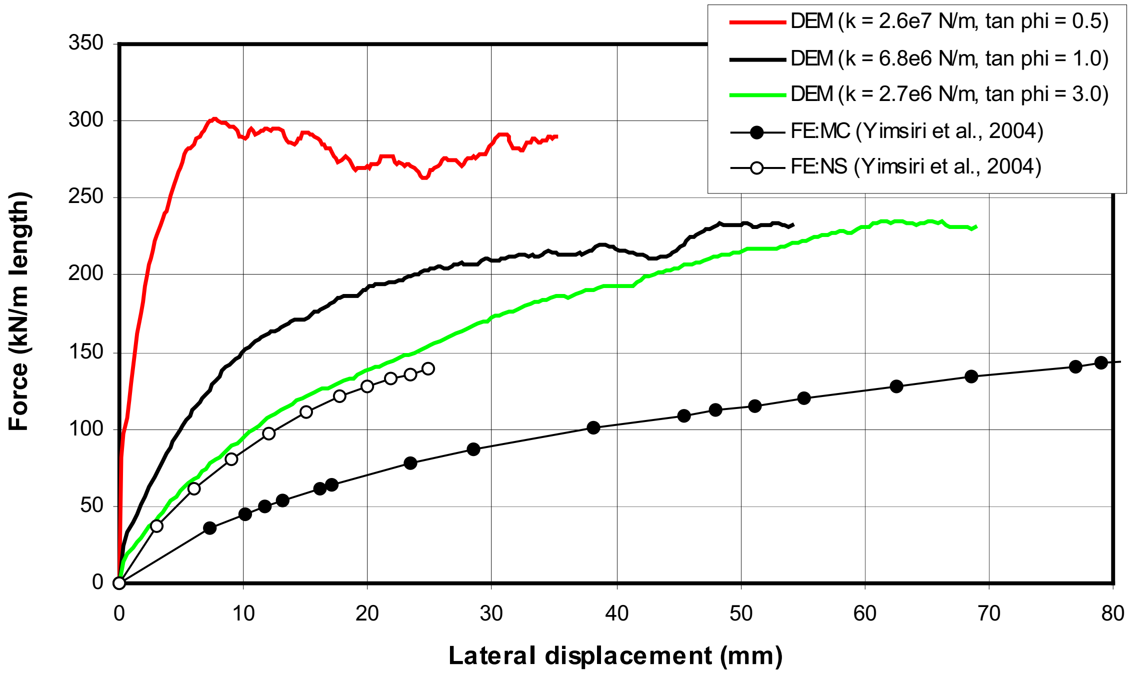

Figure A-30 *H/D* = 40, Dense sand

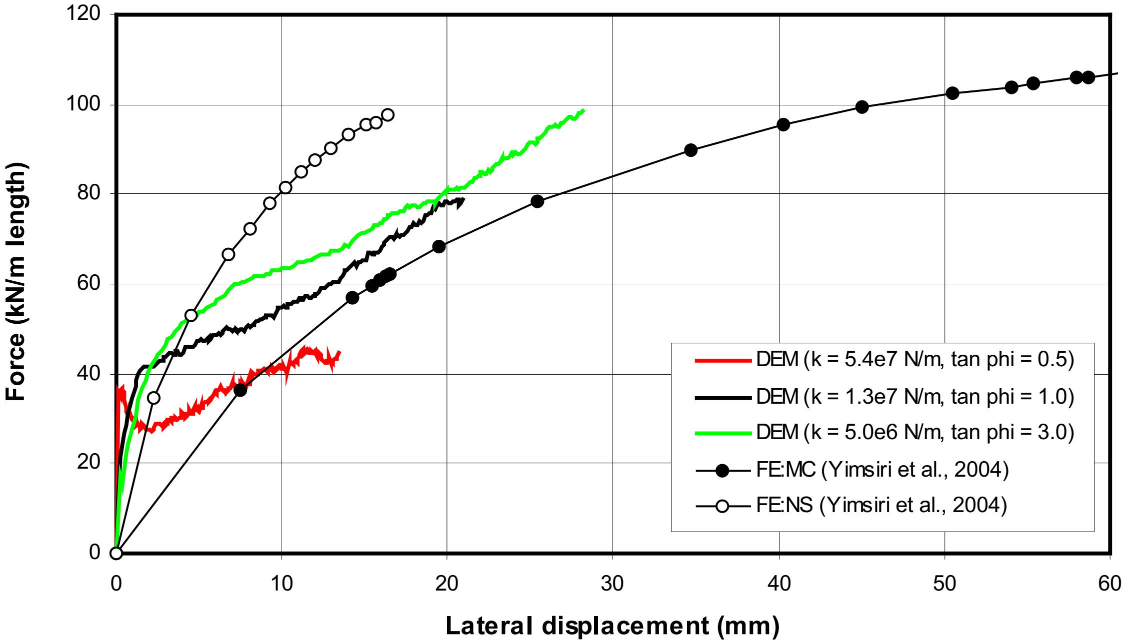

Figure A-31   *H/D* = 60, Medium sand

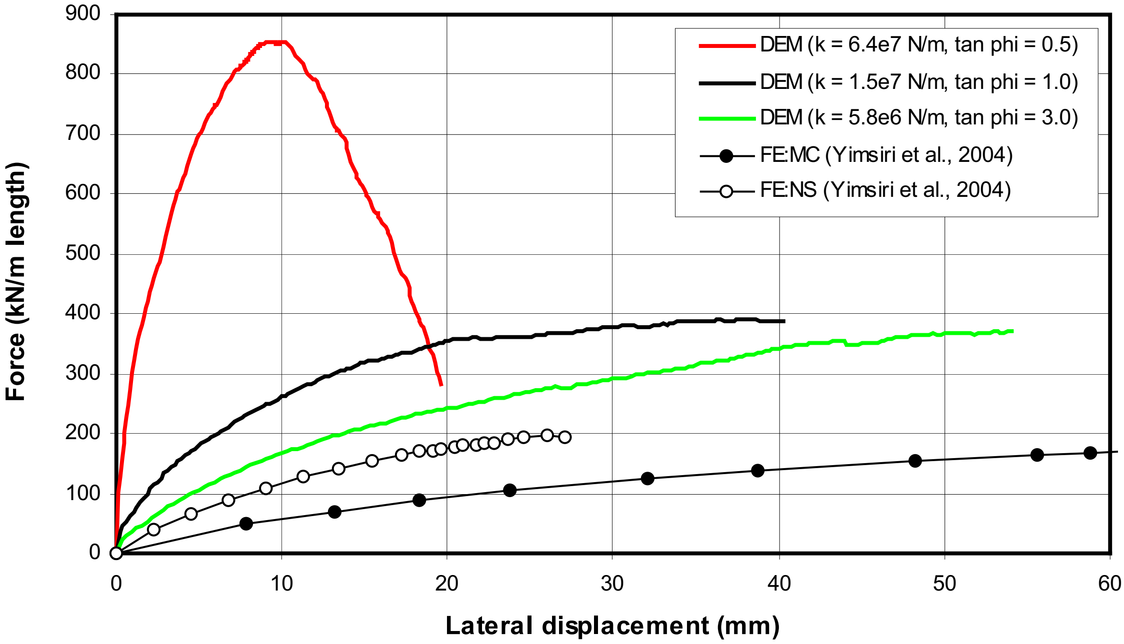

Figure A-32   *H/D* = 60, Dense sand

Appendix B

Force-Displacement Curves of Pipe under Upward Loading

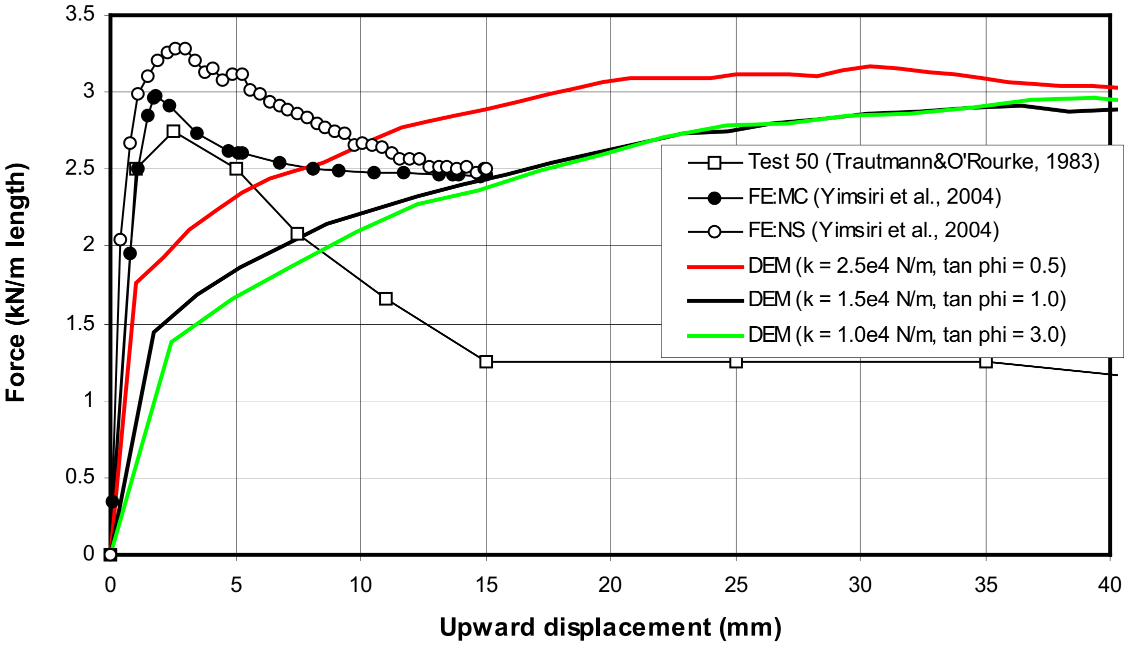

Figure B-1 $H_c/D = 4$: Dense sand

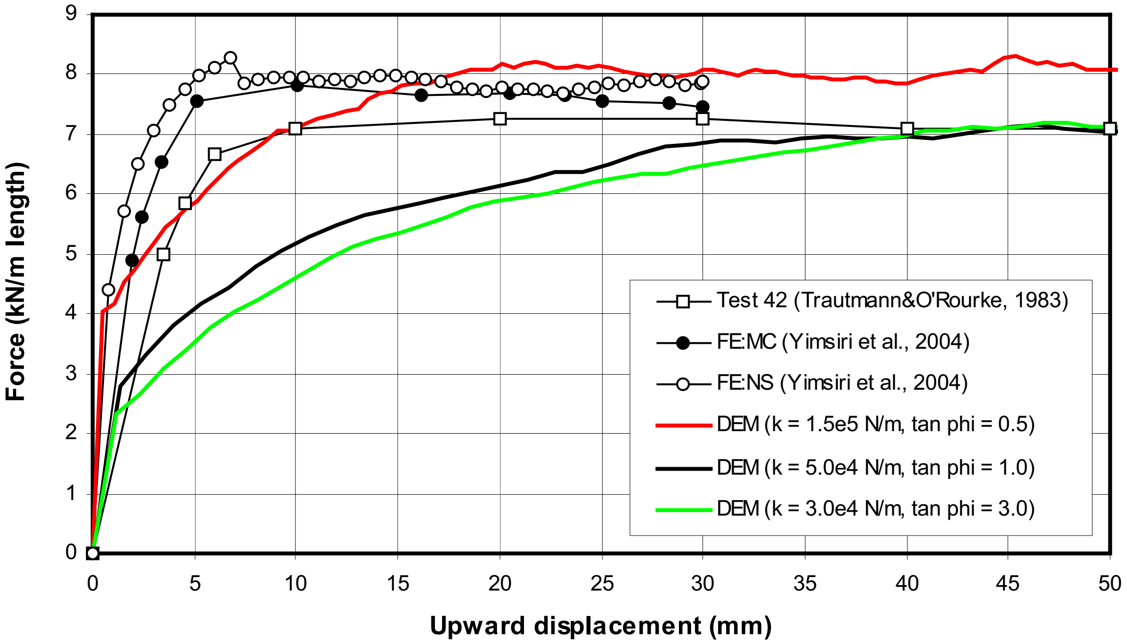

Figure B-2 $H_c/D = 8$: Medium sand

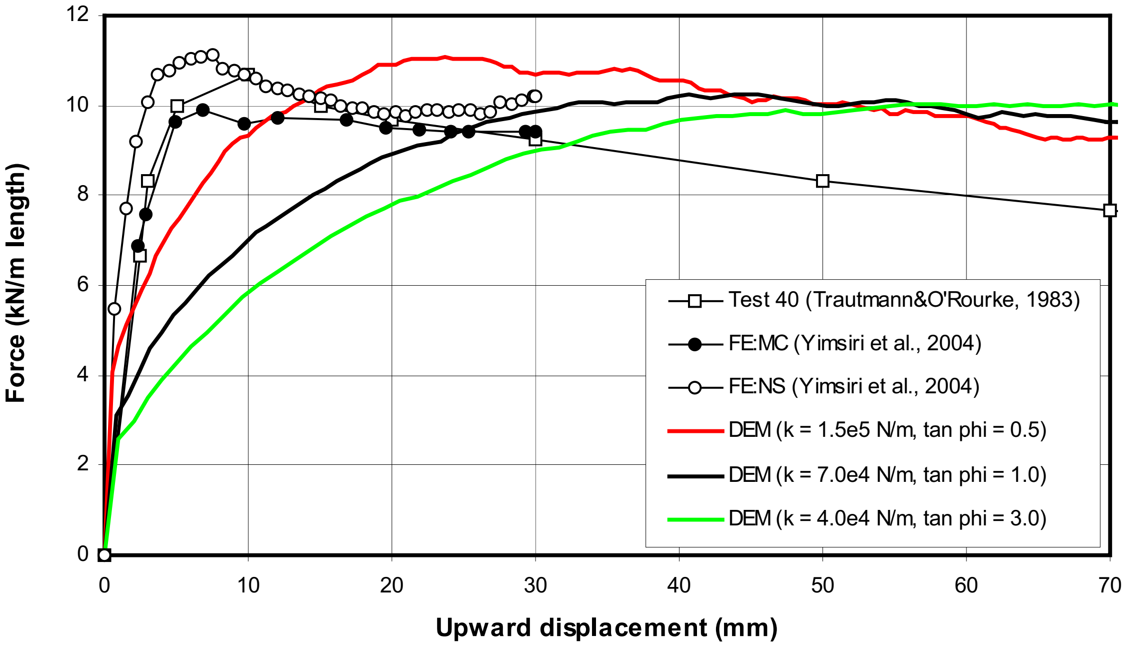

Figure B-3 $H_c/D = 8$: Dense sand

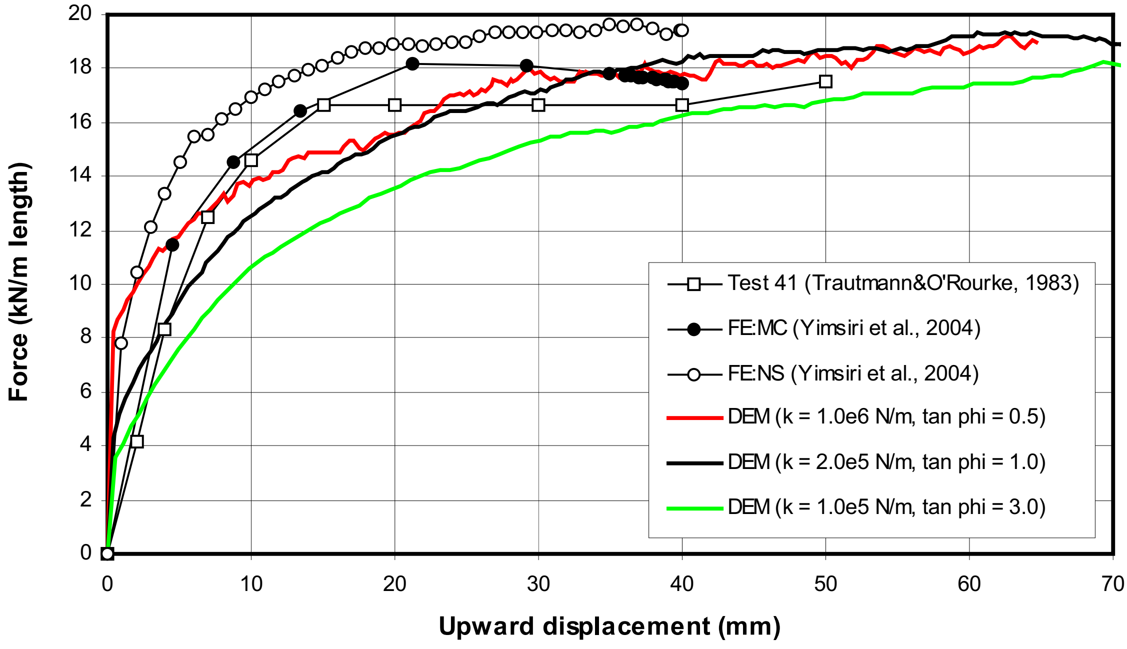

Figure B-4 *H$_c$/D* = 13: Medium sand

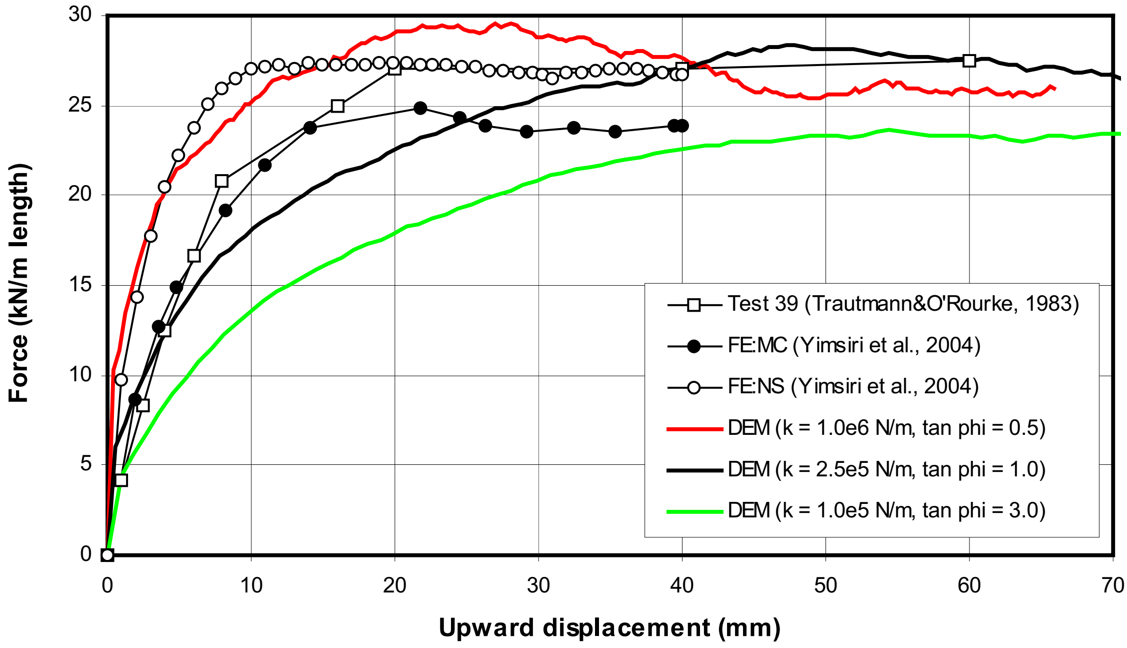

Figure B-5 *H$_c$/D* = 13: Dense sand

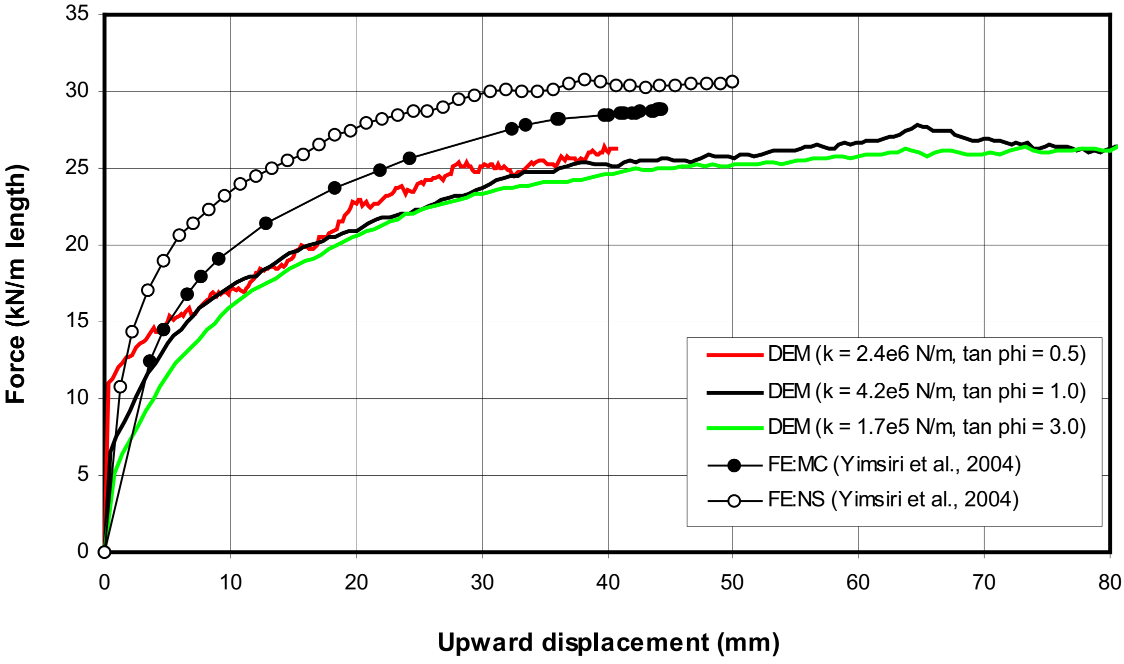

Figure B-6 H_c/D = 17, Medium sand

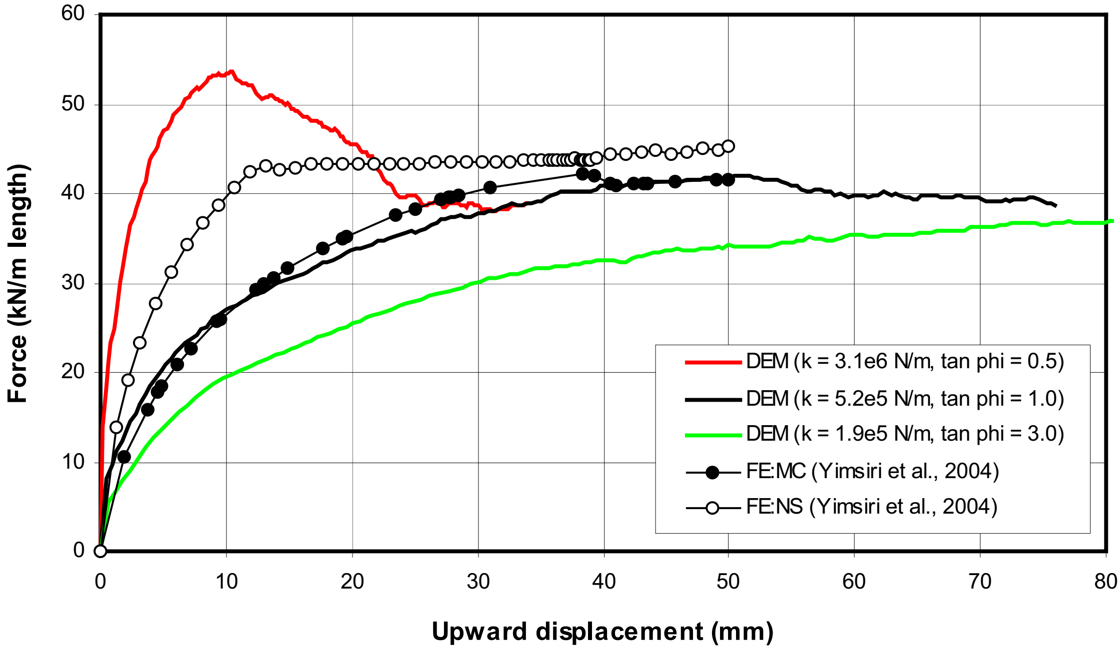

Figure B-7 H_c/D = 17, Dense sand

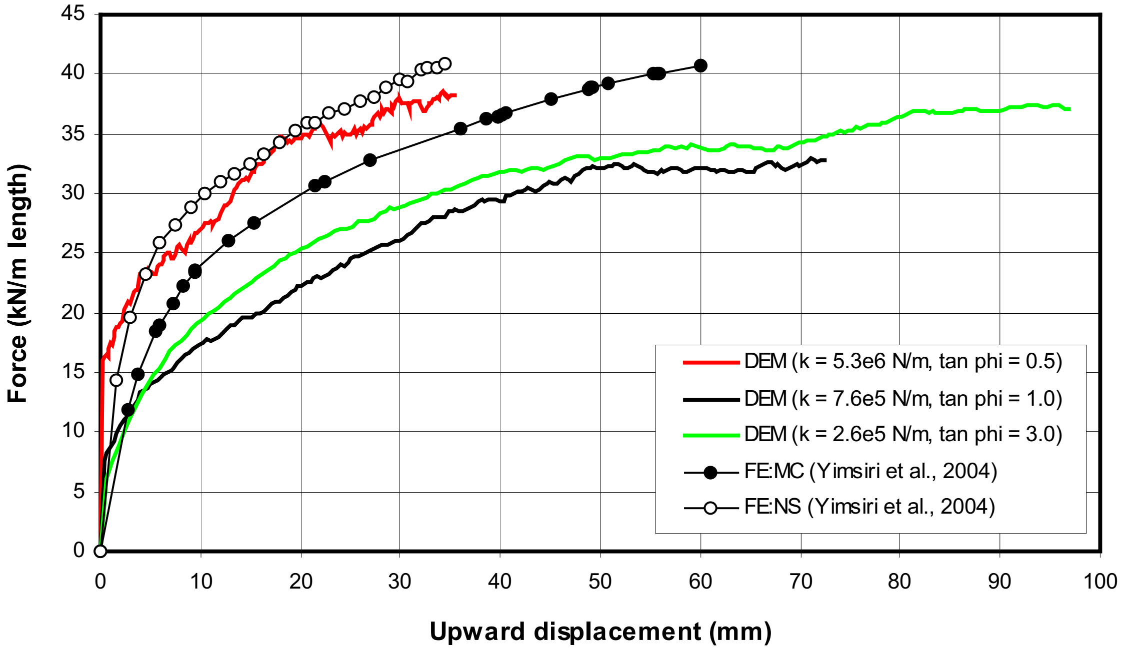

Figure B-8 $H_c/D = 21$, Medium sand

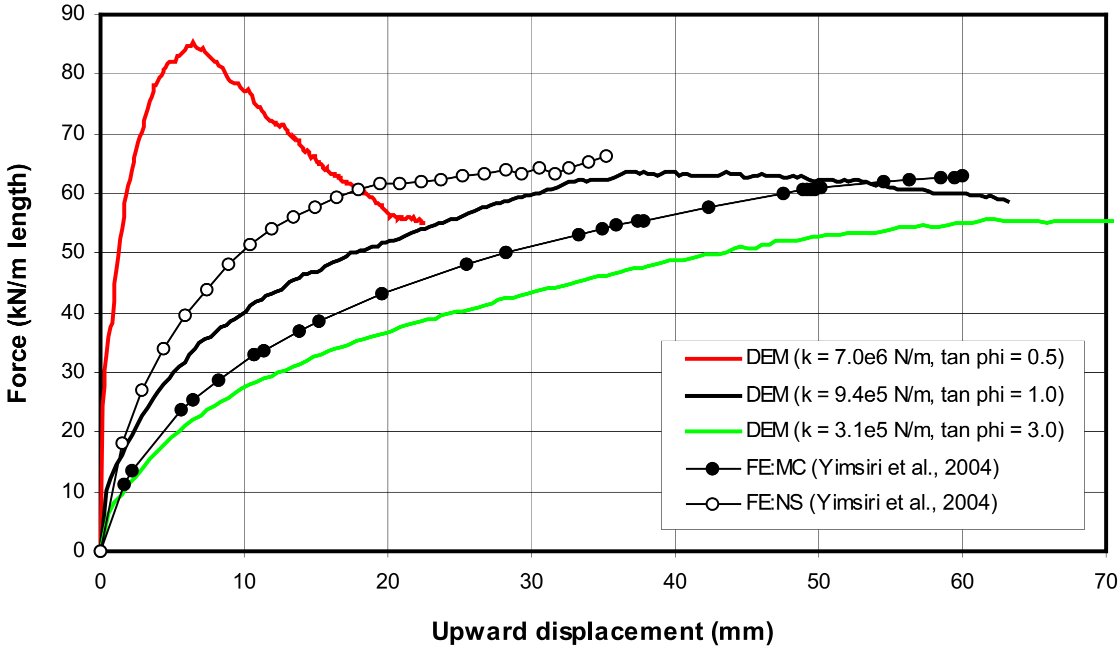

Figure B-9 $H_c/D = 21$, Dense sand

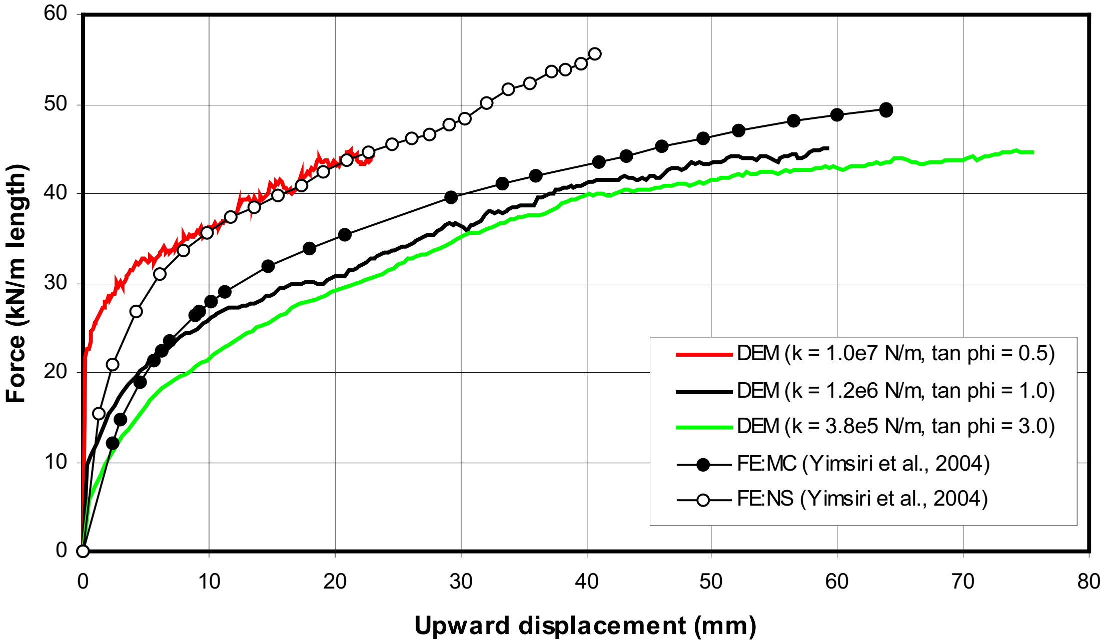

Figure B-10 $H_c/D = 25$, Medium sand

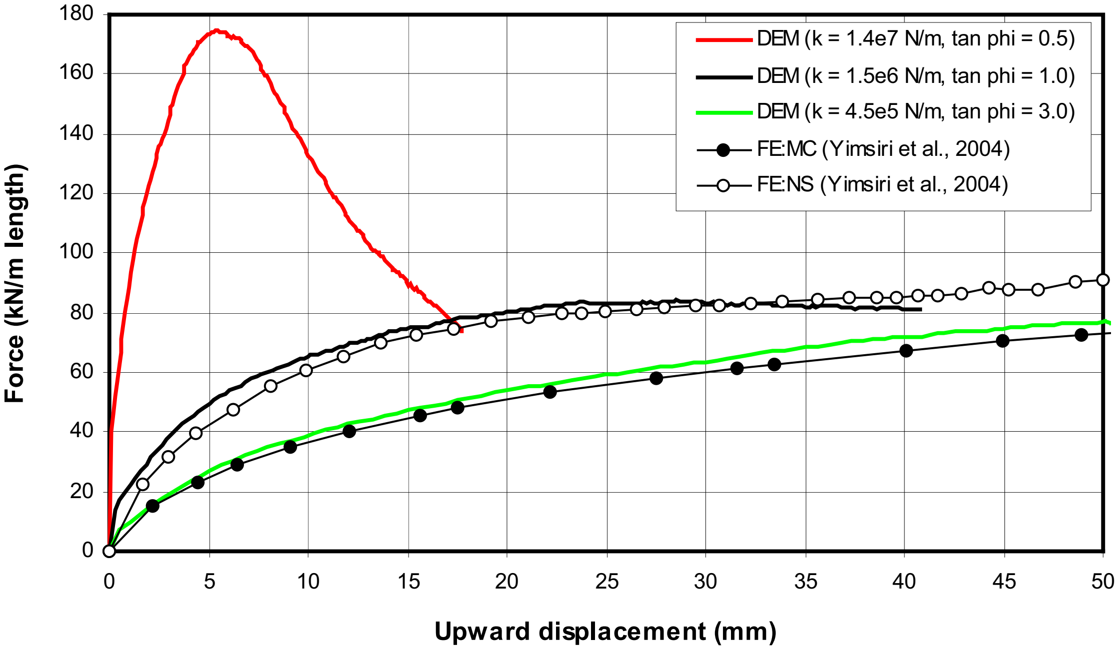

Figure B-11 $H_c/D = 25$, Dense sand

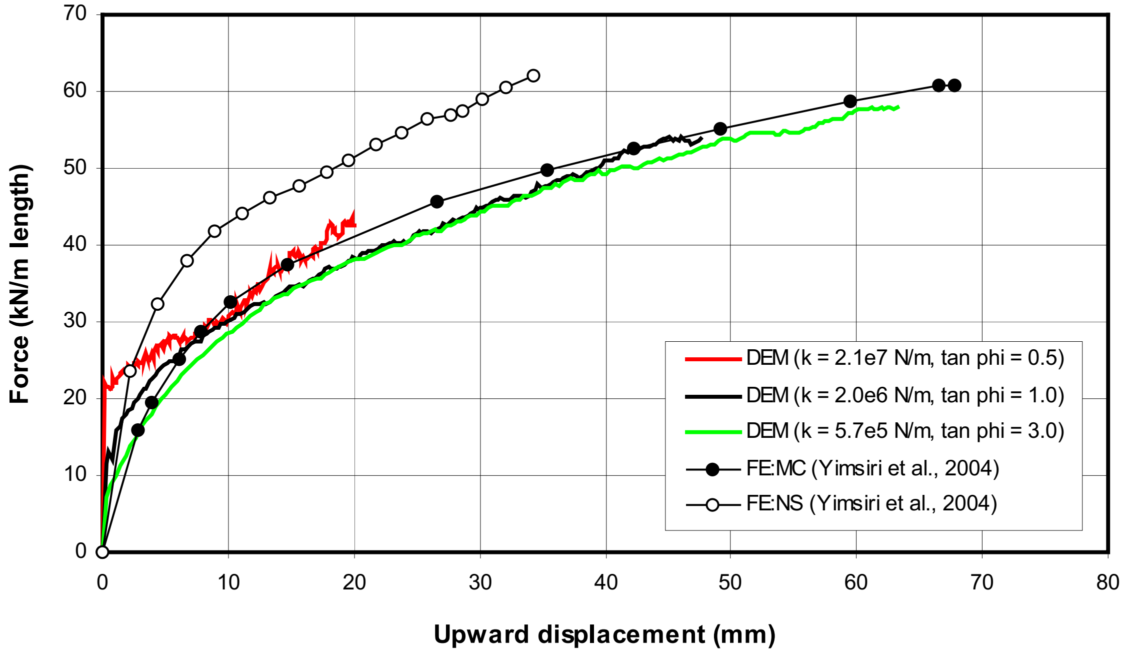

Figure B-12 $H_c/D = 30$, Medium sand

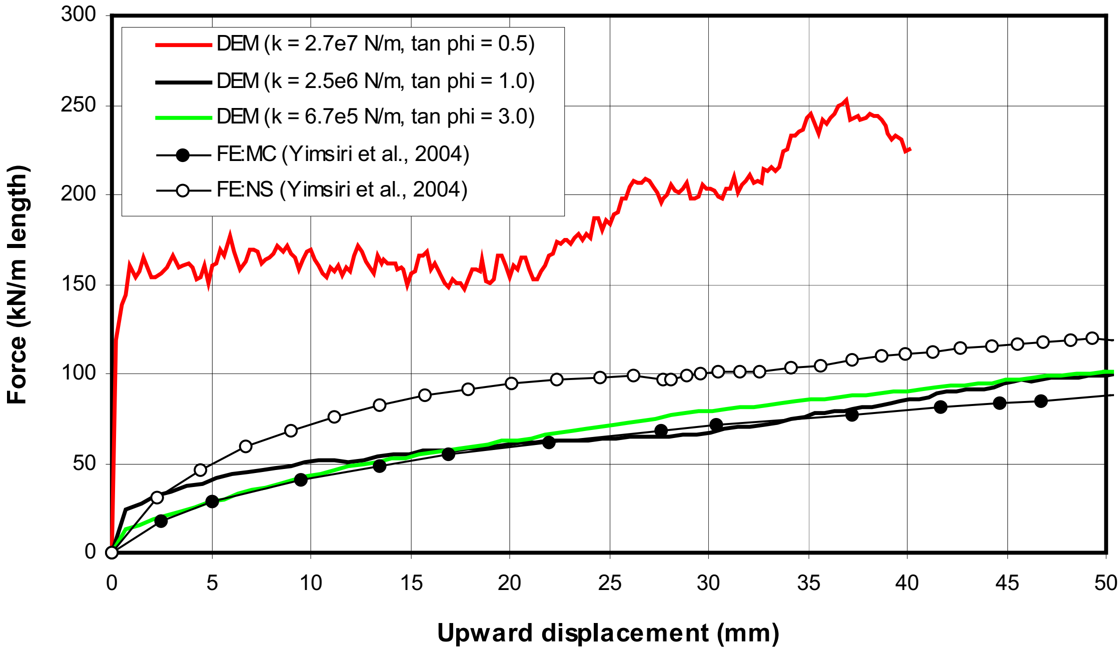

Figure B-13 $H_c/D = 30$, Dense sand

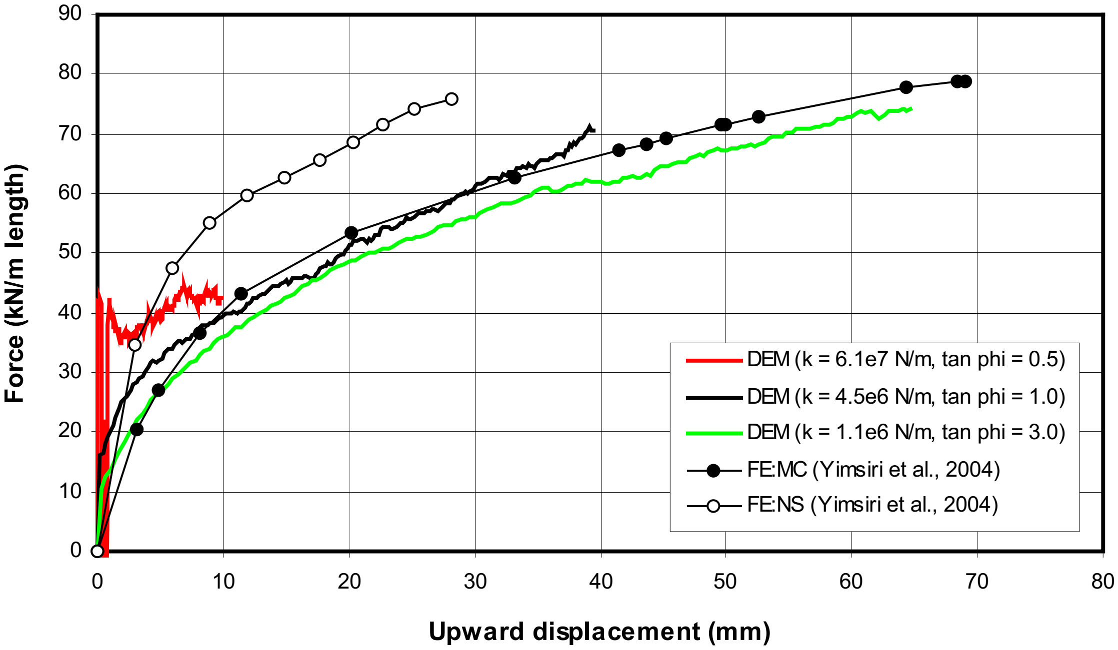

Figure B-14 H_c/D = 40, Medium sand

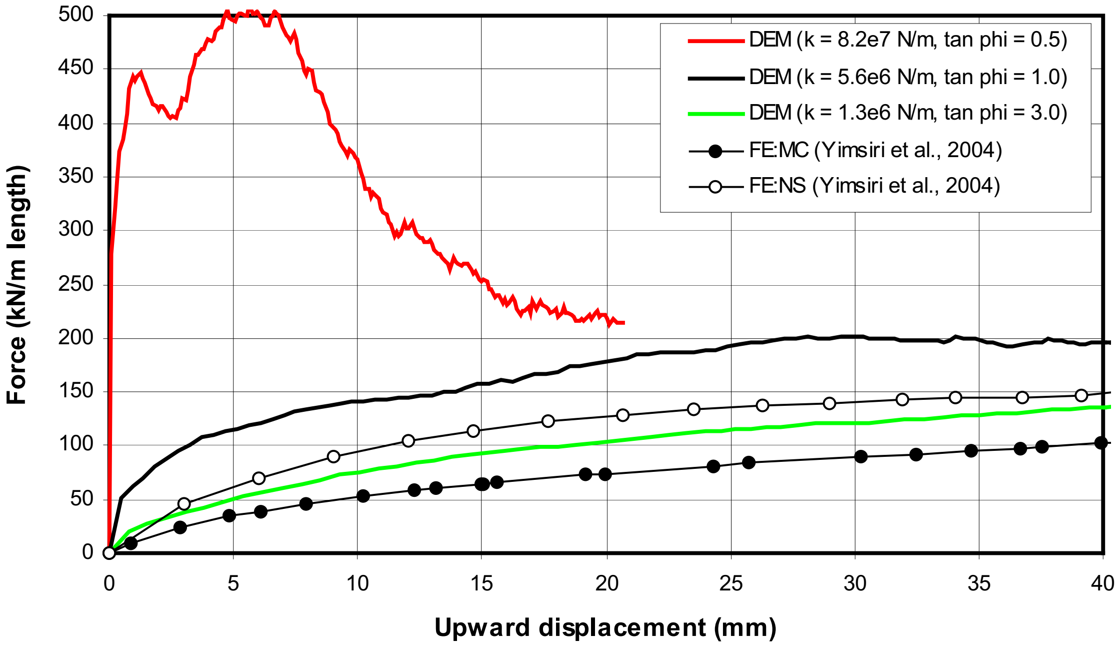

Figure B-15 H_c/D = 40, Dense sand

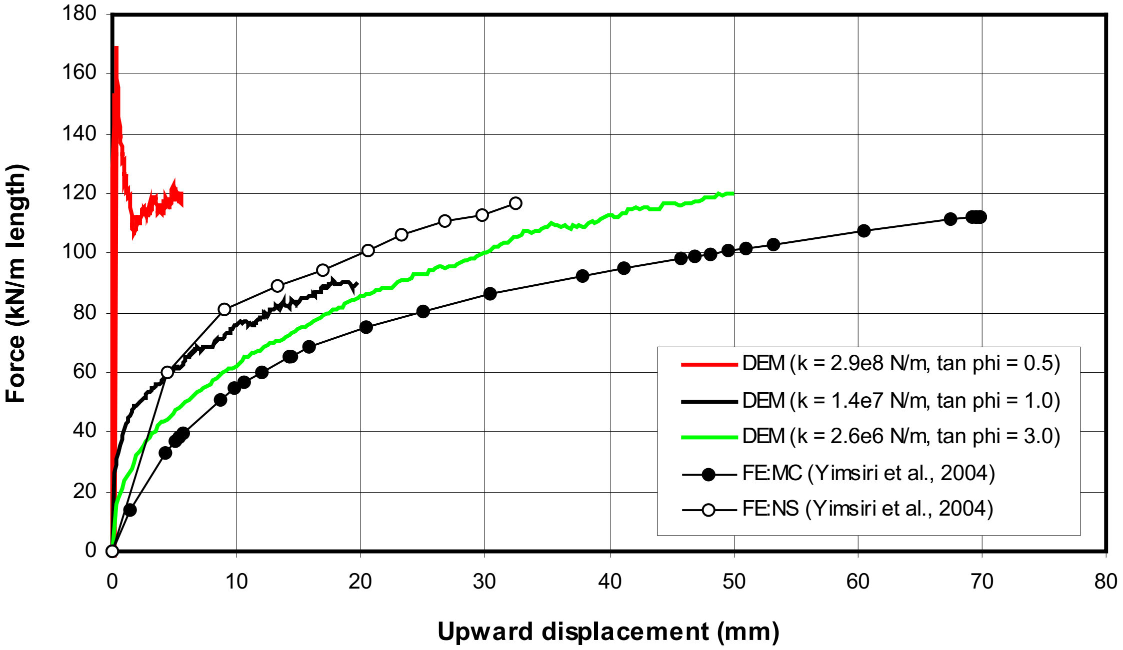

Figure B-16 *H*$_c$/*D* = 60, Medium sand

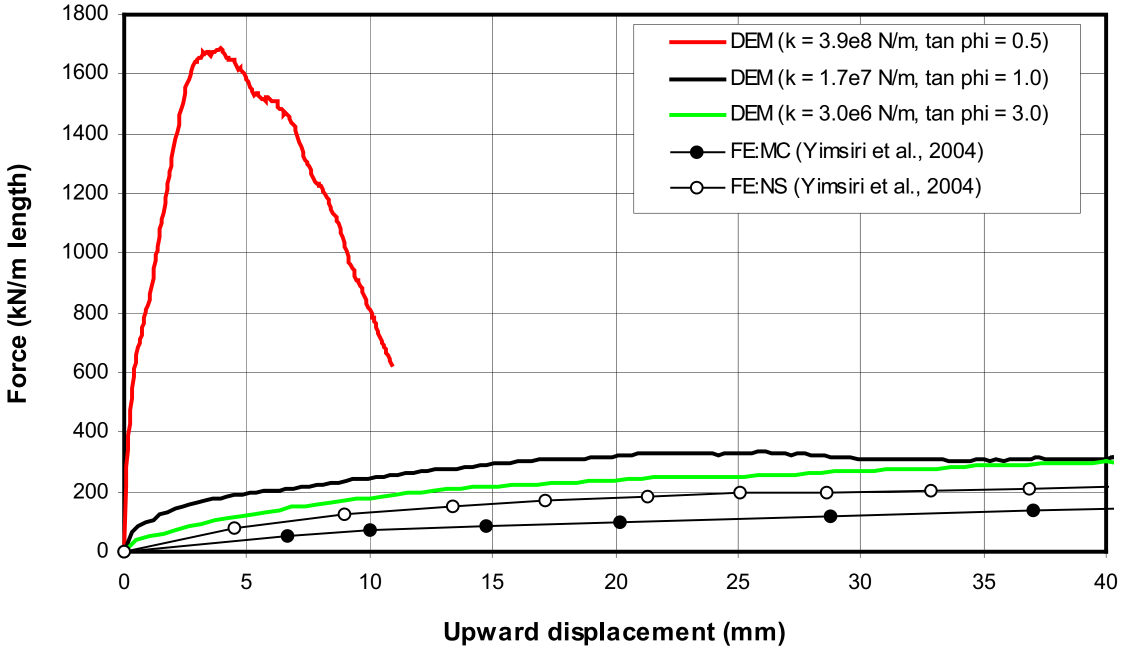

Figure B-17 *H*$_c$/*D* = 60, Dense sand

Appendix C

Displacement Pattern under Lateral Loading
(Velocity Vector)

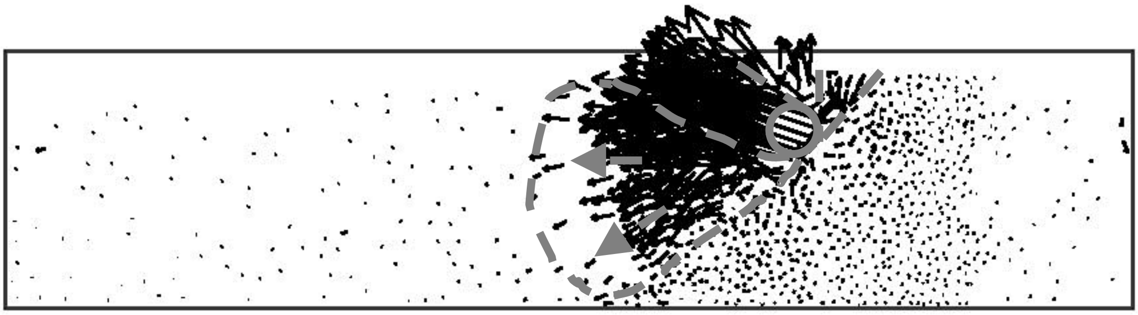

(a) Full-sized scale

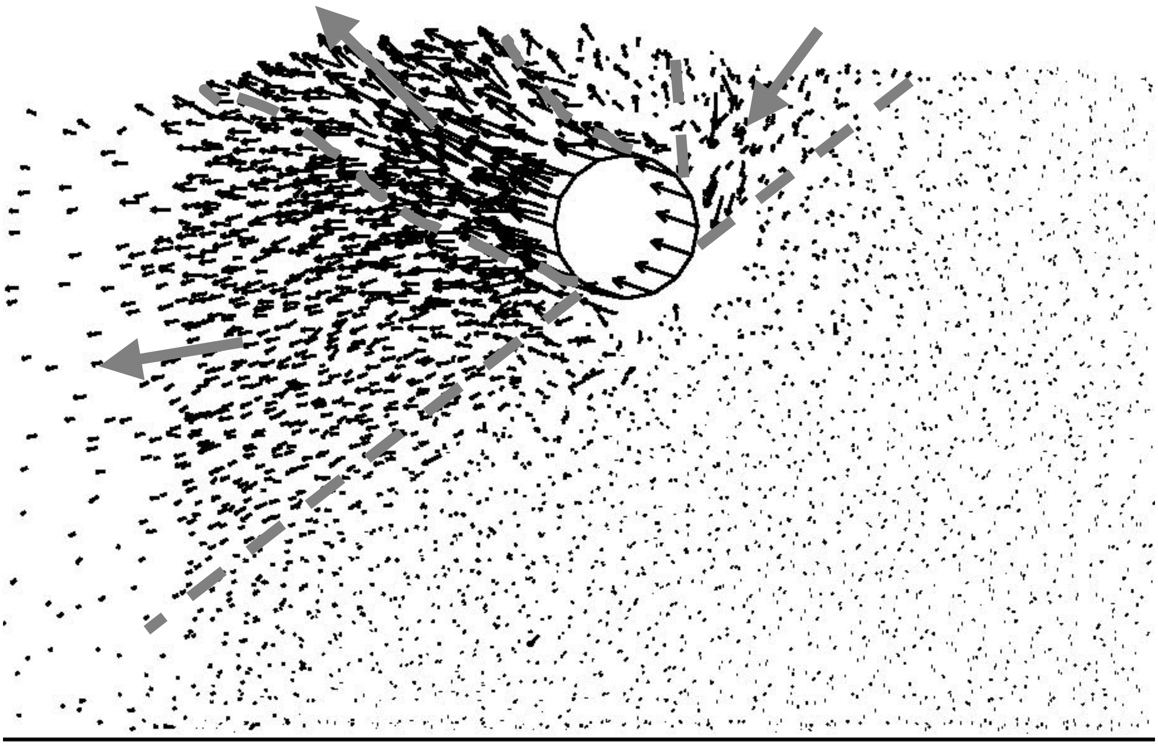

(b) Enlarged scale

Figure C-1 $H/D = 2$, Medium sand, $\tan \phi_{\mu} = 3.0$

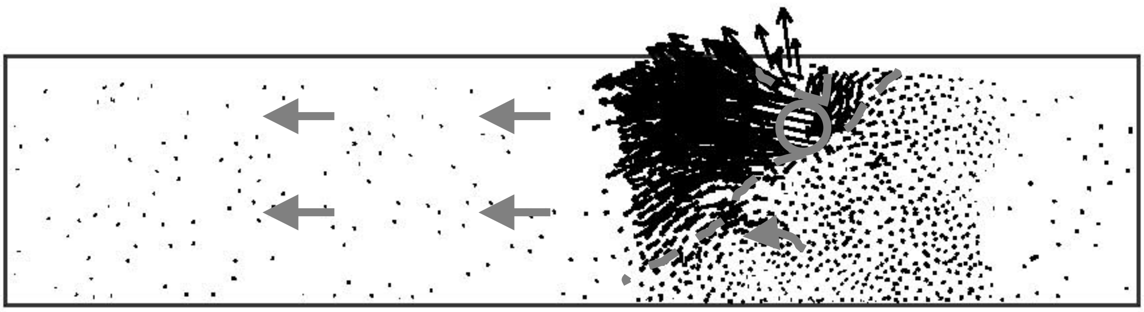

(a) Full-sized scale

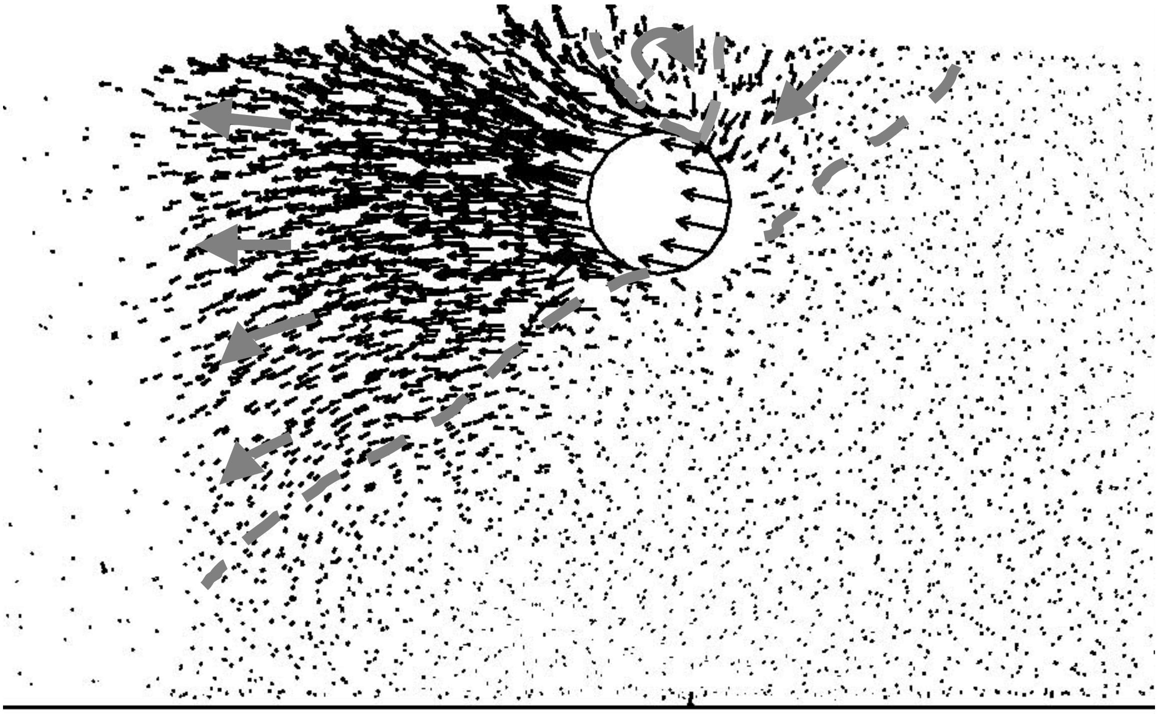

(b) Enlarged scale

Figure C-2 $H/D = 2$, Dense sand, $\tan \phi_\mu = 3.0$

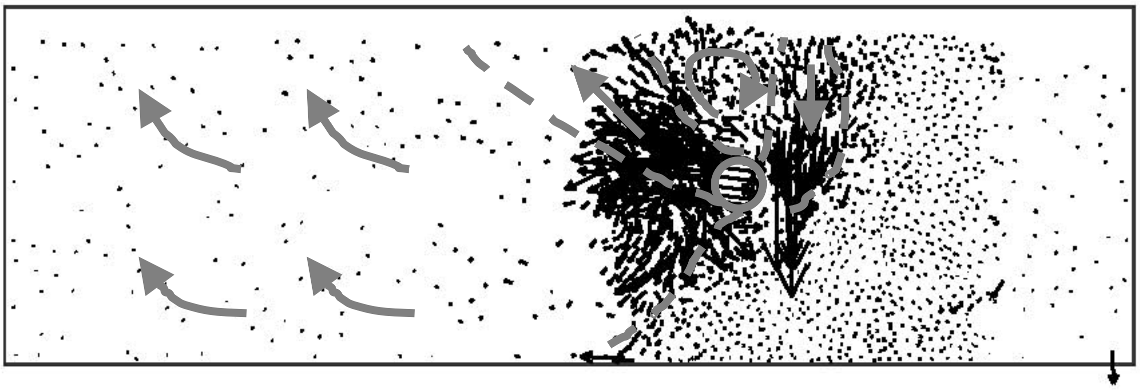

(a) Full-sized scale

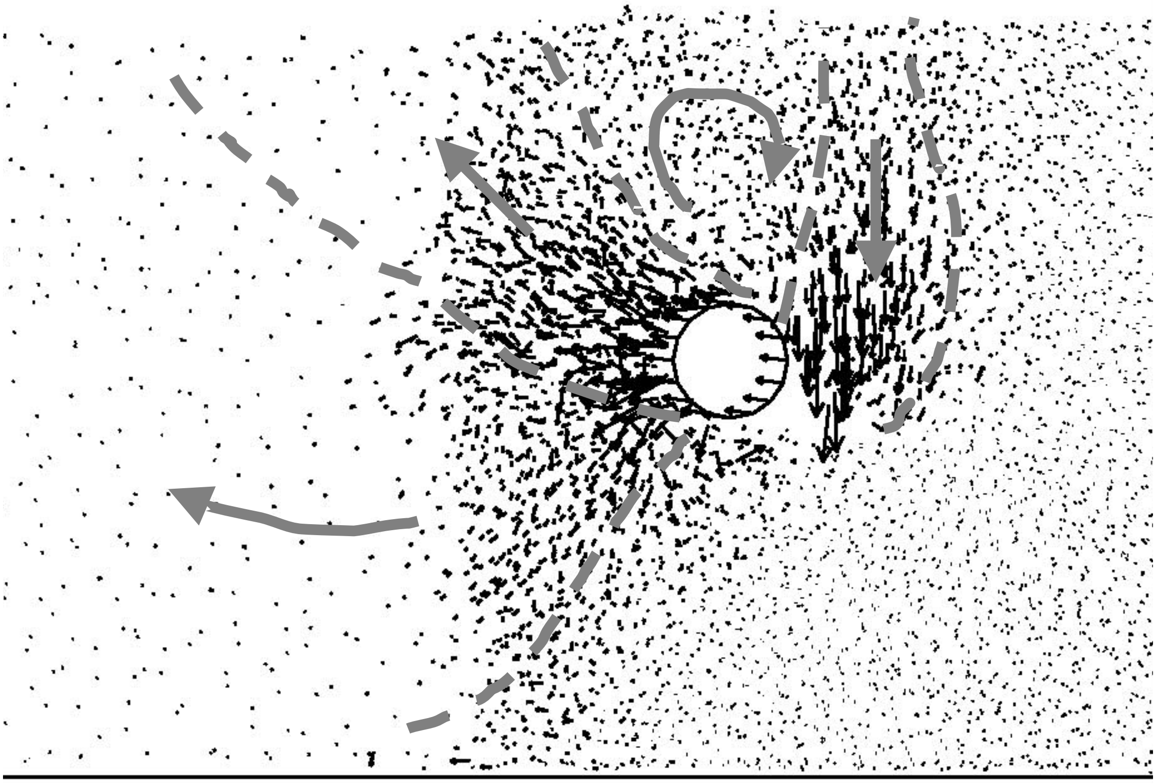

(b) Enlarged scale

Figure C-3 $H/D = 4$, Medium sand, tan $\phi_\mu = 3.0$

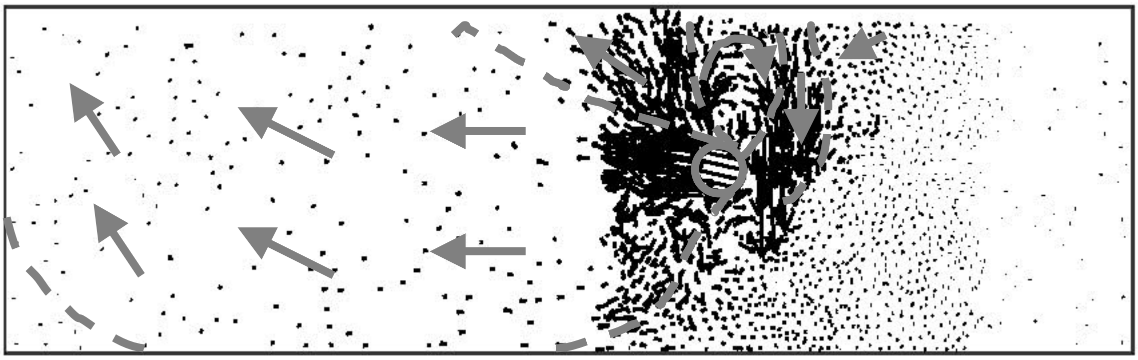

(a) Full-sized scale

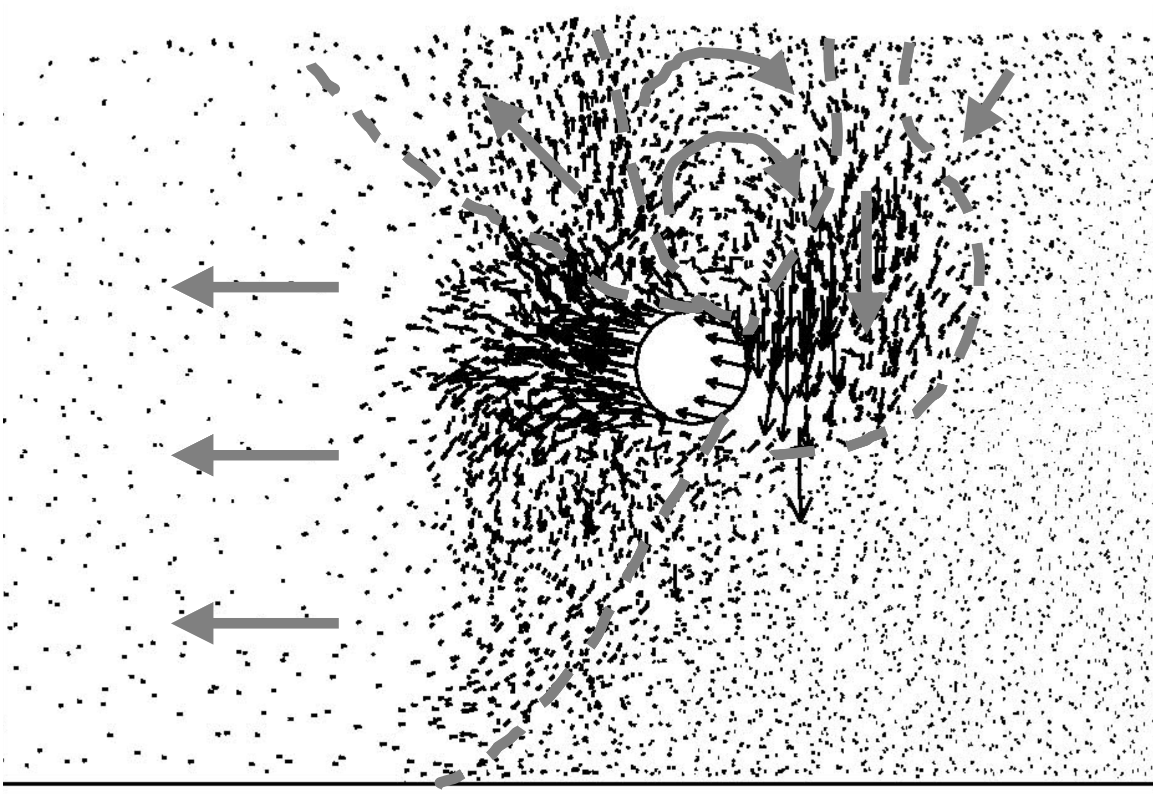

(b) Enlarged scale

Figure C-4 $H/D = 4$, Dense sand, tan $\phi_\mu = 3.0$

(a) Full-sized scale

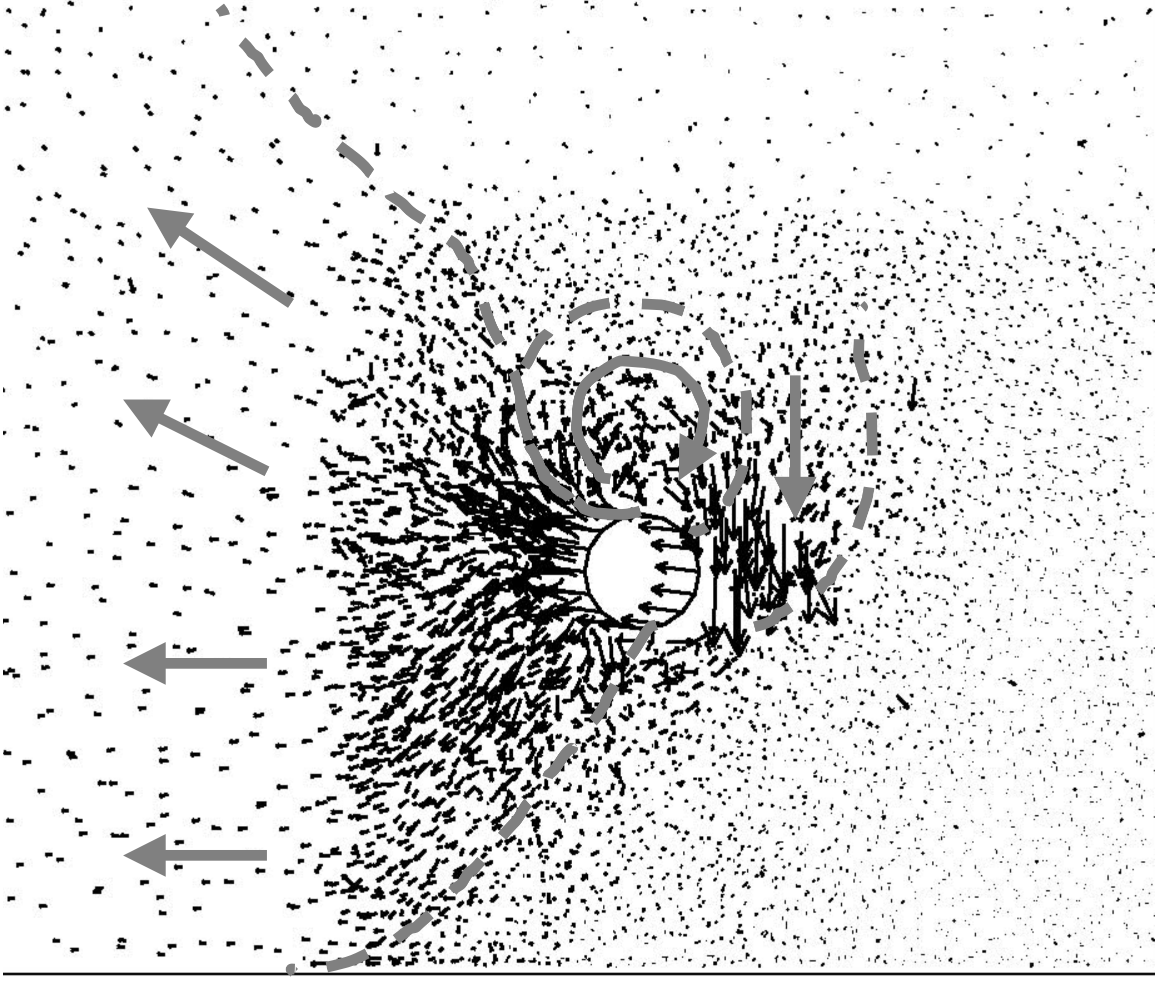

(b) Enlarged scale

Figure C-5 $H/D = 6$, Medium sand, $\tan \phi_\mu = 3.0$

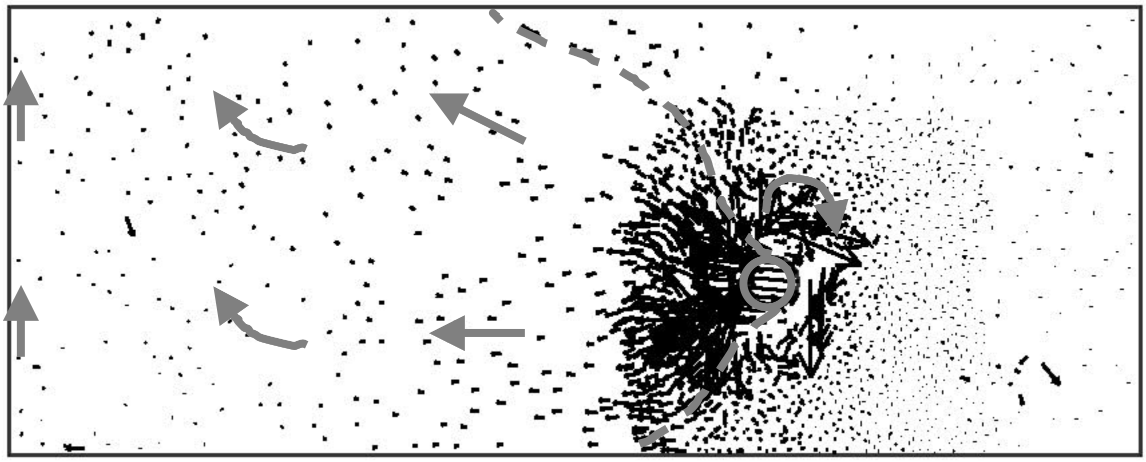

(a) Full-sized scale

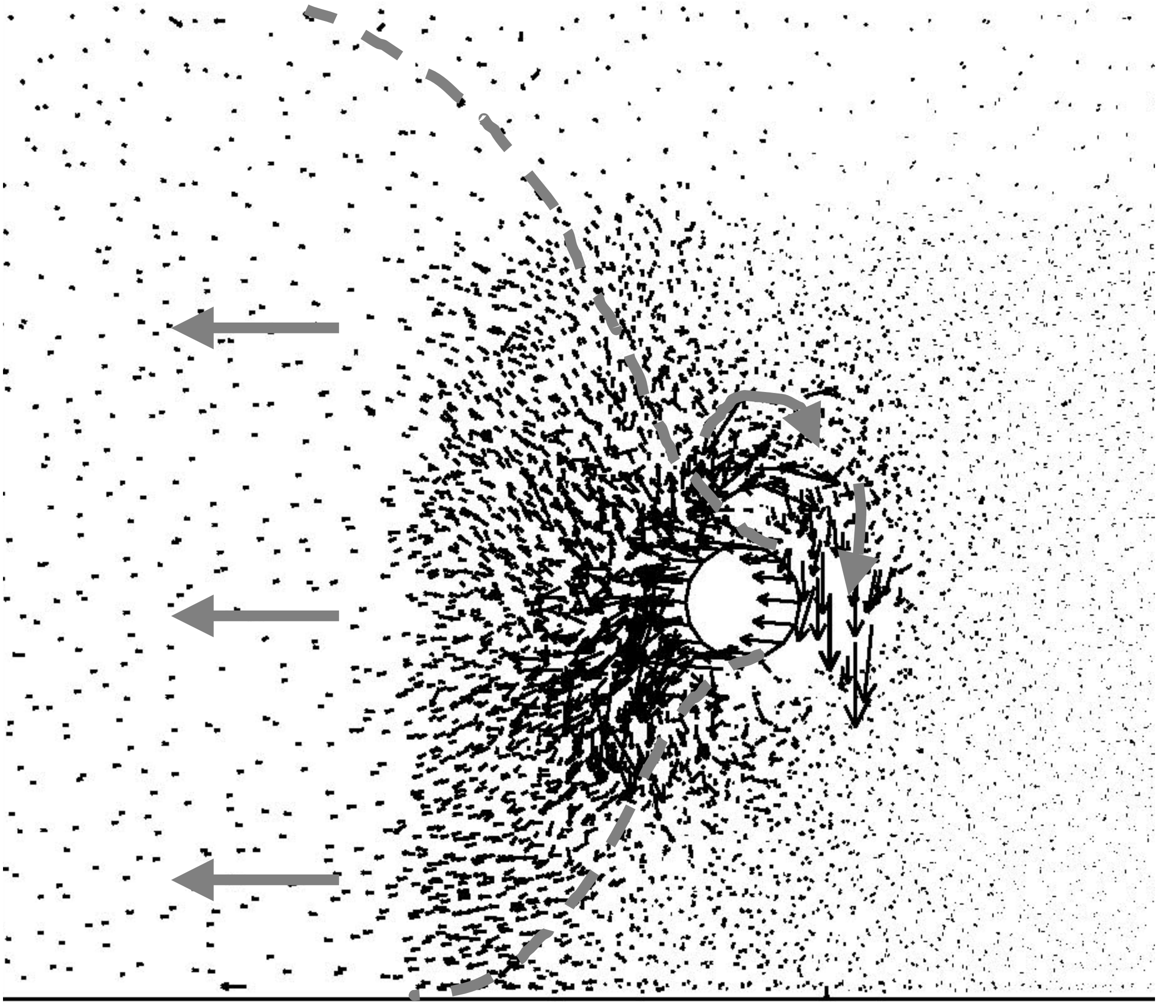

(b) Enlarged scale

Figure C-6 $H/D = 6$, Dense sand, $\tan \phi_{\mu} = 3.0$

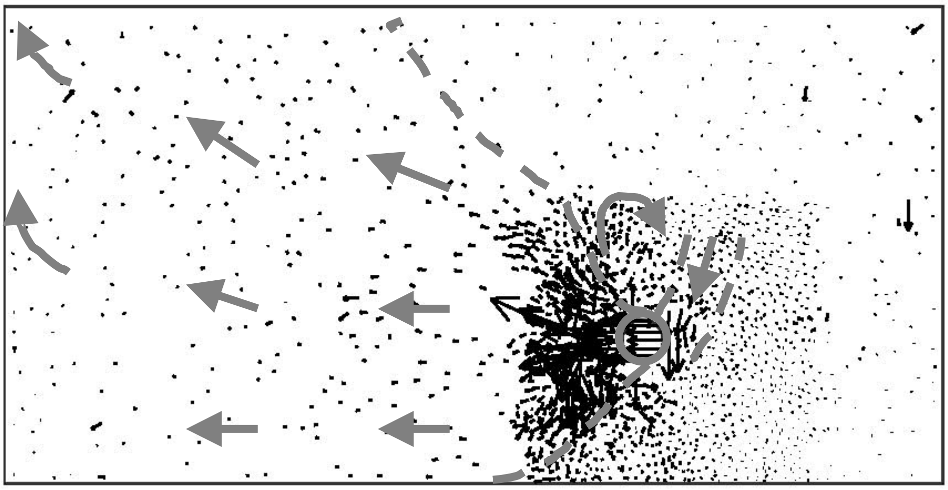

(a) Full-sized scale

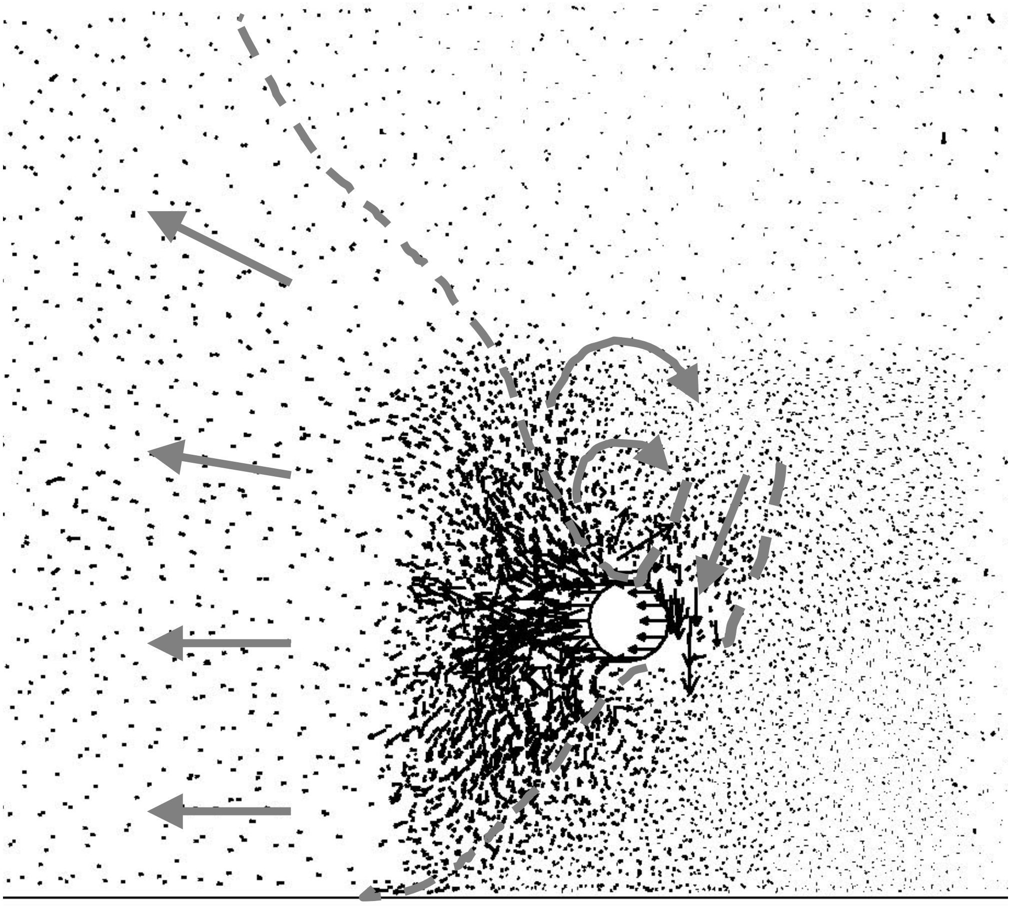

(b) Enlarged scale

Figure C-7 $H/D = 8.5$, Medium sand, $\tan\phi_\mu = 3.0$

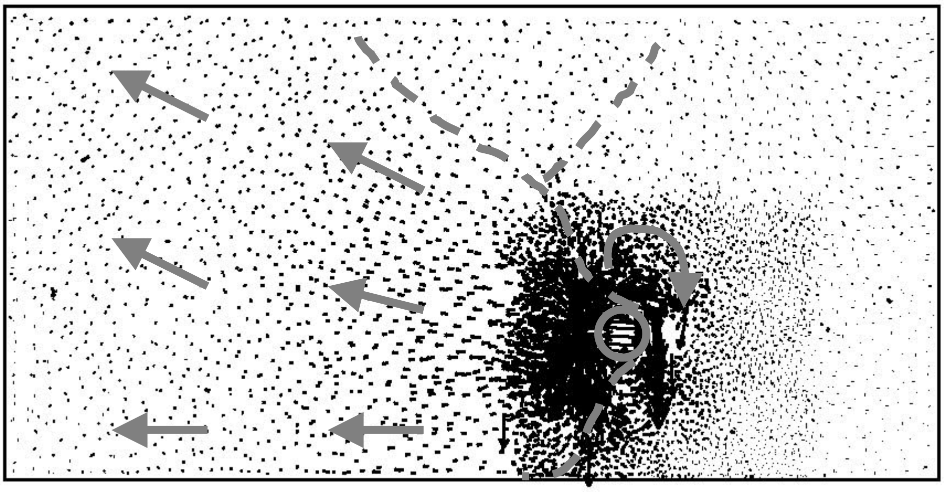

(a) Full-sized scale

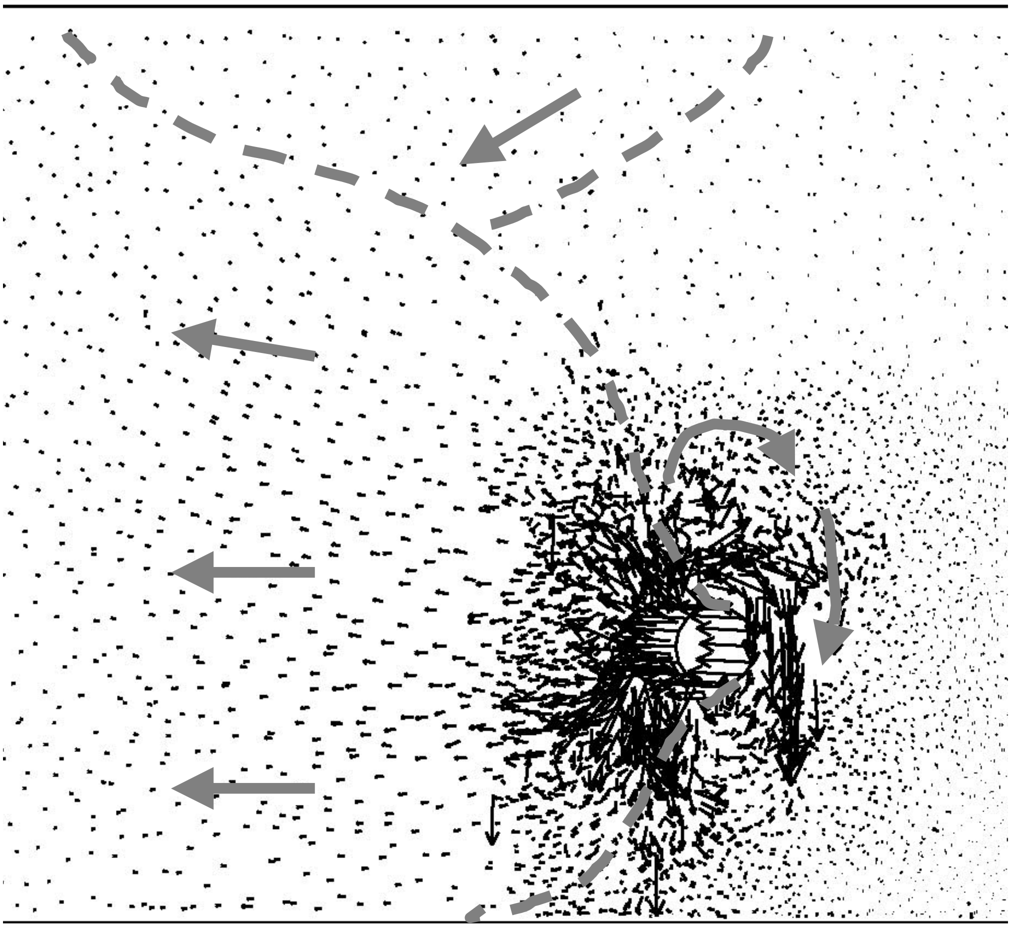

(b) Enlarged scale

Figure C-8 $H/D = 8.5$, Dense sand, $\tan\phi_\mu = 3.0$

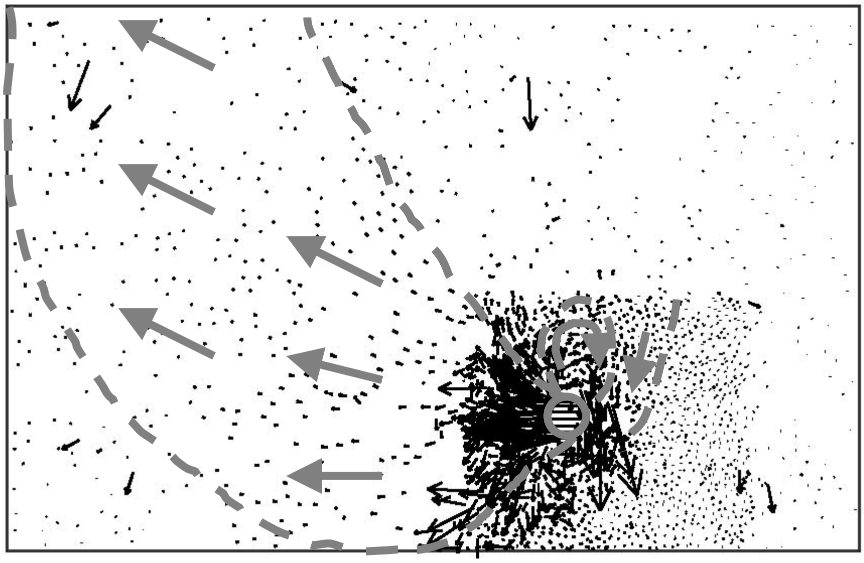

(a) Full-sized scale

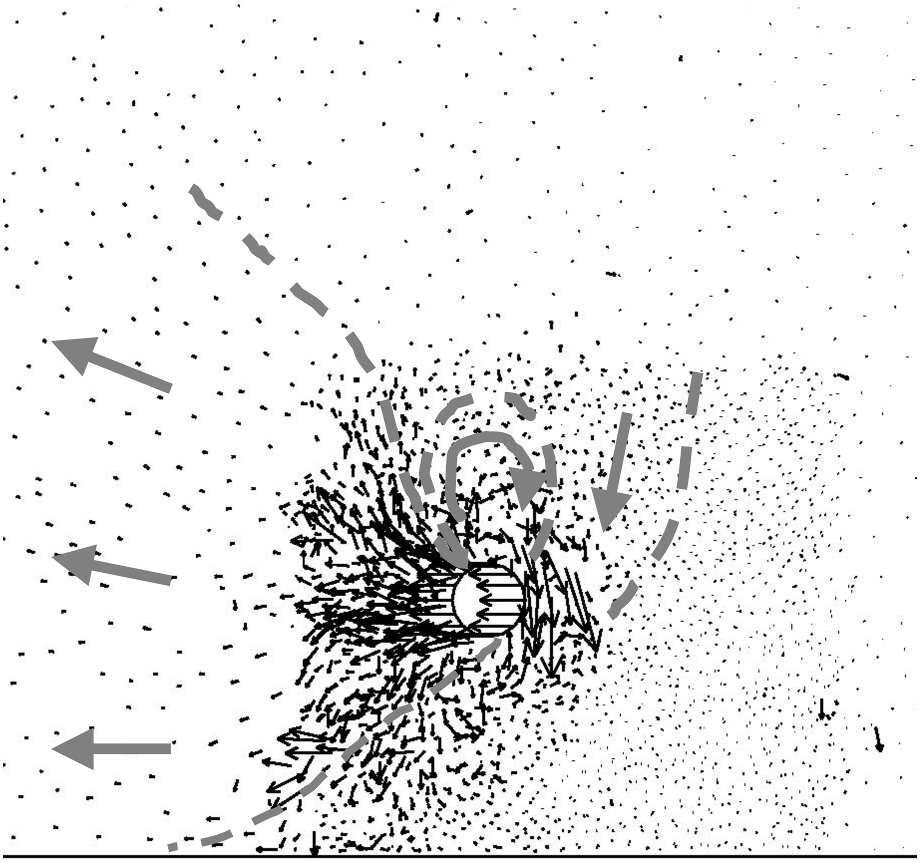

(b) Enlarged scale

Figure C-9 H/D = 11.5, Medium sand, tan ϕ_μ = 3.0

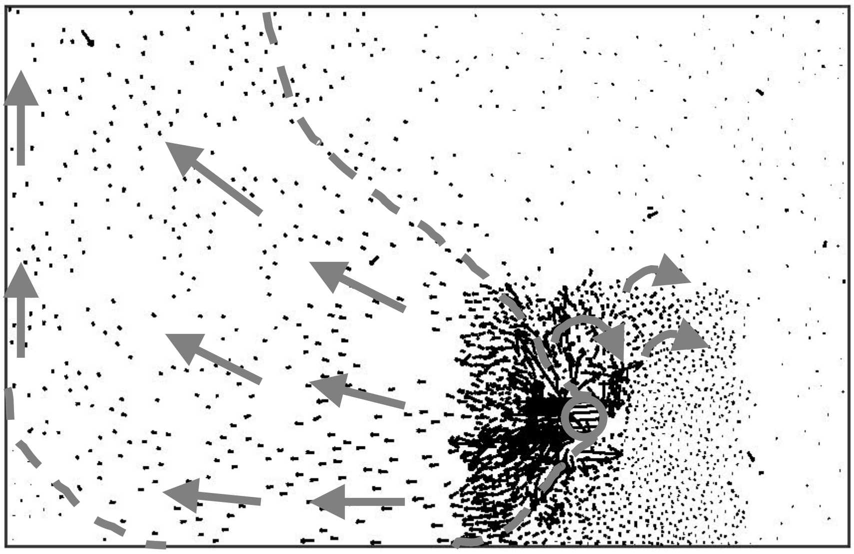

(a) Full-sized scale

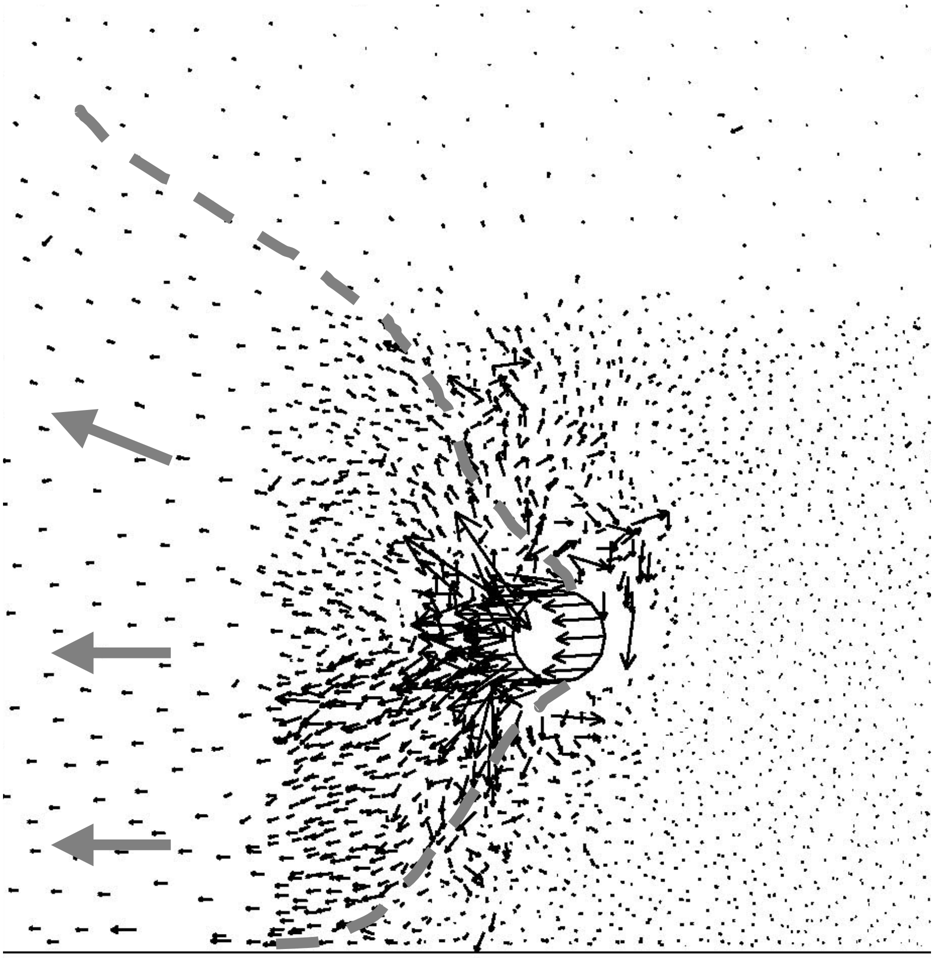

(b) Enlarged scale

Figure C-10 H/D = 11.5, Dense sand, tan ϕ_μ = 3.0

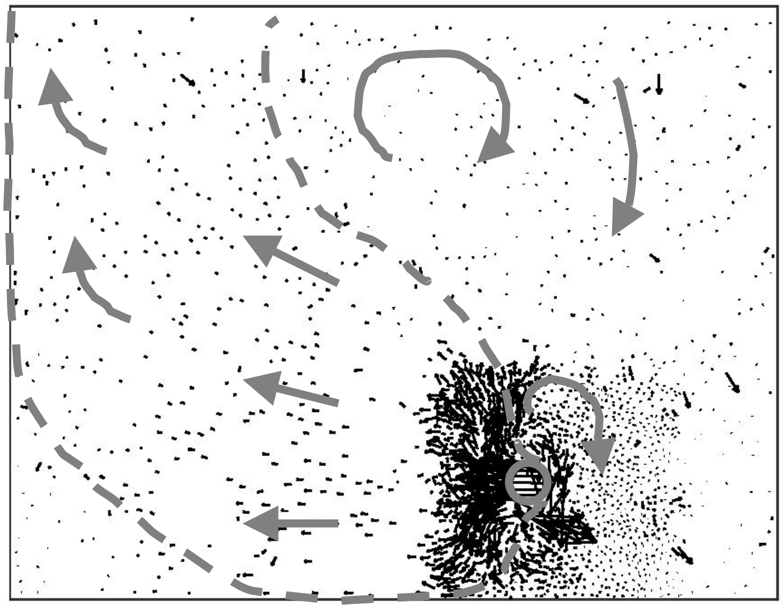

(a) Full-sized scale

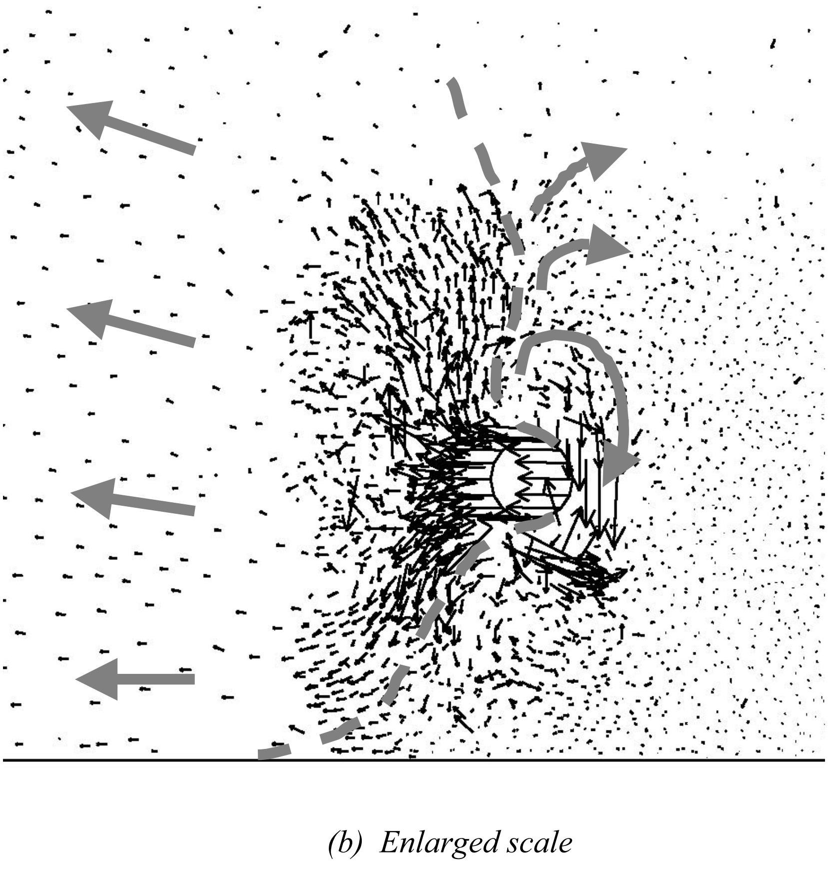

(b) Enlarged scale

Figure C-11 $H/D = 14.5$, Medium sand, $\tan \phi_\mu = 3.0$

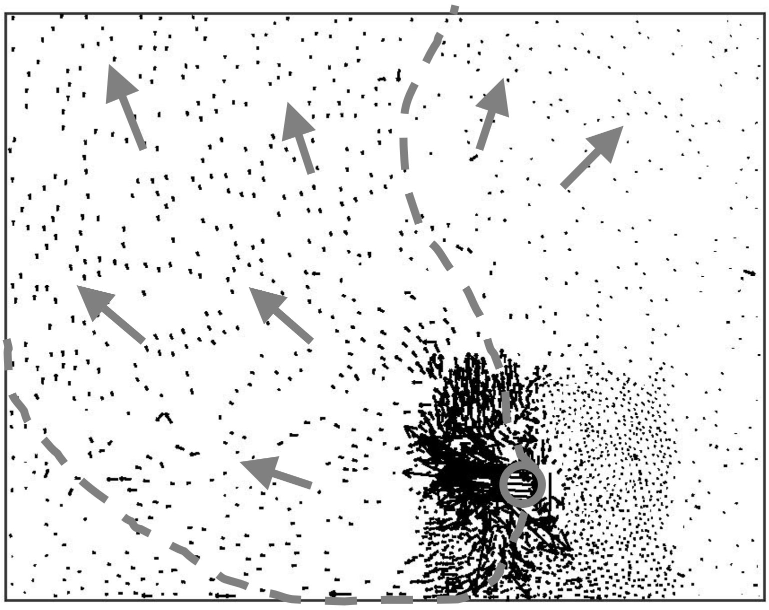

(a) Full-sized scale

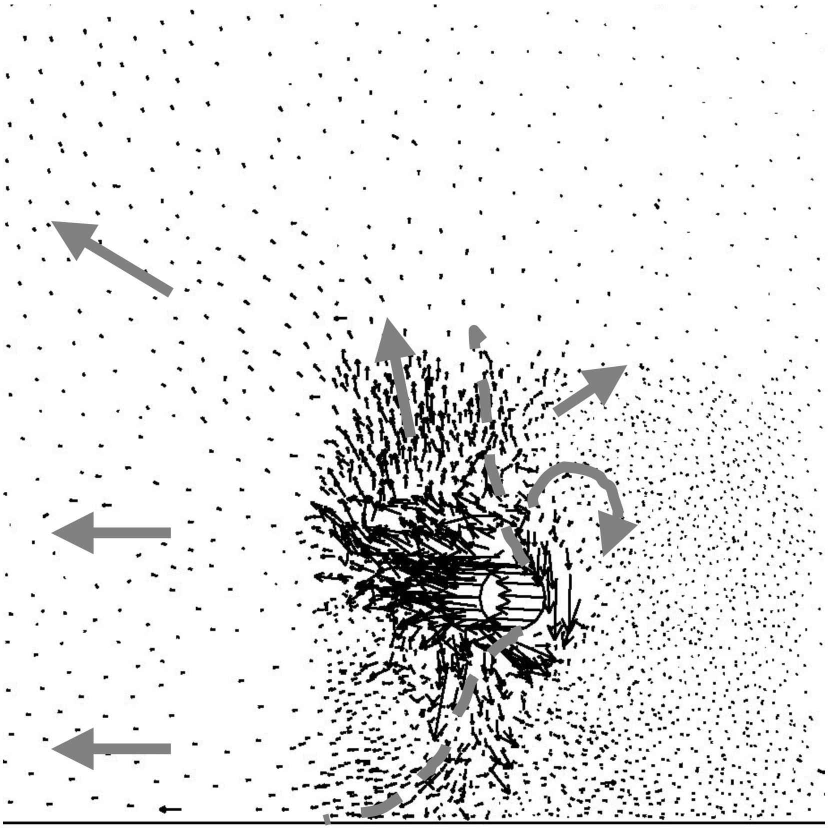

(b) Enlarged scale

Figure C-12   *H/D* = 14.5, Dense sand, tan ϕ_μ = 3.0

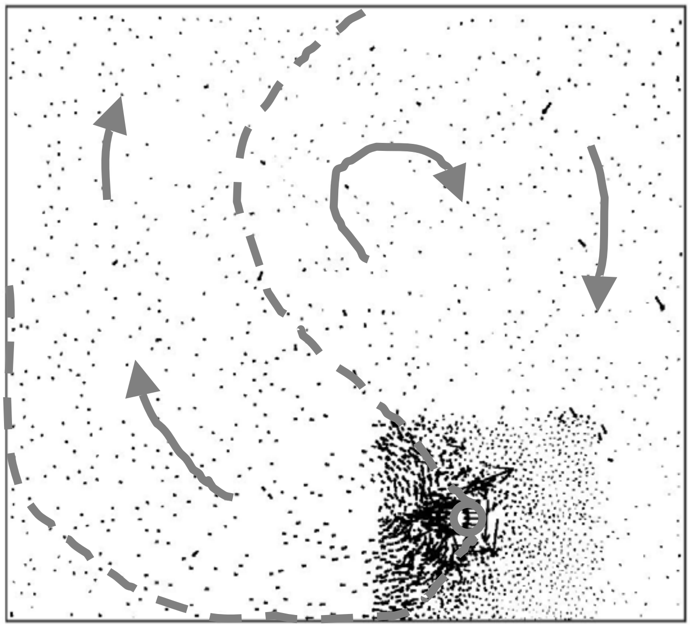

(a) Full-sized scale

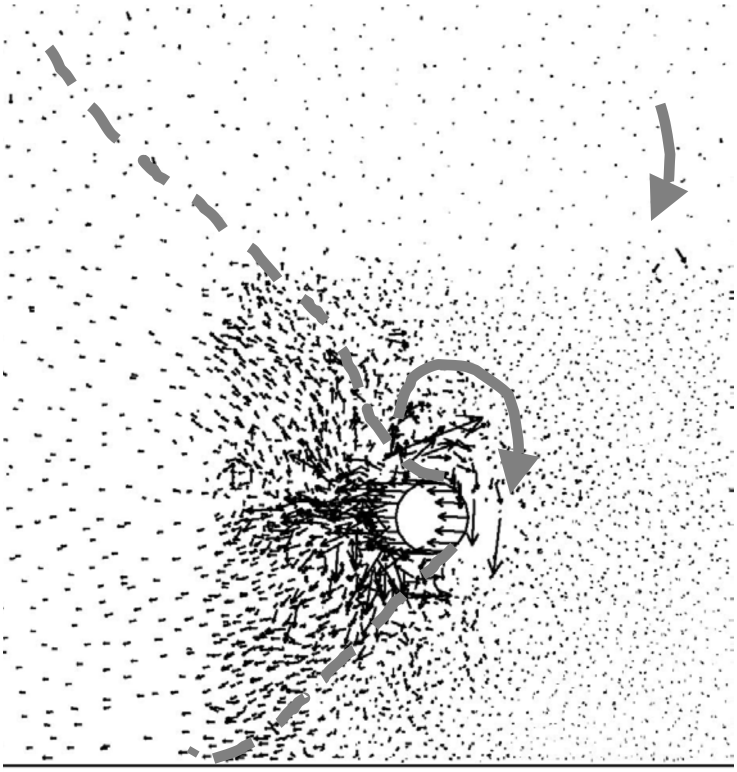

(b) Enlarged scale

Figure C-13 H/D = 17.5, Medium sand, tan ϕ_{μ} = 3.0

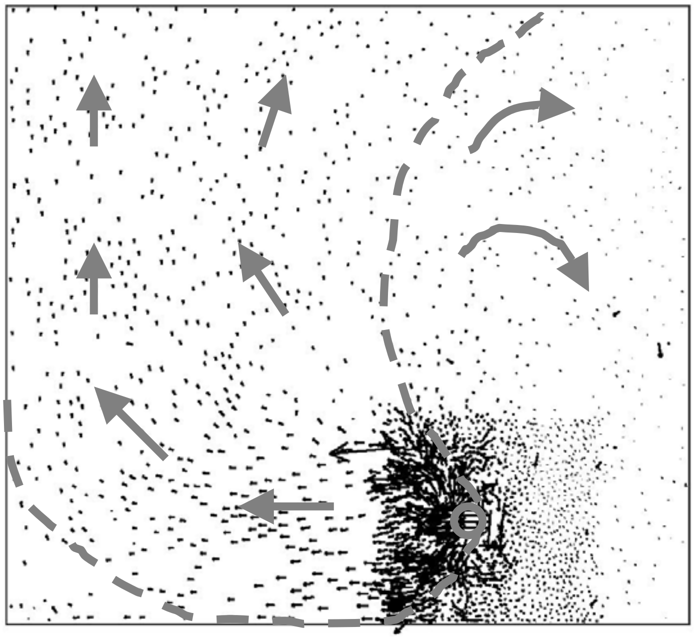

(a) Full-sized scale

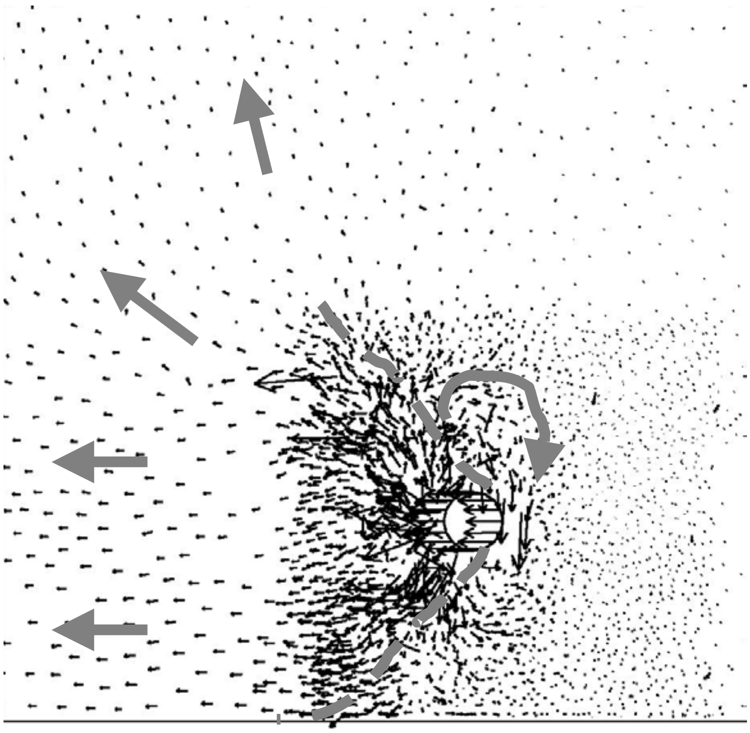

(b) Enlarged scale

Figure C-14 H/D = 17.5, Dense sand, tan ϕ_μ = 3.0

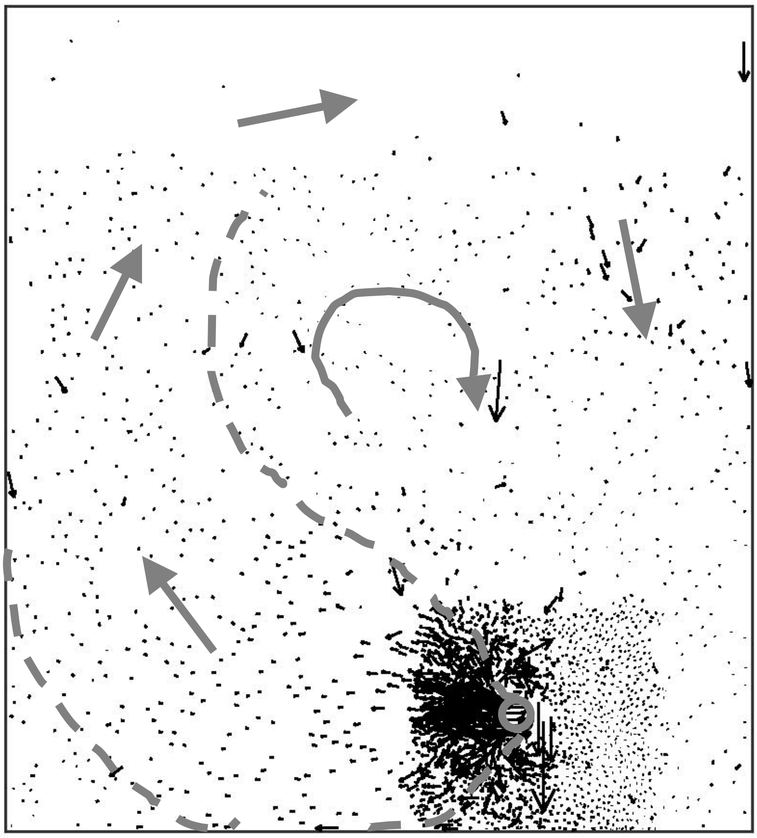

(a) Full-sized scale

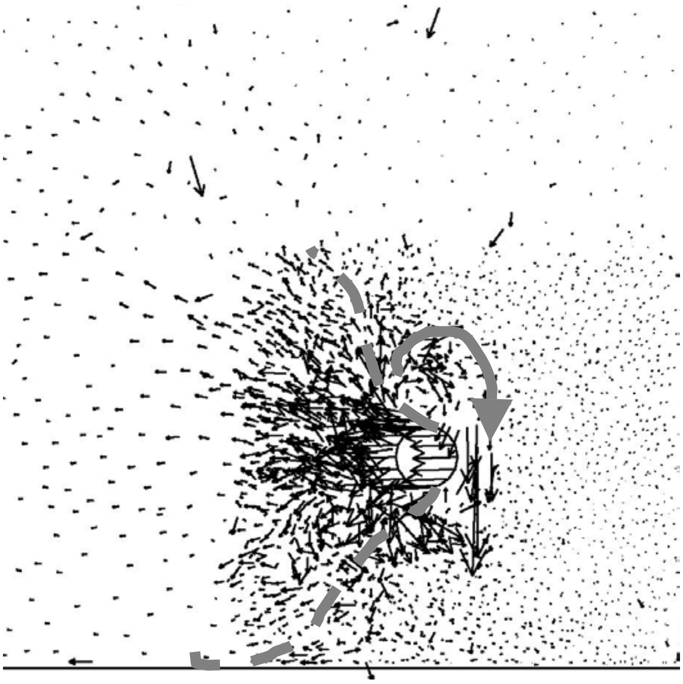

(b) Enlarged scale

Figure C-15 $H/D = 22$, Medium sand, $\tan \phi_\mu = 3.0$

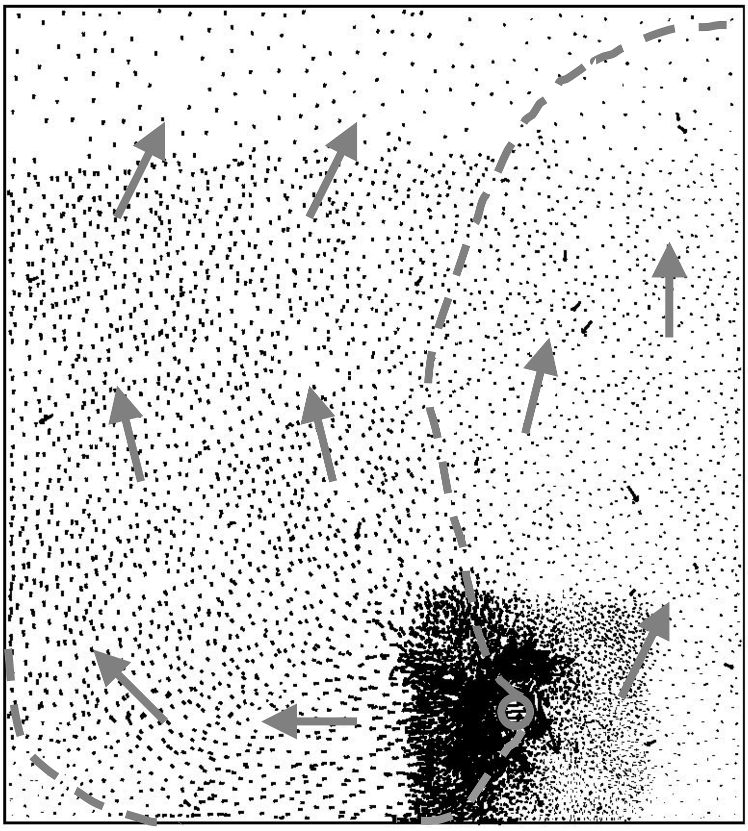

(a) Full-sized scale

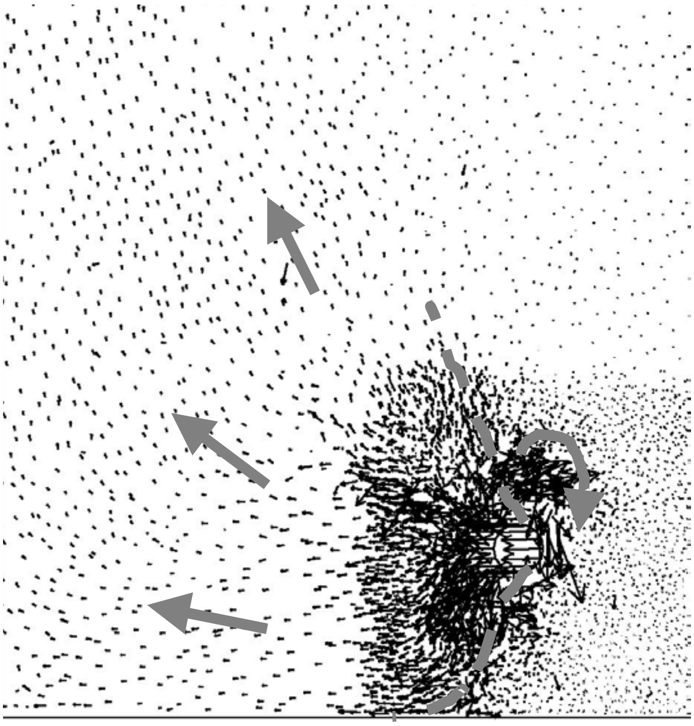

(b) Enlarged scale

Figure C-16 $H/D = 22$, Dense sand, $\tan \phi_\mu = 3.0$

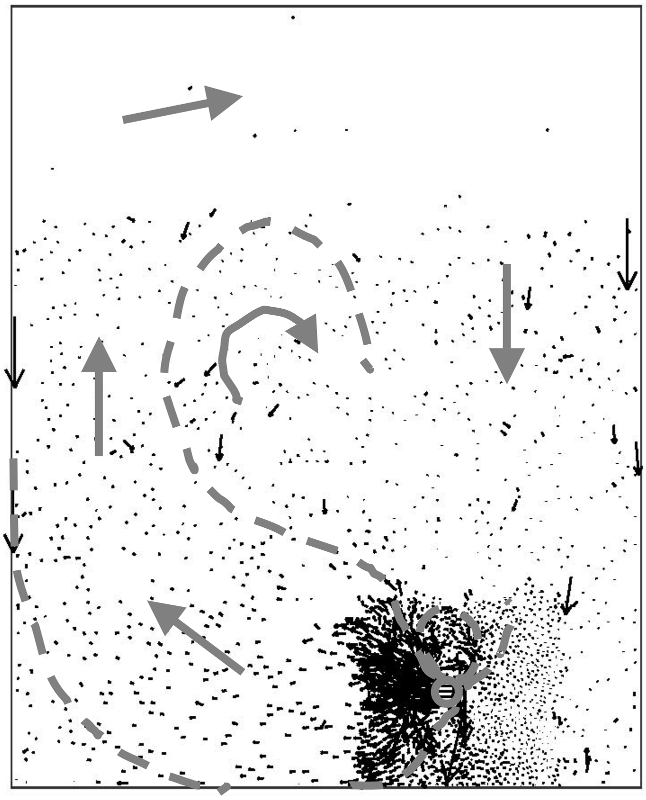

(a) Full-sized scale

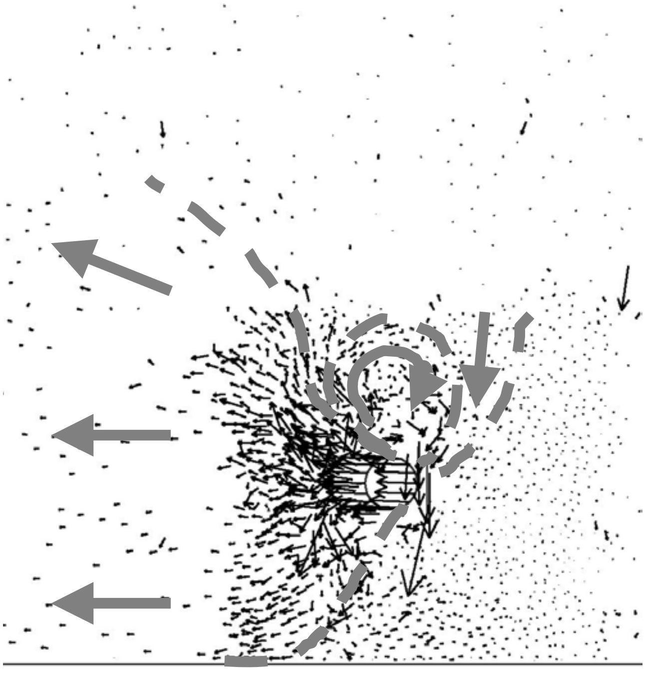

(b) Enlarged scale

Figure C-17 $H/D = 25$, Medium sand, $\tan \phi_\mu = 3.0$

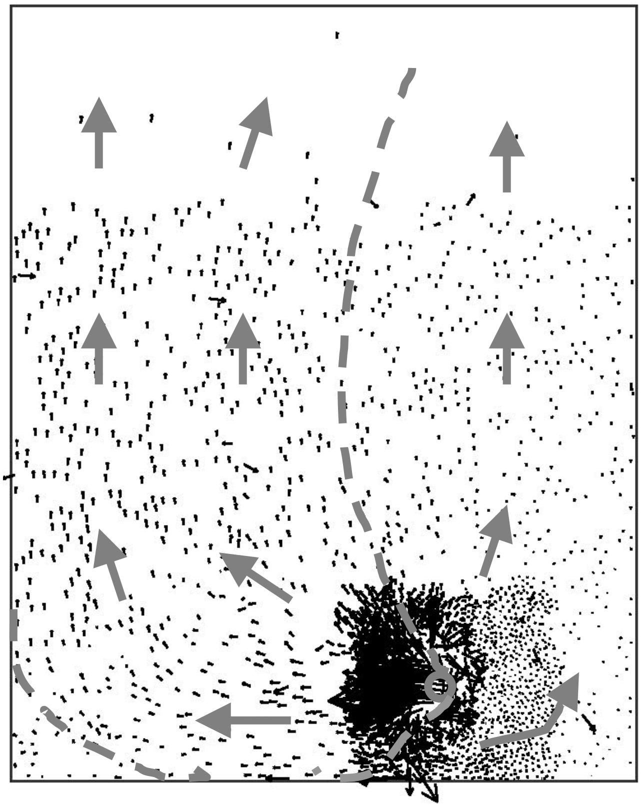

(a) Full-sized scale

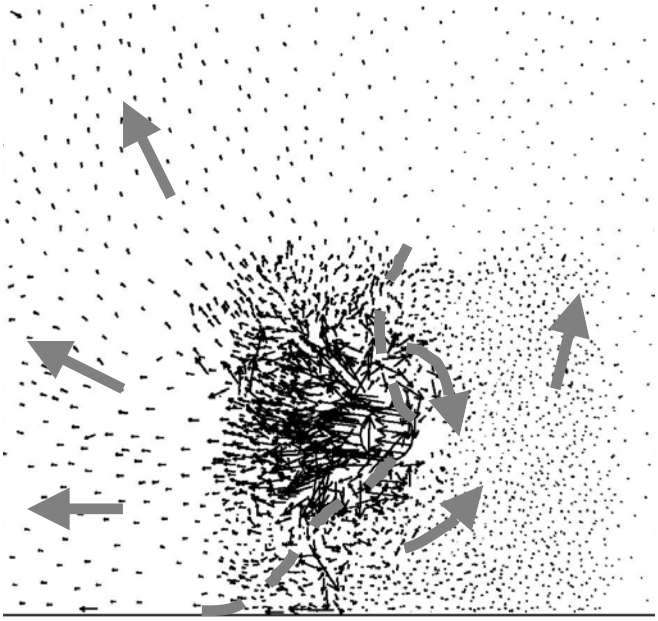

(b) Enlarged scale

Figure C-18 $H/D = 25$, Dense sand, tan $\phi_{\mu} = 3.0$

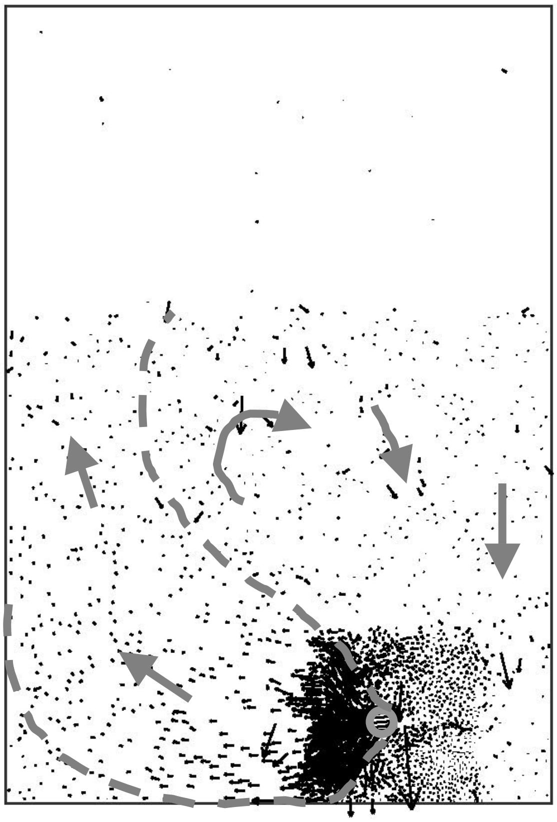

(a) Full-sized scale

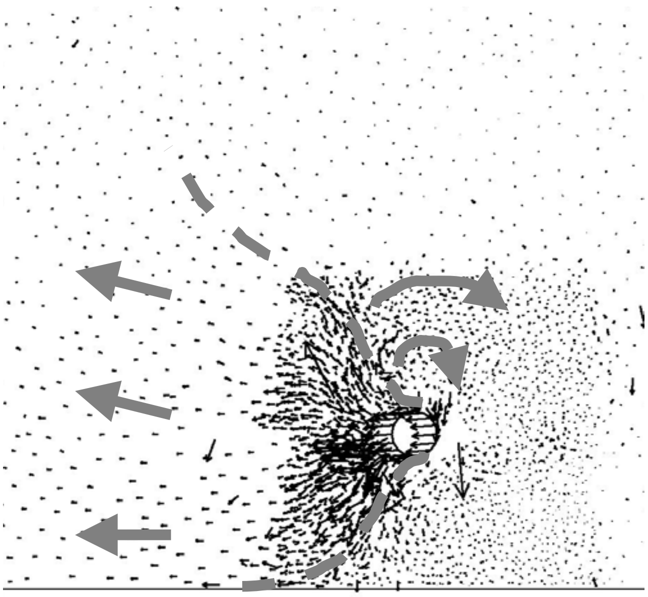

(b) Enlarged scale

Figure C-19 $H/D = 30$, Medium sand, $\tan \phi_\mu = 3.0$

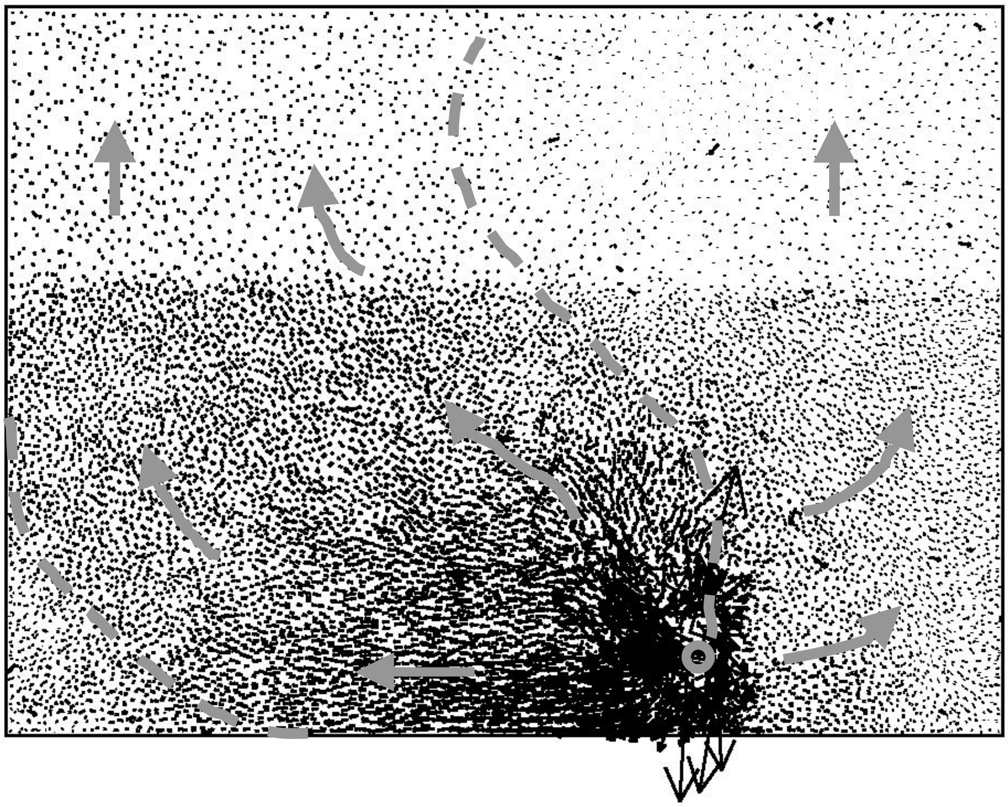

(a) Full-sized scale

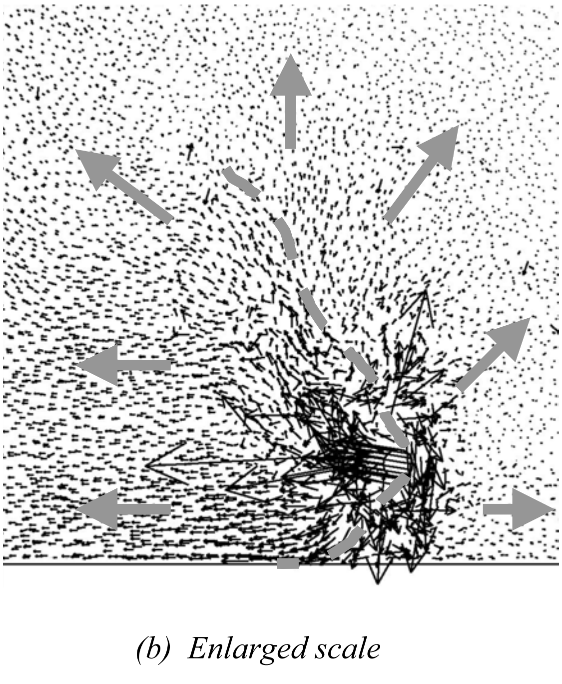

(b) Enlarged scale

Figure C-20 $H/D = 30$, Dense sand, $\tan \phi_\mu = 3.0$

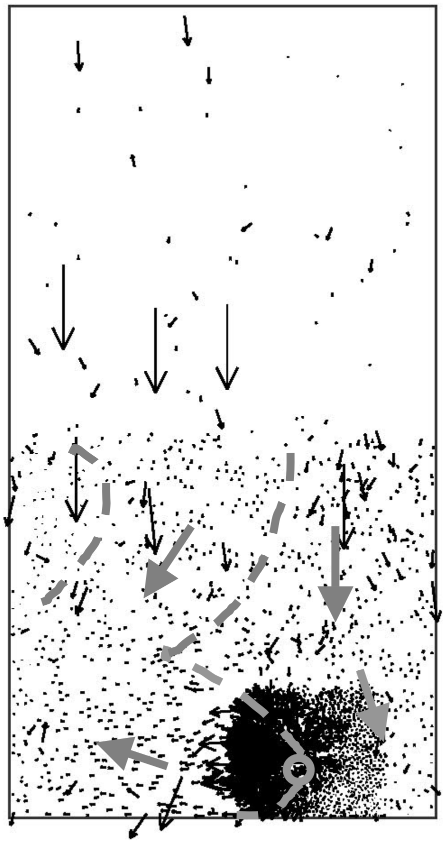

(a) Full-sized scale

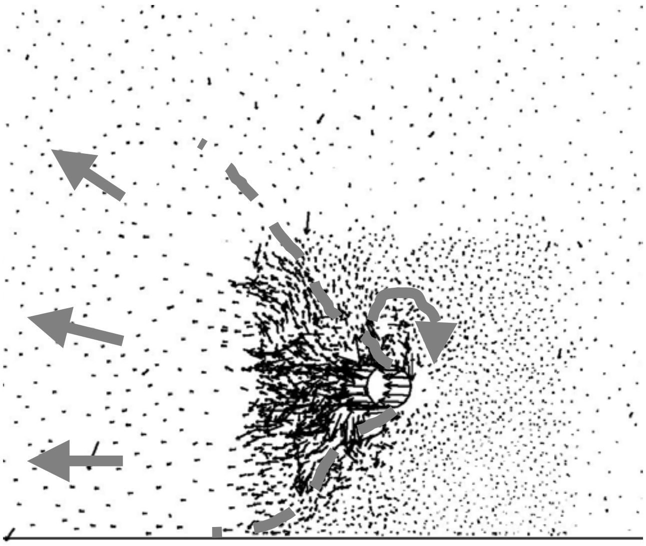

(b) Enlarged scale

Figure C-21 $H/D = 40$, Medium sand, tan $\phi_\mu = 3.0$

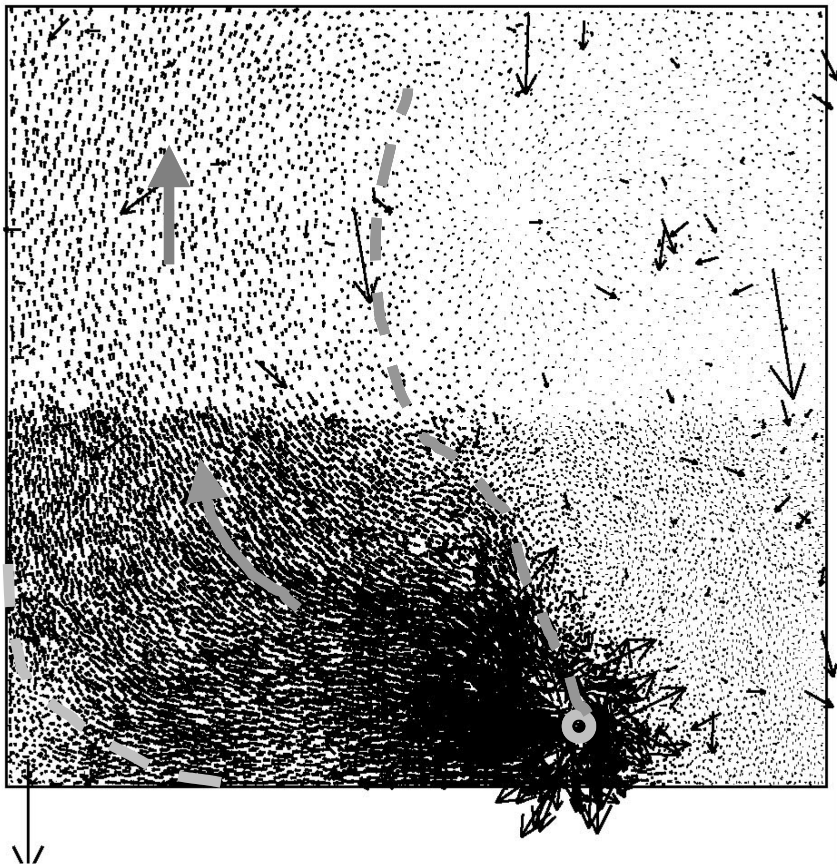

(a) Full-sized scale

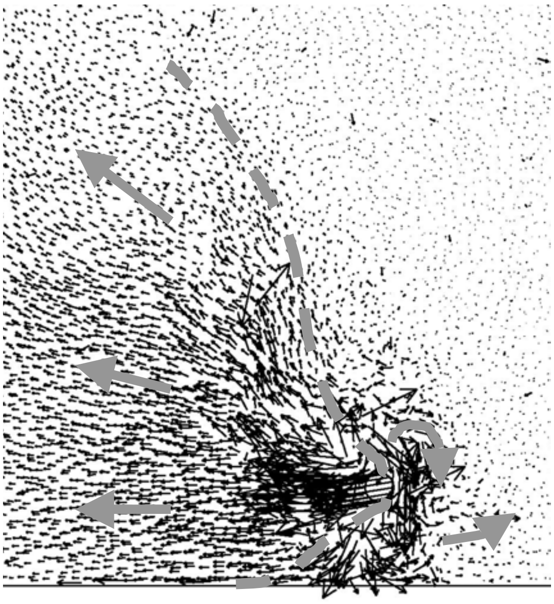

(b) Enlarged scale

Figure C-22 $H/D = 40$, Dense sand, $\tan \phi_{\mu} = 3.0$

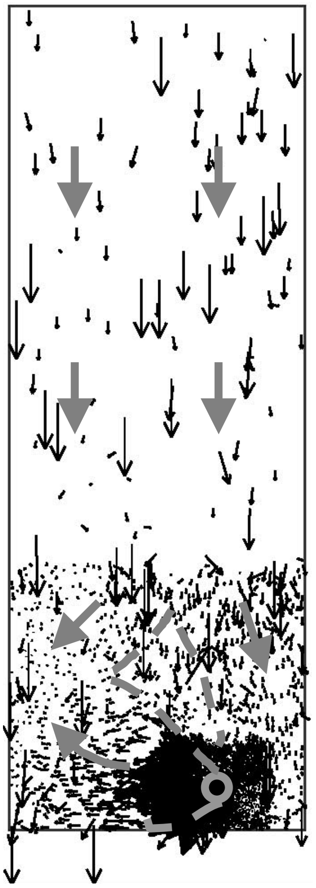

(a) Full-sized scale

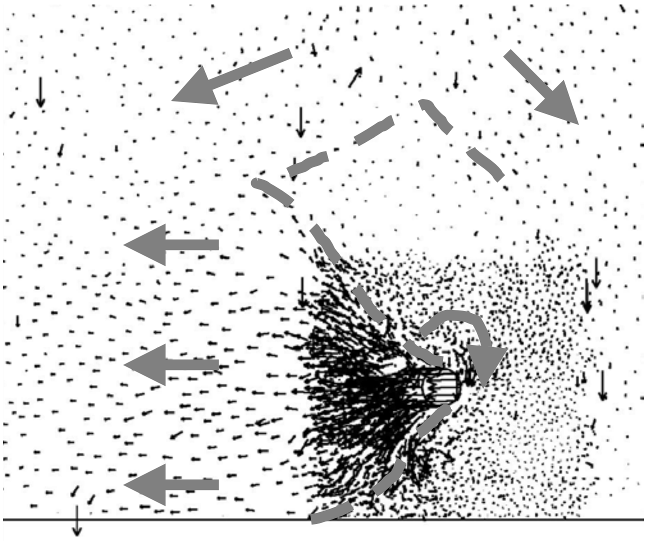

(b) Enlarged scale

Figure C-23 $H/D = 60$, Medium sand, $\tan \phi_{\mu} = 3.0$

(a) Full-sized scale

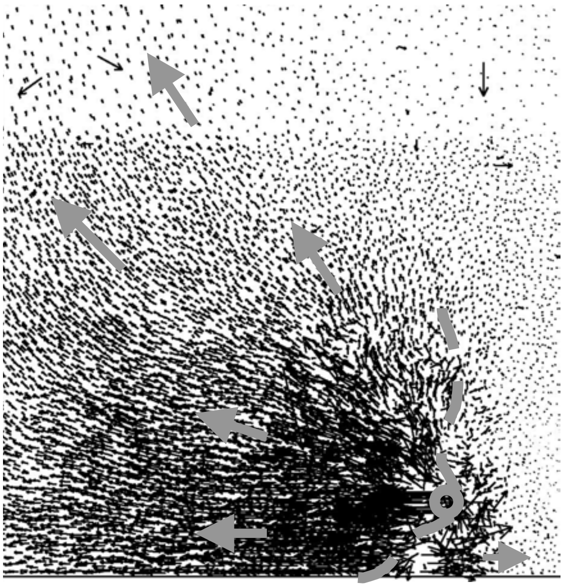

(b) Enlarged scale

Figure C-24 $H/D = 60$, Dense sand, $\tan \phi_\mu = 3.0$

Appendix D

Displacement Pattern under Upward Loading
(Velocity Vector)

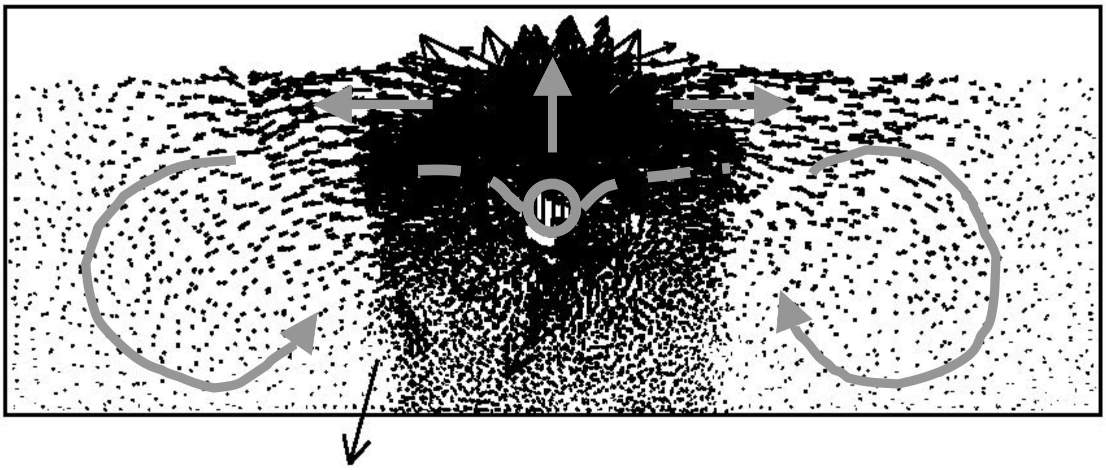

(a) Full-sized scale

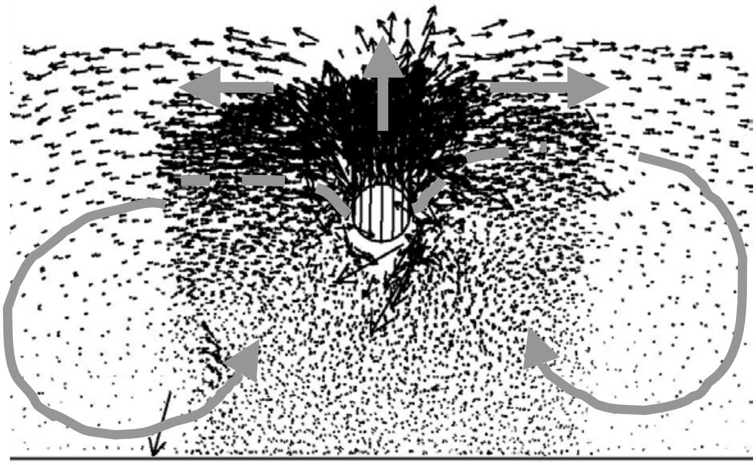

(b) Enlarged scale

Figure D-1 $H_c/D = 4$, Dense sand, tan $\phi_\mu = 3.0$

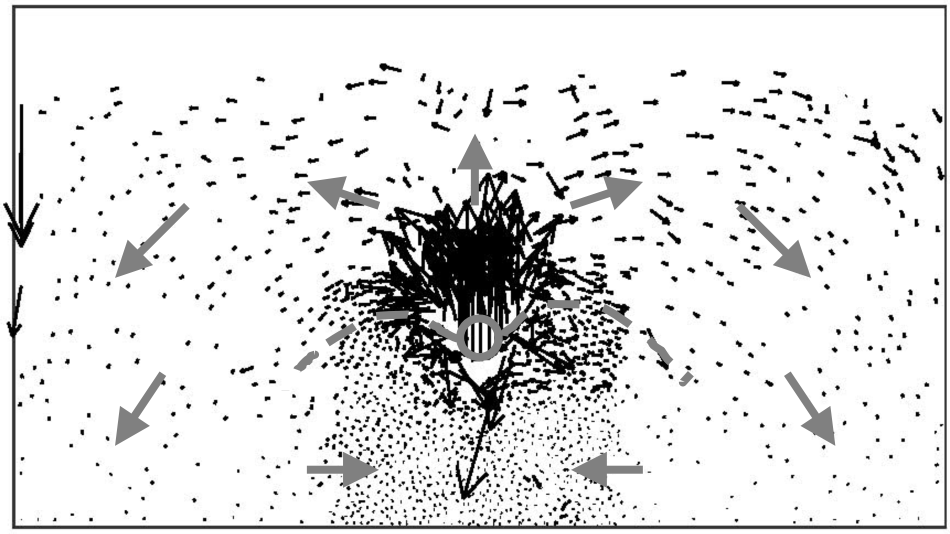

(a) Full-sized scale

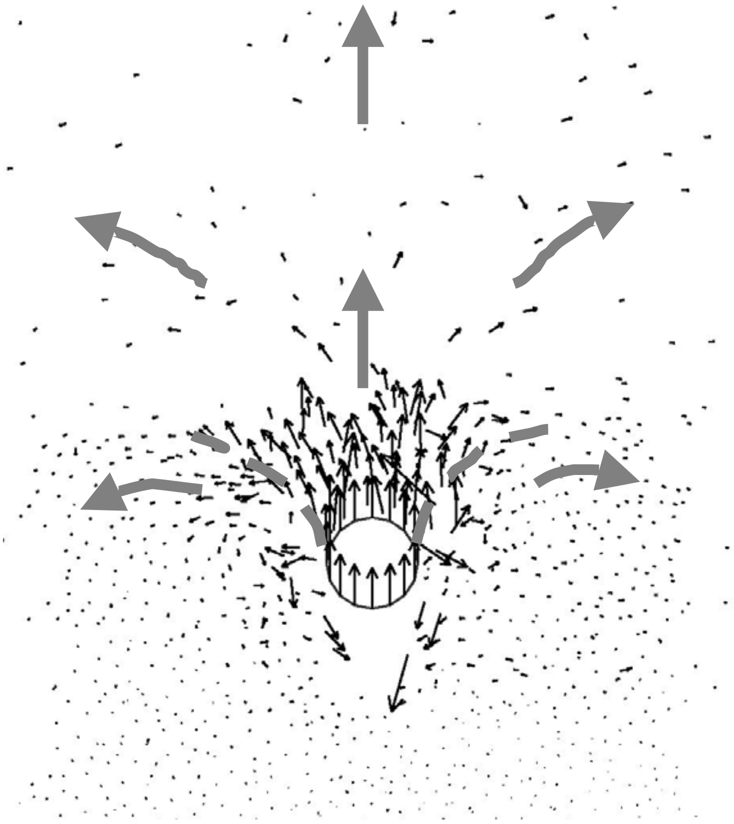

(b) Enlarged scale

Figure D-2 H_c/D = 8, Medium sand, tan ϕ_μ = 3.0

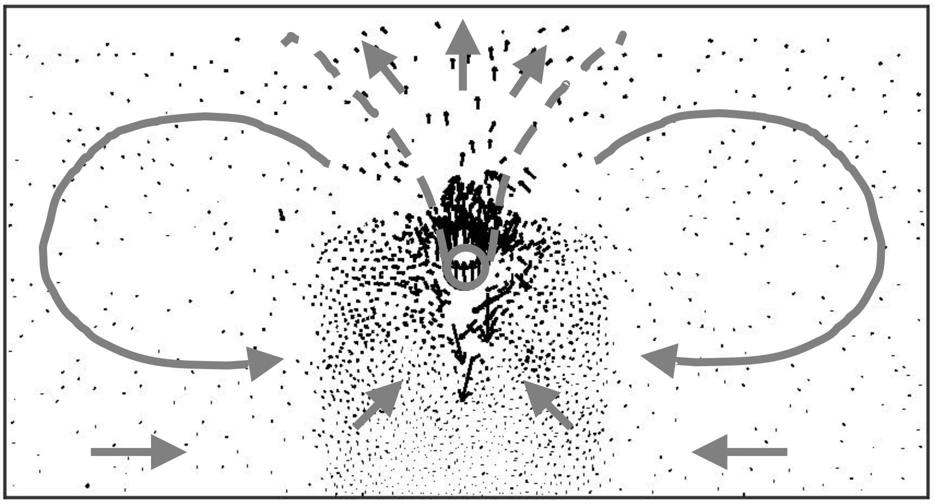

(a) Full-sized scale

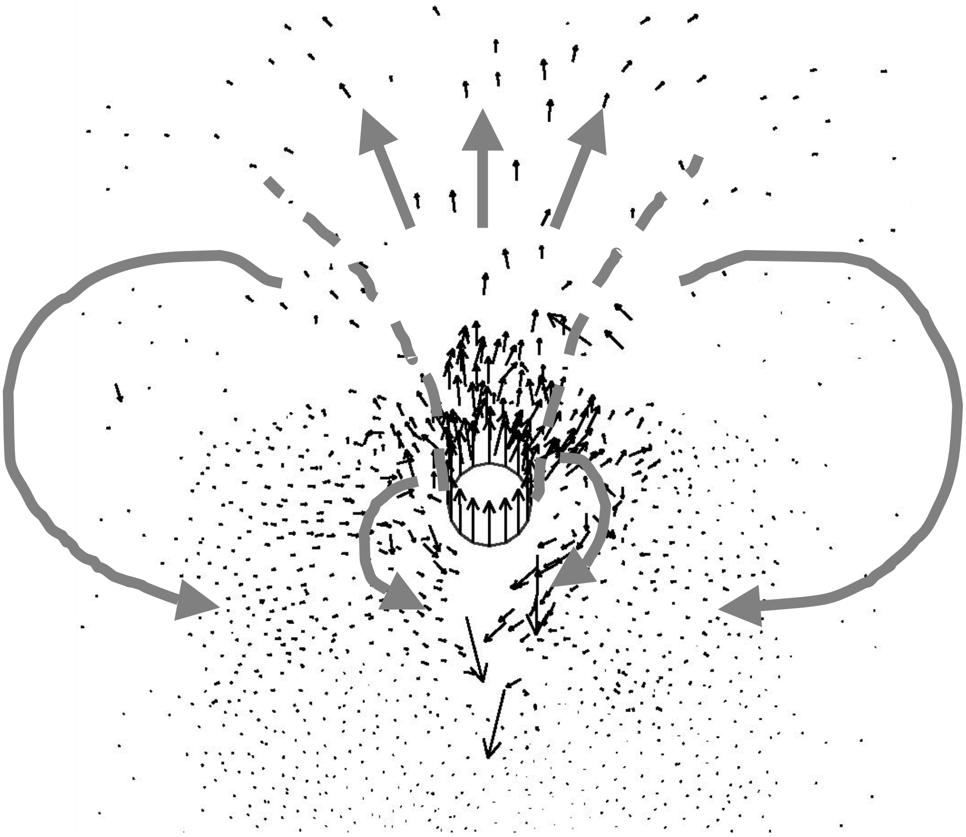

(b) Enlarged scale

Figure D-3 H_c/D = 8, Dense sand, tan ϕ_μ = 3.0

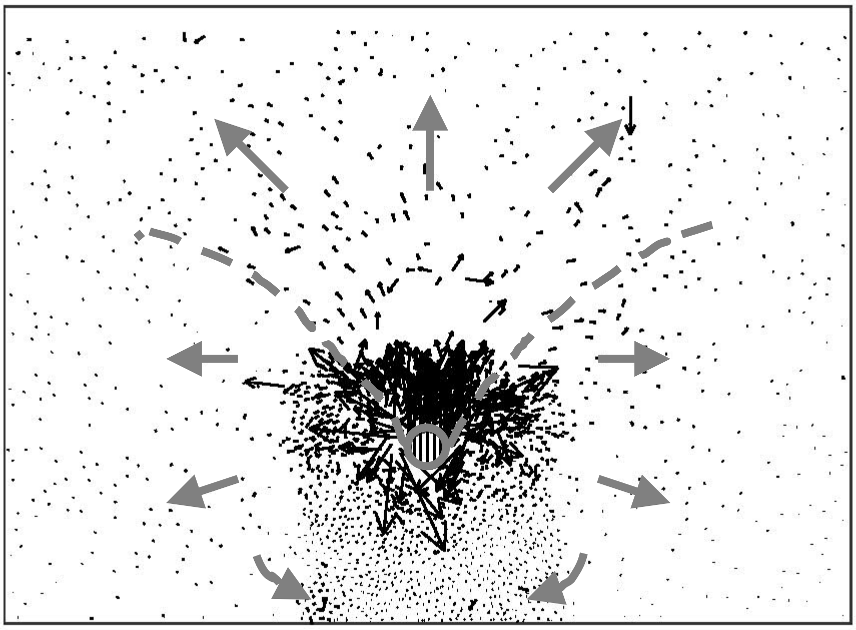

(a) Full-sized scale

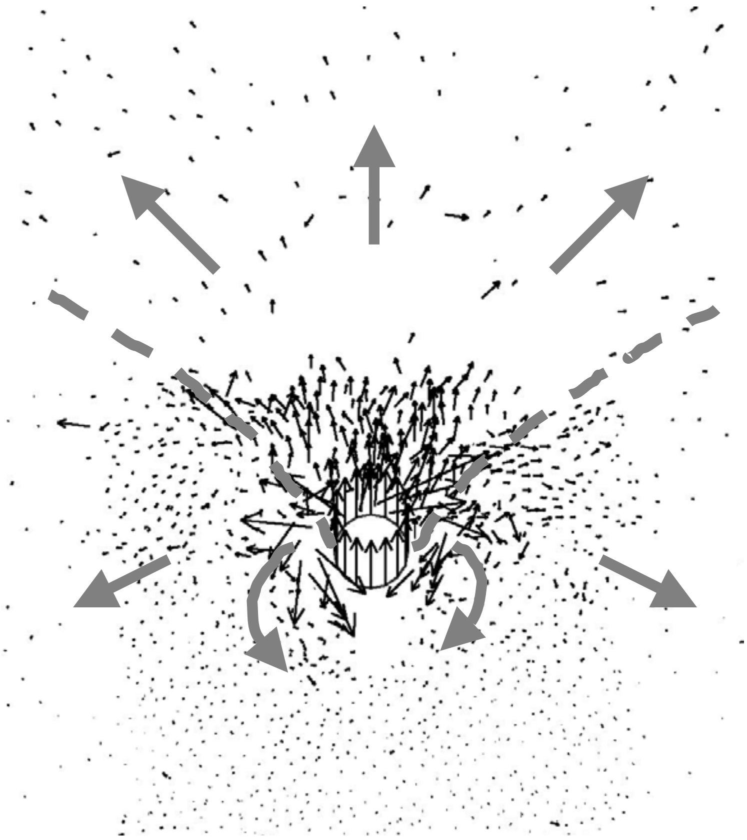

(b) Enlarged scale

Figure D-4 $H_c/D = 13$, Medium sand, tan $\phi_\mu = 3.0$

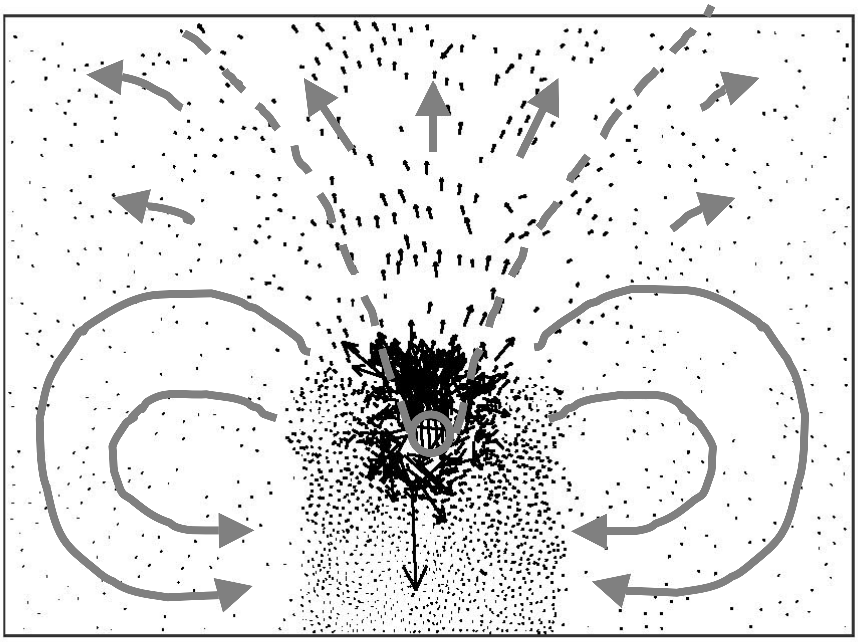

(a) Full-sized scale

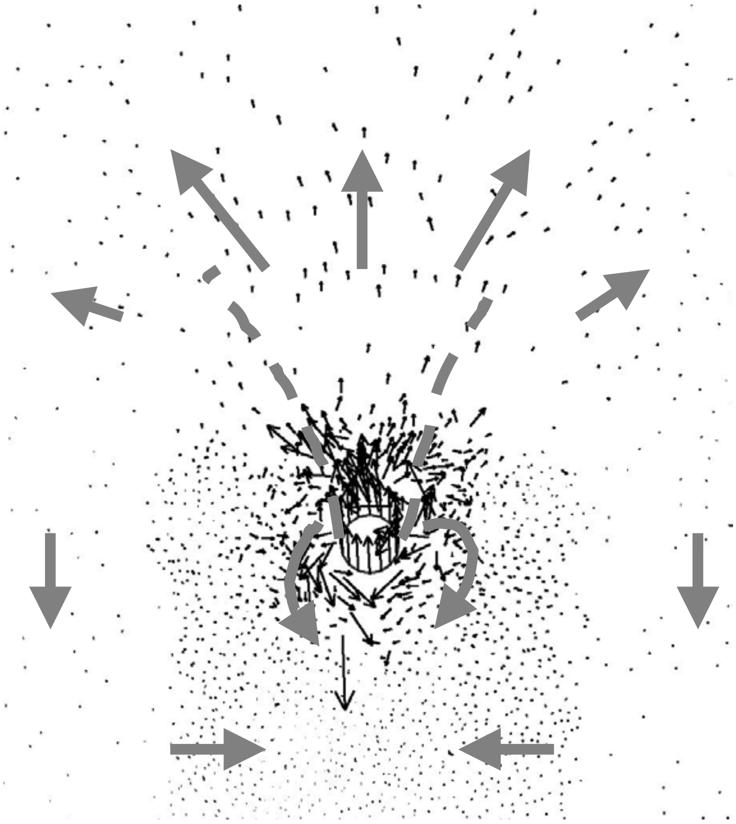

(b) Enlarged scale

Figure D-5 $H_c/D = 13$, Dense sand, $\tan \phi_\mu = 3.0$

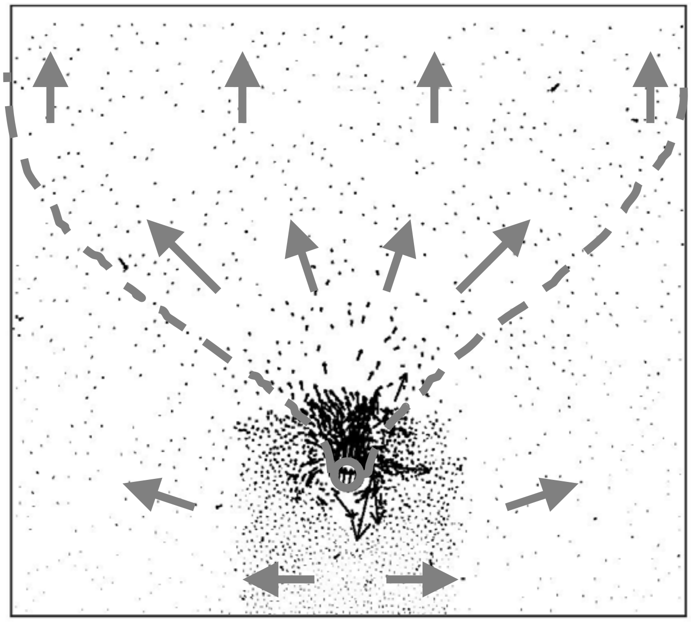

(a) Full-sized scale

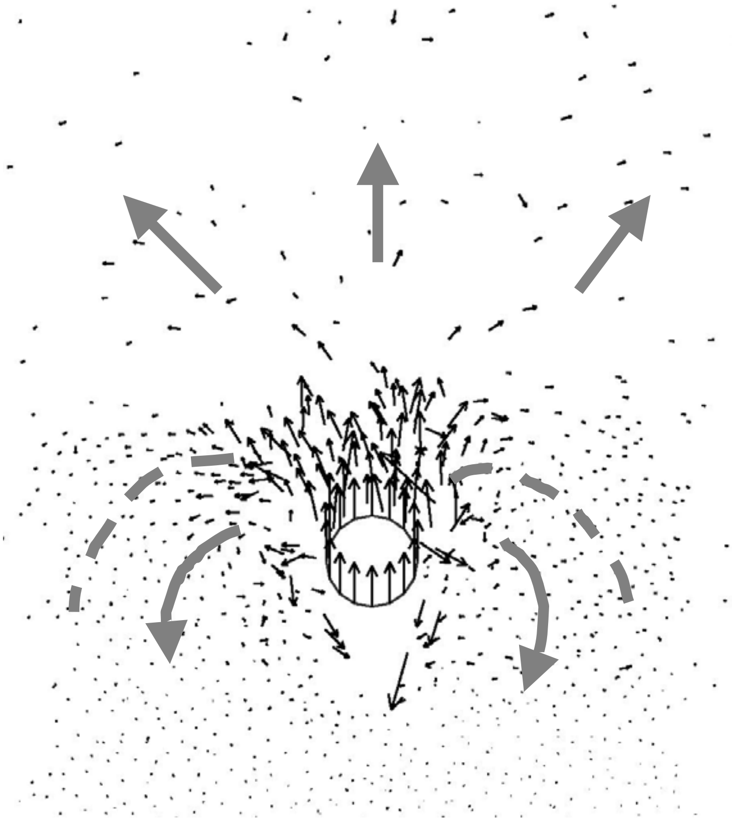

(b) Enlarged scale

Figure D-6 $H_c/D = 17$, Medium sand, $\tan\phi_\mu = 3.0$

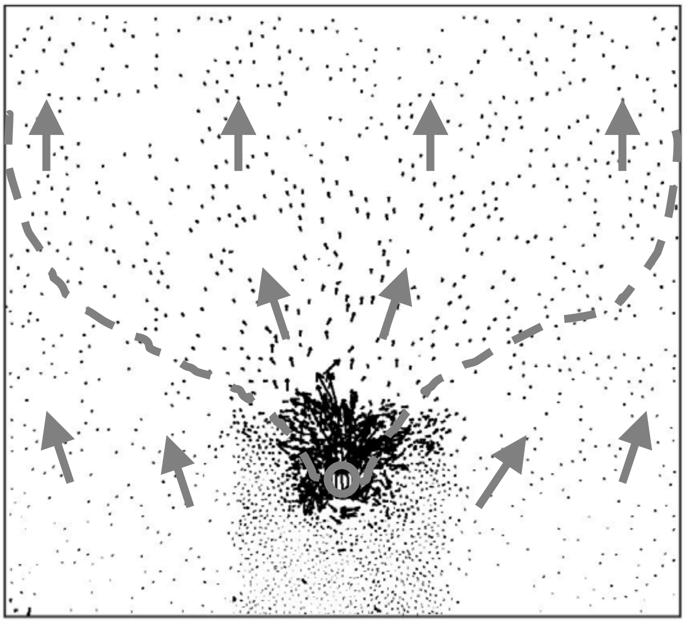

(a) Full-sized scale

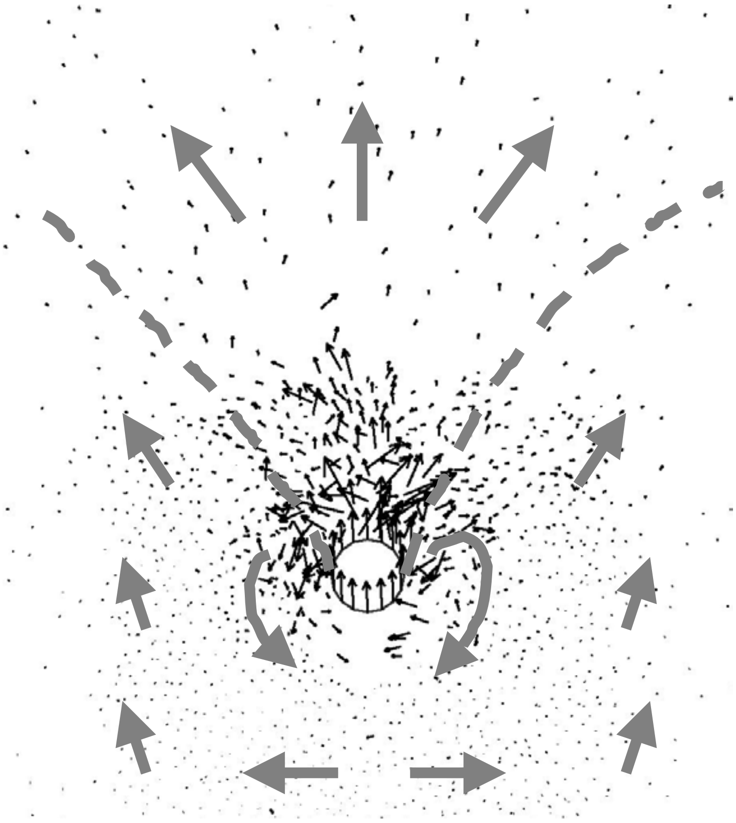

(b) Enlarged scale

Figure D-7 H_c/D = 17, Dense sand, tan ϕ_μ = 3.0

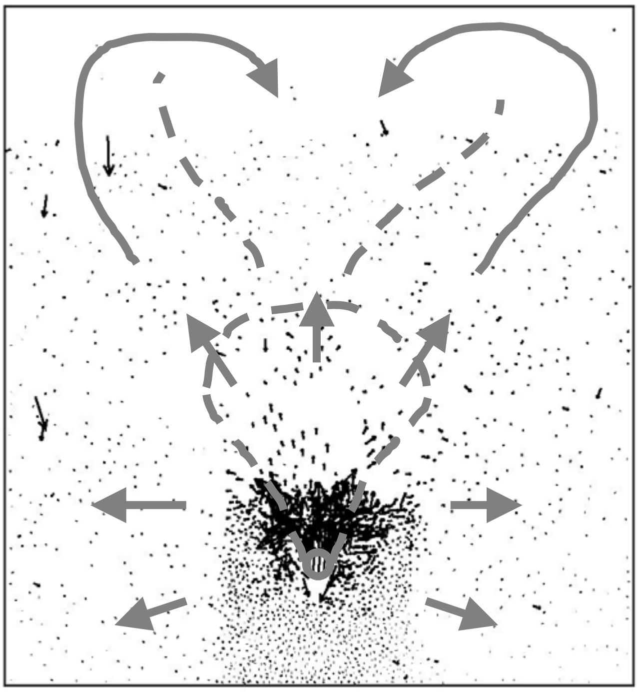

(a) Full-sized scale

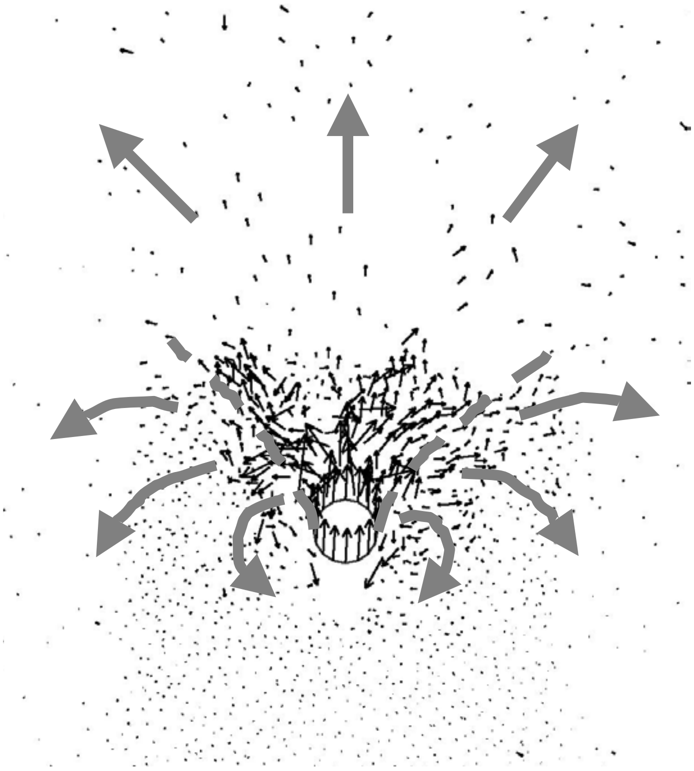

(b) Enlarged scale

Figure D-8 $H_c/D = 21$, Medium sand, tan $\phi_\mu = 3.0$

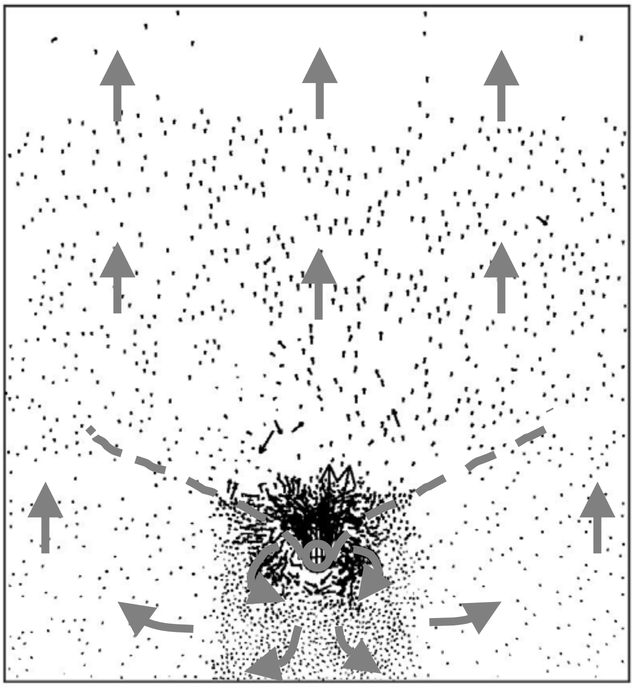

(a) Full-sized scale

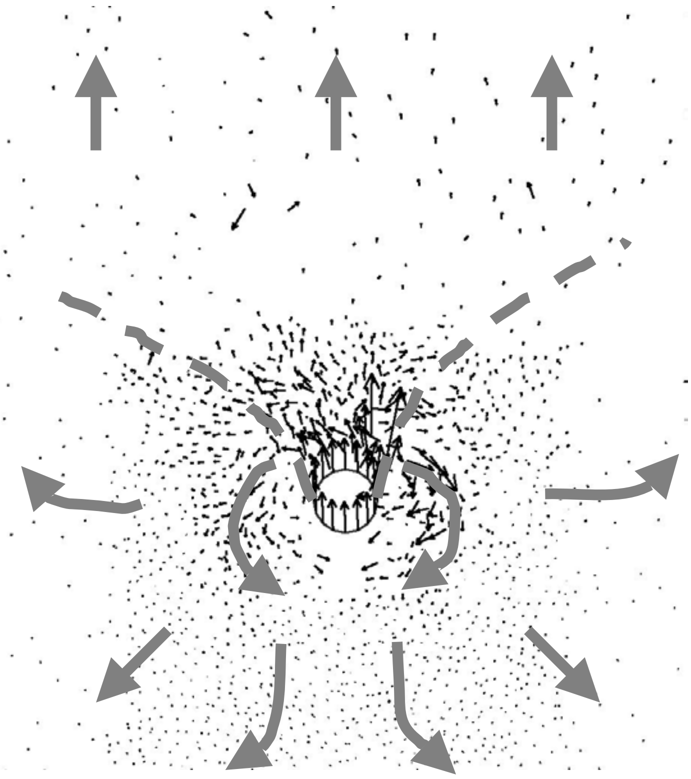

(b) Enlarged scale

Figure D-9 H_c/D = 21, Dense sand, tan ϕ_μ = 3.0

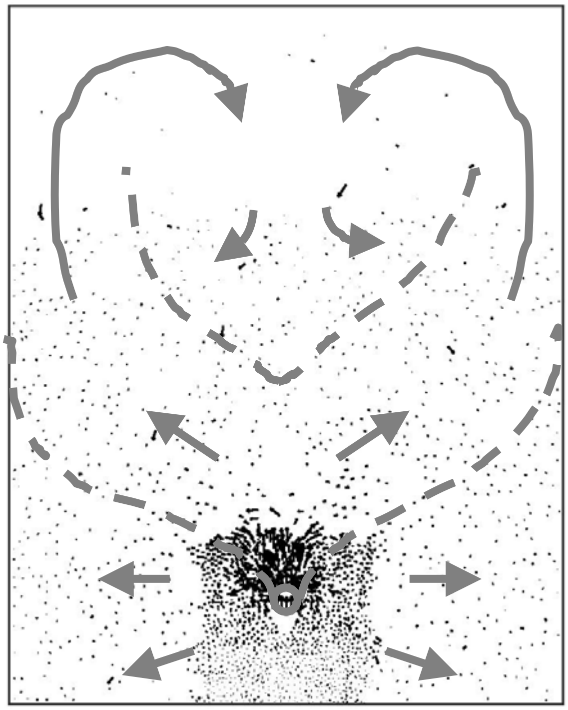

(a) Full-sized scale

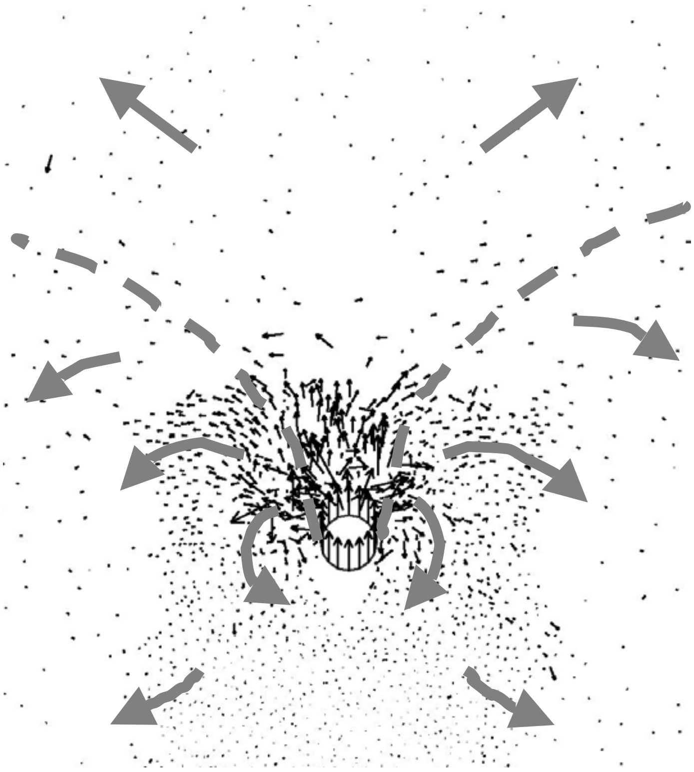

(b) Enlarged scale

Figure D-10 $H_c/D = 25$, Medium sand, $\tan \phi_\mu = 3.0$

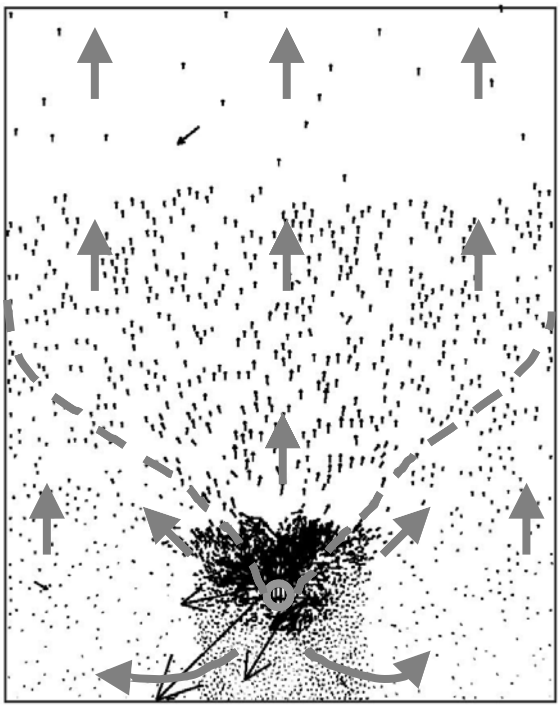

(a) Full-sized scale

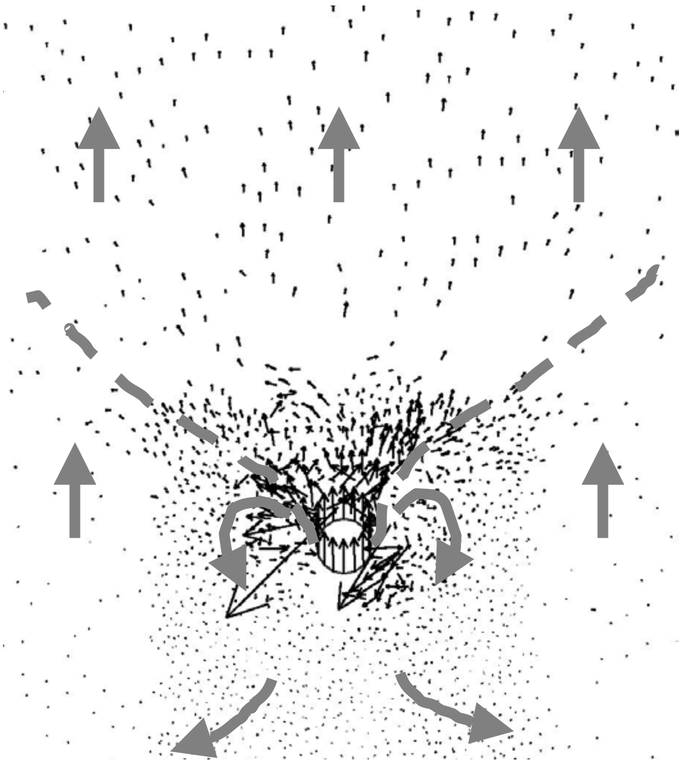

(b) Enlarged scale

Figure D-11 $H_c/D = 25$, Dense sand, tan $\phi_\mu = 3.0$

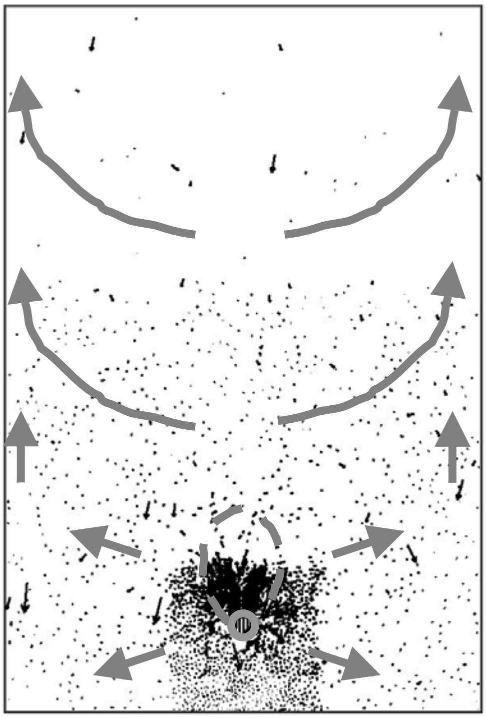

(a) Full-sized scale

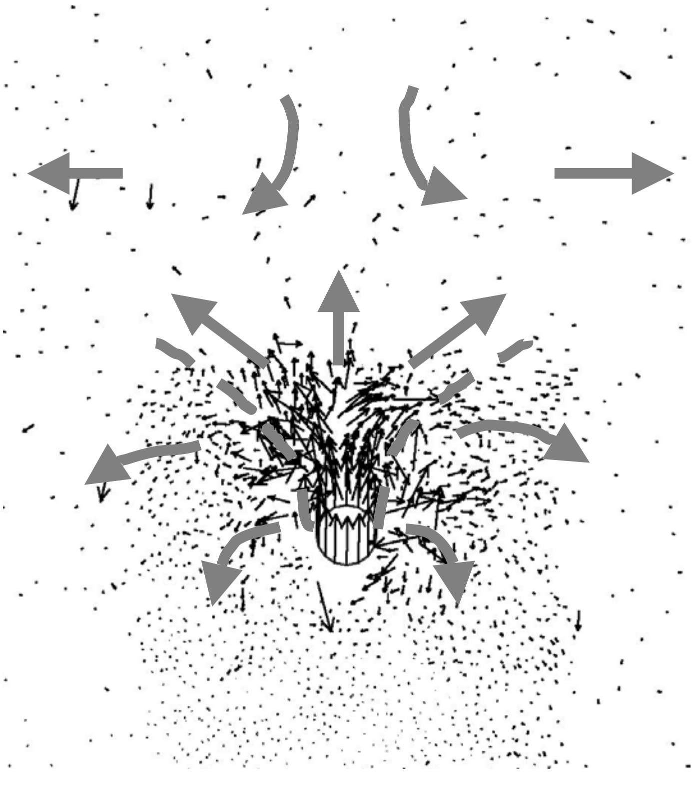

(b) Enlarged scale

Figure D-12 $H_c/D = 30$, Medium sand, $\tan\phi_\mu = 3.0$

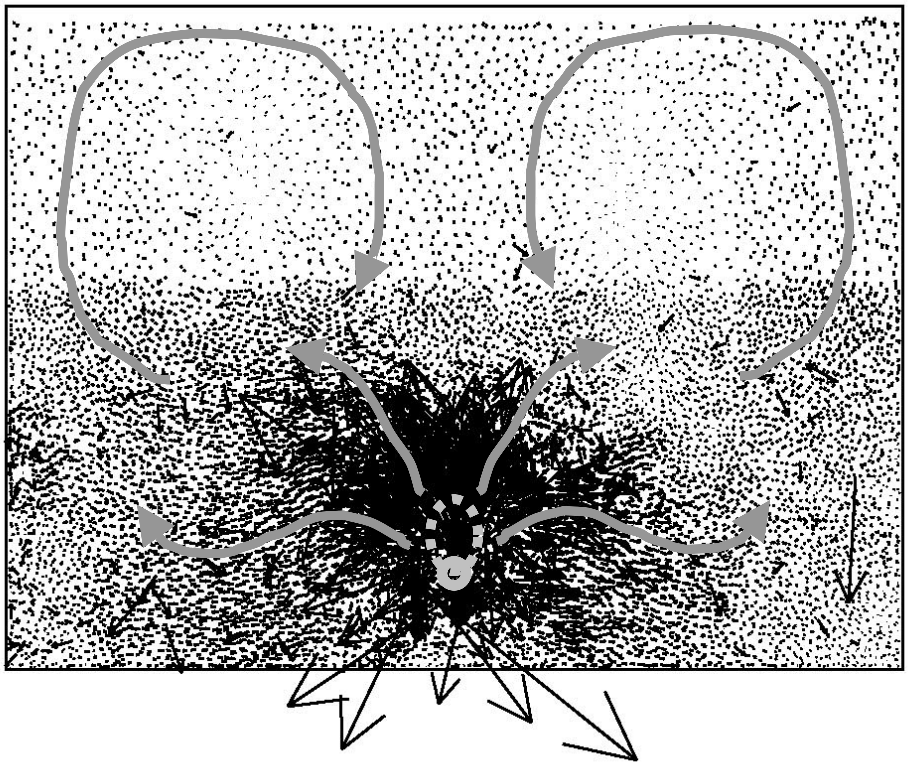

(a) Full-sized scale

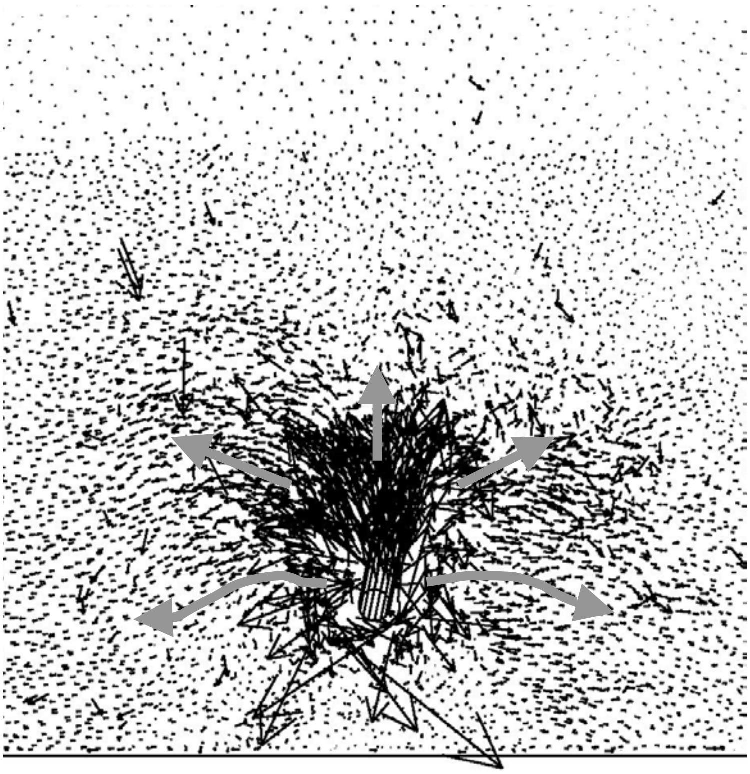

(b) Enlarged scale

Figure D-13 $H_c/D = 30$, Dense sand, $\tan \phi_\mu = 3.0$

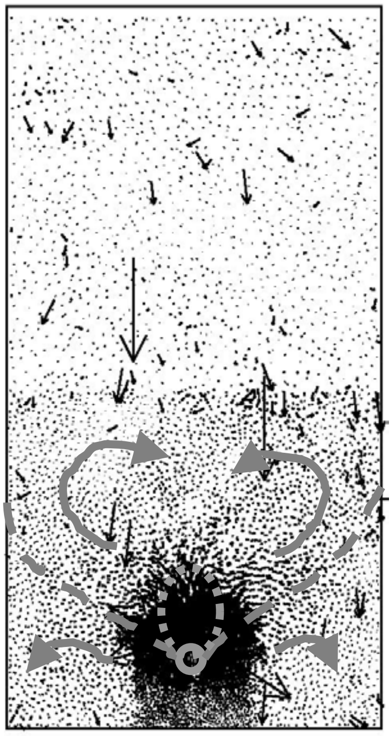

(a) Full-sized scale

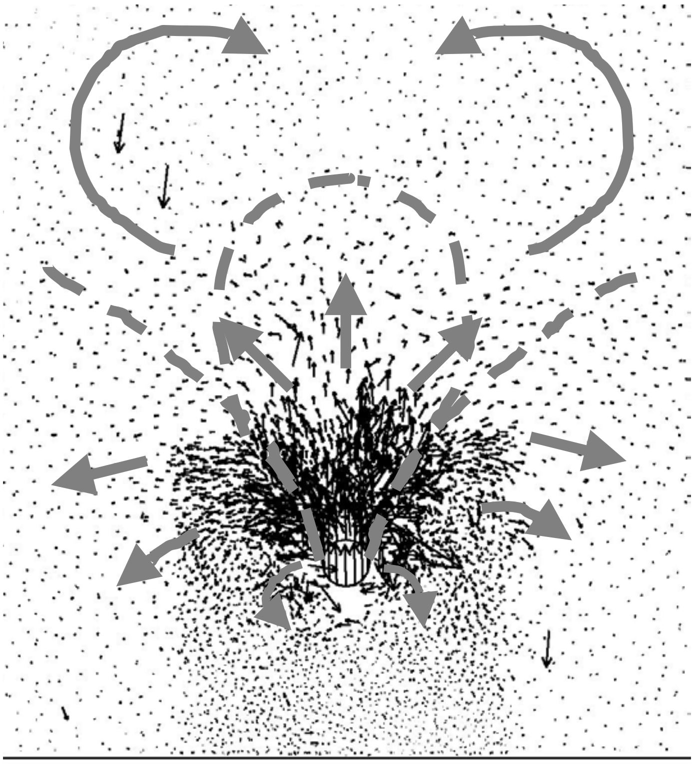

(b) Enlarged scale

Figure D-14 $H_c/D = 40$, Medium sand, $\tan\phi_\mu = 3.0$

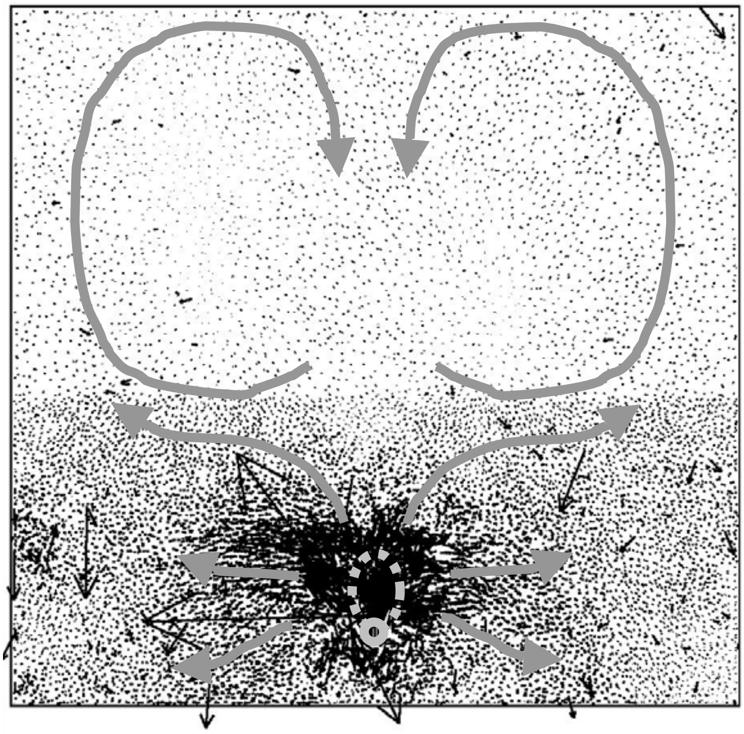

(a) Full-sized scale

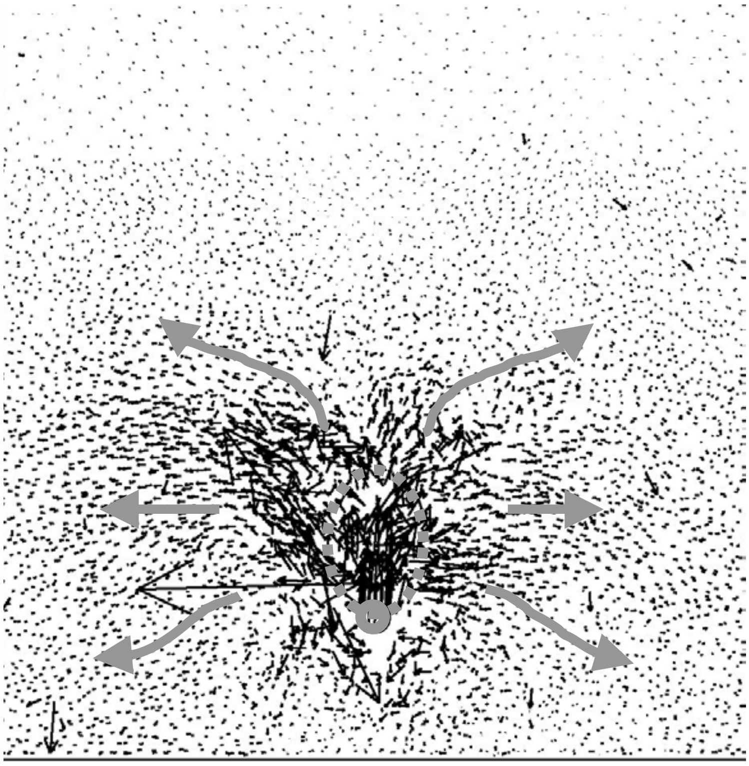

(b) Enlarged scale

Figure D-15 $H_c/D = 40$, Dense sand, $\tan \phi_\mu = 3.0$

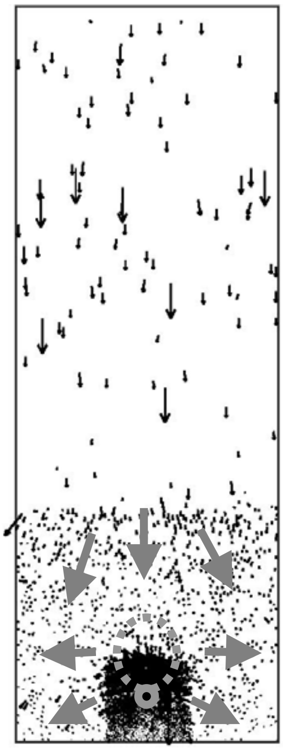

(a) Full-sized scale

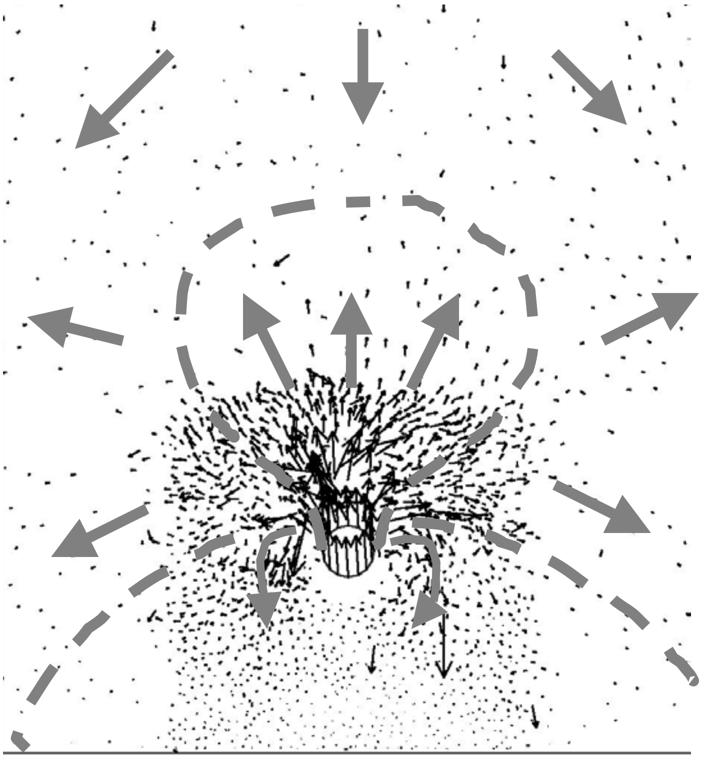

(b) Enlarged scale

Figure D-16 H_c/D = 60, Medium sand, tan ϕ_μ = 3.0

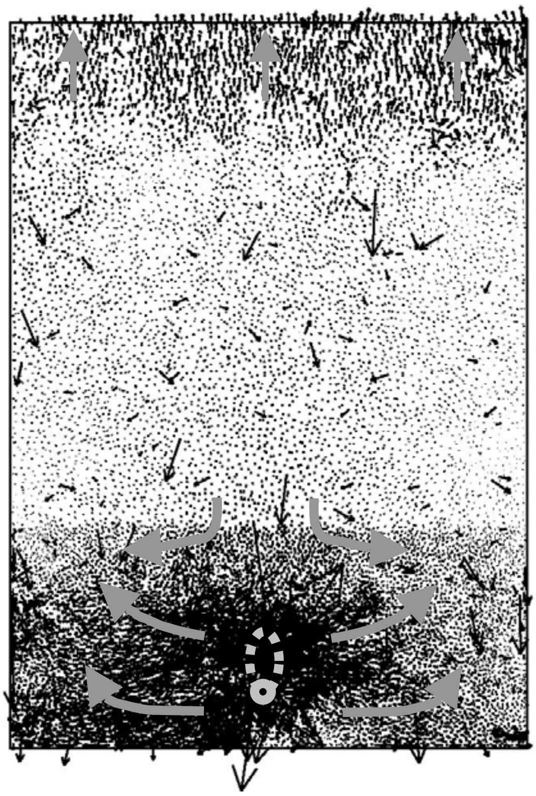

(a) Full-sized scale

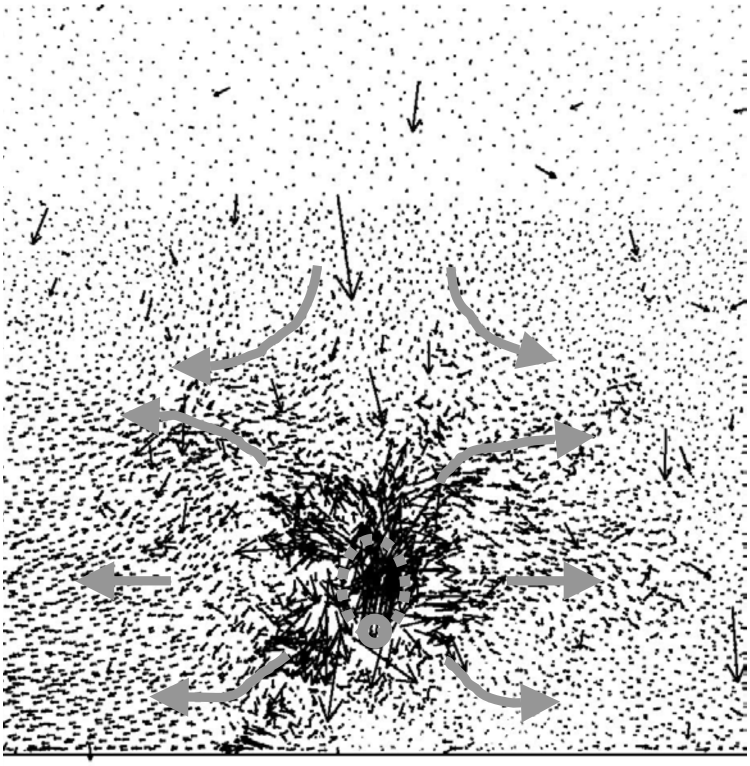

(b) Enlarged scale

Figure D-17 H_c/D = 60, Dense sand, tan ϕ_μ = 3.0

Appendix E

Contact Force Pattern under Lateral Loading

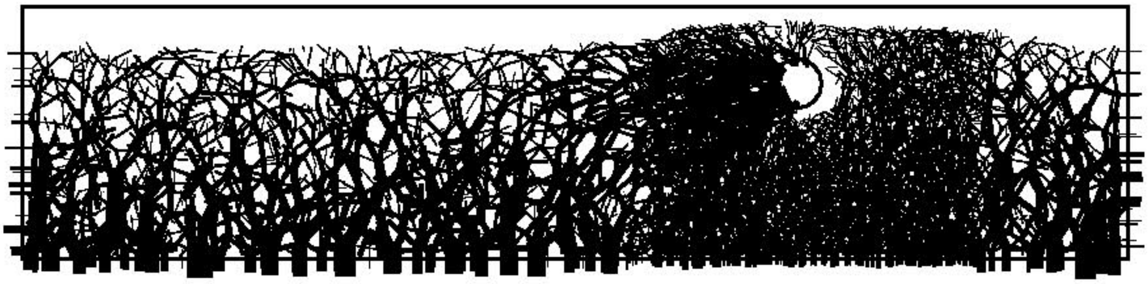

Figure E-1 *H/D* = 2, Medium sand, tan ϕ_μ = 3.0

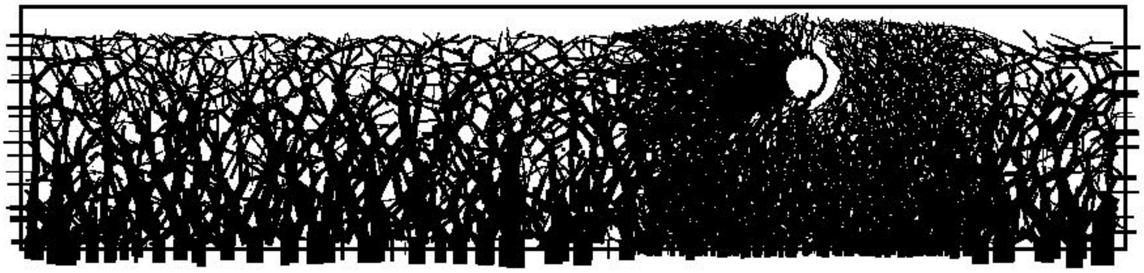

Figure E-2 *H/D* = 2, Dense sand, tan ϕ_μ = 3.0

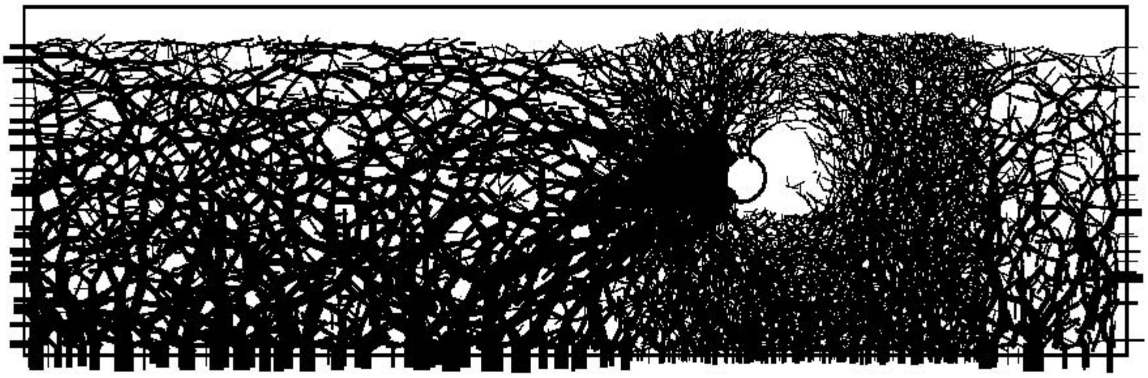

Figure E-3 *H/D* = 4, Medium sand, tan ϕ_μ = 3.0

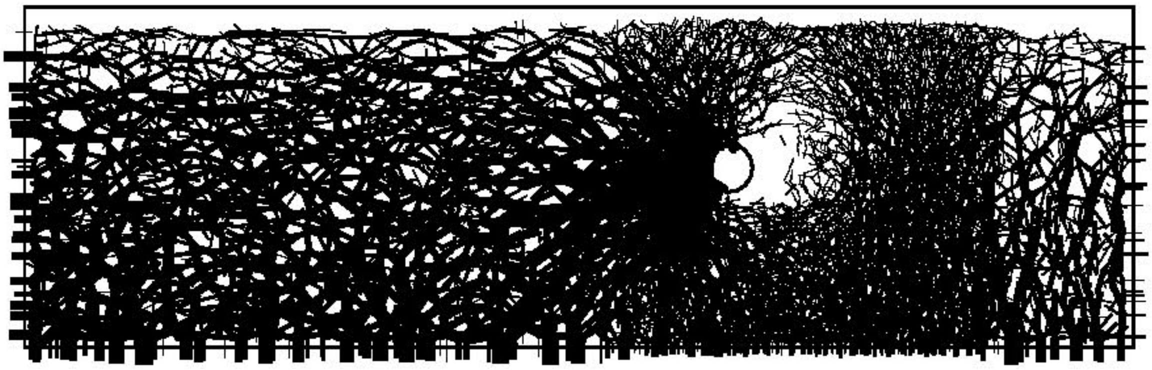

Figure E-4 *H/D* = 4, Dense sand, tan ϕ_μ = 3.0

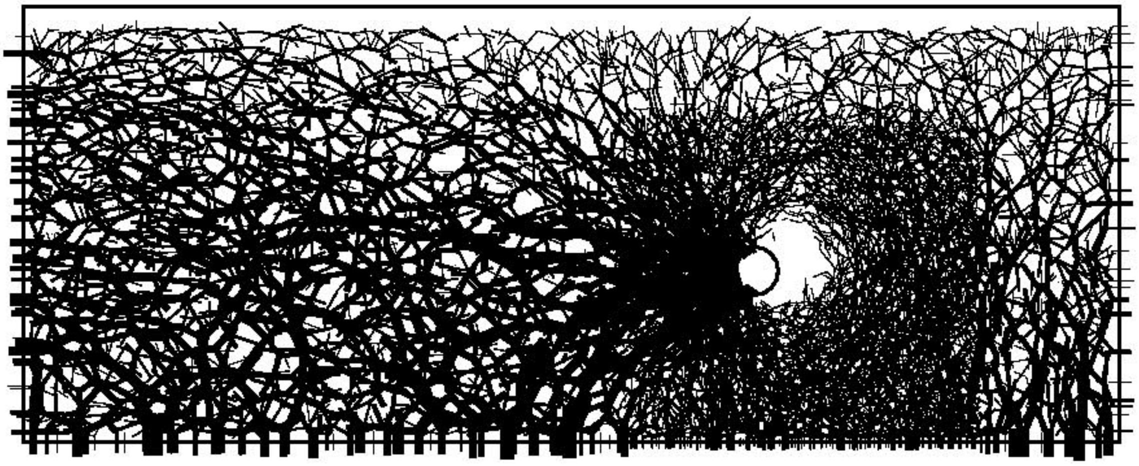

Figure E-5 *H/D* = 6, Medium sand, tan ϕ_{μ} = 3.0

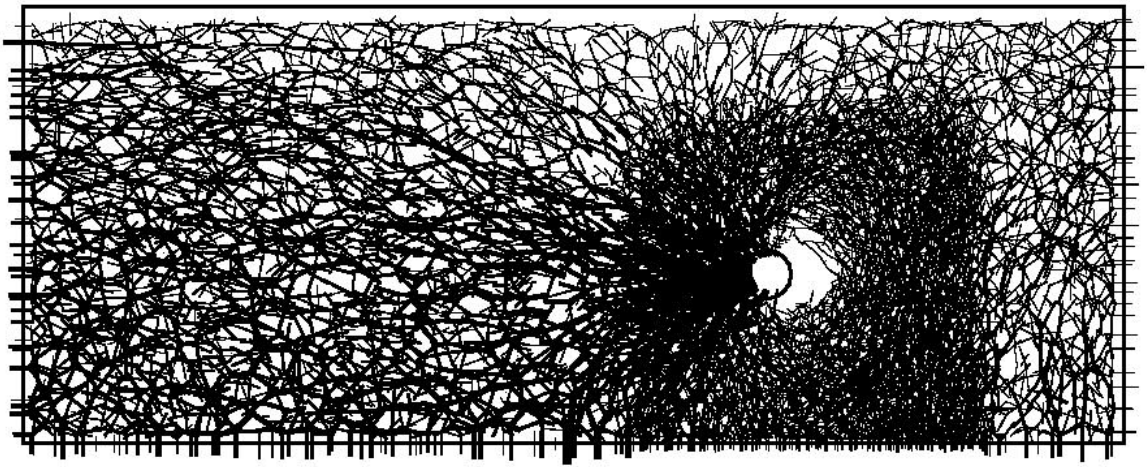

Figure E-6 *H/D* = 6, Dense sand, tan ϕ_{μ} = 3.0

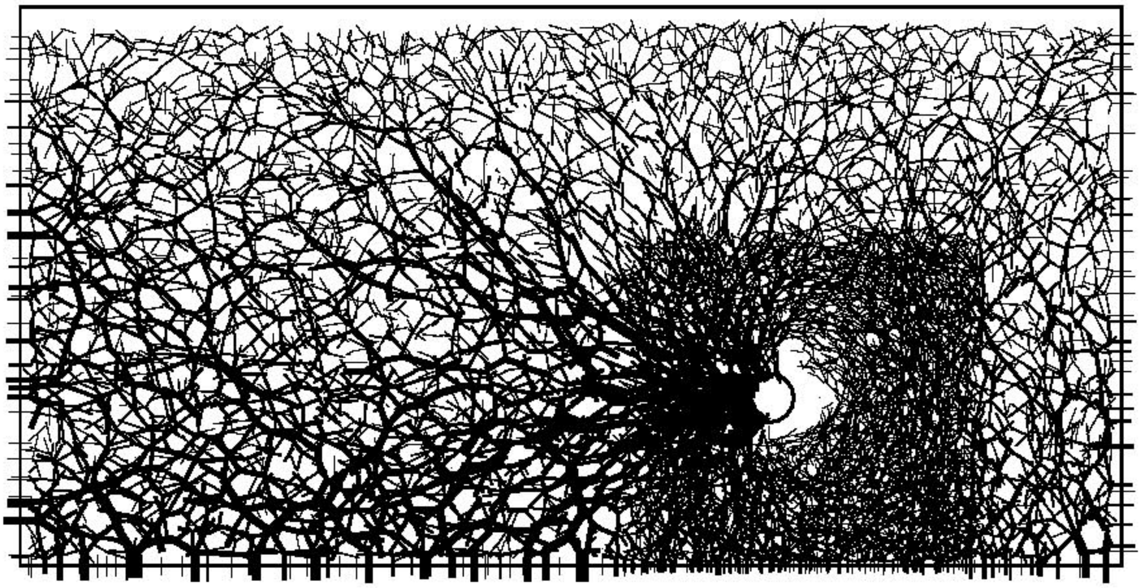

Figure E-7 *H/D* = 8.5, Medium sand, tan ϕ_μ = 3.0

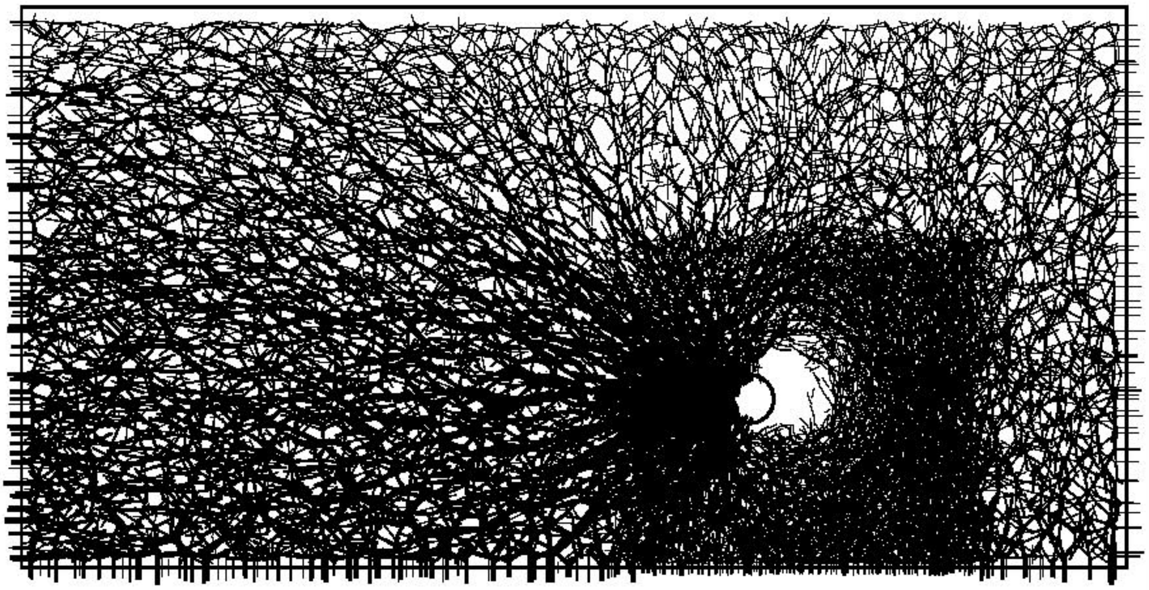

Figure E-8 *H/D* = 8.5, Dense sand, tan ϕ_μ = 3.0

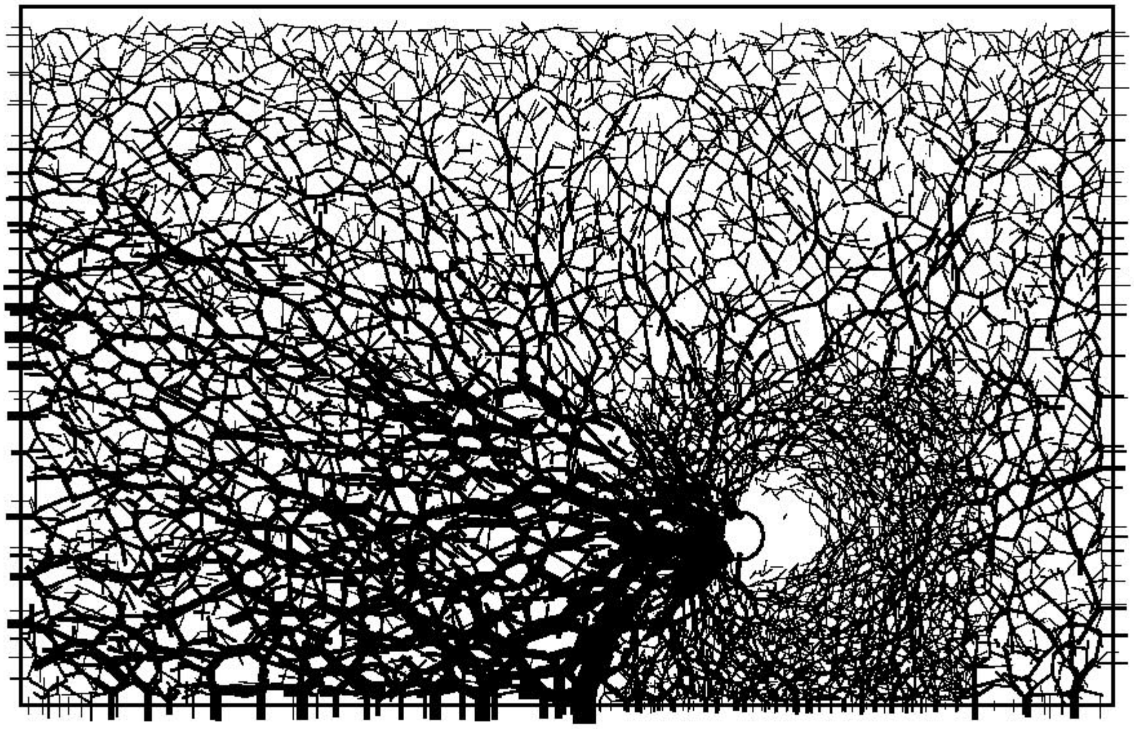

Figure E-9 *H/D* = 11.5, Medium sand, tan $\phi_\mu = 3.0$

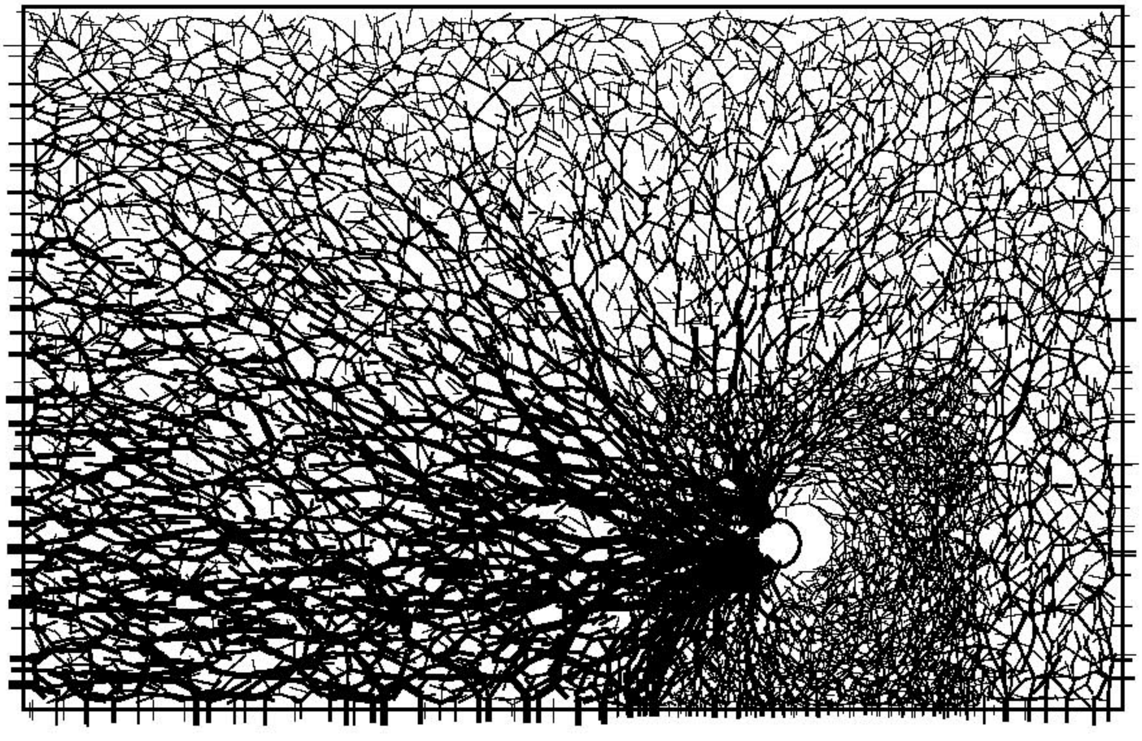

Figure E-10 *H/D* = 11.5, Dense sand, tan $\phi_\mu = 3.0$

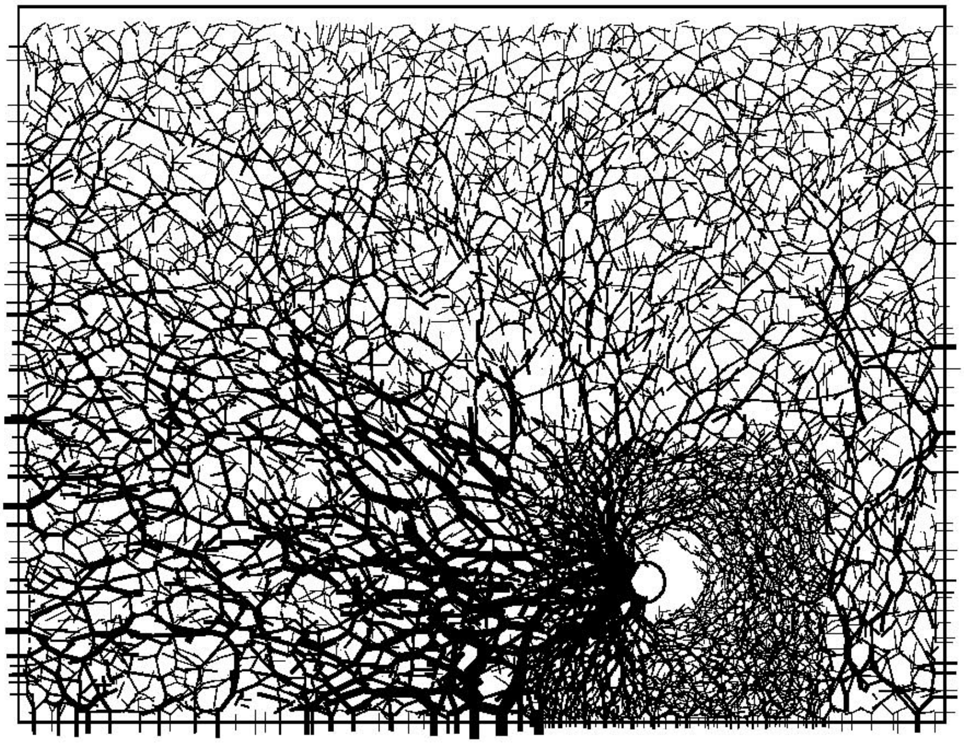

Figure E-11   *H/D* = 14.5, Medium sand, tan ϕ_μ = 3.0

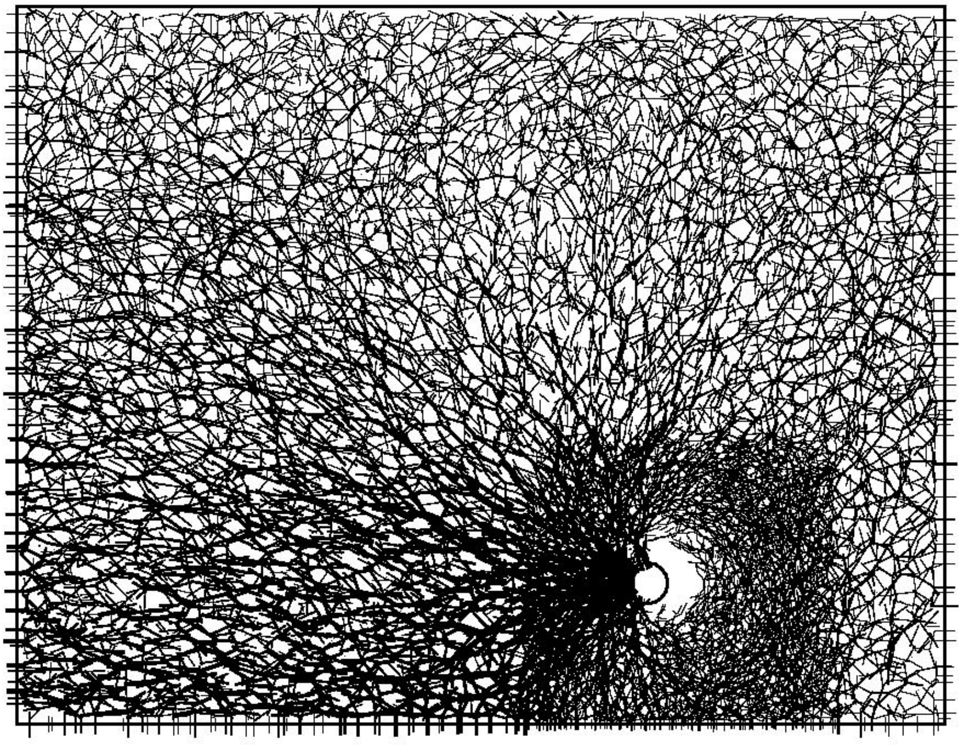

Figure E-12   *H/D* = 14.5, Dense sand, tan ϕ_μ = 3.0

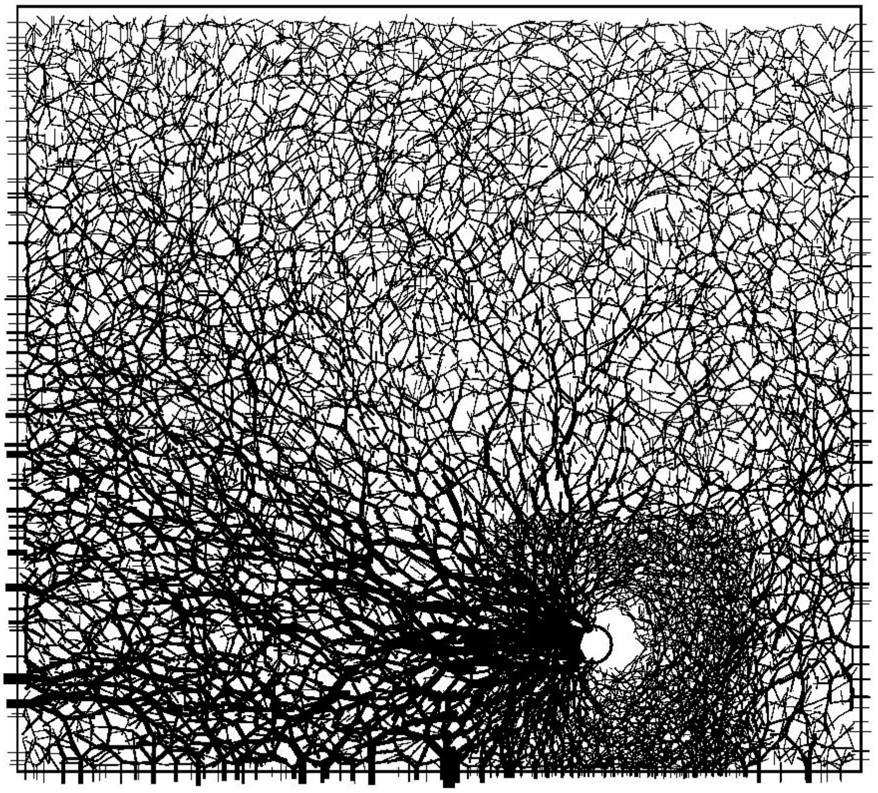

Figure E-13 *H/D* = 17.5, Medium sand, tan ϕ_μ = 3.0

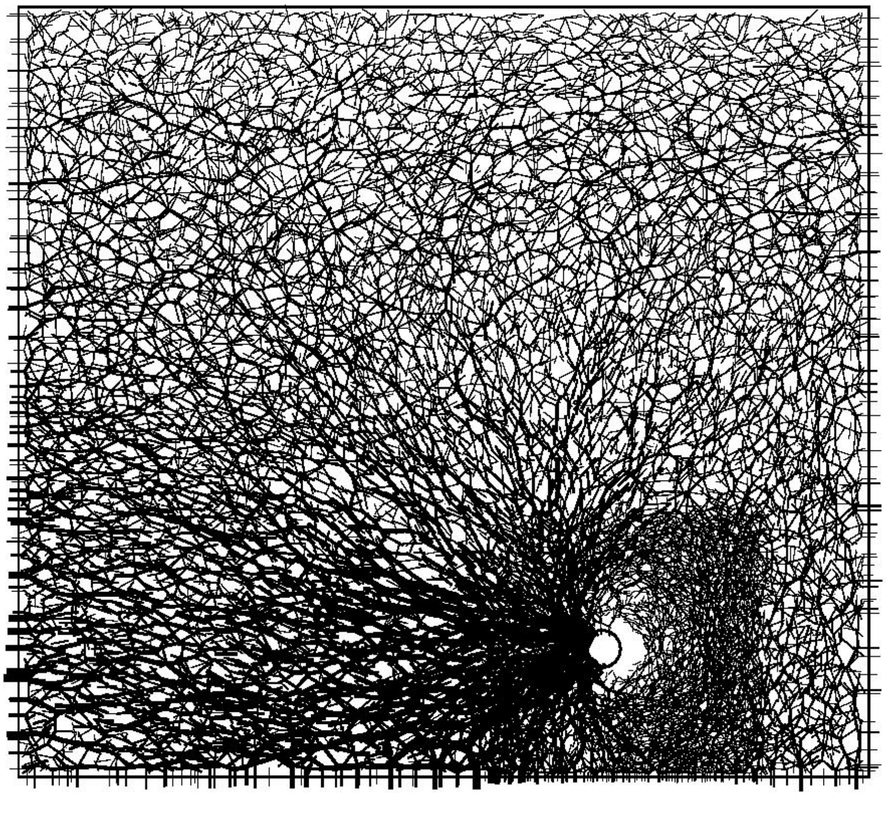

Figure E-14 *H/D* = 17.5, Dense sand, tan ϕ_μ = 3.0

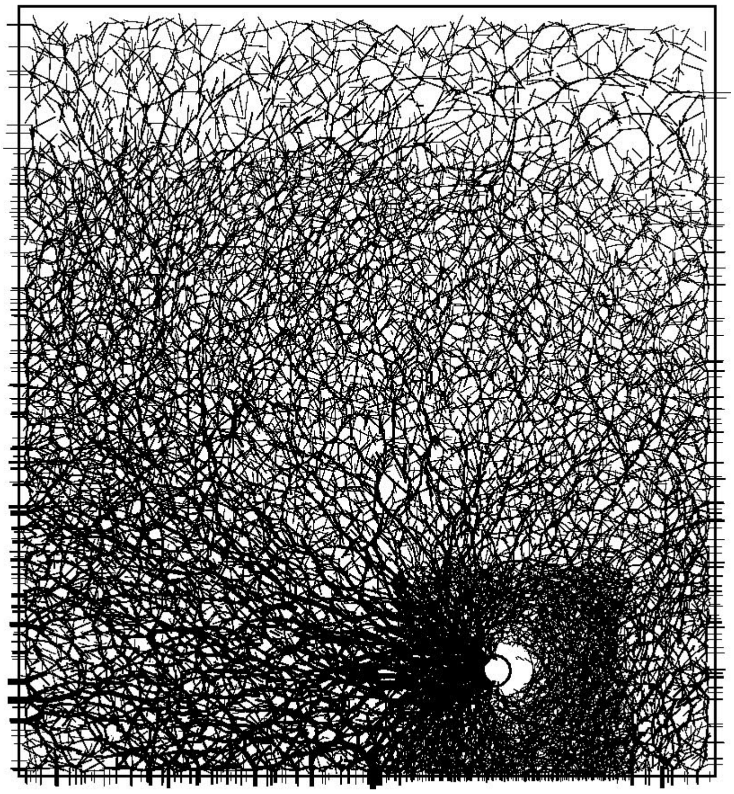

Figure E-15 *H/D* = 22, Medium sand, tan ϕ_μ = 3.0

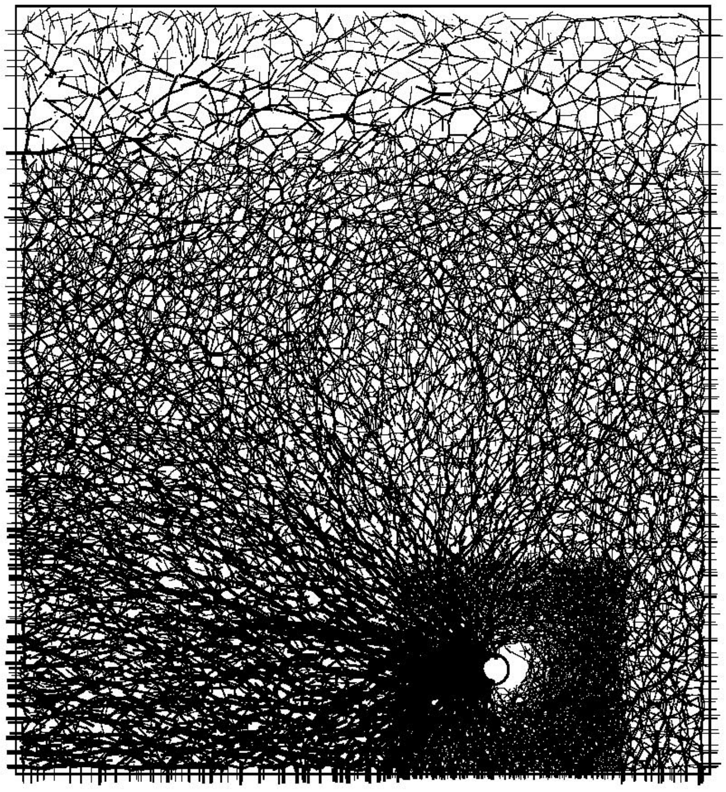

Figure E-16 *H/D* = 22, Dense sand, tan ϕ_μ = 3.0

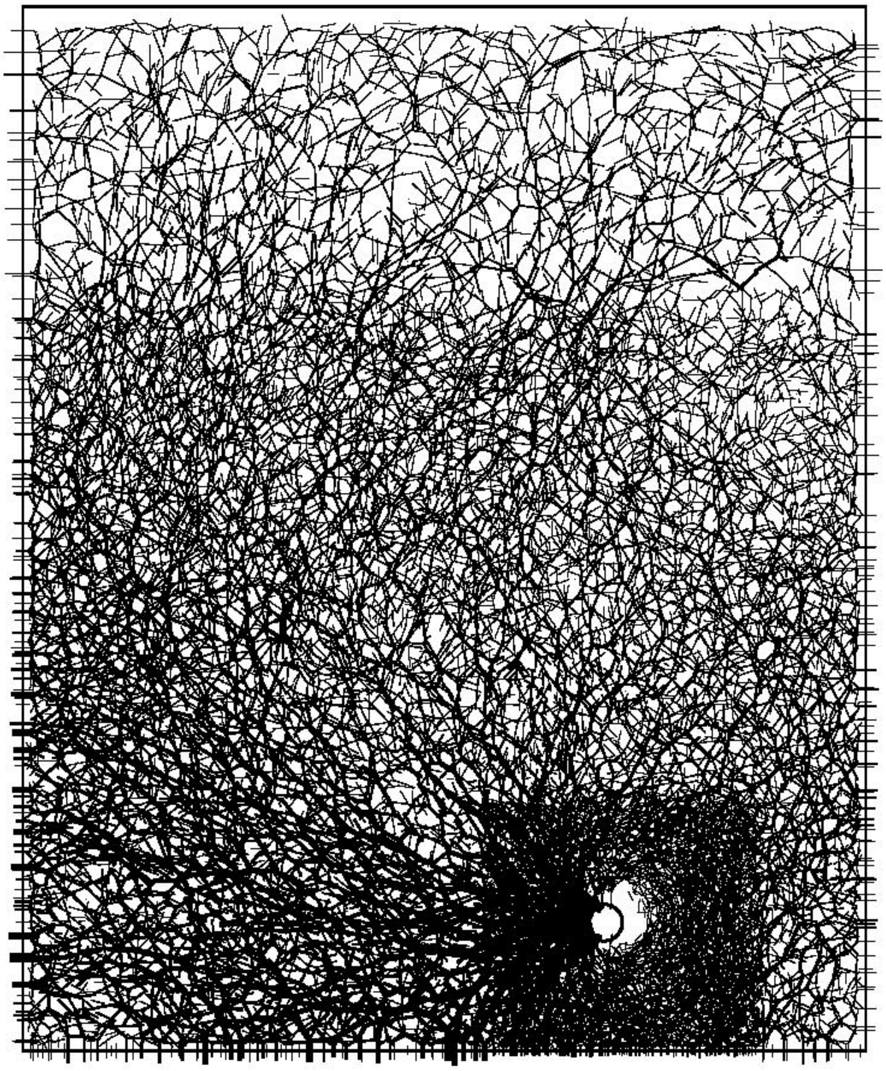

Figure E-17 $H/D = 25$, Medium sand, $\tan \phi_\mu = 3.0$

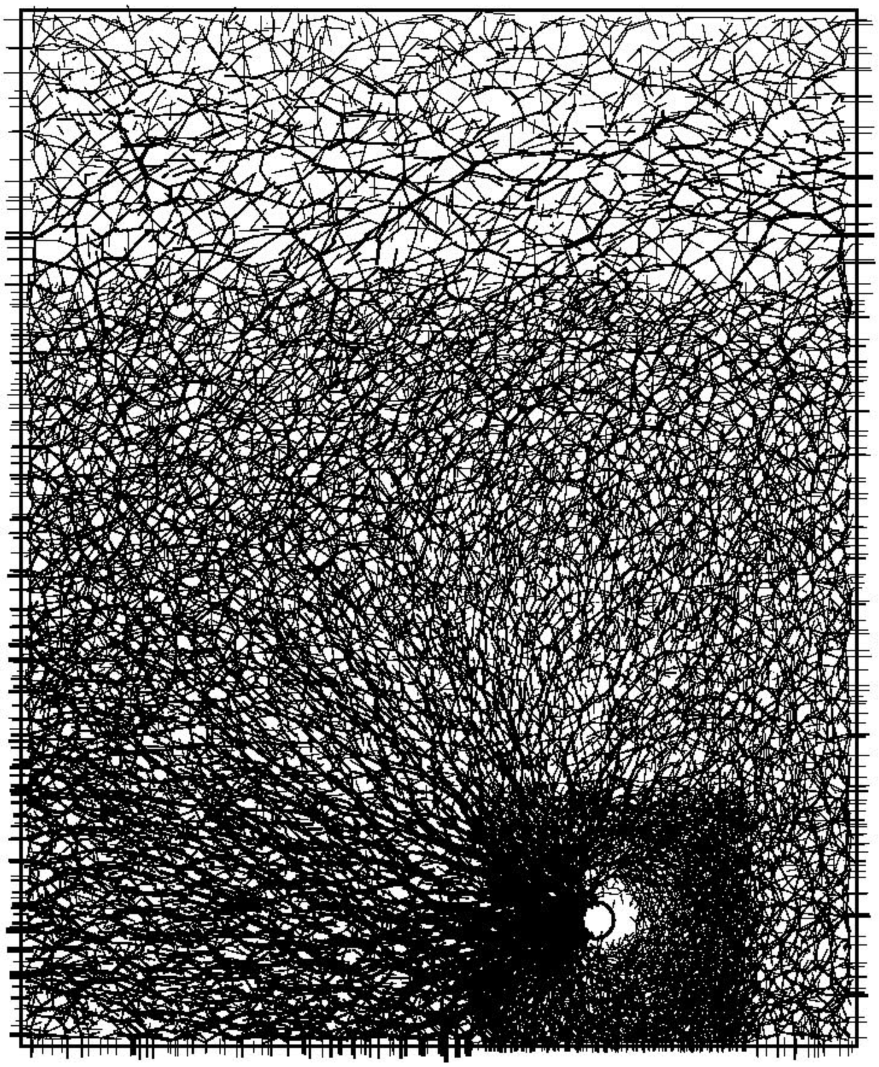

Figure E-18 $H/D = 25$, Dense sand, $\tan \phi_\mu = 3.0$

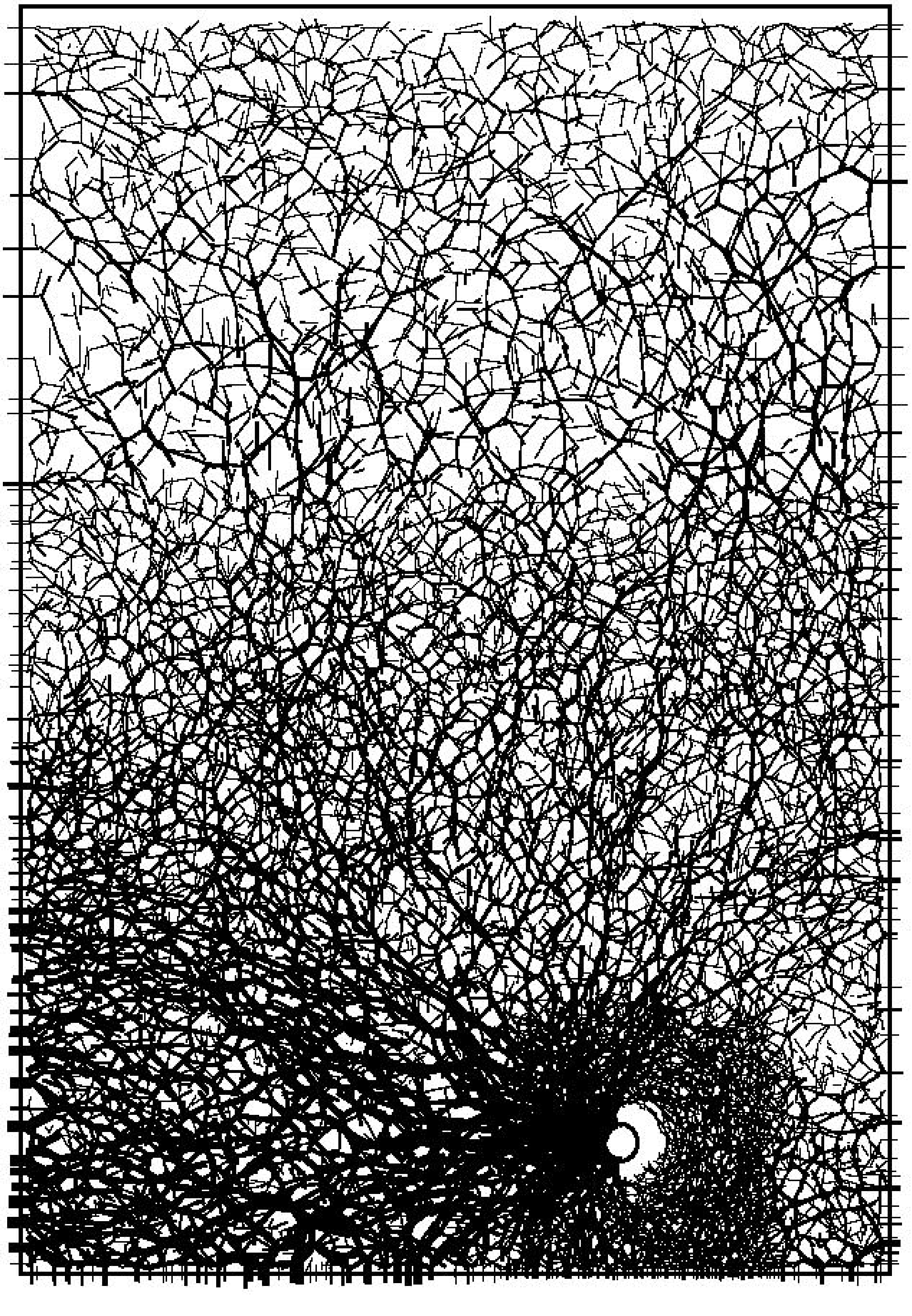

Figure E-19 *H/D* = 30, Medium sand, tan ϕ_μ = 3.0

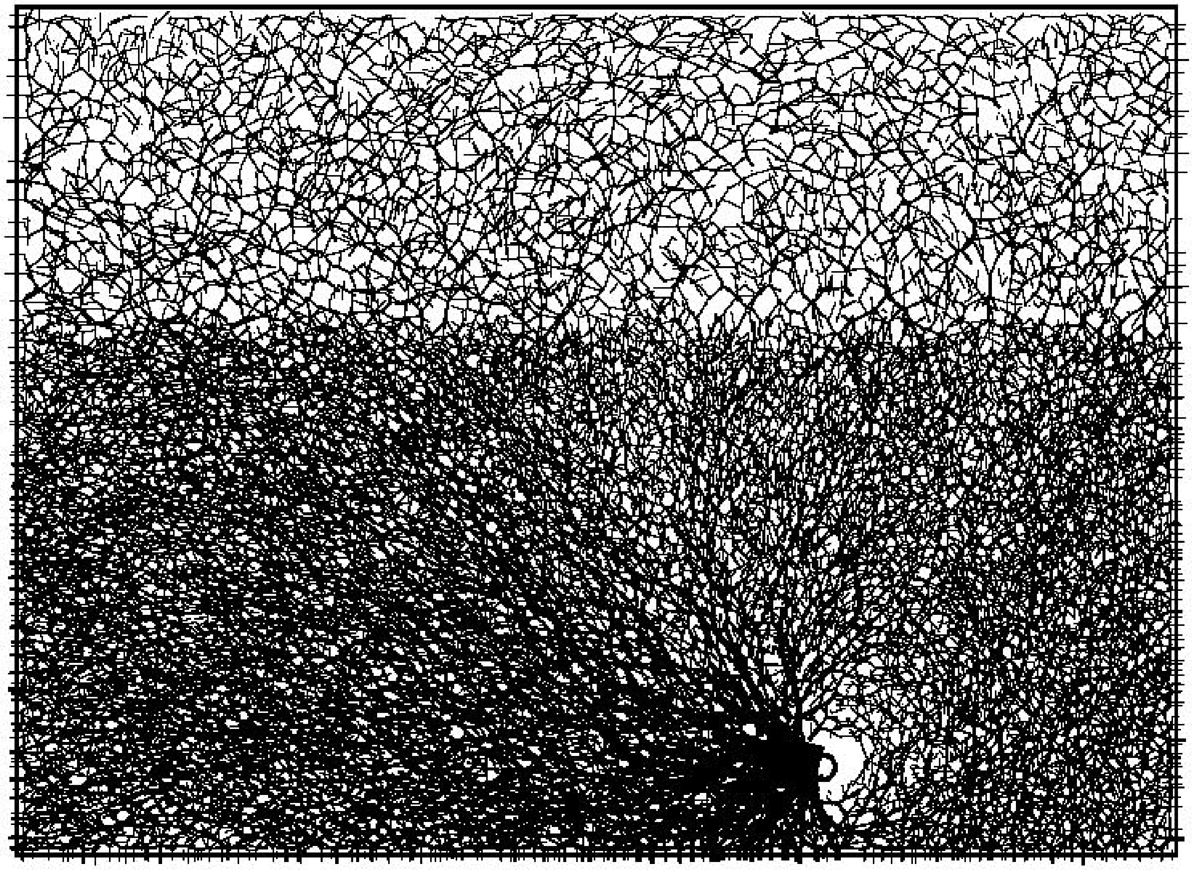

Figure E-20 $H/D = 30$, Dense sand, $\tan \phi_\mu = 3.0$

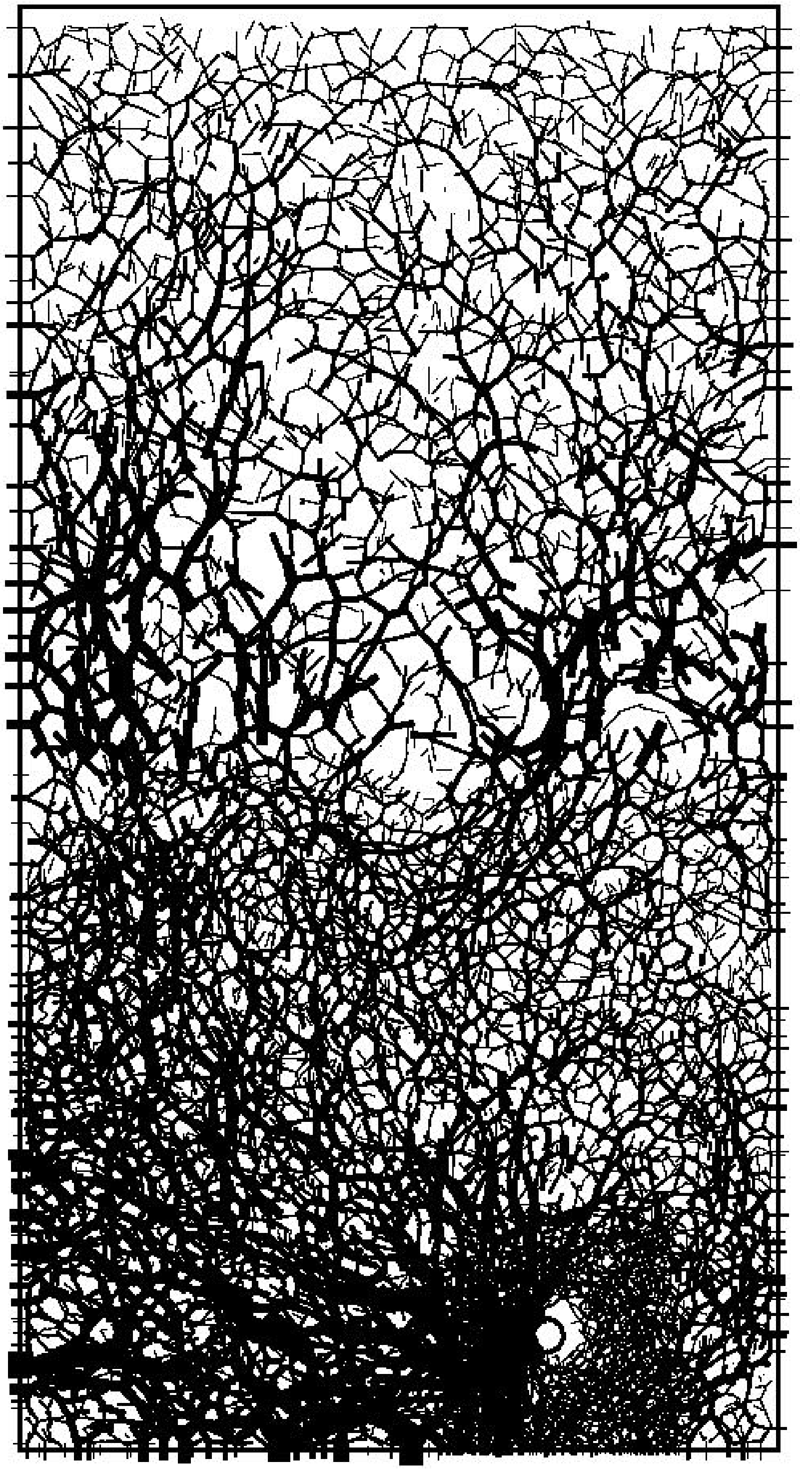

Figure E-21 $H/D = 40$, Medium sand, $\tan \phi_\mu = 3.0$

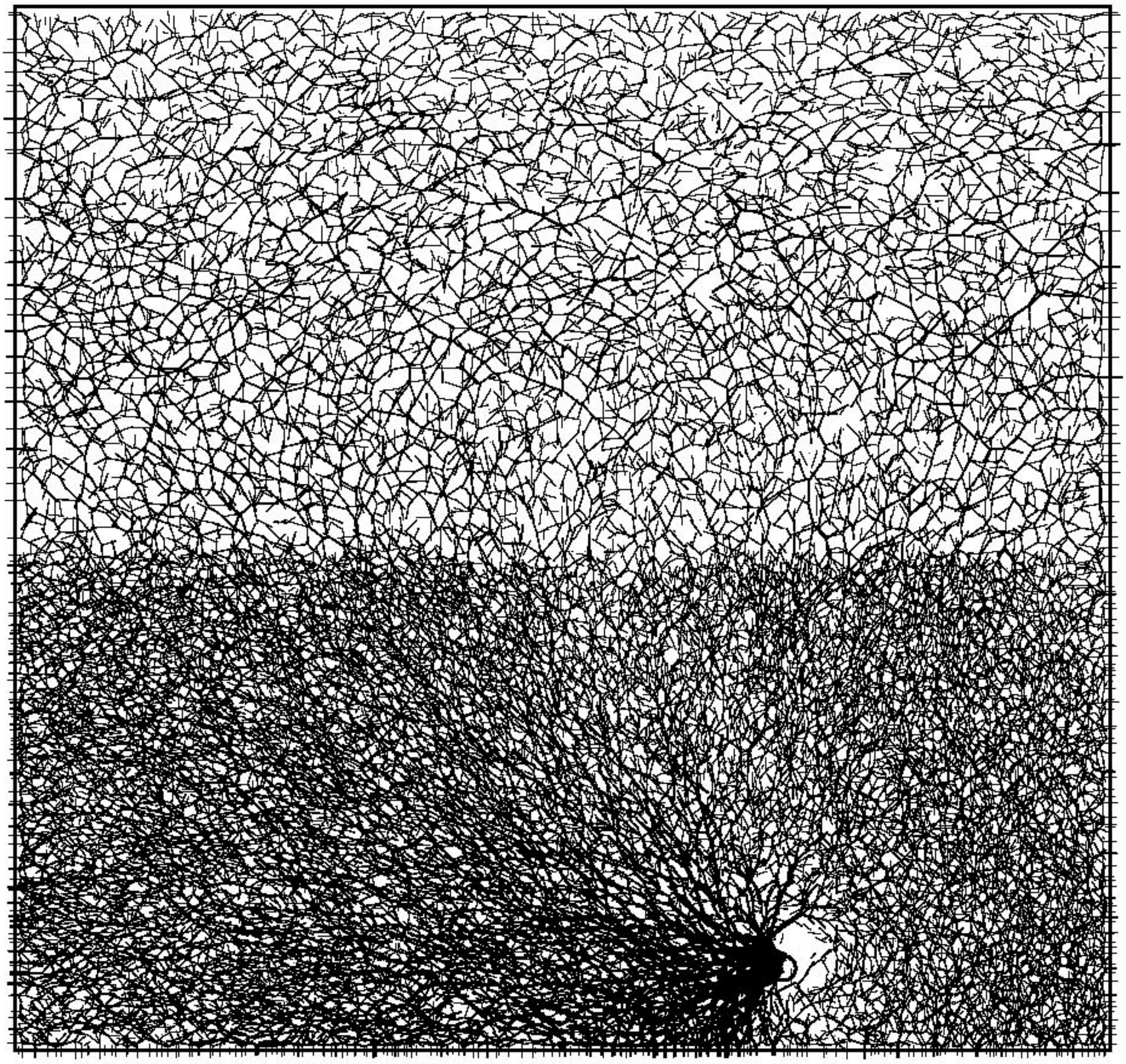

Figure E-22 $H/D = 40$, Dense sand, $\tan \phi_{\mu} = 3.0$

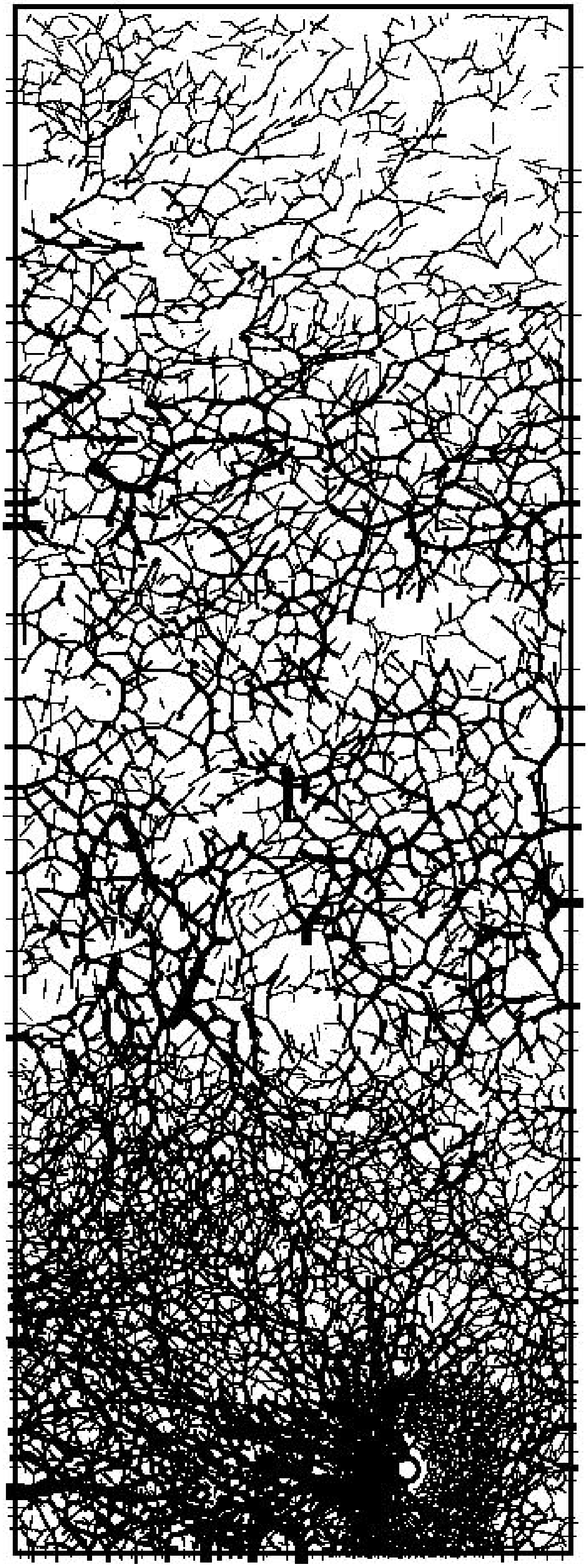

Figure E-23 $H/D = 60$, Medium sand, tan $\phi_\mu = 3.0$

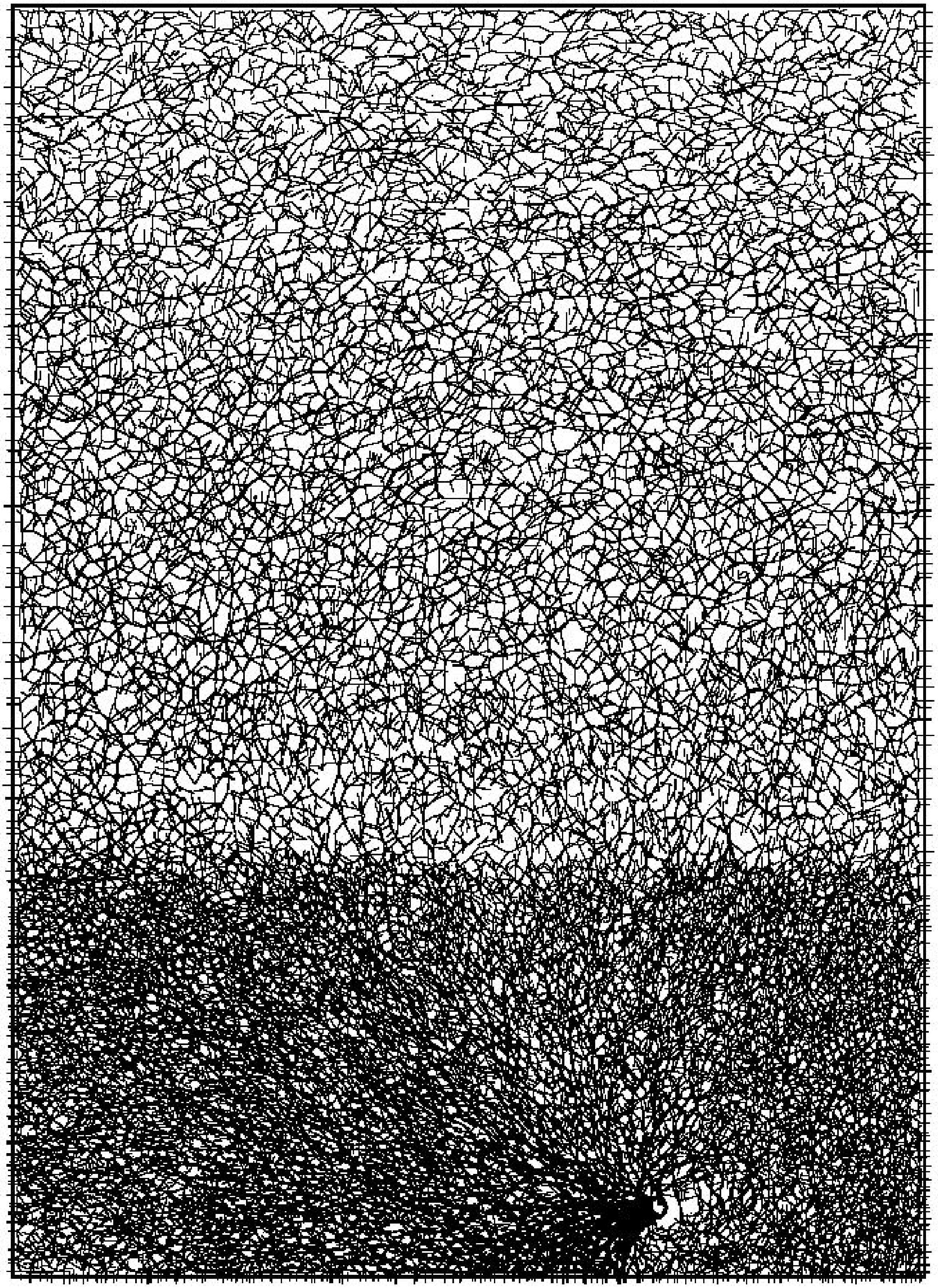

Figure E-24 $H/D = 60$, Dense sand, $\tan \phi_{\mu} = 3.0$

Appendix F

Contact Force Pattern under Upward Loading

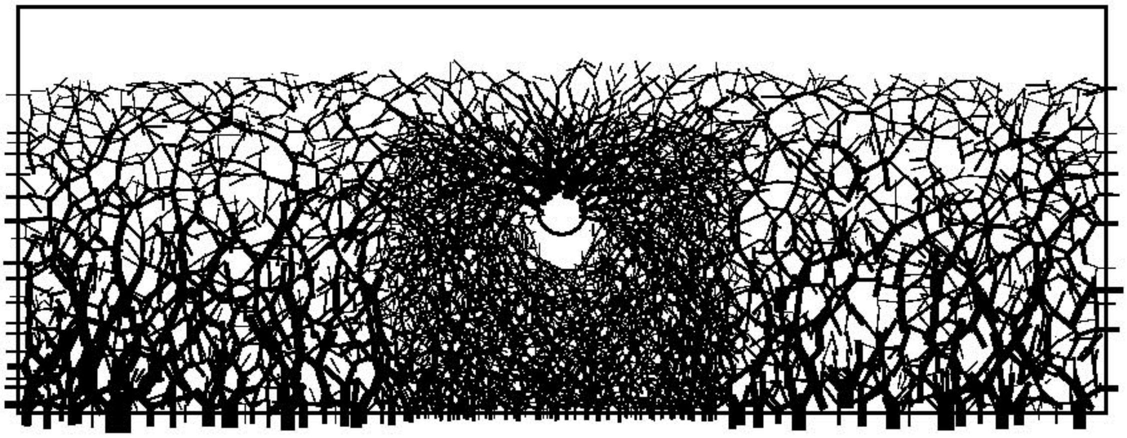

Figure F-1 $H_c/D = 4$, Dense sand, tan $\phi_\mu = 3.0$

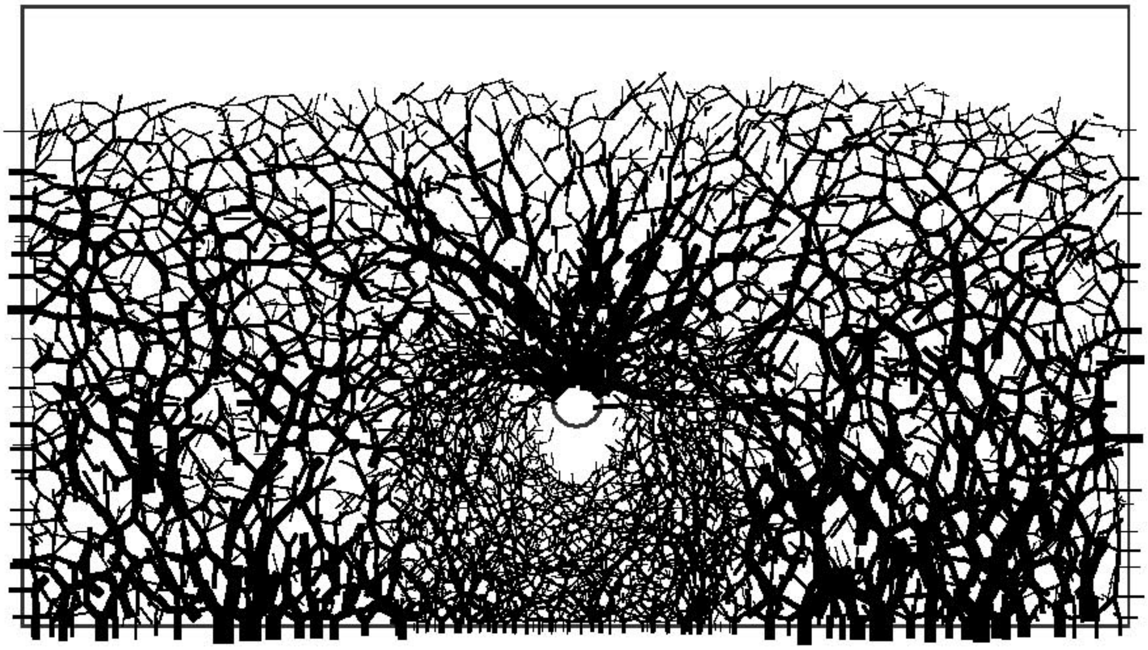

Figure F-2 $H_c/D = 8$, Medium sand, tan $\phi_\mu = 3.0$

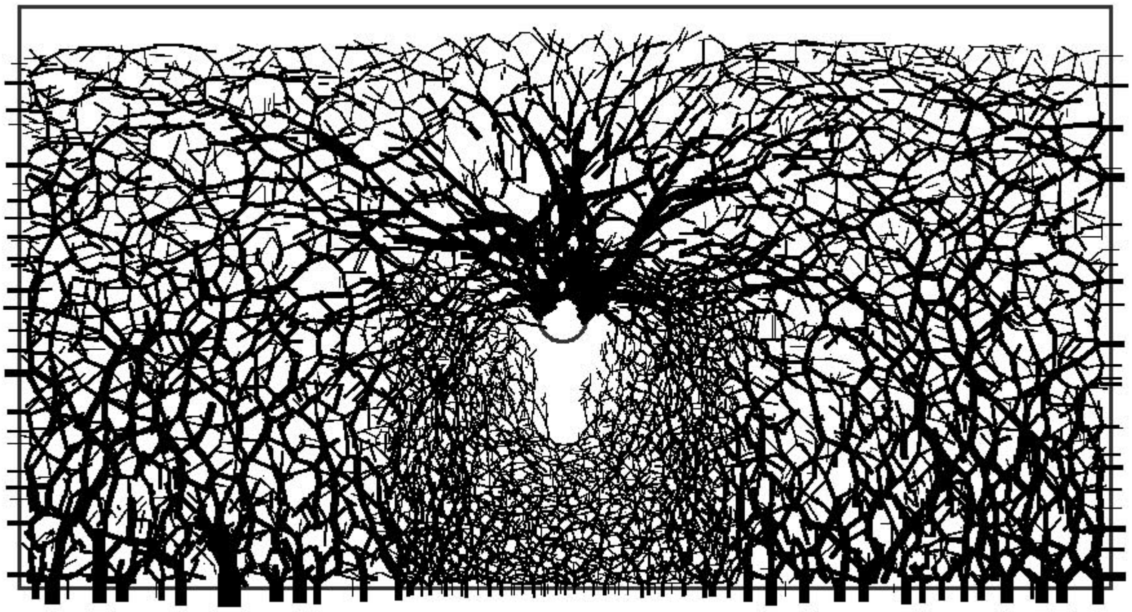

Figure F-3 $H_c/D = 8$, Dense sand, tan $\phi_\mu = 3.0$

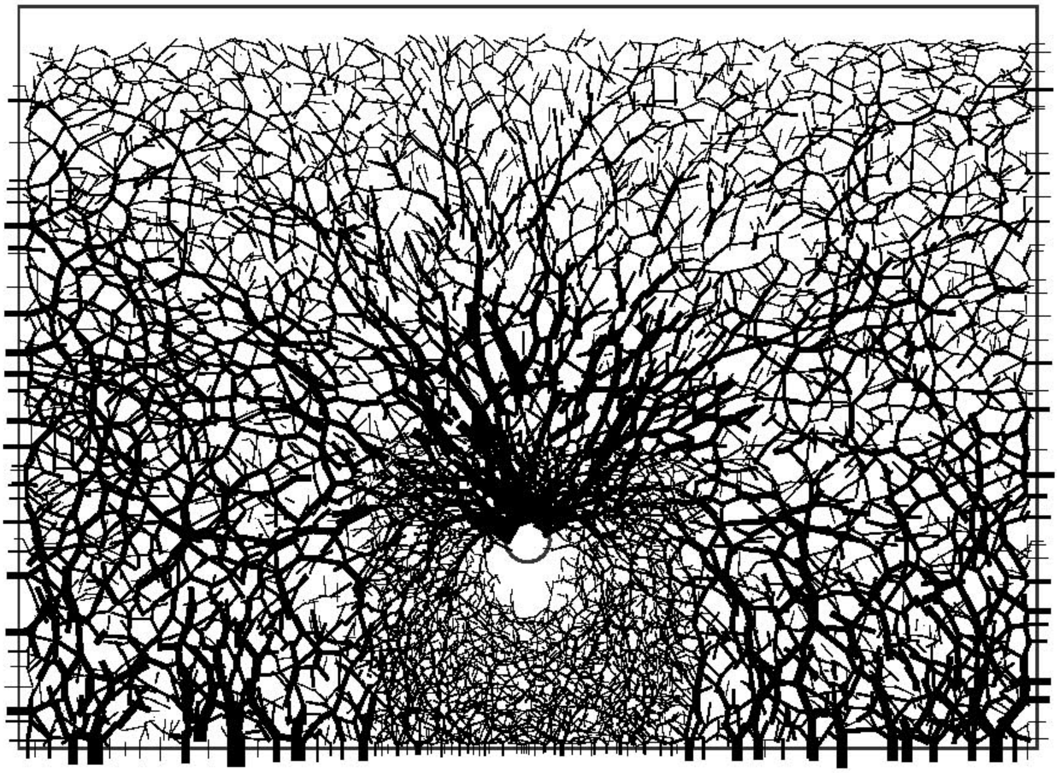

Figure F-4 H_c/D = 13, Medium sand, tan ϕ_μ = 3.0

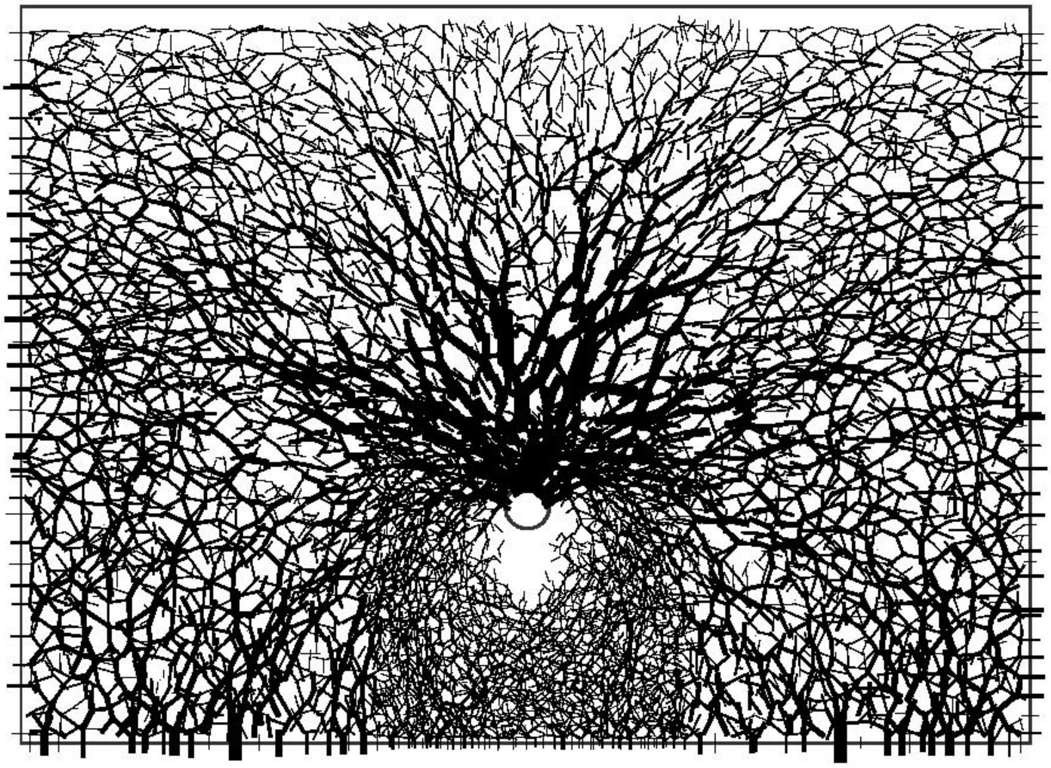

Figure F-5 H_c/D = 13, Dense sand, tan ϕ_μ = 3.0

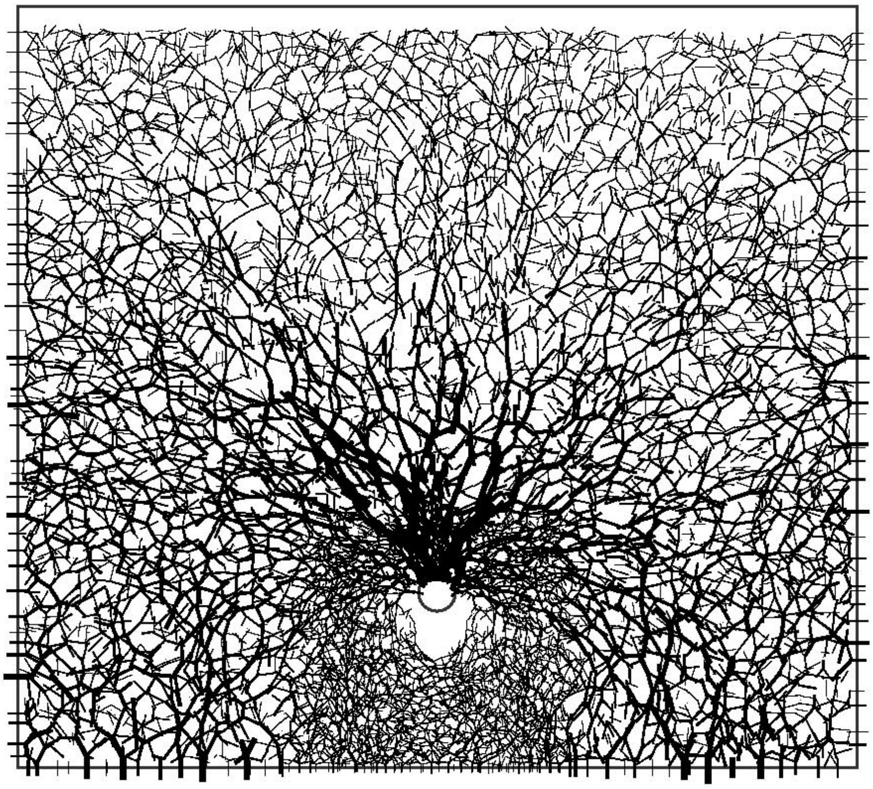

Figure F-6 $H_c/D = 17$, Medium sand, tan $\phi_\mu = 3.0$

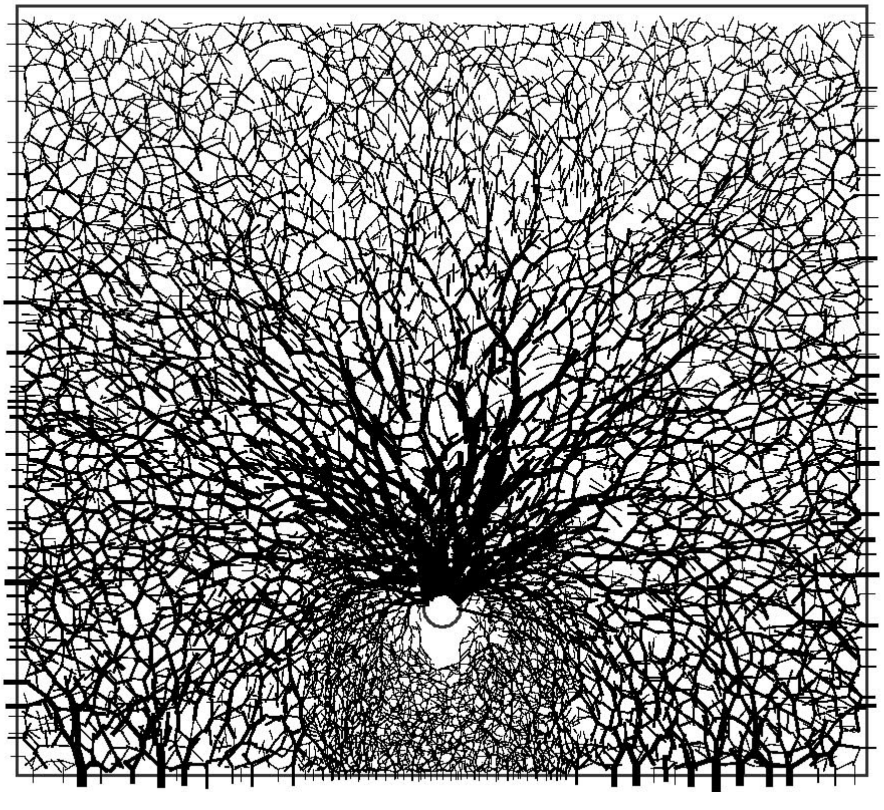

Figure F-7 $H_c/D = 17$, Dense sand, tan $\phi_\mu = 3.0$

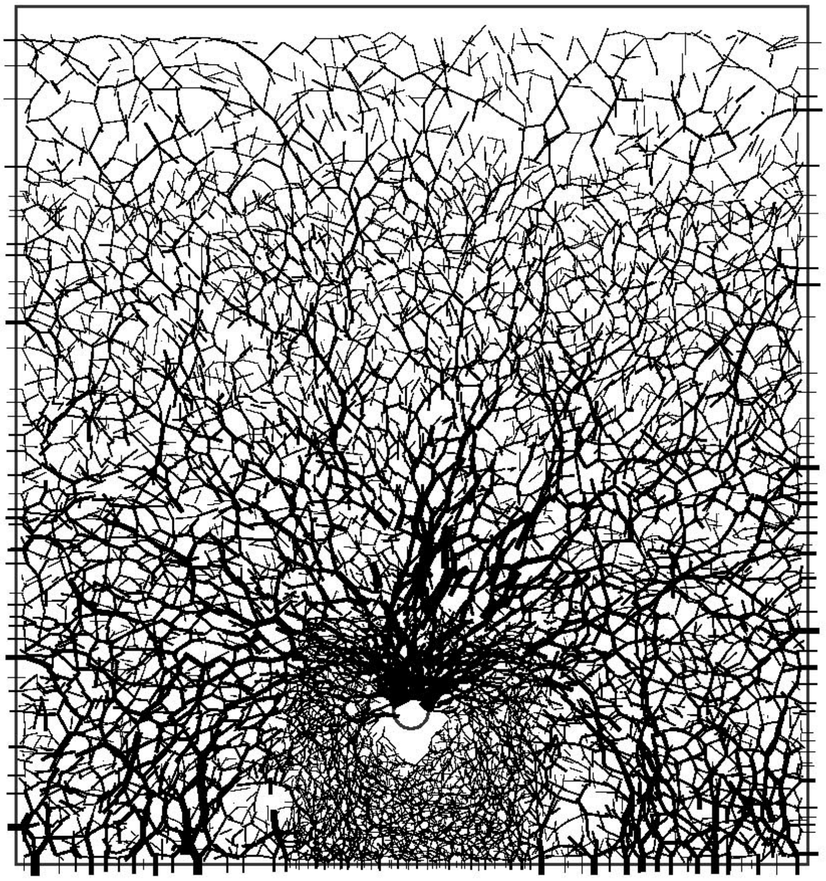

Figure F-8 $H_c/D = 21$, Medium sand, tan $\phi_\mu = 3.0$

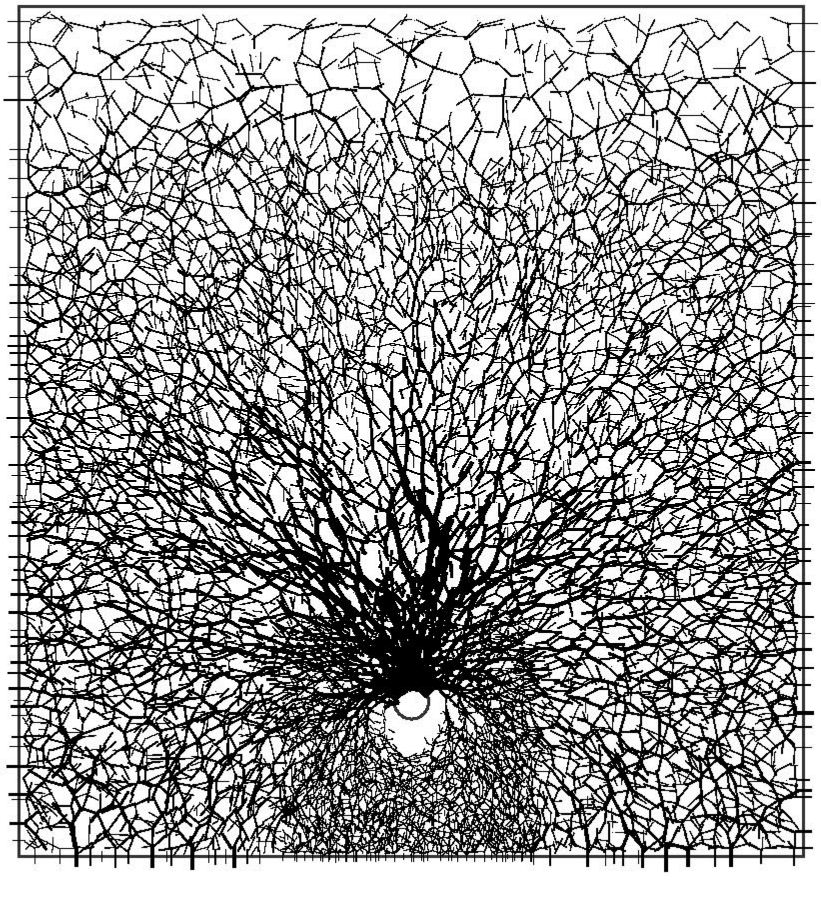

Figure F-9 $H_c/D = 21$, Dense sand, $\tan \phi_\mu = 3.0$

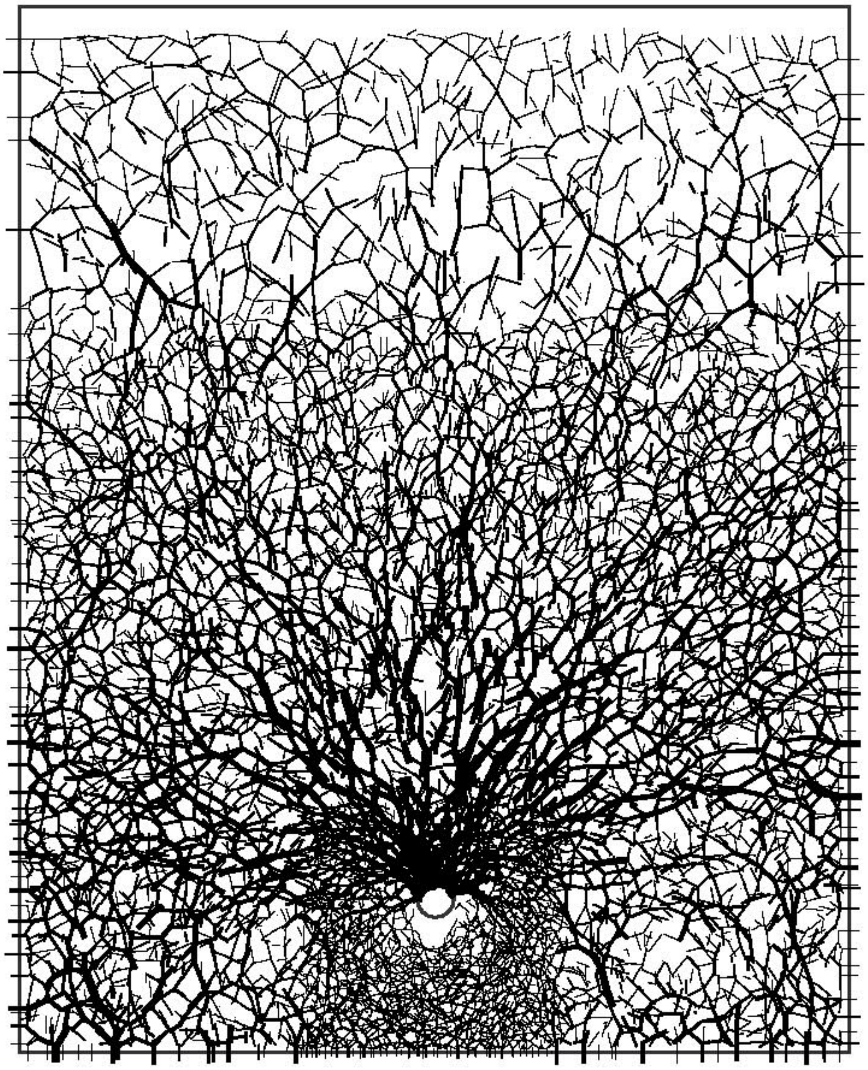

Figure F-10 $H_c/D = 25$, Medium sand, $\tan \phi_\mu = 3.0$

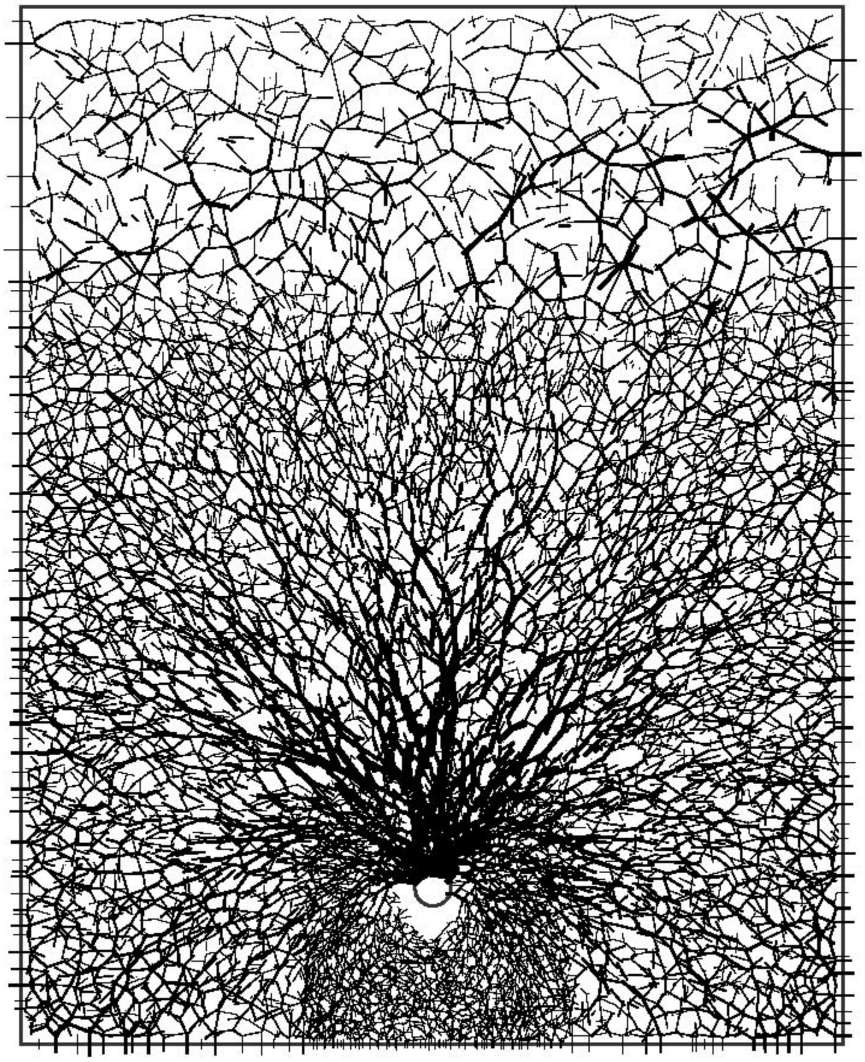

Figure F-11 $H_c/D = 25$, Dense sand, $\tan \phi_\mu = 3.0$

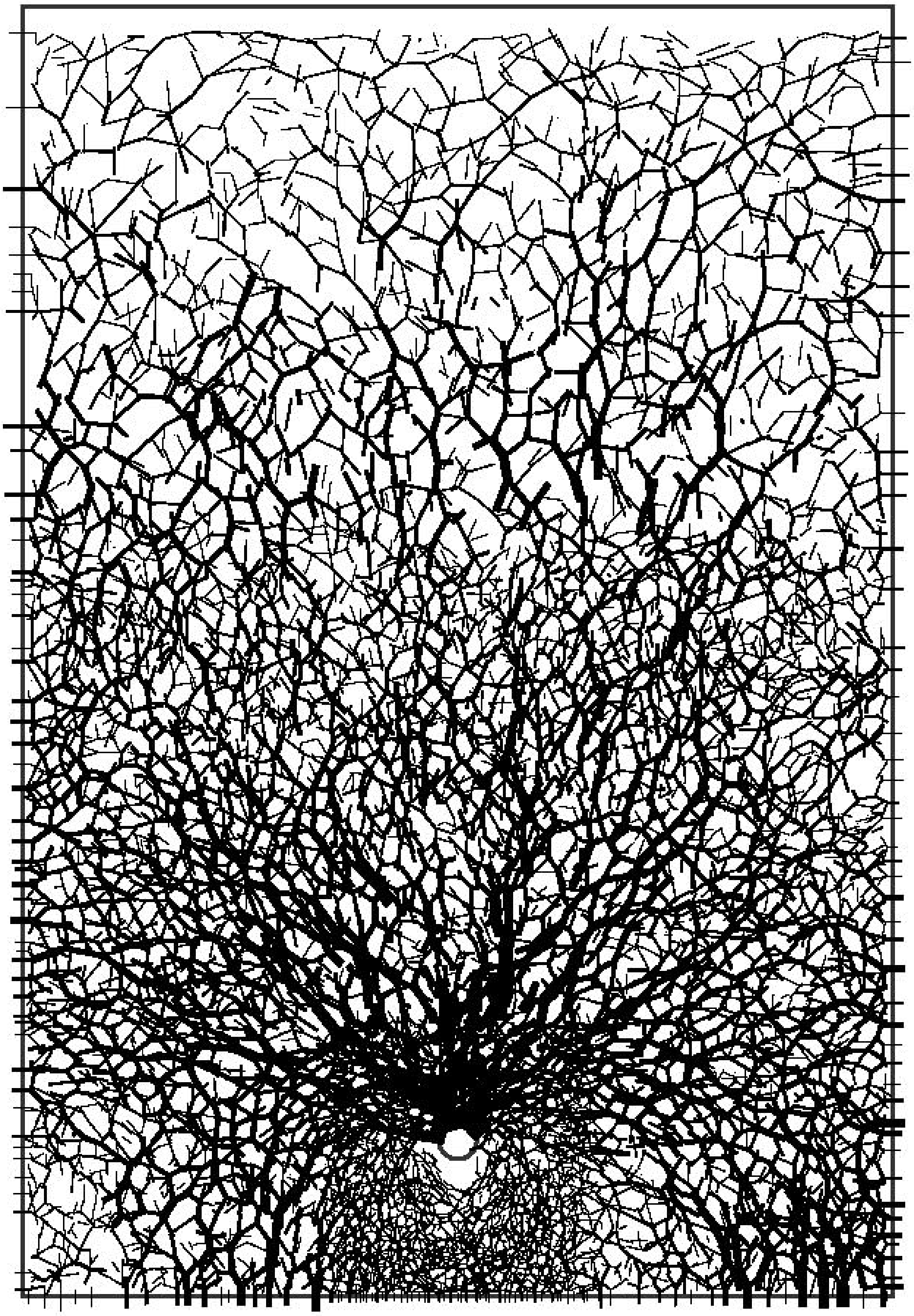

Figure F-12 $H_c/D = 30$, Medium sand, $\tan \phi_\mu = 3.0$

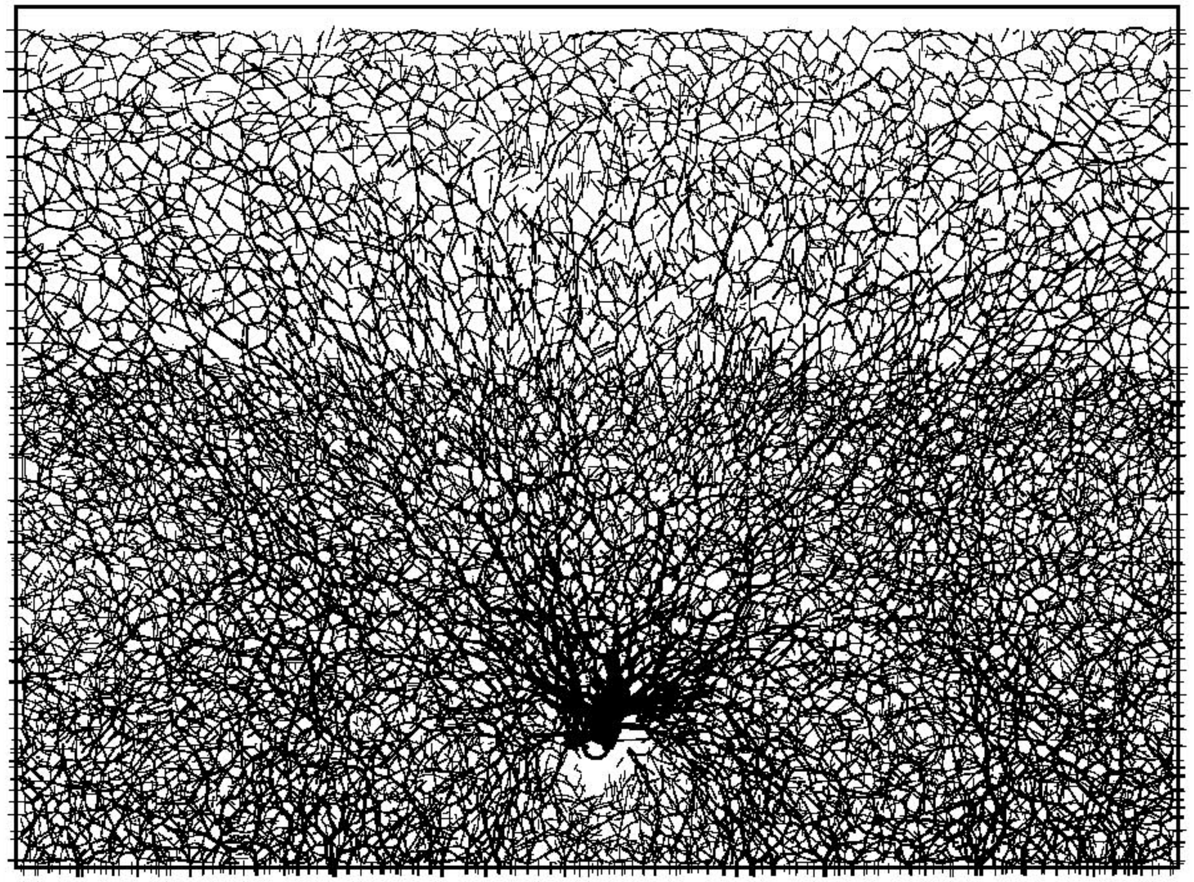

Figure F-13 $H_c/D = 30$, Dense sand, tan $\phi_\mu = 3.0$

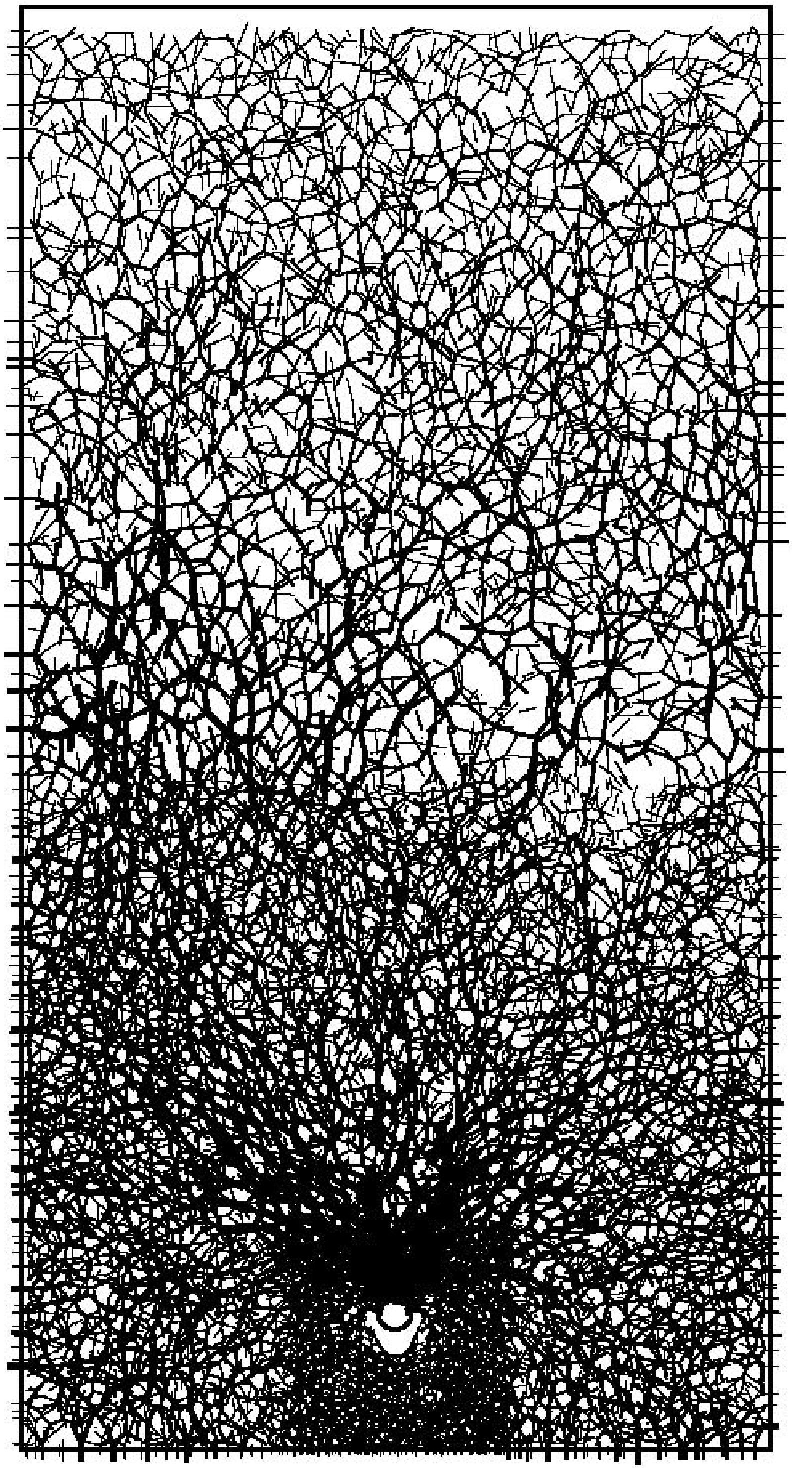

Figure F-14 $H_c/D = 40$, Medium sand, $\tan \phi_\mu = 3.0$

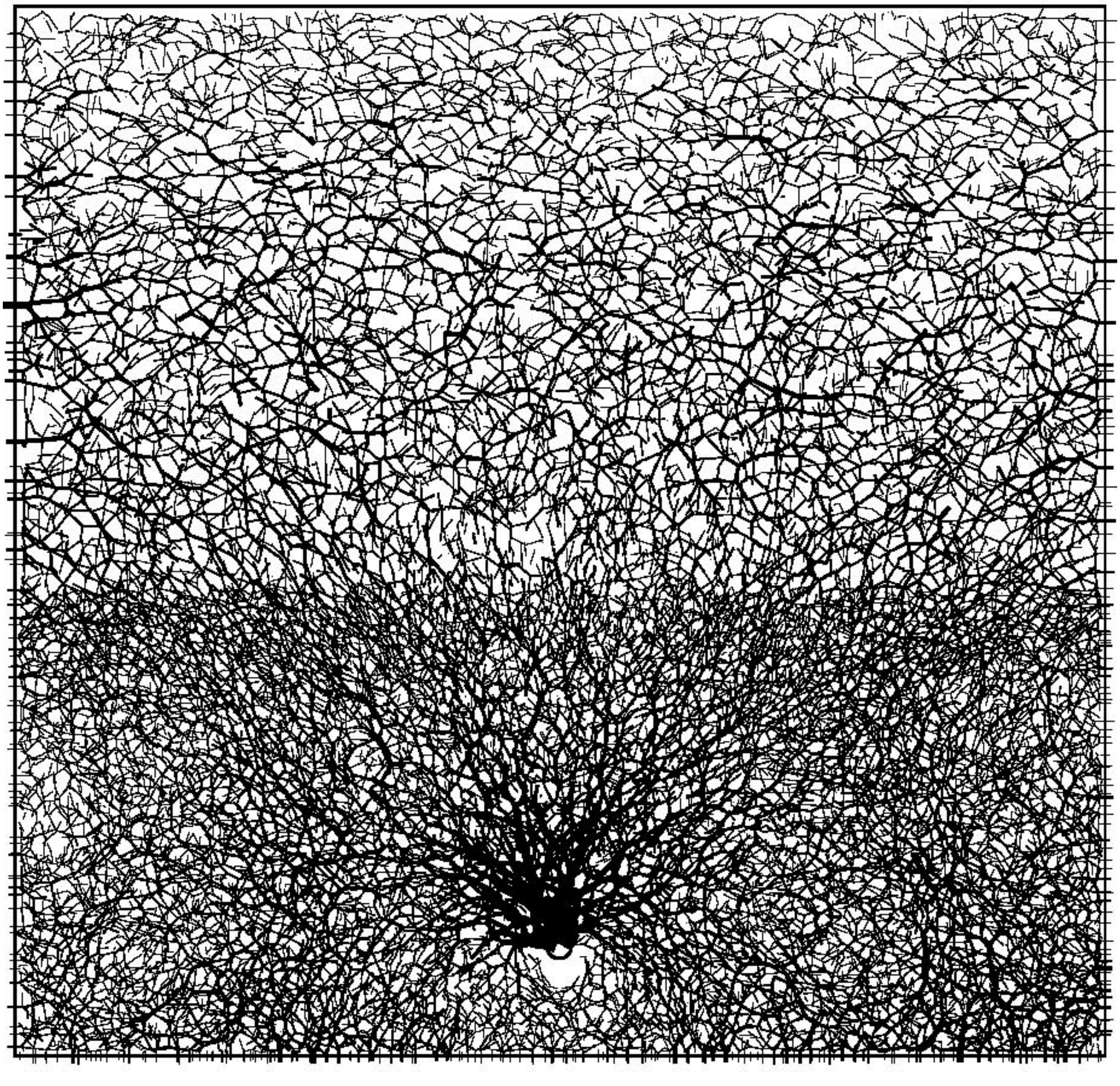

Figure F-15 $H_c/D = 40$, Dense sand, $\tan \phi_\mu = 3.0$

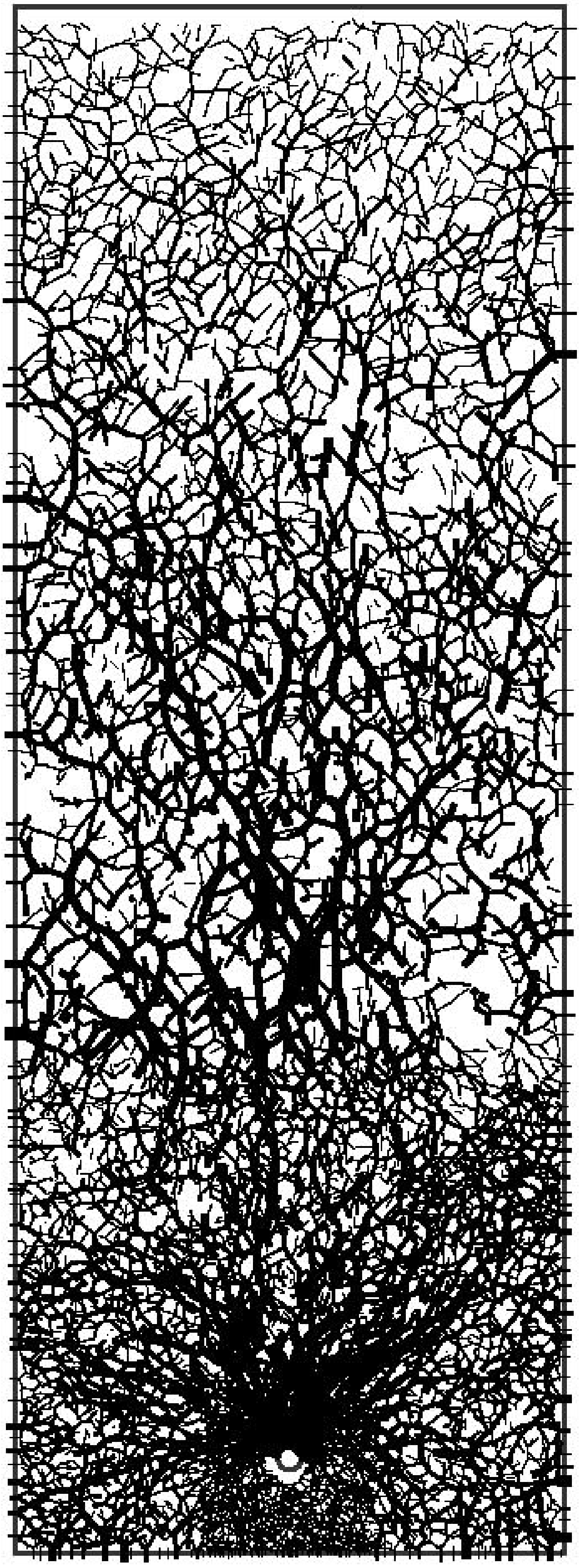

Figure F-16 $H_c/D = 60$, Medium sand, tan $\phi_\mu = 3.0$

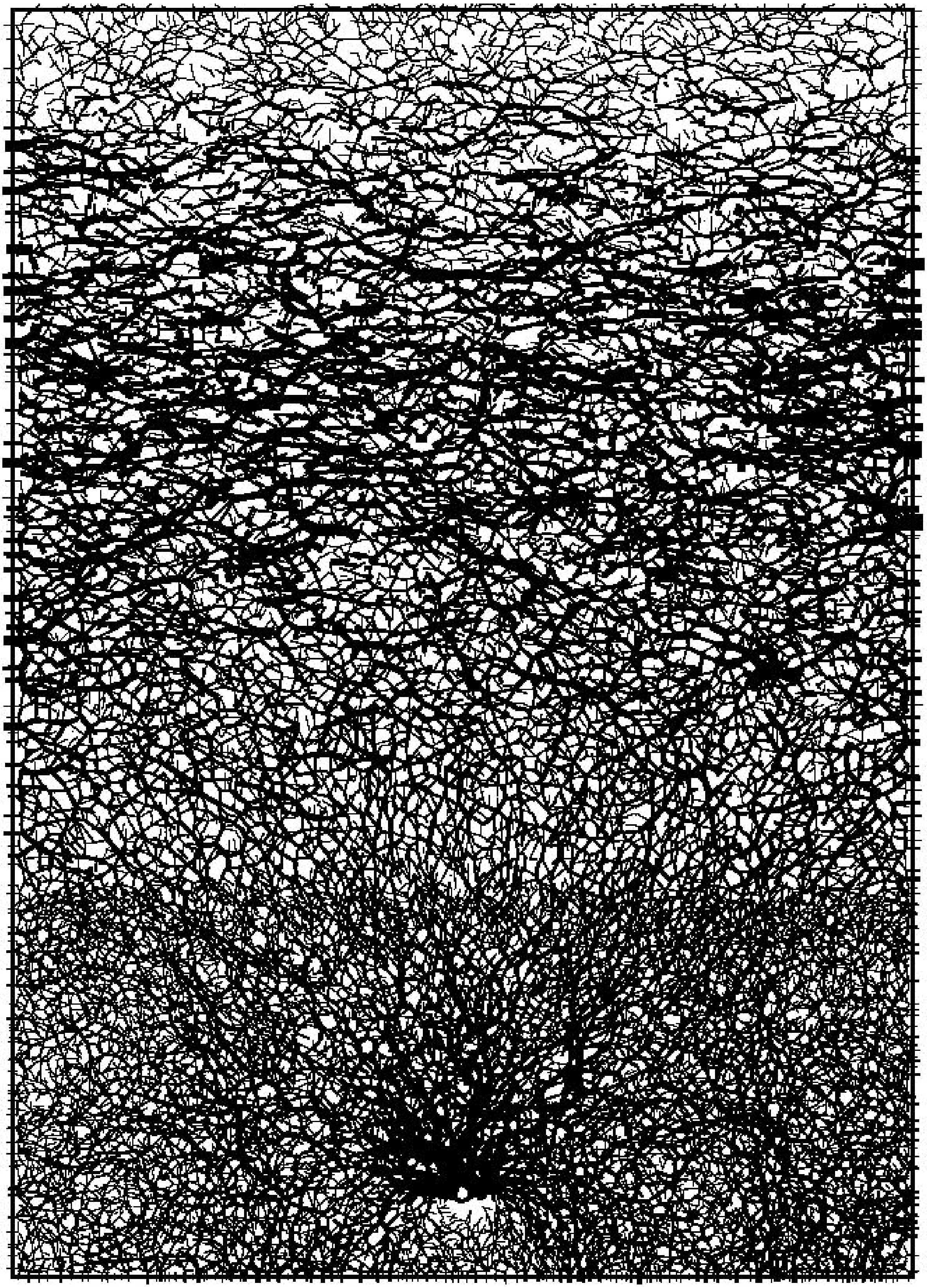

Figure F-17 $H_c/D = 60$, Dense sand, $\tan \phi_\mu = 3.0$

Appendix G

Parametric Study of DEM Simulation of Triaxial Test

Appendix G

Parametric study of DEM simulation of triaxial test

G.1 General

Parametric study was carried out to examine the effects of the key parameters on the DEM simulation of triaxial tests. The results of this study are presented in this appendix.

G.2 DEM simulation of triaxial test

The triaxial test Test D-2 (CIDC) by Turner & Kulhawy (1987) was used as a controlled test for this study. The nonuniform-sized particles contained within six rigid boundary walls were used as a simulated soil specimen. The particle size of sands follows normal distribution with an average diameter of 5 cm and standard deviation of 1 cm. The specimen size is 1 m by 1 m section and 2 m high. The specimen size was chosen to be relatively large compared with the particle size and accommodated 2402 particles. Fig. G-1 shows the specimen before compression shearing stage. Triaxial test are simulated by moving the top and bottom walls at a specified strain-rate while using servo-controlled to maintain specified stress of the side walls. The parameters of interested are (i) normal contact stiffness, (ii) tangential contact stiffness, and (iii) inter-particle friction angle. The detail of each test is shown in Table G-1. The triaxial test results of Test A (control test) are shown in Fig. G-2.

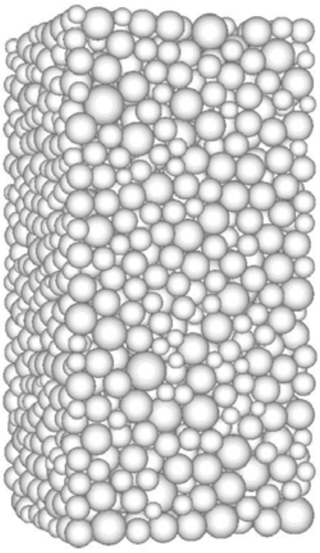

Figure G-1   Specimen before shearing (Test A)

Table G-1 Test details for parametric study

Test No.	p_o' (kPa)	e_o (after consoln)	$k_{N,sand}$ (N/m)	$k_{T,sand}$ (N/m)	tan ϕ_μ	$k_{N,wall}$ (N/m)
Test A*	69	0.490	1.0×10^6	1.0×10^6	1.0	1.0×10^5
Test B	69	0.541	1.0×10^7	1.0×10^6	1.0	1.0×10^5
Test C	69	0.513	1.0×10^6	1.0×10^7	1.0	1.0×10^5
Test D	69	0.497	1.0×10^6	1.0×10^6	5.0	1.0×10^5

Note: tan ϕ_{wall} = 0.0
$k_{T,wall}$ = 0.0
* control test

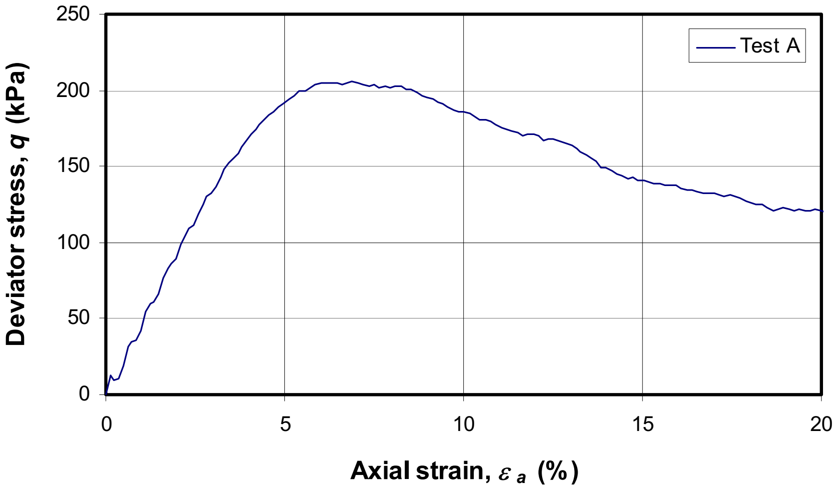

(a) Stress-strain relationship

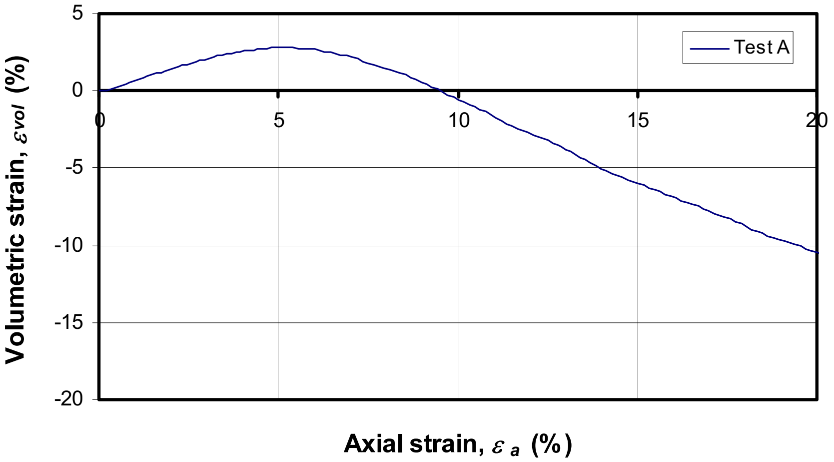

(b) Volumetric strain – axial strain relationship

Figure G-2 Control test (Test A)

G-3 Effects of normal contact stiffness

The effects of normal contact stiffness on triaxial test results are shown in Fig. G-3 by comparing the results of Test A ($k_{N,sand} = 1.0 \times 10^6$ N/m) with Test B ($k_{N,sand} = 1.0 \times 10^7$ N/m). The results show that the normal contact stiffness affects the stiffness from triaxial test without affecting the strength. Fig. G-3(a) shows that, as the normal contact stiffness increases, the stiffness from triaxial test also increases, as can be seen that the slope of the stress-strain curve before failure becomes steeper, with relatively unchanged in peak strength. The strength from Test B is slightly smaller than that from Test A because Test B has slightly larger void ratio (see Table G-1). Fig. G-3(b) shows that, as the normal contact stiffness increases, the specimen becomes more dilative.

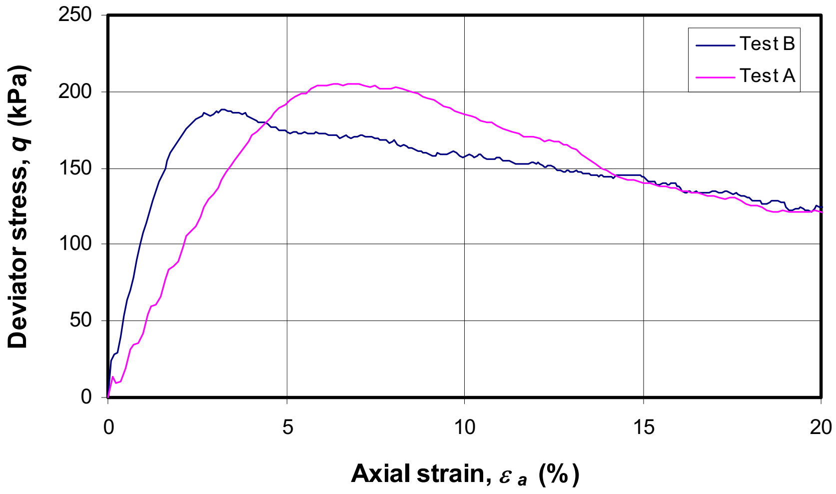

(a) Stress-strain relationship

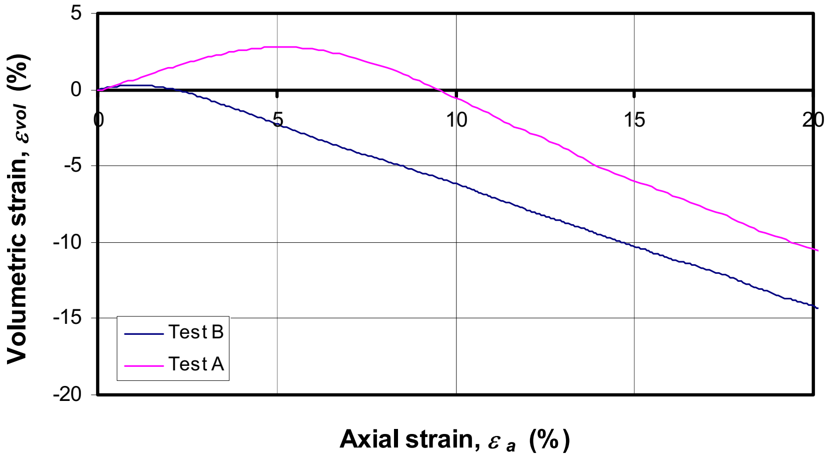

(b) Volumetric strain – axial strain relationship

Figure G-3 Effects of normal contact stiffness

G-4 Effects of tangential contact stiffness

The effects of tangential contact stiffness on triaxial test results are shown in Fig. G-4 by comparing the results of Test A ($k_{T,sand} = 1.0 \times 10^6$ N/m) with Test C ($k_{T,sand} = 1.0 \times 10^7$ N/m). The results show that the change in tangential contact stiffness (within the range studied) has negligible effects on the triaxial test results for both strength and volume change behavior.

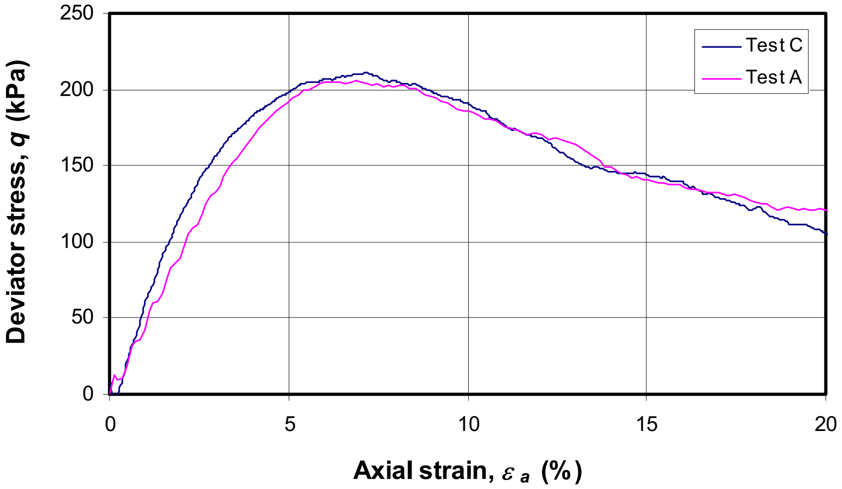

(a) Stress-strain relationship

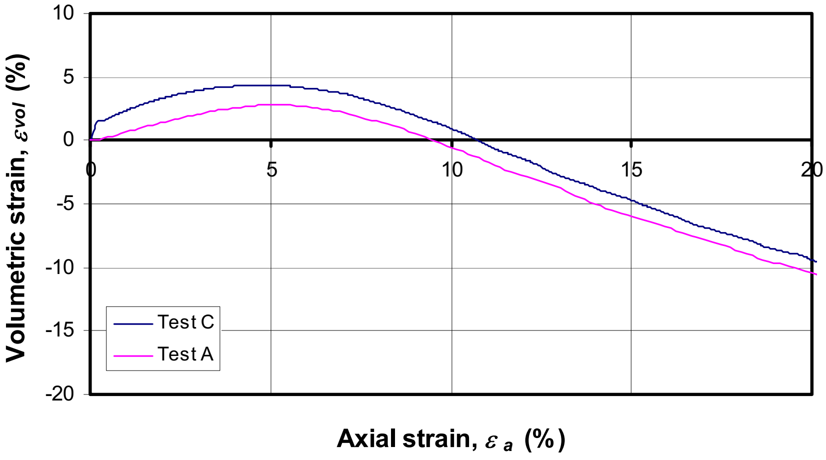

(b) Volumetric strain – axial strain relationship

Figure G-4   Effects of tangential contact stiffness

G-5 Effects of inter-particle friction angle

The effects of inter-particle friction angle on triaxial test results are shown in Fig. G-5 by comparing the results of Test A (tan $\phi_\mu = 1.0$ or $\phi_\mu = 45°$) with Test D (tan $\phi_\mu = 5.0$ or $\phi_\mu = 79°$). Fig. G-5(a) shows that the inter-particle friction angle affects the strength from triaxial test without affecting the stiffness. As the inter-particle friction angle increases, the peak strength becomes larger with relatively unchanged in triaxial stiffness, as can be seen from the unchanged slope of the stress-strain curve before failure. Fig. G-5(b) shows that the inter-particle friction angle does not show obvious effects on the volume change behavior. As the inter-particle friction angle increases, the dilation behavior is still unchanged at small strain, becomes less dilative (more compressive) at intermediate strain, and becomes more dilative at large strain.

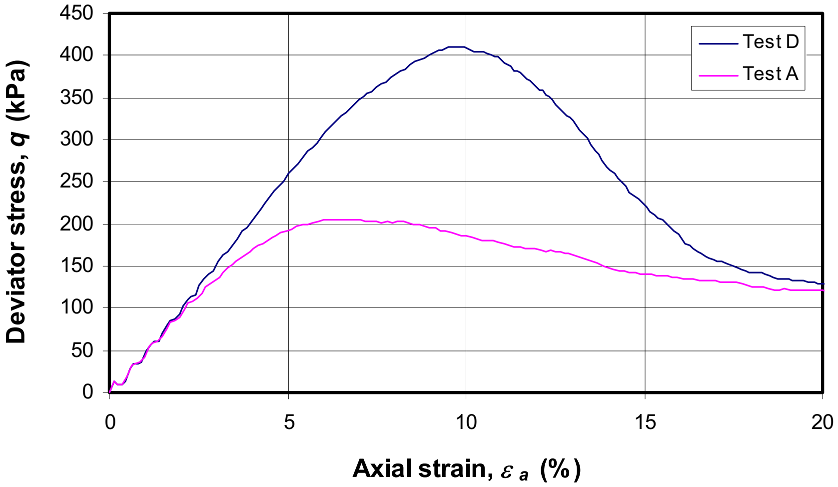

(a) Stress-strain relationship

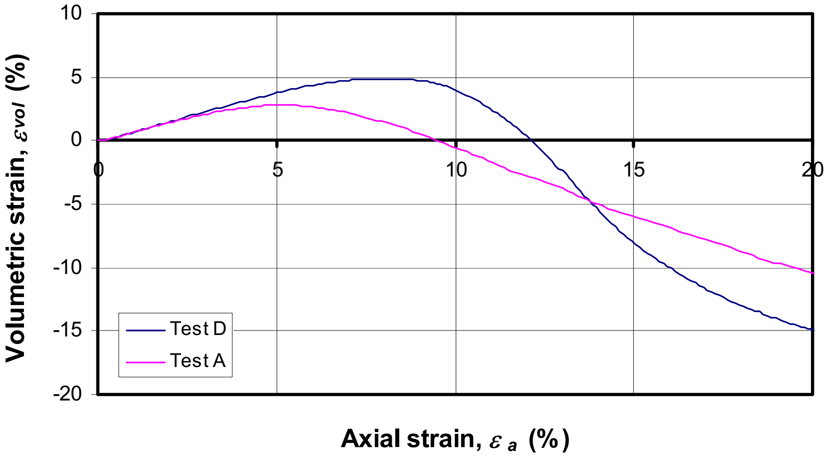

(b) Volumetric strain – axial strain relationship

Figure G-5 Effects of inter-particle friction angle

G-6 Summary

The results of the parametric study can be summarized as shown in Table G-2.

Table G-2 Results of parametric study of triaxial test

Microscopic parameters	Effects on macroscopic parameters when the values of microscopic parameter increases		
	Triaxial stiffness	Triaxial strength	Dilation
Normal contact stiffness	↑	—	↑
Tangential contact stiffness	—	—	—
Inter-particle friction angle	—	↑	inconclusive

where — = negligible change
↑ = increase
↓ = decrease

Appendix H

Parametric Study of DEM Simulation of Lateral Pipe Loading

Appendix H

Parametric study of DEM simulation of lateral pipe loading

H.1 General

Parametric studies were carried out to examine the effects of key parameters on the DEM analysis results of lateral pipe loading. The case of medium sand with *H/D* = 11.5 was selected for a parametric study. The parameters investigated include normal contact stiffness of particle, tangential contact stiffness of particle, inter-particle friction angle, normal contact stiffness of pipe, tangential contact stiffness of pipe, pipe surface friction angle, pipe pulling velocity, and extent of fine particles. The input parameters for the parametric study are shown in Table H-1. The DEM analysis result of the control test is shown in Figure H-1.

Table H-1 Input parameters for parametric study of lateral pipe loading

Parameters	**Test A***	**Test B**	**Test C**	**Test D**	**Test E**	**Test F**	**Test G**	**Test H**	**Test I**
Particle normal contact stiffness, $k_{N,sand}$ (N/m)	5.0×10^5	2.5×10^6	5.0×10^5	5.0×10^5	5.0×10^5	5.0×10^5	5.0×10^5	5.0×10^5	5.0×10^5
Particle tangential contact stiffness, $k_{T,sand}$ (N/m)	5.0×10^5	5.0×10^5	2.5×10^6	5.0×10^5	5.0×10^5	5.0×10^5	5.0×10^5	5.0×10^5	5.0×10^5
Inter-particle friction angle, tan ϕ_μ	1.0	1.0	1.0	3.0	1.0	1.0	1.0	1.0	1.0
Pipe normal contact stiffness, $k_{N,pipe}$ (N/m)	5.0×10^5	5.0×10^5	5.0×10^5	5.0×10^5	2.5×10^6	5.0×10^5	5.0×10^5	5.0×10^5	5.0×10^5
Pipe tangential contact stiffness, $k_{T,pipe}$ (N/m)	5.0×10^5	5.0×10^5	5.0×10^5	5.0×10^5	5.0×10^5	2.5×10^6	5.0×10^5	5.0×10^5	5.0×10^5
Pipe surface friction, tan ϕ_{pipe}	0.41	0.41	0.41	0.41	0.41	0.41	1.0	0.41	0.41
Pipe pulling velocity, V (m/s)	0.3	0.3	0.3	0.3	0.3	0.3	0.3	0.15	0.3
Extent of fine particles (as shown in Fig. 4-3)	✓	✓	✓	✓	✓	✓	✓	✓	✗

* control test

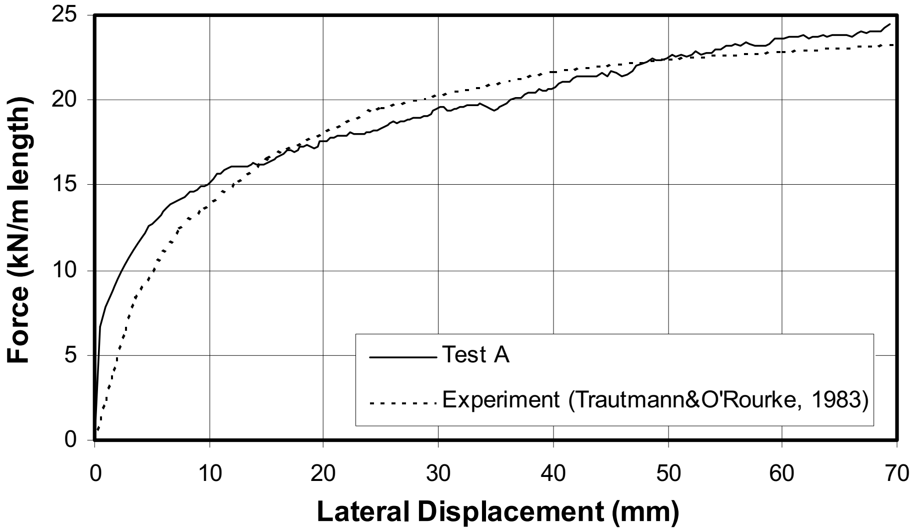

(a) Force – displacement relationship

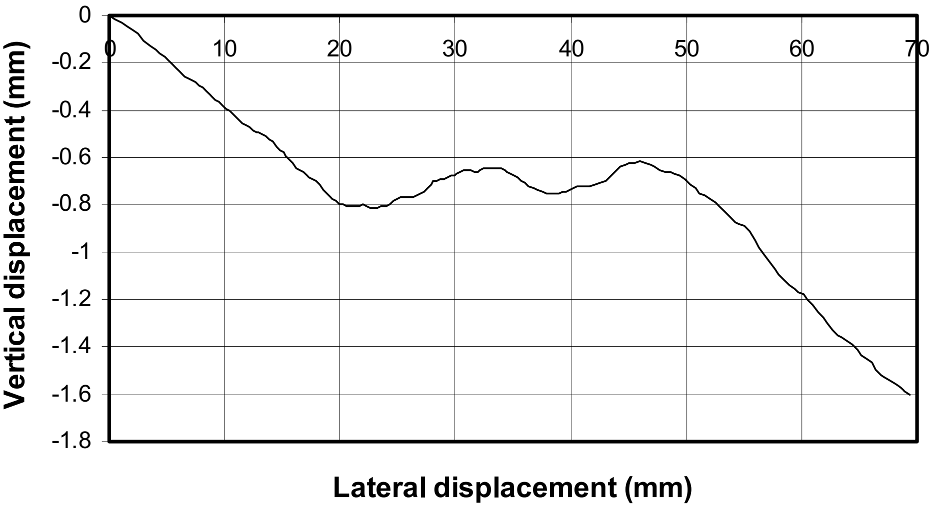

(b) Vertical –lateral displacement relationship

Figure H-1 Control test (Test A)

H-2 Effects of particle normal contact stiffness

The effects of particle normal contact stiffness on lateral pipe loading results are shown in Fig. H-2 by comparing the results of Test A ($k_{N,sand} = 5.0 \times 10^5$ N/m) with Test B ($k_{N,sand} = 2.5 \times 10^6$ N/m (increased by 5 times)). The results show that the peak force becomes larger as the particle normal contact stiffness increases. This is contrary to the effects of particle contact stiffness on the triaxial test results which show that contact stiffness affects only stiffness (modulus) but not strength (see Appendix G). This may be due to the more complex mode of shearing in pipe loading problem.

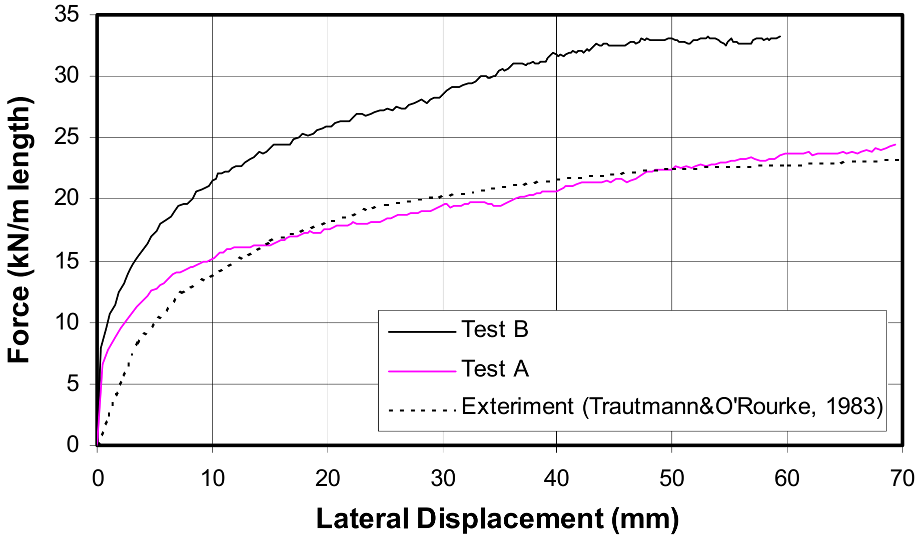

(a) Force – displacement relationship

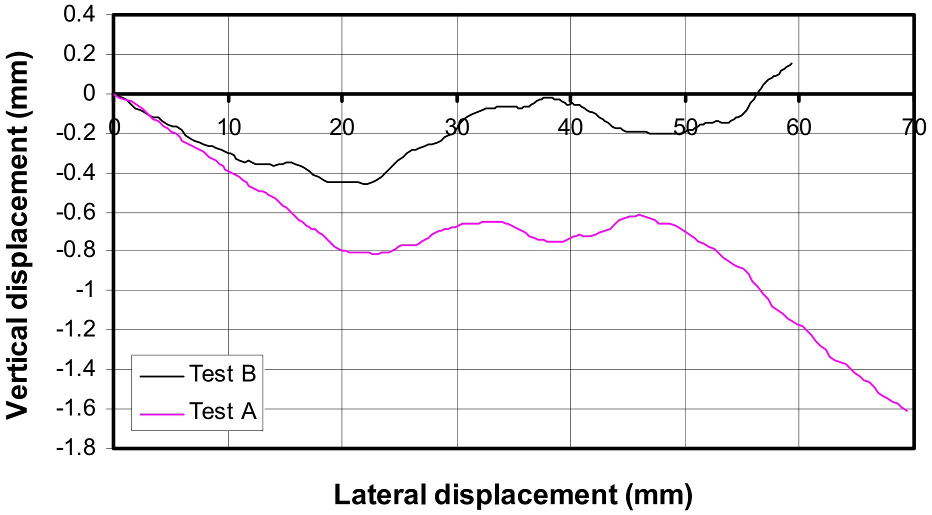

(b) Vertical –lateral displacement relationship

Figure H-2 Effects of particle normal contact stiffness

H-3 Effects of particle tangential contact stiffness

The effects of particle tangential contact stiffness on lateral pipe loading results are shown in Fig. H-3 by comparing the results of Test A ($k_{T,sand} = 5.0 \times 10^5$ N/m) with Test C ($k_{T,sand} = 2.5 \times 10^6$ N/m (increased by 5 times)). The results show that the change in particle tangential contact stiffness (within the range studied) has minimal effects on the lateral pipe loading results.

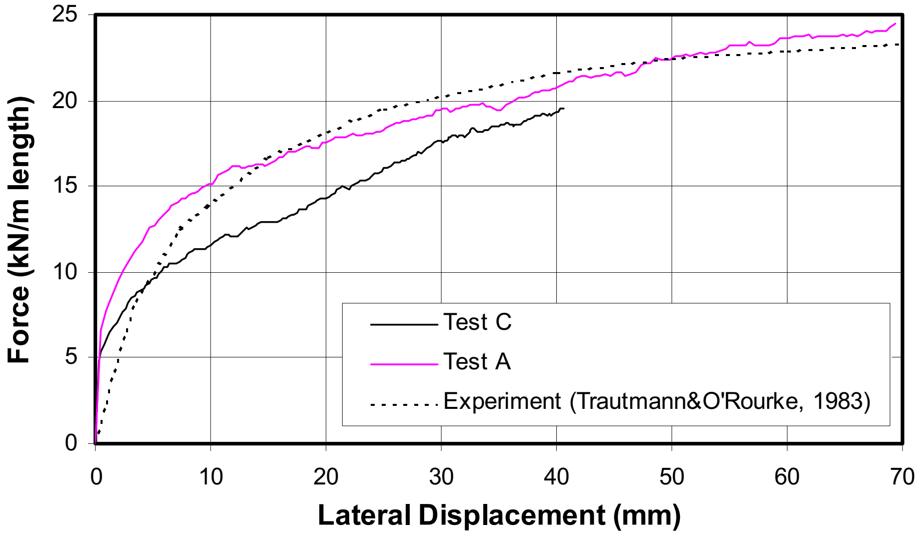

(a) Force – displacement relationship

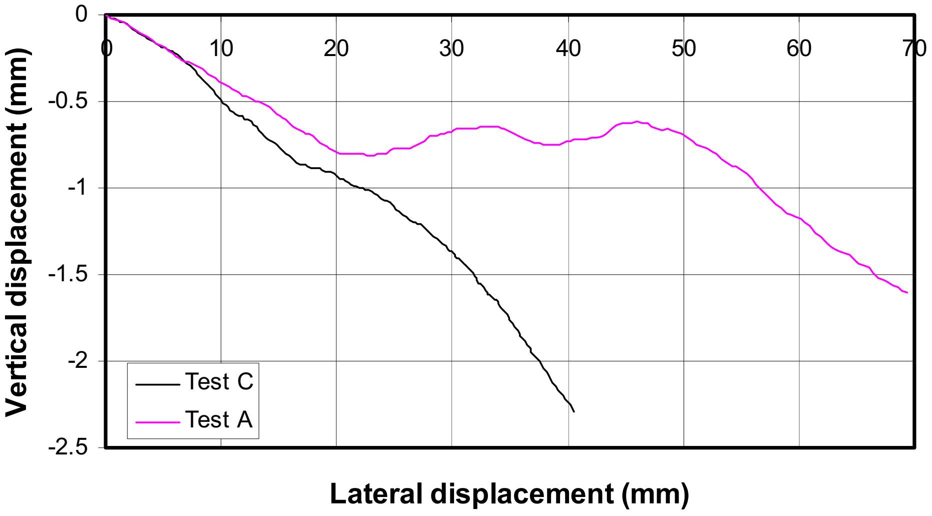

(b) Vertical –lateral displacement relationship

Figure H-3 Effects of particle tangential contact stiffness

H-4 Effects of inter-particle friction angle

The effects of inter-particle friction angle on lateral pipe loading results are shown in Fig. H-4 by comparing the results of Test A (tan $\phi_\mu = 1.0$ or $\phi_\mu = 45°$) with Test D (tan $\phi_\mu = 3.0$ or $\phi_\mu = 72°$). The results show that the peak force becomes larger as the inter-particle friction angle increases. This is consistent with the effects of inter-particle friction angle on triaxial test results which show that an increase in the inter-particle friction angle yields an increase in strength (see Appendix G).

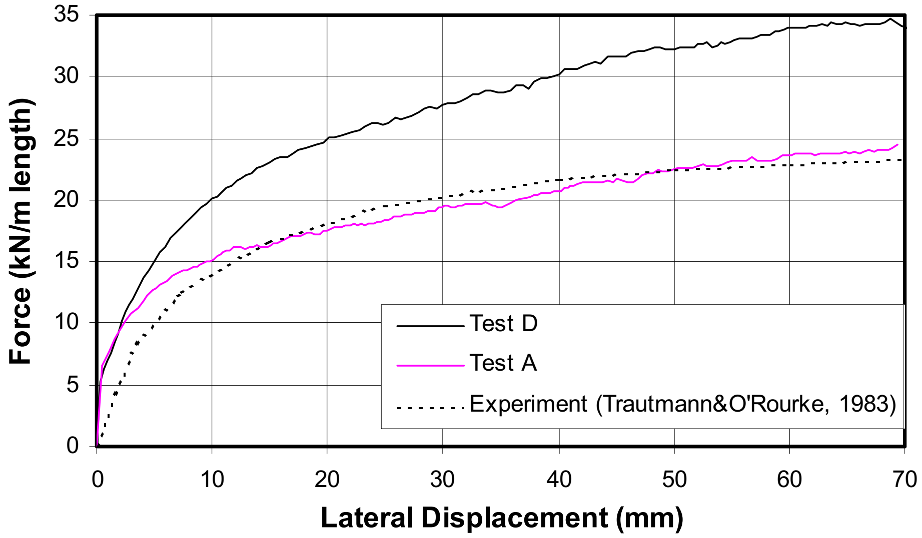

(a) Force – displacement relationship

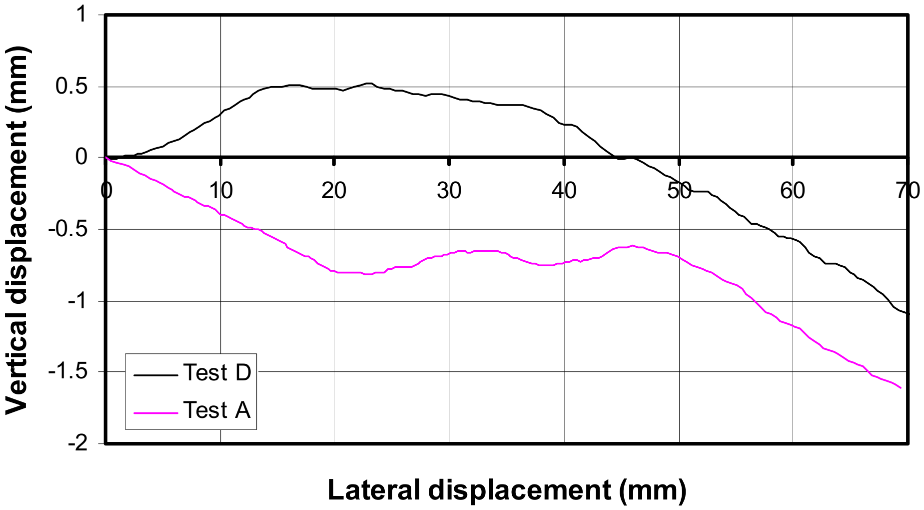

(b) Vertical –lateral displacement relationship

Figure H-4 Effects of inter-particle friction angle

H-5 Effects of pipe normal contact stiffness

The effects of pipe normal contact stiffness on lateral pipe loading results are shown in Fig. H-5 by comparing the results of Test A ($k_{N,pipe} = 5.0 \times 10^5$ N/m) with Test E ($k_{N,pipe} = 2.5 \times 10^6$ N/m (increased by 5 times)). The results show that the change in pipe normal contact stiffness (within the range studied) has negligible effects on the lateral pipe loading results. In the present DEM analysis, the pipe normal contact stiffness is equal to the particle normal contact stiffness.

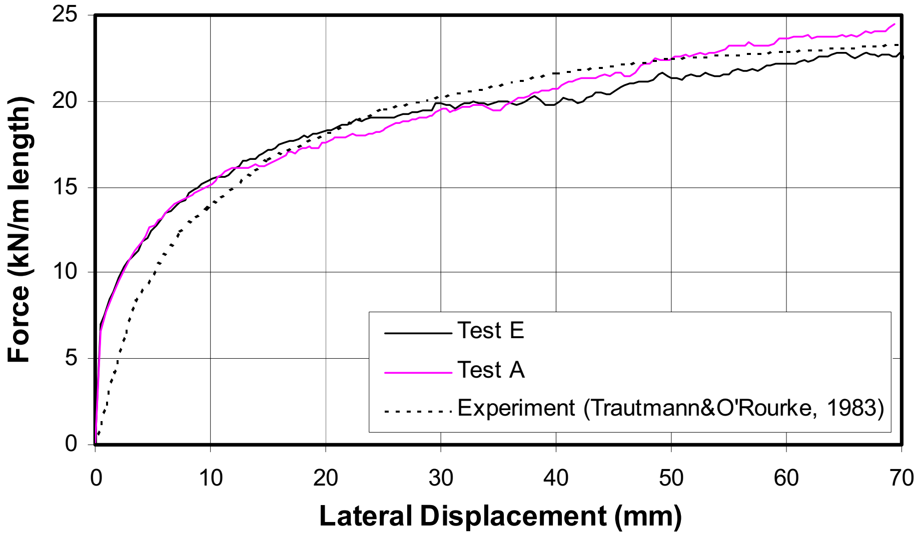

(a) Force – displacement relationship

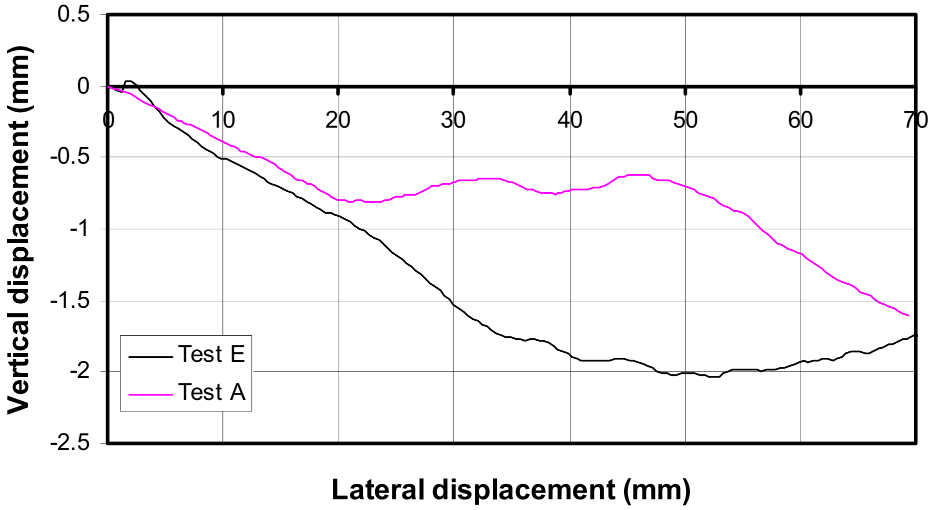

(b) Vertical –lateral displacement relationship

Figure H-5 Effects of pipe normal contact stiffness

H-6 Effects of pipe tangential contact stiffness

The effects of pipe tangential contact stiffness on lateral pipe loading results are shown in Fig. H-6 by comparing the results of Test A ($k_{T,pipe} = 5.0 \times 10^5$ N/m) with Test F ($k_{T,pipe} = 2.5 \times 10^6$ N/m (increased by 5 times)). The results show that the change in pipe tangential contact stiffness (within the range studied) has negligible effects on the lateral pipe loading results. In the present DEM analysis, the pipe tangential contact stiffness is equal to the pipe normal contact stiffness.

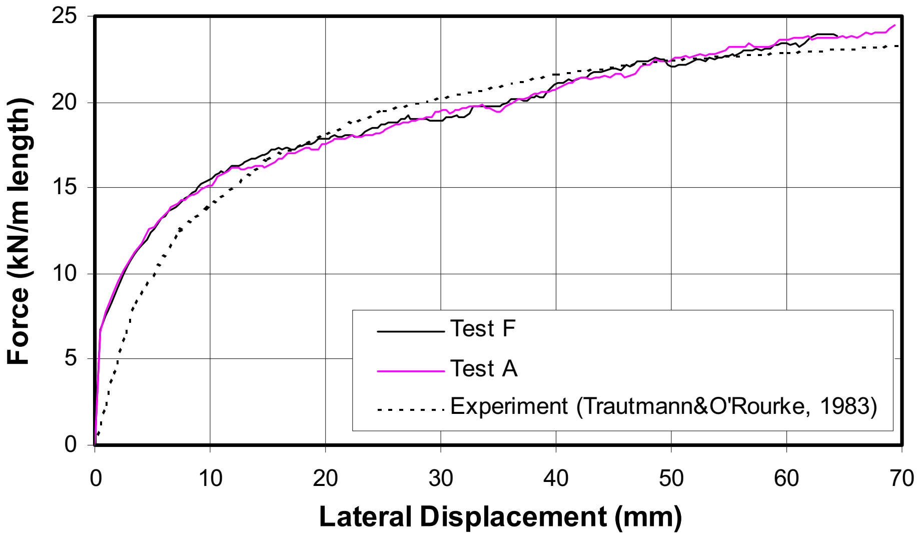

(a) *Force – displacement relationship*

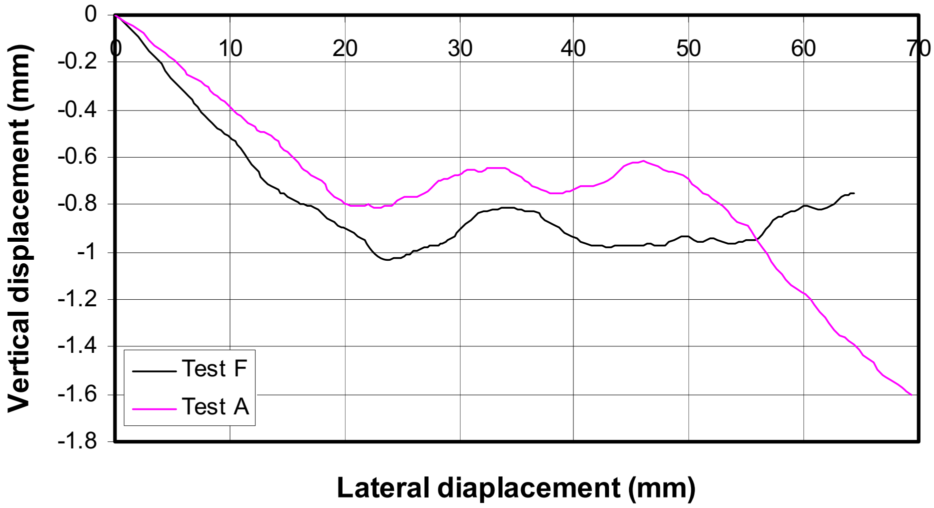

(b) *Vertical –lateral displacement relationship*

Figure H-6 Effects of pipe tangential contact stiffness

H-7 Effects of pipe surface friction

The effects of pipe surface friction on lateral pipe loading results are shown in Fig. H-7 by comparing the results of Test A (tan $\phi_{pipe} = 0.41$ or $\phi_{pipe} = \phi_\mu/2$) with Test G (tan $\phi_{pipe} = 1.0$ or $\phi_{pipe} = \phi_\mu$). The results show that the change in pipe surface friction (between $\phi_{pipe} = \phi_\mu/2$ and $\phi_{pipe} = \phi_\mu$) has negligible effects on the lateral pipe loading results.

The pipe surface friction angle ϕ_{pipe} generally ranges from about 20° to a value equal to the friction angle of the soil. The larger values would be characteristic of rough uncoated pipes with rusting or corroded surface and the lower values would correspond to pipes with smooth coatings. The condition of the surface of the pipe in the experiments by Trautmann & O'Rourke (1983) was described as rough, scaly surfaces with minor rust patches. Therefore, the ϕ_{pipe} was assumed to be $\phi_\mu/2$ in the present DEM analysis. The real ϕ_{pipe} can probably lie between $\phi_\mu/2$ and ϕ_μ which gives negligible difference. Rowe & Davis (1982) also suggested that the effects of pipe surface friction is expected to decrease as the depth of the pipe increases. According to their computations, pipe surface roughness has the greatest influence on shallow vertical anchors resisting horizontal forces. The effects were found to be minimal for deep anchors and for anchors resisting uplift forces.

In the present DEM analysis, the sidewall and base of the test tank were assumed to be perfectly smooth. Although Trautmann & O'Rourke (1983) reported that the smooth Formica, which has $\phi_\mu = 0.6\ \phi_{max}$, was used as the sidewall and base, the assumption of smooth sidewall and base is still considered justifiable because the far boundary in the experiment configuration should exclude the boundary effects (except for some cases of dense sand with deep embedment depth). Moreover, since the test tank was made to be relatively wide, the assumption of plane strain condition in the DEM analysis is also justifiable.

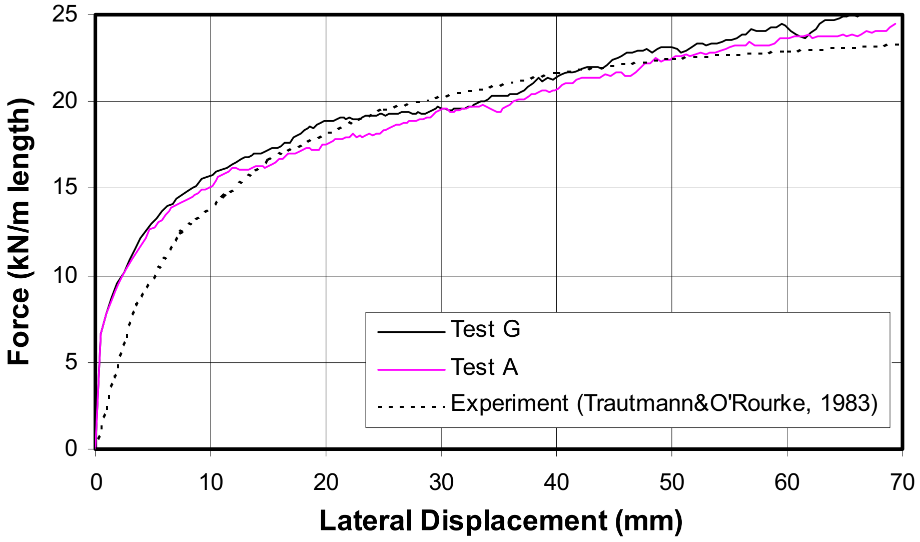

(a) Force – displacement relationship

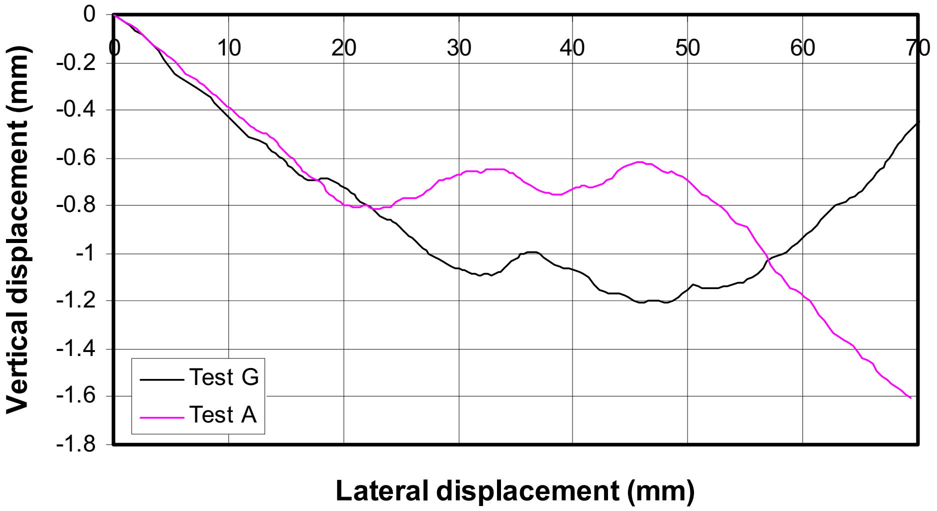

(b) Vertical –lateral displacement relationship

Figure H-7 Effects of pipe surface friction

H-8 Effects of pipe pulling velocity

The effects of pipe pulling velocity on lateral pipe loading results are shown in Fig. H-8 by comparing the results of Test A (V = 0.3 m/s) with Test H (V = 0.15 m/s (reduced by half)). The results show that the decrease in the pipe pulling velocity results in a slight decrease in the peak force (approximately 20% reduction). However, the selection of the pipe pulling velocity must consider the required time to complete the analysis. A slower pipe pulling velocity may give a small decrease in the peak force; however, the selected pipe pulling velocity of 0.3 m/s is consider justifiable considering the required analysis time. Moreover, by default, PFC^{3D} operates in “static” mode – that is, internal damping is applied that causes the system of particles to reach equilibrium in a minimum number of cycles.

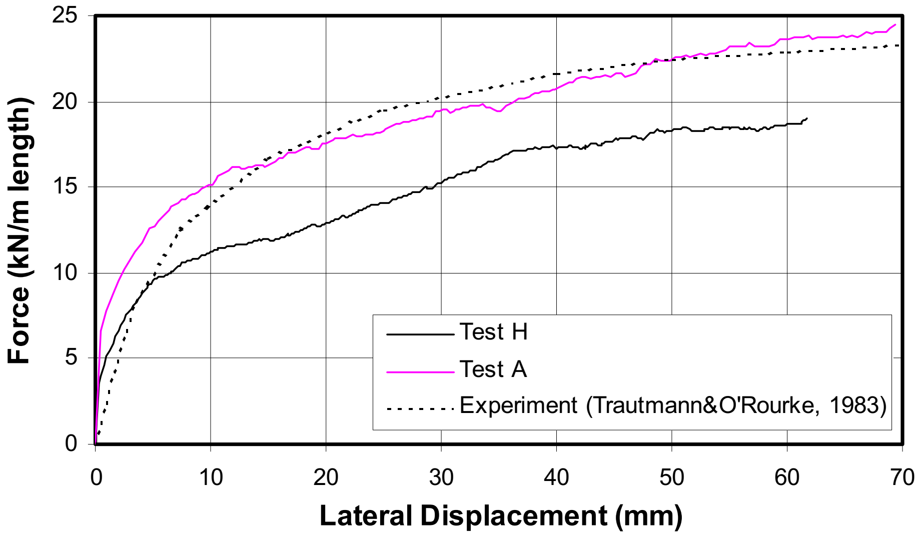

(a) Force – displacement relationship

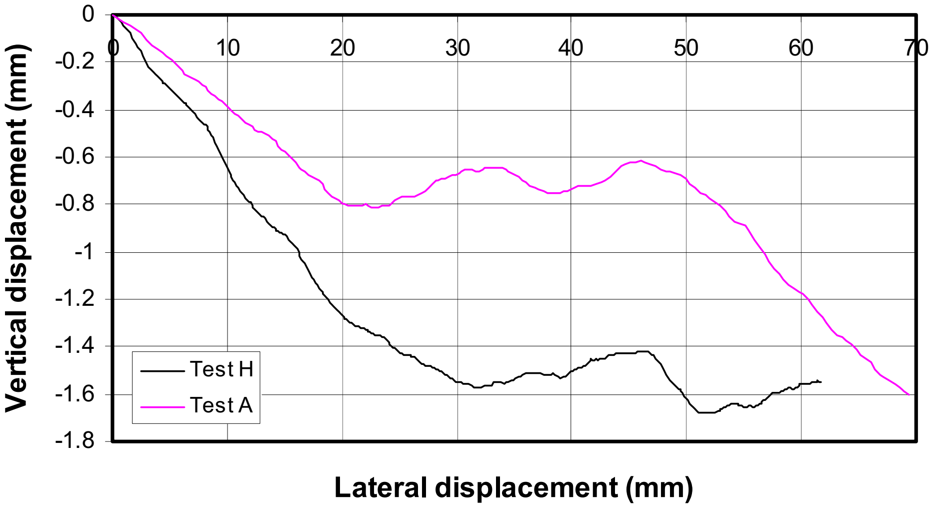

(b) Vertical –lateral displacement relationship

Figure H-8 Effects of pipe pulling velocity

H-9 Effects of extent of fine particle

The effects of extent of fine particle on lateral pipe loading results are shown in Fig. H-9 by comparing the results of Test A (with fine particles (Region A in Fig. 4-3)) with Test I (without fine particles (without Region A in Fig. 4-3)). The results show that the extent of fine particle has minimal effects on the lateral pipe loading results. In the present DEM analysis, the extent of fine particle is included.

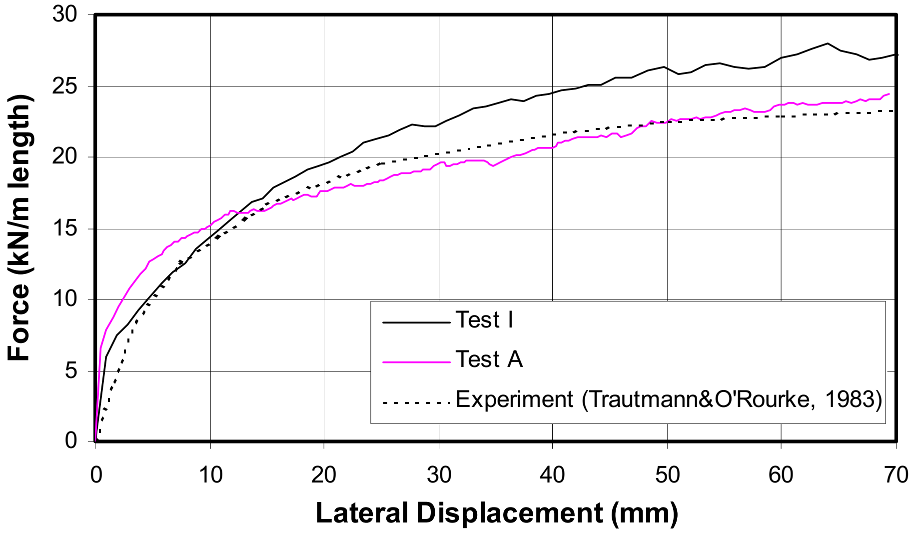

(a) Force – displacement relationship

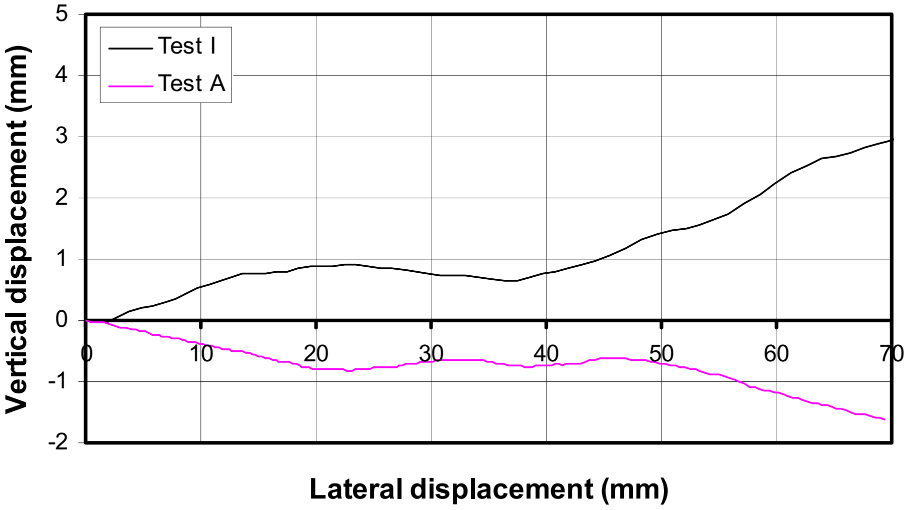

(b) Vertical –lateral displacement relationship

Figure H-9 Effects of extent of fine particle

H-10 Summary

The results of the parametric study can be summarized as shown in Table H-2.

Table H-2 Results of parametric study of lateral pipe loading

Parameters	**Effects on peak force when the values of the parameters increase**
Particle normal contact stiffness, $k_{N,sand}$ (N/m)	↑
Particle tangential contact stiffness, $k_{T,sand}$ (N/m)	—
Inter-particle friction angle, tan ϕ_μ	↑
Pipe normal contact stiffness, $k_{N,pipe}$ (N/m)	—
Pipe tangential contact stiffness, $k_{T,pipe}$ (N/m)	—
Pipe surface friction, tan ϕ_{pipe}	—
Pipe pulling velocity, V (m/s)	↑ (small)
Extent of fine particles (as shown in Fig. 4-3)	—

where — = negligible change
↑ = increase
↓ = decrease
small = the effects are small

Appendix I

Parametric Study of DEM Simulation of Upward Pipe Loading

Appendix I

Parametric study of DEM simulation of upward pipe loading

I.1 General

Parametric studies were carried out to examine the effects of the key parameters on the DEM analysis results of upward pipe loading. The case of medium sand with $H_c/D = 13$ was selected for a parametric study. The parameters investigated include normal contact stiffness of particle, tangential contact stiffness of particle, inter-particle friction angle, normal contact stiffness of pipe, tangential contact stiffness of pipe, pipe friction angle, pipe pulling velocity, and extent of fine particle. The input parameters for the parametric study are shown in Table I-1. The DEM analysis result of the control test is shown in Figure I-1.

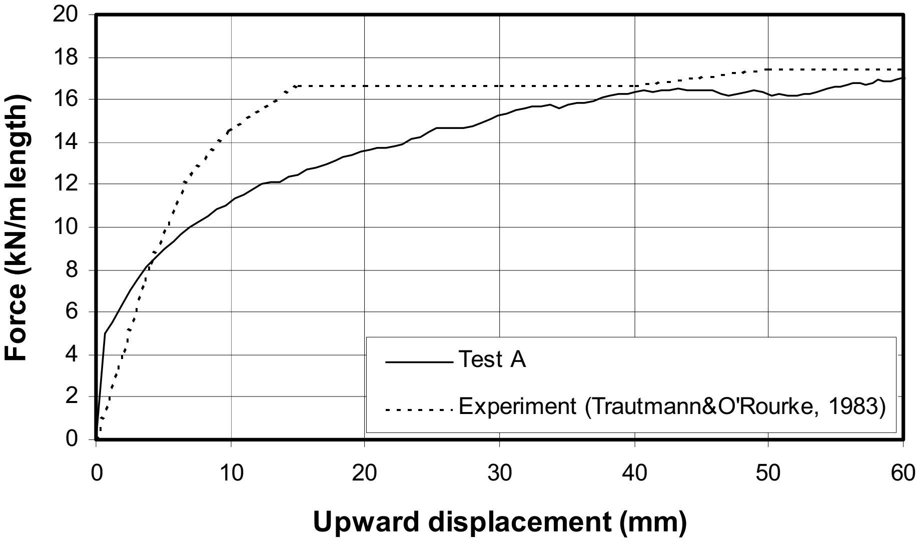

Figure I-1 Control test (Test A)

Table I-1 Input parameters for parametric study of upward pipe loading

Parameters	**Test A***	**Test B**	**Test C**	**Test D**	**Test E**	**Test F**	**Test G**	**Test H**	**Test I**
Particle normal contact stiffness, $k_{N,sand}$ (N/m)	2.0×10^5	1.0×10^6	2.0×10^5	2.0×10^5	2.0×10^5	2.0×10^5	2.0×10^5	2.0×10^5	2.0×10^5
Particle tangential contact stiffness, $k_{T,sand}$ (N/m)	2.0×10^5	2.0×10^5	1.0×10^6	2.0×10^5	2.0×10^5	2.0×10^5	2.0×10^5	2.0×10^5	2.0×10^5
Inter-particle friction angle, tan ϕ_μ	1.0	1.0	1.0	3.0	1.0	1.0	1.0	1.0	1.0
Pipe normal contact stiffness, $k_{N,pipe}$ (N/m)	2.0×10^5	2.0×10^5	2.0×10^5	2.0×10^5	1.0×10^6	2.0×10^5	2.0×10^5	2.0×10^5	2.0×10^5
Pipe tangential contact stiffness, $k_{T,pipe}$ (N/m)	2.0×10^5	2.0×10^5	2.0×10^5	2.0×10^5	2.0×10^5	1.0×10^6	2.0×10^5	2.0×10^5	2.0×10^5
Pipe surface friction, tan ϕ_{pipe}	0.41	0.41	0.41	0.41	0.41	0.41	1.0	0.41	0.41
Pipe pulling velocity (m/s)	0.3	0.3	0.3	0.3	0.3	0.3	0.3	0.15	0.3
Extent of fine particle (as shown in Fig. 4-3)	✓	✓	✓	✓	✓	✓	✓	✓	✗

* control test

I-2 Effects of particle normal contact stiffness

The effects of particle normal contact stiffness on upward pipe loading results are shown in Fig. I-2 by comparing the results of Test A ($k_{N,sand} = 2.0 \times 10^5$ N/m) with Test B ($k_{N,sand} = 1.0 \times 10^6$ N/m (increased by 5 times)). The results show that the peak force becomes larger as the particle normal contact stiffness increases. This is contrary to the effects of particle normal contact stiffness on the triaxial test results which show that contact stiffness affects only stiffness (modulus) but not strength (see Appendix G). This may be due to the more complex mode of shearing in pipe loading problem.

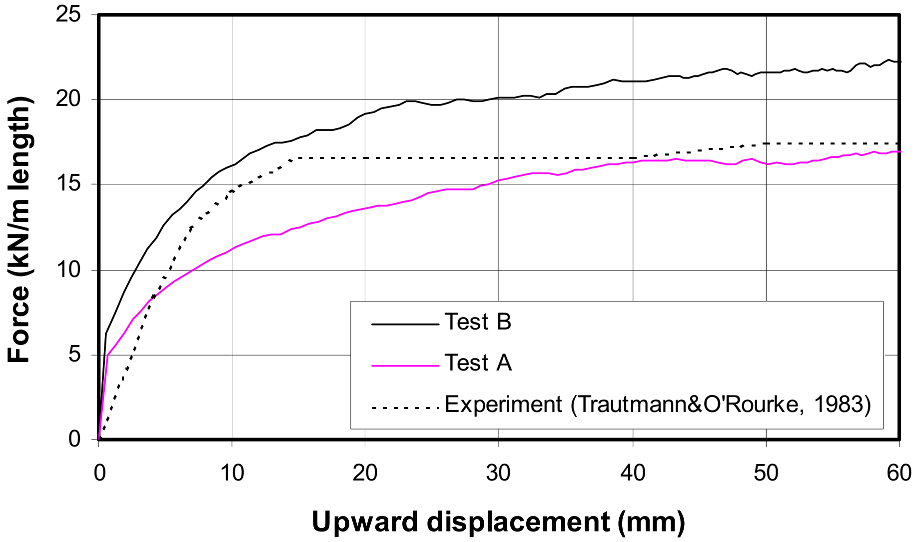

Figure I-2 Effects of particle normal contact stiffness

I-3 Effects of particle tangential contact stiffness

The effects of particle tangential contact stiffness on upward pipe loading results are shown in Fig. I-3 by comparing the results of Test A ($k_{T,sand} = 2.0 \times 10^5$ N/m) with Test C ($k_{T,sand} = 1.0 \times 10^6$ N/m (increased by 5 times)). The results show that the change in particle tangential contact stiffness (within the range studied) has minimal effects on the upward pipe loading results.

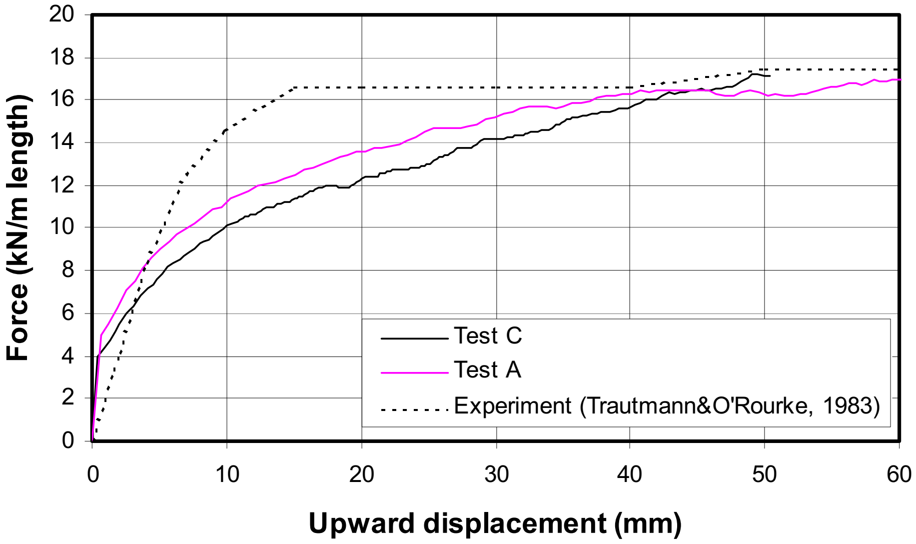

Figure I-3 Effects of particle tangential contact stiffness

I-4 Effects of inter-particle friction angle

The effects of inter-particle friction angle on upward pipe loading results are shown in Fig. I-4 by comparing the results of Test A (tan ϕ_μ = 1.0 or ϕ_μ = 45°) with Test D (tan ϕ_μ = 3.0 or ϕ_μ = 72°). The results show that the peak force becomes larger as the inter-particle friction angle increases. This is consistent with the effects of inter-particle friction angle on triaxial test results which show that an increase in the inter-particle friction angle yields an increase in strength (see Appendix G).

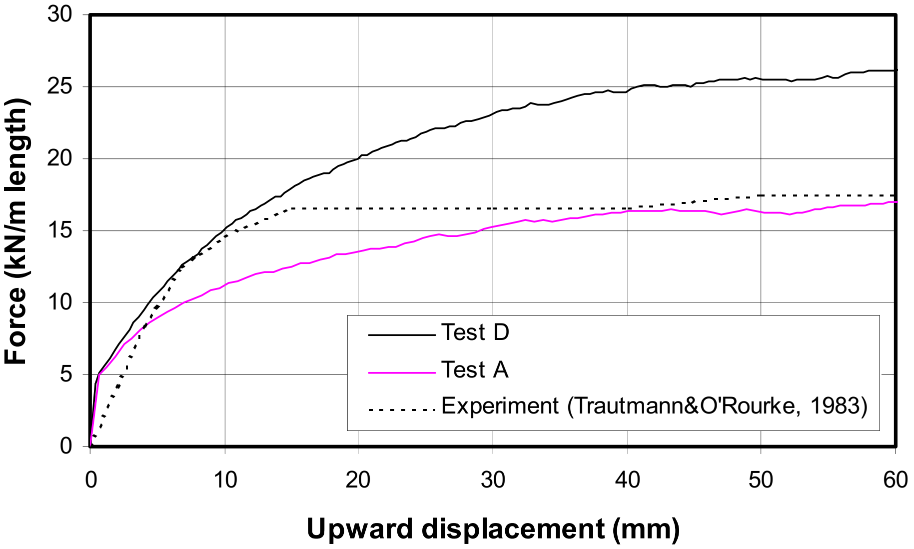

Figure I-4 Effects of inter-particle friction angle

I-5 Effects of pipe normal contact stiffness

The effects of pipe normal contact stiffness on upward pipe loading results are shown in Fig. I-5 by comparing the results of Test A ($k_{N,pipe} = 2.0 \times 10^5$ N/m) with Test E ($k_{N,pipe} = 1.0 \times 10^6$ N/m (increased by 5 times)). The results show that the change in pipe normal contact stiffness (within the range studied) has negligible effects on the upward pipe loading results. In the present DEM analysis, the pipe normal contact stiffness is equal to the particle normal contact stiffness.

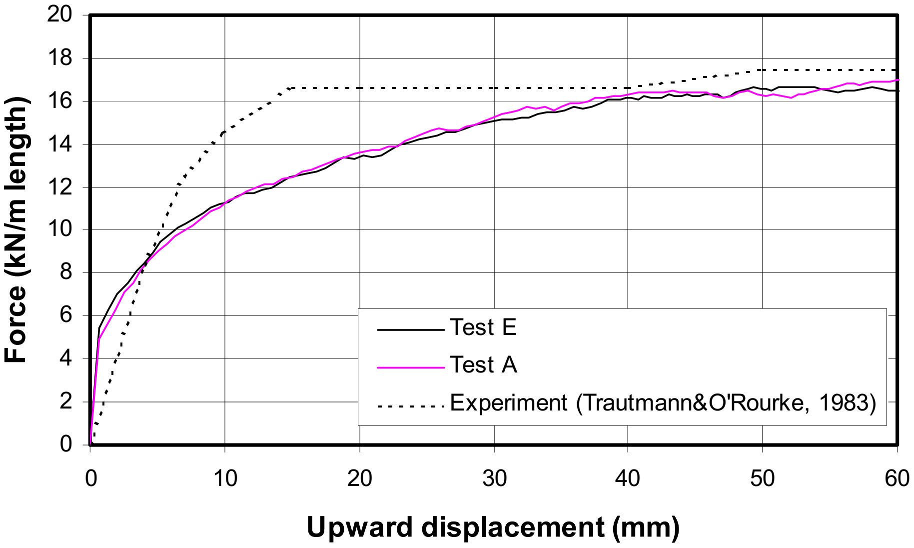

Figure I-5 Effects of pipe normal contact stiffness

I-6 Effects of pipe tangential contact stiffness

The effects of pipe tangential contact stiffness on upward pipe loading results are shown in Fig. I-6 by comparing the results of Test A ($k_{T,pipe}$ = 2.0 × 10^5 N/m) with Test F ($k_{T,pipe}$ = 1.0 × 10^6 N/m (increased by 5 times)). The results show that the change in pipe tangential contact stiffness (within the range studied) has negligible effects on the upward pipe loading results. In the present DEM analysis, the pipe tangential contact stiffness is equal to the pipe normal contact stiffness.

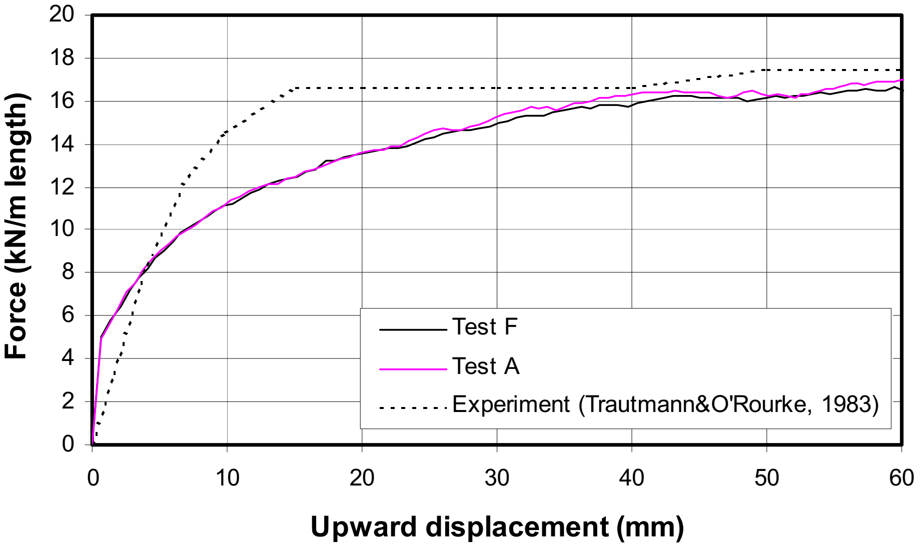

Figure I-6   Effects of pipe tangential contact stiffness

I-7 Effects of pipe surface friction

The effects of pipe surface friction on upward pipe loading results are shown in Fig. I-7 by comparing the results of Test A (tan ϕ_{pipe} = 0.41 or $\phi_{pipe} = \phi_\mu/2$) with Test G (tan ϕ_{pipe} = 1.0 or $\phi_{pipe} = \phi_\mu$). The results show that the change in pipe surface friction (between $\phi_{pipe} = \phi_\mu/2$ and $\phi_{pipe} = \phi_\mu$) has negligible effects on the upward pipe loading results. The small effects of pipe surface friction is consistent with the FE analysis results presented by Rowe & Davis (1982). In the present DEM analysis, the ϕ_{pipe} was assumed to be $\phi_\mu/2$.

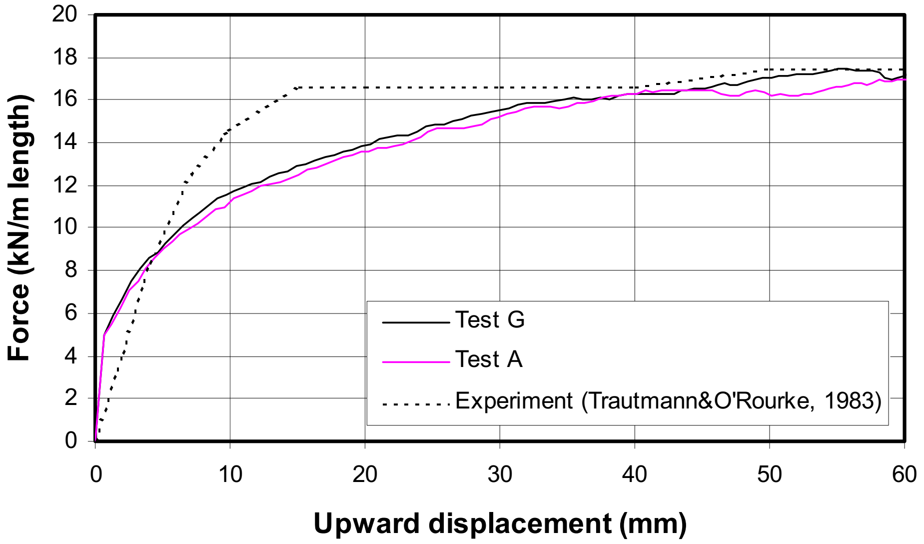

Figure I-7 Effects of pipe surface friction

I-8 Effects of pipe pulling velocity

The effects of pipe pulling velocity on upward pipe loading results are shown in Fig. I-8 by comparing the results of Test A (V = 0.3 m/s) with Test H (V = 0.15 m/s (reduced by half)). The results show that the decrease in the pipe pulling velocity results in a slight decrease in the peak force (approximately 15% reduction). However, the selection of the pipe pulling velocity must consider the required time to complete the analysis. A slower pipe pulling velocity may give a small decrease in the peak force; however, the selected pipe pulling velocity of 0.3 m/s is consider justifiable considering the required analysis time.

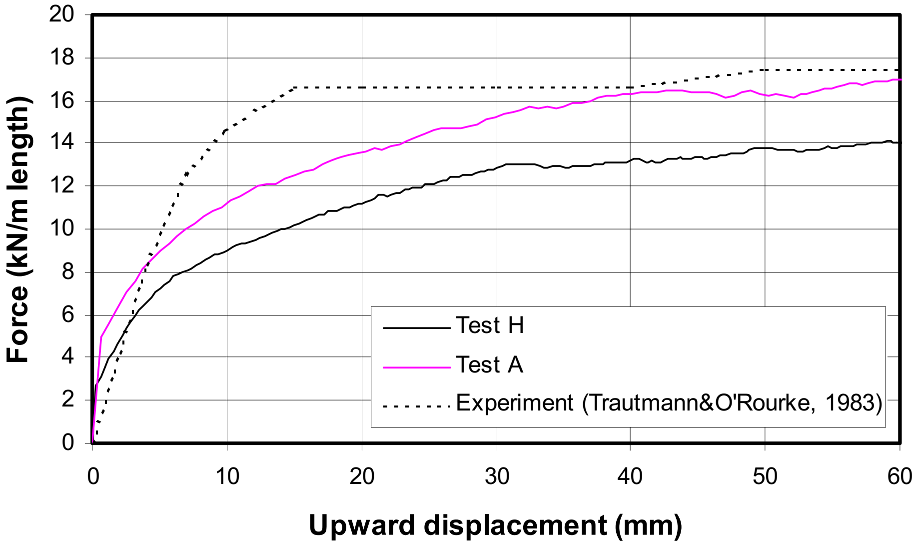

Figure I-8 Effects of pipe pulling velocity

I-9 Effects of extent of fine particle

The effects of extent of fine particle on upward pipe loading results are shown in Fig. I-9 by comparing the results of Test A (with fine particles (Region A in Fig. 4-3)) with Test I (without fine particles (without Region A in Fig. 4-3)). The results show that the extent of fine particle has minimal effects on the upward pipe loading results. In the present DEM analysis, the extent of fine particle is included.

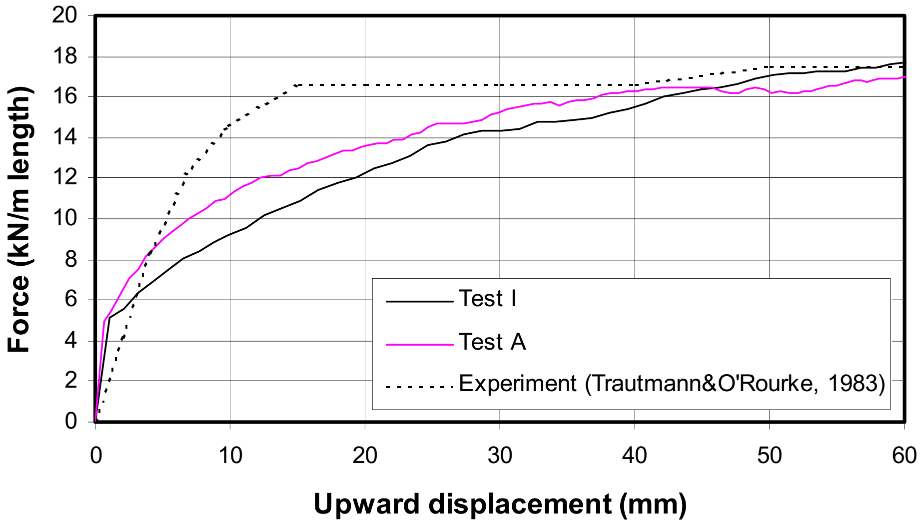

Figure I-9 Effects of extent of fine particles

I-10 Summary

The results of the parametric study can be summarized as shown in Table I-2.

Table I-2 Results of parametric study of upward pipe loading

Parameters	**Effects on peak force when the values of the parameters increase**
Particle normal contact stiffness, $k_{N,sand}$ (N/m)	↑
Particle tangential contact stiffness, $k_{T,sand}$ (N/m)	—
Inter-particle friction angle, tan ϕ_{μ}	↑
Pipe normal contact stiffness, $k_{N,pipe}$ (N/m)	—
Pipe tangential contact stiffness, $k_{T,pipe}$ (N/m)	—
Pipe surface friction, tan ϕ_{pipe}	—
Pipe pulling velocity, V (m/s)	↑ (small)
Extent of fine particles (as shown in Fig. 4-3)	—

where — = negligible change
↑ = increase
↓ = decrease
small = the effects are small

Appendix J

Resulting Publications from Current Research Project

Appendix J

Resulting Publications from Current Research Project

The outcome of the current research project has been published into two papers, the details of which are as following. The manuscripts of these two papers are included in this appendix.

1. Yimsiri, S. and Soga, K. (2005), "Distinct element analysis of soil-pipeline interaction in sand under upward movement at deep embedment condition", *Proc. of the 16th International Conference on Soil Mechanics and Geotechnical Engineering*, Osaka, Japan (accepted)
2. Yimsiri, S. and Soga, K. (2005), "DEM analysis of soil-pipeline interaction in sand under lateral and upward movements at deep embedment", *Geotechnical Engineering*, Journal of the Southeast Asian Geotechnical Society (submitted)

Distinct element analysis of soil-pipeline interaction in sand under upward movement at deep embedment condition

Analyse par éléments discrets de l'interaction sol sableux-oléoduc soumis à un déplacement vertical dans des conditions d'enfouissement profond

S. Yimsiri
Department of Civil Engineering, Burapha University, Thailand

ABSTRACT: The distinct element analysis of the soil-pipeline interactions in sand under upward movements at deep embedment conditions is undertaken. Available analytical solutions provide a wide range of predicted peak dimensionless forces and there is limited information regarding the transition of the peak dimensionless force from shallow to deep embedment conditions. Recently, finite element analysis of soil-pipeline interactions at deep embedment conditions has been performed. In the current study, distinct element analysis is employed to reinvestigate this problem because it is considered that the distinct element analysis may give more accurate results due to its discontinuous nature which more closely simulates sand behavior. The obtained results are compared with the previously published results and it is found that the results from distinct element and finite element are consistent except for the case of dense sand at deep embedment. The possibilities of the discrepancy are discussed.

RÉSUMÉ: Ce papier présente une analyse par éléments discrets des interactions sol sableux-oléoduc soumis à un déplacement vertical dans des conditions d'enfouissement profond. Il existe un grand nombre de solutions analytiques pour déterminer la force adimensionnelle limite, cependant il existe peu de solutions simultanément valables à faibles et grandes profondeurs. Récemment, une analyse par éléments finis en conditions d'enfouissement profond a été menée. Dans la présente publication, ce problème est revisité par le biais des éléments distincts dont la nature discontinue est considérée comme plus représentative du comportement mécanique des sables. Les résultats ainsi obtenus sont en accord avec les résultas publiés précédemment dans la littérature à l'exception du cas des sables denses et profond. Les causes possibles de cette divergence sont discutées dans ce papier.

1. INTRODUCTION

The standard formulations of the force-displacement characteristics for soil-pipeline interactions in sand under upward movement are given by ASCE in the "Guideline for the Seismic Design of Oil and Gas Pipeline System (1984)". According to this, the peak force per unit length F_{peak} applied to a pipeline is obtained by the following equation.

$$F_{peak} = \bar{\gamma} H_c N_{qc} D \tag{1}$$

where $\bar{\gamma}$ is the effective unit weight of soil, H_c is the depth to the center of the pipeline, and D is the external pipe diameter. N_{qc} is the peak dimensionless force and is a function of soil friction angle and embedment ratio H_c/D. These recommendations are derived from the experimental data by Trautmann and O'Rourke (1983) of a pipe with $H_c/D \leq 13$.

Available analytical solutions give a wide range of predicted peak dimensionless forces and there is limited information regarding the transition of the peak dimensionless force from shallow to deep embedment conditions. Yimsiri et al (2003) have recently presented a design chart for deep embedment conditions using finite element analysis. In this study, the Distinct Element Method (DEM) is employed to investigate the same problem again. Due to its discontinuous nature, it is considered that DEM should better simulate the soil movement close to the pipe at large pipe displacement and, hence, may yield more accurate results to the problem. In the past, the DEM has been used mainly for the study of micromechanical behavior of sand. This study provides an example of the use of the DEM for more practical problem. The DEM analysis is firstly calibrated against large-scale tank tests data reported by Trautmann and O'Rourke (1983) to determine the micromechanical input parameters that are not possible to be estimated from laboratory tests. By calibrating the model, the DEM analysis is extended to deeper embedment conditions. The DEM results are compared with the previous study of the same problem using Finite Element Method (FEM) (Yimsiri et al., 2003).

2. DISTINCT ELEMENT ANALYSIS

The pipe loading experiments were simulated using the distinct element method based on the approach by Cundall and Strack (1979). The distinct element code PFC^{3D} (Itasca, 1999) was employed. The code models soil particles as a collection of distinct and arbitrarily sized spherical particles. The particles are treated as rigid bodies and allowed to overlap one another at the contact points. The contacts between particles are characterized through the stiffness and slip condition. The constitutive behavior of the particles enables the simulation of macroscale plasticity. No bonding between particles is employed in this study to simulate uncemented sand.

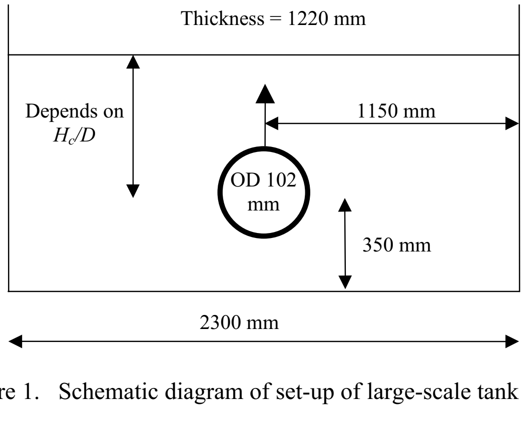

Figure 1. Schematic diagram of set-up of large-scale tank test.

DEM analysis requires knowledge of a force-displacement law at particle contacts. The linear elastic contact model was employed; the contact force and relative contact displacement are linearly related by a constant contact stiffness. Two stiffness values are required for each contact; they are (i) normal contact stiffness k_N and (ii) tangential contact stiffness k_T (force/displacement). Particle sliding occurs when the tangential contact force reaches its maximum allowable value, which is taken to be the coefficient of inter-particle friction angle between the two contacting entities multiplied by the magnitude of the normal contact force.

3. NUMERICAL MODELING

Trautmann and O'Rourke (1983) performed large-scale tank experiments at shallow depth to investigate the pipeline behavior. Their results were used here as benchmarks in order to examine the capability of the current DEM analysis technique. The schematic diagram of the test set-up is shown in Fig. 1. The tests were performed for different H_c/D values up to 13. Cornell filter sand was used for all the tests. It is a clean, subangular, fluvio-glacial sand, having a coefficient of uniformity C_u of 2.6 and an effective grain size D_{10} of 0.2 mm. The 102-mm pipe was fabricated from ASTM Grade A-36 steel. Soil-pipe interaction at three different densities was tested; 14.8 (loose), 16.4 (medium), and 17.7 (dense) kN/m^3, which corresponded to the relative density of 0, 45, and 80%, respectively. In practice, the sand placed around a pipeline is often in the state of medium to dense conditions. Hence, the behavior in medium and dense sands was of interest in this study and these test cases were simulated.

The tank and pipe were modeled by series of planar wall. The dimensions of the tank were the same as the actual tank. The tank wall was assumed to be smooth; the tank model has a normal contact stiffness equal to that of the particles but has zero tangential contact stiffness and zero surface friction. The pipe has identical contact stiffness in both normal and tangential directions and equal to that of the particles. The pipe has its surface friction angle equal to half of the inter-particle friction angle of sand (Yimsiri et al., 2003).

Sand is modeled as a collection of spherical particles and its size distribution follows normal distribution. The sand particles are modeled by using larger sizes than actual sand with varying sizes in various regions of the model (see Fig. 2). Due to computational limitation, it was not possible to model using the actual particle size (D_{10} = 0.2 mm and D_{60} = 0.52 mm). At the region near the pipe (Region A), the particles are smaller with $r_{average}$ = 12.5 mm and standard deviation = 2.5 mm (25 times larger than actual sand). Further away (Region B), the particles are larger with $r_{average}$ = 25.0 mm and standard deviation = 5.0 mm (50 times larger). For the cases with $H_c/D \geq 17$, there is Region C with the particle size of $r_{average}$ = 37.5 mm and standard deviation = 7.5 mm (75 times larger). This allowed the number of particles to be less than 130,000 for deepest case. An example of the DEM models is shown in Fig. 3.

4. DETERMINATION OF INPUT PARAMETERS

The input parameters for DEM modeling are listed in Table 1. Most of the parameters were determined by calibrating the numerical results with the experimental data of (i) triaxial test results of the sands used for the tank experiments (Turner and Kulhawy, 1987) and (ii) the actual pipe loading test results at shallow depths (Trautmann and O'Rourke, 1983).

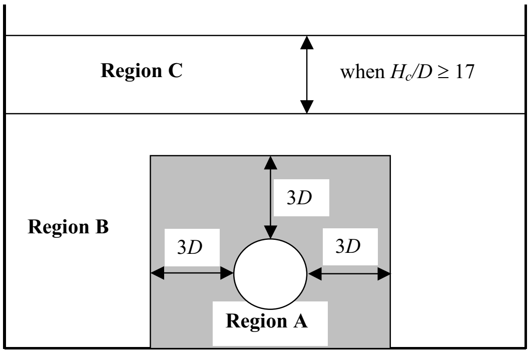

Figure 2. Various regions of the DEM model.

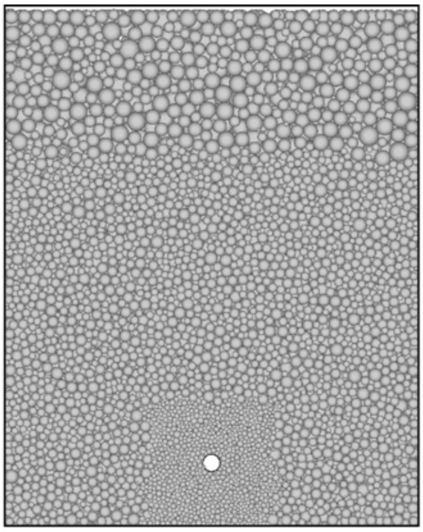

Figure 3. Example of DEM model (medium sand, H_c/D = 25).

Table 1: Input parameters for DEM analysis

Parameters	Values
Normal contact stiffness of particle, $k_{N,sand}$	From Eq. (2)
Tangent contact stiffness of particle, $k_{T,sand}$	$k_{T,sand} = k_{N,sand}$
Normal contact stiffness of pipe, $k_{N,pipe}$	$k_{N,pipe} = k_{N,sand}$
Tangent contact stiffness of pipe, $k_{T,pipe}$	$k_{T,pipe} = k_{N,pipe}$
Normal contact stiffness of wall, $k_{N,wall}$	$k_{N,wall} = k_{N,sand}$
Tangent contact stiffness of wall, $k_{T,wall}$	$k_{T,wall} = 0$
Inter-particle friction angle, $\phi_{\mu,sand}$	$\tan \phi_{\mu,sand}$ = 0.5, 1.0, 3.0
Pipe friction angle, $\phi_{\mu,pipe}$	$\phi_{\mu,pipe} = \phi_{\mu,sand}/2$
Tank wall friction angle, $\phi_{\mu,wall}$	$\phi_{\mu,wall} = 0$
Density of particle, ρ (kg/m^3)	2740
Radius of particle, r	Varies in Regions A, B, C

Results from the triaxial test simulations show that the DEM analysis (using $k_N = k_T$) can simulate the stress-strain relationship by using a high value of inter-particle friction angle ($\tan \phi_\mu$ = 3.0) as shown in Fig. 4. This is due to the use of spherical particles, which allows excessive particle rolling (e.g. Thomas and Bray, 1999). The contact stiffness depends on confining pressure (e.g. Yimsiri and Soga, 2000); however, it was not possible to derive the pressure-dependent stiffness values from the triaxial test results because the data did not span for a wide range of confining pressure. Instead, the contact stiffness was derived by fitting the DEM analysis results with the pipe loading data at shallow depths by using tan ϕ_μ = 0.5, 1.0, 3.0. The obtained relationship between the contact stiffness and the vertical effective stress at center of pipe is shown in Fig. 5 and the following relationships are proposed.

$$\left.\begin{array}{ll} k\ (\text{N/m}) = 6.714\sigma_c'^{3.813} & \text{for } \tan\phi_\mu = 0.5 \\ k\ (\text{N/m}) = 41.072\sigma_c'^{2.761} & \text{for } \tan\phi_\mu = 1.0 \\ k\ (\text{N/m}) = 112.859\sigma_c'^{2.176} & \text{for } \tan\phi_\mu = 3.0 \end{array}\right\} \qquad (2)$$

σ_c' (kPa) = vertical effective stress at center of pipe

It is noted that various combinations of the contact stiffness and tan ϕ_μ can yield similar peak forces. With larger tan ϕ_μ, the required contact stiffness is lower. It is interesting to find that the contact stiffness affects the strength (peak force) for this problem, which is not the case for triaxial problem where the contact stiffness affects only modulus, not strength. This may be due to the more complex mode of shearing in pipe loading problem. It is also noted that the obtained power is greater than 0.5 which is the normal value for soil (Hardin and Black, 1966); this may be also due to the complexity of mode of loading. The peak force values employed for fitting is governed by complex deformation at relatively large strain; however, the contact stiffness is the behavior at very small strain.

Examples of the computed force-displacement relationships are shown in Fig. 6. In case of medium sand, the results from all cases show small difference and match the experimental data well. However, for dense sand, the results from tan ϕ_μ = 0.5 show stiffest behavior which best match the experimental result, while other cases show more ductile behavior.

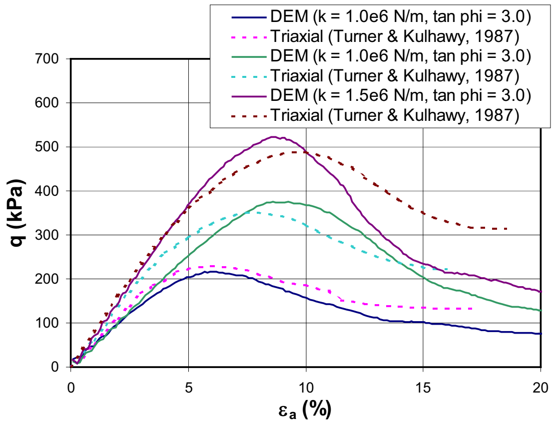

Figure 4. Calibration of DEM results against triaxial tests.

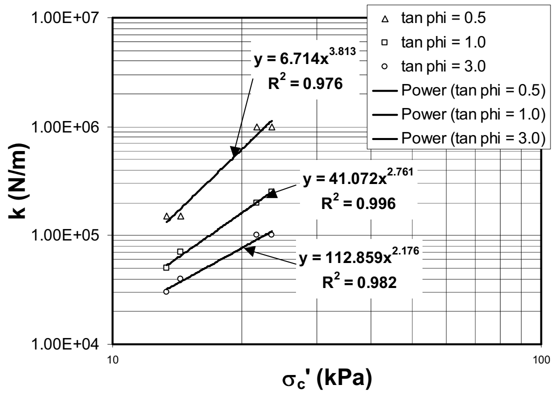

Figure 5. Relationship between contact stiffness and stress.

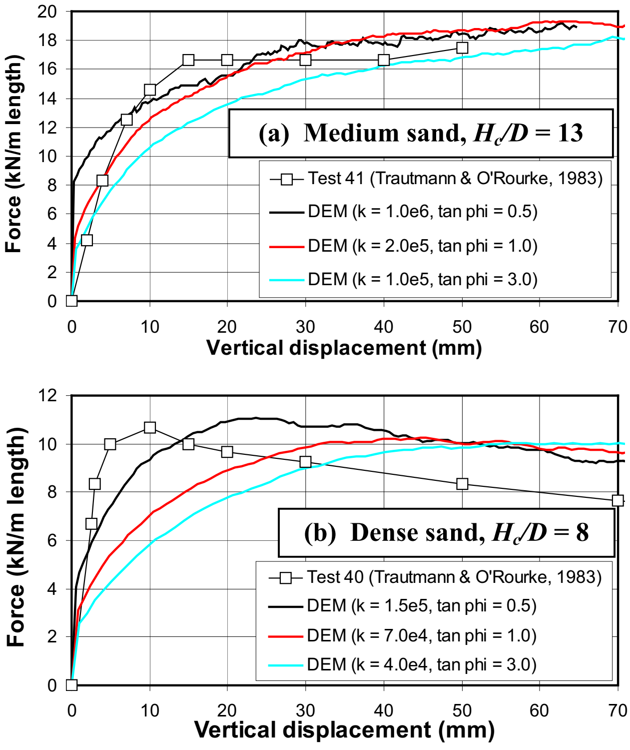

Figure 6. Calibration of DEM results against pipe loading tests.

5. RESULTS OF DEEP PIPE LOADING

After calibrating the DEM models with triaxial tests as well as the tank experiments, deep pipe loading cases were simulated using the input parameters derived from the shallow pipe loading cases. An example of the computed force-displacement curves are shown in Fig. 7 along with the result from the finite element analysis (Yimsiri et al., 2003). In case of medium sand, the results from DEM of all tan ϕ_μ cases are consistent with the FEM results. In case of dense sand, however, the result from DEM of tan ϕ_μ = 0.5 is considerably larger and the results become lesser for the cases of tan ϕ_μ = 1.0 and 3.0. The results for the case of tan ϕ_μ = 3.0 is closest to the FE result; however, its peak force is still somewhat larger. It is interesting to note that the DEM results of tan ϕ_μ = 0.5 better match the pipe loading test results at shallow depth, whereas the case of tan ϕ_μ = 3.0 better match the deep depth case.

Figure 8 shows the relationships between the peak dimensionless force and embedment ratio obtained from the DEM, FEM, and analytical solution by Meyerhof and Adams (1968). For some DEM simulations, the peak force was difficult to determine because the load-displacement curve exhibited ductile behavior with no distinctive peak. In such cases, the force-displacement data were fitted to a hyperbolic curve and the peak force was determined using the procedure used by Trautmann and O'Rourke (1983) for the actual test data. In case of medium sand, the DEM analysis of all tan ϕ_μ cases yield consistent results with FEM. In case of dense sand, however, the DEM analysis of all tan ϕ_μ cases yield consistent results with FEM only for $H_c/D \le 21$. When $H_c/D > 21$, the results from DEM become larger than FEM; the lesser the tan ϕ_μ employed (the larger the contact stiffness), the larger the overestimation. Only the case of tan ϕ_μ = 3.0 shows similar results to FEM with a tendency to give somewhat larger peak dimensionless force at deeper embedment depth ($H_c/D > 60$). The cases of tan ϕ_μ = 0.5 and 1.0 do not show any transition from shallow to deep failure. All results from numerical analysis (DEM and FEM) are larger than the analytical solution by Meyerhof and Adams (1968) which is the only analytical solution that can predict the transition from shallow to deep failure.

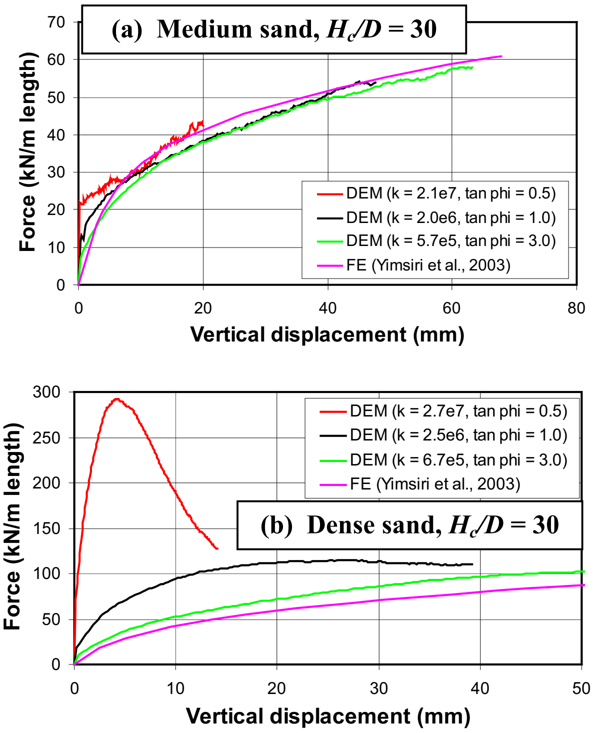

Figure 7. DEM results of deep pipe loading.

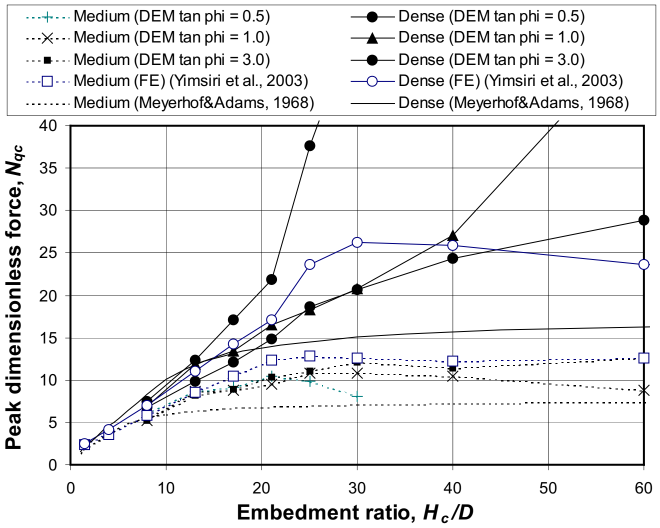

Figure 8. Comparison of peak dimensionless force.

6. DISSCUSSIONS

The displacement patterns from DEM and FEM for the case of shallow depth are quite similar. At deeper depth, the displacement pattern of medium sand shows local shear failure around pipe which is consistent with the deep shear failure behavior observed in Fig. 8. However, the displacement pattern of dense sand show overbreak failure, not local shear failure, and this tendency is more for lower tan ϕ_μ employed (higher contact stiffness) as can be seen from the steeper slope at deep depth in Fig. 8.

The advantage of DEM than FEM is its ability to present clearer movement of soil closely around the pipe due to the fact that the DEM analysis allows the soil particles to move freely. Also, the DEM analysis can continue with unlimited movement of the pipe until it reaches ultimate peak force (or further), unlike FEM which has to stop at some pipe displacement before peak force can be reached because large deformation of the mesh causes numerical convergence problem. The investigation of the particle movement around the pipe in detail is under way.

7. SUMMARY AND CONCLUSIONS

The soil-pipeline interactions under upward movements in sand were investigated using DEM analysis. The simulations were performed for both medium and dense sand conditions at different embedment ratios H_c/D from 8 to 60. The transition of the maximum dimensionless force from shallow to deep embedment conditions was observed and the critical embedment ratio and the corresponding critical maximum dimensionless forces were evaluated. The DEM results were also consistent with the previously published FEM results especially for the case of medium sand. For the case of dense sand, the DEM results show a tendency to give larger peak dimensionless force at deeper embedment depth ($H_c/D > 60$). This is due to the fact that the local failure was not achieved. The results from this DEM analysis together with earlier FEM analysis will serve as a Class-A predictions of the future full-scale tank test of this problem.

ACKNOWLEDGEMENTS

The Author would like to thank Dr. Kenichi Soga for his advice. This work is supported by a grant from the Thailand Research Fund (TRF).

REFERENCES

ASCE 1984. *Guidelines for the Seismic Design of Oil and Gas Pipeline Systems*

Cundall, P. A. and Strack, O. D. L. 1979. A discrete numerical model for granular assemblies. *Geotechnique*, 29(1), 47-65.

Hardin, B. O. and Black, W. L. 1966. Sand stiffness under various triaxial stresses. *J. of Soil Mech. and Foundations*, ASCE, 92(SM2), 27-42.

Itasca. 1999. *PFC^{3D}*, Version 2.0

Meyerhof, G. G. and Adams, J. I. 1968. The ultimate uplift capacity of foundations. *Canadian Geotech J*, 5(4), 225-244.

Thomas, P. A. and Bray, J. D. 1999. Capturing Nonspherical Shape of Granular Madia with Disk Clusters. *J of Geotech and Geoenviron Eng*, ASCE, 125(3), 169-178.

Trautmann, C. H. and O'Rourke, T. D. 1983. Behavior of Pipe in Dry Sand Under Lateral and Uplift Loading. *Geotechnical Eng Report 83-7*, Cornell University

Turner, J. P. and Kulhawy, F. H. 1987. Experimental Analysis of Drilled Shaft Foundations Subjected to Repeated Axial Loads Under Drained Conditions. *Report to Electric Power Research Institute*, Cornell University

Yimsiri, S. and Soga, K. 2000. Micromechanics-based stress-strain behaviour of soils at small strains. *Geotechique*, 50(5), 559-571.

Yimsiri, S., Soga, K., Yoshizaki, K., and Dasari, G. R. 2003. Soil-Pipelines Interaction in Sand under Upward Movement at Deep Embedment Condition. *12th Asian Regional Conference on Soil Mechanics and Geotechnical Engineering*, 1, 891-894.

DEM ANALYSIS OF SOIL-PIPELINE INTERACTION IN SAND UNDER LATERAL AND UPWARD MOVEMENTS AT DEEP EMBEDMENT

by

S. Yimsiri and K. Soga

A Technical Paper submitted for review and possible publication in
Geotechnical Engineering, Journal of the Southeast Asian Geotechnical Society

First submission: 27th July 2005

Authors:

1. Dr. Siam Yimsiri

   Assistant Professor, Department of Civil Engineering, Burapha University, Saensook, Muang, Chonburi 20131, Thailand

   Member of the Southeast Asian Geotechnical Society

2. Dr. Kenichi Soga

   Reader, Department of Engineering, University of Cambridge, Trumpington Street, Cambridge CB2 1PZ, UK

Corresponding author: Dr. Siam Yimsiri
Department of Civil Engineering,
Burapha University,
Saensook, Muang,
Chonburi 20131
THAILAND
Tel: +66-38-745900 ext 3358
Fax: +66-38-745806
email: ysiam@buu.ac.th

DEM ANALYSIS OF SOIL-PIPELINE INTERACTION IN SAND UNDER LATERAL AND UPWARD MOVEMENTS AT DEEP EMBEDMENT

S. Yimsiri[1] and K. Soga[2]

Abstract

The soil-pipeline interactions under lateral and upward pipe movements in sand are investigated using DEM analysis. The simulations are performed for both medium and dense sand conditions at different embedment ratios of up to 60. The comparison of peak dimensionless forces from the DEM and earlier FEM analyses shows that, for medium sand, both methods show similar peak dimensionless forces. For dense sand, the DEM analysis gives more gradual transition of shallow to deep failure mechanisms than the FEM analysis and the peak dimensionless forces at very deep depth are higher in the DEM analysis than in the FEM analysis. Comparison of the deformation mechanism suggests that this is due to the differences in soil movements around the pipe associated with its particulate nature. The DEM analysis provides supplementary data of the soil-pipeline interaction in sand at deep embedment condition.

1. Introduction

An understanding of pipeline response to vertical and lateral ground movements is essential in pipeline design. Rational design under these conditions requires knowledge of soil forces resulting from the relative soil-pipeline displacement. The design formulations of the load-displacement characteristics for soil-pipeline interactions are given by ASCE's

---

[1] Assistant Professor, Department of Civil Engineering, Burapha University, Saensook, Muang, Chonburi 20131, Thailand

[2] Reader, Department of Engineering, University of Cambridge, Trumpington Street, Cambridge CB2 1PZ, UK

"Guideline for the Seismic Design of Oil and Gas Pipeline System (1984)". This Guideline recommends that the peak dimensionless forces and the displacement at peak forces are functions of the embedment depth of the pipe and soil friction angle, and that the non-linear relationship between the force and displacement is modeled by a rectangular hyperbola. These design values are derived from the database of pipe testing at relatively shallow embedment depths. However, there are situations where the pipe embedment ratios can be deeper than the values given in the guideline. Typical scenarios are the construction of a large embankment over an area with existing pipelines and installation of deep pipelines due to already congested underground space. If the design is based on a linear extrapolation from the ASCE data, the Guideline would provide very large values for the peak load exerted on the pipe and the stiffness of the soil-pipeline interaction. This potential overestimation would in turn results in uneconomical design.

The deep embedded pipeline problem has been investigated by Yimsiri et al. (2004). They examined various analytical solutions available for the peak forces onto a pipe or strip anchor and showed that there are large differences in the computed peak dimensionless forces for deep embedment conditions. It was concluded that a linear extrapolation from the ASCE data derived from shallow depth condition should not be employed because of the change in failure mechanism from shallow (i.e. ground surface dependent) to deep embedment conditions (i.e. ground surface independent). They performed finite element analysis to examine the transition in both medium and dense sands. Unfortunately, it is not possible to validate their findings because full-scale pipe loading experimental results or any other supplementary data are not available.

This study has been undertaken to provide supplementary data for deep embedded pipes using the Distinct Element Method (DEM). First, DEM analysis was conducted for shallow embedment depth conditions to calibrate the input parameters by comparing the results to the experimental data reported by Trautmann & O'Rourke (1983). The analysis was then extended to deeper embedment conditions. Due to its discontinuous nature, it is considered that DEM should better simulate the soil movement close to the pipe at large pipe displacements and, hence, may yield more realistic results to the problem compared to the continuum-based finite element analysis.

2. Distinct Element Method Analysis

2.1 Model assumptions

The pipe loading experiments were simulated using the distinct element method based on the approach by Cundall & Strack (1979). The distinct element code PFC^{3D} (Itasca, 1999) was employed. Arbitrarily sized spherical particles are treated as rigid bodies and are allowed to overlap one another at the contact points creating interparticle forces. The contacts between particles are characterized through the stiffness and slip condition. No bonding between particles is employed in this study to simulate uncemented dry sand.

The linear elastic contact model was employed; the contact force and relative contact displacement are linearly related by a constant contact stiffness. Two stiffness values are required for each contact; they are (i) normal contact stiffness k_N and (ii) tangential contact stiffness k_T (force/displacement). In this study, they are assumed to be equal ($k_{N,sand} = k_{T,sand}$). The parametric study shows that the change in the particle tangential contact stiffness has minimal effects on the pipe loading results; the change in $k_{T,sand}$ from $k_{N,sand}$ to $5k_{N,sand}$ results in negligible change in the force-displacement curve. Particle sliding occurs when the tangential contact force reaches its maximum allowable value, which is computed from the coefficient of inter-particle friction angle between the two contacting entities multiplied by the normal contact force.

The tank and pipe were modeled by series of planar wall. The dimensions of the tank are the same as the actual tank used by Trautmann & O'Rourke (1983) for the cases of H/D or $H_c/D < 30$ (see Fig. 1), whereas the width was doubled for the cases of H/D or $H_c/D \geq 30$ to reduce any boundary effects (see Fig. 2). Herein, H is the depth to the bottom of the pipe (normally used in lateral pipe loading cases), H_c is the depth to the center of the pipe (normally used in upward pipe loading cases), and D is the pipe diameter. The circular cross-section of the pipe was modeled by a 16-side polygon. The tank wall was assumed to be smooth; that is, it has a normal contact stiffness equal to that of the particles but has zero tangential contact stiffness and zero surface friction. The pipe has identical contact stiffness in both normal and tangential directions and the values are equal to that of the particles. The pipe has its surface friction angle (ϕ_{pipe}) equal to half of the inter-particle friction angle of sand (ϕ_μ). The parametric study shows that the change in the pipe surface friction angle between $\phi_{pipe} = \phi_\mu/2$ and $\phi_{pipe} = \phi_\mu$ has a negligible effect on the force-displacement curve.

Sand was modeled as a collection of spherical particles with its size distribution following the normal Gaussian distribution. Due to computational limitation, it was not possible to model using the actual size particles (D_{10} = 0.2 mm and D_{60} = 0.52 mm). Therefore, the sand particles were modeled with larger size particles. To increase the computational speed, the size of the particles was also varied in various regions of the model; smaller particles were used in the region where large soil deformation is expected. For the cases of H/D or $H_c/D < 30$, typical numerical models used for the simulations are shown in Fig. 1. At the region near the pipe (Region A), the particles have $r_{average}$ = 12.5 mm with standard deviation = 2.5 mm (25 times larger than the actual sand used in the experiments). Further away (Region B), the particles have $r_{average}$ = 25.0 mm with standard deviation = 5.0 mm (50 times larger). When $H/D \geq 17.5$ or $H_c/D \geq 17$, another region (Region C) was added and it has particle sizes of $r_{average}$ = 37.5 mm with standard deviation = 7.5 mm (75 times larger). Fig. 2 shows typical soil models for cases with H/D or $H_c/D \geq 30$. The width is twice as large as that used in the shallow embedment cases in order to reduce the boundary effects. At Region D, the particles have $r_{average}$ = 25.0 mm with standard deviation = 5.0 mm (50 times larger than actual sand). Further away (Region E), larger particles are placed; $r_{average}$ = 37.5 mm and standard deviation = 7.5 mm (75 times larger). This allowed the number of particles to be less than 180,000 even for the deepest case. Results from the parametric study on particle size effects show that the case without small particles (12.5 mm average diameter) near the pipe computes a slightly larger peak force than the case with small particles. However, the difference was less than 8%. Hence, in relation to the pipe diameter, the particle size used was considered to be small enough in order to evaluate pipe loads.

The DEM analysis consists of the following four steps.

1. Tank set-up: Test tank was filled with predetermined number of reduce-sized particles. The radius of the spheres was expanded to a specified value to obtain a pre-determined void ratio.

2. Initial condition: The generated balls were subjected to gravitational force to reach the geostatic condition. During this stage, there were some movements of balls due to the deformations at the particle contacts which resulted in some changes in void ratio and embedment depth. This was taken into account by trial & error of the initial void ratio and embedment depth during the tank set-up stage. Typical void ratios obtained were 0.63 – 0.69 for medium sand (0.67 was the target value) and 0.56 – 0.62 for dense sand (0.58 was the target value).

3. Pipe installation: The pipe was placed into the model by deleting the balls that were located at the desired pipe location. The model was then permitted to reach equilibrium by allowing the pipe to slightly adjust its location by maintaining the equilibrium

conditions of the pipe. The examples of the DEM models after pipe installation are shown in Fig. 3.

4. Pipe pulling: The pipe was pulled in lateral or upward directions by imposing displacements to the pipe. The other direction was free to move. The rotation of the pipe was not allowed, which is consistent with the experimental set-up by Trautmann & O'Rourke (1983).

2.2 Material input parameters

The input parameters for DEM analysis are listed in Table 1. Most of the parameters were determined by calibrating the numerical results with the experimental data of (i) triaxial test results of the sands used for the tank experiments (Turner & Kulhawy, 1987) and (ii) the actual pipe loading test results at shallow depths (Trautmann & O'Rourke, 1983).

Results from the triaxial test simulations show that the DEM analysis (using $k_{N,sand} = k_{T,sand}$) can simulate the measured stress-strain relationship by using a high value of inter-particle friction angle ($\tan \phi_{\mu} = 3.0$) as shown in Fig. 4. This unusually high value is mainly due to the use of smooth spherical particles, which allows excessive particle rolling (e.g. Thomas & Bray, 1999). At low values of the inter-particle friction angle, it was not possible to achieve a good fit to the experimental data. The contact stiffness was also varied in order to fit the data. Fig. 5 shows the contact stiffness evaluated at different confining stresses and the following empirical relationship was obtained.

$$k \text{ (N/m)} = 204340\, p_o'^{0.41} \qquad (p_o' \text{ in kPa}) \qquad \ldots\ldots\ldots\ldots \qquad (1)$$

Initially this relationship was used for the pipe loading simulations by assigning the initial effective overburden stress at the pipe level as p_o'. Unfortunately, it was found that the calculated pipe force was smaller and the force-displacement characteristic was less stiff than the measured ones by Trautmann & O'Rourke (1983). This is primarily because there is a significant increase in the mean pressure in front of the pipe as the pipe displaces the surrounding soil. The increase of mean pressure from the initial p_o' is much greater than that observed in typical triaxial testing. This in turn resulted in large increase in contact stiffness of the soil around the pipe. By considering that the mean pressure and hence the contact stiffness vary at various parts of the model during pipe loading, a strict application of Eq. (1) is possible by implementing it into the stress dependent contact stiffness model $k = \mathrm{f}(f_N)$, where f_N is the inter-particle normal contact force. Instead, however, a different approach was employed in this study. As described in the next section, the contact stiffness and interparticle friction values at different embedment depths were first back-calculated by fitting the DEM pipe loading curve to the experimental data at shallow depths reported by Trautmann & O'Rourke (1983) and then the calibrated values were used to simulate the deep embedment cases.

3. DEM results

3.1 Calibration analysis using shallow embedment cases

Trautmann & O'Rourke (1983) performed large-scale tank experiments at shallow depths with embedment ratios ranging from 1.5 to 13. Their results were used here to calibrate the DEM input parameters. The simulations were performed with tan ϕ_μ = 0.5, 1.0, 3.0. At first, it was intended to use tan ϕ_μ = 3.0 only, which was consistent with the value found from the triaxial simulation. However, it was found that lower values of inter-particle friction could also be used to achieve reasonable match to the experimental data if large contact stiffness values were adopted. The examples of the computed force-displacement relationships of lateral and upward pipe loading are shown in Figs. 6 and 7, respectively. The curves are similar to the experimental data as well as the finite element analysis results reported by Yimsiri et al. (2004). The FE analysis has been undertaken with two soil models, i.e. Mohr-Coulomb model (MC) and Nor-Sand model (NS).

The peak dimensionless forces obtained from the DEM analysis are compared with the experimental results in Fig. 8. The peak forces were evaluated either by (i) the distinct peaks or the constant ultimate values in the load-displacement curves, or (ii) the values obtained from hyperbolic fitting of the load-displacement curves if the ultimate values did not reach a constant value (i.e. the procedure of which was used by Trautmann & O'Rourke (1983)). In upward pipe loading, it was not possible to run the cases of very shallow depths due to instability of model set-up.

The contact stiffness evaluated from this curve fitting exercise and the initial vertical effective stress at the pipe level are plotted in Fig. 9 and the following empirical relationships suitable for the two boundary value problems are obtained.

<u>Lateral pipe loading</u>

$$\left.\begin{array}{ll} k\ (\mathrm{N/m}) = 2118.095\sigma_c{}'^{2.201} & \text{for } \tan\phi_\mu = 0.5 \\ k\ (\mathrm{N/m}) = 1576.395\sigma_c{}'^{1.956} & \text{for } \tan\phi_\mu = 1.0 \\ k\ (\mathrm{N/m}) = 753.261.859\sigma_c{}'^{1.909} & \text{for } \tan\phi_\mu = 3.0 \end{array}\right\} \ldots\ldots\ldots\ldots\ldots\ldots \quad (2)$$

σ_c' (kPa) = vertical effective stress at bottom of pipe

Upward pipe loading

$$\left.\begin{array}{ll} k\ (\text{N/m}) = 6.714\sigma_c'^{3.813} & \text{for } \tan\phi_\mu = 0.5 \\ k\ (\text{N/m}) = 41.072\sigma_c'^{2.761} & \text{for } \tan\phi_\mu = 1.0 \\ k\ (\text{N/m}) = 112.859\sigma_c'^{2.176} & \text{for } \tan\phi_\mu = 3.0 \end{array}\right\} \ldots\ldots\ldots\ldots\ldots\ldots \quad (3)$$

σ_c' (kPa) = vertical effective stress at center of pipe

These relationships were used to assign input parameters for the DEM analysis of deep embedment conditions.

3.2 DEM analysis of deep embedment cases

Loading of a deep embedded pipe was simulated using the input parameters calibrated by the shallow pipe loading cases. Examples of the computed force-displacement curves are shown in Figs. 10 and 11 along with the result from the finite element analysis reported by Yimsiri et al. (2004). In case of medium sand, the DEM results are consistent with the FEM results (Figs. 10(a) and 11(a)). In case of dense sand, the computed peak forces from the DEM analysis of tan ϕ_μ = 0.5 are considerably larger than the FEM results. This is due to larger contact stiffness employed for the cases of tan ϕ_μ = 0.5 and the side boundary is influencing the results as discussed later. The force-displacement curves for the case of tan ϕ_μ = 3.0 are closest to the FEM data; however, its peak force is still somewhat larger (Figs. 10(b) and 11(b)).

Fig. 12 shows the relationships between the peak dimensionless force and embedment ratio obtained from the DEM, FEM, and analytical solutions. The results from the cases of dense sand with tan ϕ_μ = 0.5 are not included due to the side boundary effect. For lateral pipe movement in medium sand, the DEM analysis yields consistent results with FEM analysis. In case of dense sand, however, the DEM analysis yields consistent results with FEM only when H/D is smaller than 30. For $H/D > 30$, the DEM gives somewhat larger peak dimensionless force than the FEM and a more gradual transition from shallow to deep failure mechanisms is observed. Fig. 12 (a) also includes the relationship proposed by Oversen (1964), which is recommended in the ASCE Guideline. Oversen's model gives relatively good match to the computed transition of the peak dimensionless force from shallow to deep embedment conditions but slightly overestimates the peak dimensionless forces. At H/D of 40, Oversen's model overestimates the peak dimensionless forces from the DEM analysis by approximately 20% for both medium and dense sand cases.

Similar observation can be made for upward pipe movement as shown in Fig. 12(b). For medium sand, the DEM analysis yields consistent results with FEM analysis. For dense sand, the DEM analysis yields consistent results with FEM only when H_c/D is smaller than 40. For $H_c/D > 40$, the peak forces computed from the DEM analysis are somewhat greater compared to those by FEM and the DEM data exhibit a more gradual transition from shallow to deep failure mechanism. Fig. 12(b) also includes the relationship proposed by Meyerhof & Adams (1968). Meyerhof & Adams' model does not match the computed transition of the peak dimensionless force from shallow to deep embedment conditions and underestimates the critical peak dimensionless forces. At $H_c/D = 60$, Meyerhof & Adams' model underestimates the critical peak dimensionless forces from the DEM results by approximately 30% and 40% for medium and dense sands, respectively.

4. Discussion

4.1 Soil deformation pattern

The soil displacement patterns from the experiments, FEM, and DEM (tan $\phi_\mu = 3.0$) analyses of pipeline movement in medium sand at a shallow embedment depth are shown in Figs. 13 and 14 for lateral ($H/D = 11.5$) and upward ($H_c/D = 13$) pipe loading cases, respectively. Similarly, Figs. 15 and 16 show the soil displacement patterns for the dense sand cases. The DEM simulates circular motion of soil behind the pipe, which was observed in the experiments. It appears that a larger soil mass is influenced by the pipe loading in the DEM compared to the FEM, especially for dense sand. This may be the reason for the fact that the DEM computes larger peak forces at deeper depths.

The computed soil displacements from the DEM analysis of lateral pipe loading at a deep embedment depth ($H/D = 30$) are shown in Fig. 17. For medium sand, the deformation pattern shows deep failure mechanism, whereby the upward soil deformation does not extend to the ground surface. However, for dense sand, shallow failure mechanism with upward soil deformation at the ground surface is still observed. This is consistent with the peak dimensionless force plot presented in Fig. 12(a), which shows that a deep failure mechanism is reached at $H/D = 30$ for medium sand but the mechanism at the same embedment ratio is still in the transition state in dense sand.

The computed soil displacements from the DEM analysis of upward pipe loading at a deep embedment depth ($H_c/D = 30$) are shown in Fig. 18. For medium sand, the deformation pattern shows deep failure mechanism; however, for dense sand, shallow failure mechanism is shown. This is also consistent with the peak dimensionless force plot presented in Fig. 12(b), which indicates that a deep failure mechanism is reached at $H_c/D = 30$ for medium sand but the mechanism at the same embedment ratio is still in the transition state for dense sand.

The extent of soil mass involved in the pipe loading increases as the contact stiffness increases or the inter-particle friction angle decreases. It was found that the soil at the model boundary moves significant amount for the case of tan $\phi_\mu = 0.5$, indicating that the model boundary is influencing the pipe loading force. This is consistent with the large peak forces computed for the cases of tan $\phi_\mu = 0.5$ as shown in Figs. 10(b) and 11(b).

4.2 Selection of input parameters

In this study, the values for the contact stiffness and inter-particle friction angle were selected by fitting the triaxial compression data and pipe loading data. The fitting exercise indicates that both values are equally important and various combinations of the contact stiffness and tan ϕ_μ can yield similar peak forces. When a larger value of contact stiffness is used, a smaller inter-particle friction angle needs to be selected to fit the experimental data. Hence, the back-calculated values require proper evaluation.

As discussed before, the use of a high value of the inter-particle friction angle is due to the use of smooth spherical particles, which allow excessive particle rolling. This is indicated from the triaxial compression test simulation where tan ϕ_μ needs to be greater than 3.0 to fit the DEM data to the experimental results. For pipe loading simulation, it was possible to use smaller values of inter-particle friction angle (i.e. tan $\phi_\mu = 0.5$ and 1.0) if larger values of the contact stiffness are adopted. However, the low inter-particle friction angle produced unrealistic soil deformation pattern by pipe loading. Hence, the case of tan $\phi_\mu = 3.0$ is more realistic than the case of tan $\phi_\mu = 0.5$. This is confirmed by the fact that the force-displacement relationship obtained from the DEM analysis of the case of tan $\phi_\mu = 3.0$ matched well to the experimental data.

The power coefficient for the stress dependency on contact stiffness was 0.41 from the triaxial compression test simulation (see Eq. (1)). This is within the normal values for soils, which is approximately 0.5 (Hardin & Black, 1966). It has been shown that the triaxial stiffness (Young's modulus) has a relationship with confining stress in the same manner as the contact stiffness does (Chang & Liao, 1994). The power coefficient derived from the pipe loading simulations was much greater than the normal values for soils (see Eqs. (2) and (3)). In the simulations, a constant value of contact stiffness was assigned throughout the model. As the contact stiffness varies with mean pressure, a strict application of Eq. (1) is possible by implementing it into the stress dependent contact stiffness model. This approach was not pursued in this study due to computational complication. Hence, it should be noted that Eqs. (2) and (3) are model fitting parameters suitable for the particular boundary value problems investigated in this study and should not be considered as a real soil behavior.

5. Conclusions

The soil-pipeline interactions under lateral and upward pipe movements in sand were investigated using DEM. The simulations were performed for both medium and dense sand conditions at different embedment ratios of up to 60. For medium sand, the comparison of the peak dimensionless forces from the DEM and FEM analysis shows good match. For dense sand, the DEM data show more gradual transition from the shallow to deep failure mechanism and have a tendency to give somewhat larger peak forces at very deep depths. The investigation of the soil displacement patterns computed by DEM shows larger soil mass movement compared to FEM data, especially for dense sand. The advantage of DEM over FEM is its ability to simulate large movement of soil around the pipe. Also, the DEM analysis can continue with unlimited pipe movement until it reaches ultimate peak force (or further), whereas the continuum based FEM often stops at some pipe displacements before the peak force can be reached because large distortion of the mesh causes numerical convergence problem.

The DEM results from this study confirm the findings by Yimsiri et al (2004) that the calculation of the soil-pipeline interaction at deep embedment conditions should not base on a linear extrapolation from the ASCE data of shallower embedment depths. However, the DEM results suggest that (i) there may be a possibility of underestimation of the peak dimensionless force at very deep embedment depths if the design chart proposed by Yimsiri et al. (2004) is employed and (ii) the transition from shallow to deep failure mechanism may proceed more gradually than suggested by Yimsiri et al. (2004). The results from this DEM analysis together with earlier FEM analysis will serve as a Class-A prediction of future full-scale tank tests of this problem.

Acknowledgement

The research work reported in this paper was supported by a grant from the Thailand Research Fund (TRF).

References

ASCE COMMITTEE ON GAS AND LIQUID FUEL LIFELINES (1984). *Guidelines for the Seismic Design of Oil and Gas Pipeline Systems*, ASCE Technical Council on Lifeline Earthquake Engineering.

CHANG, C. S. and LIAO, C. L. (1994). Estimates of elastic modulus for media of randomly packed granules. *Applied Mechanics Review*, Vol. 47, No. 1, Part 2, pp. S197-S206.

CUNDALL, P. A. and STRACK, O. D. L. (1979). A discrete numerical model for granular assemblies. *Geotechnique* 29, No. 1, pp. 47-65.

HARDIN, B. O. and BLACK, W. L. (1966). Sand stiffness under various triaxial stresses. *Journal of the Soil Mechanics and Foundations Division*, ASCE, Vol. 92, No. SM2, pp. 27-42.

ITASCA CONSULTING GROUP, INC. (1999). *PFC^{3D}: Particle Flow Code in 3 Dimensions, Version 2.0*, Vol. 1, 2, 3.

MEYERHOF, G. G. and ADAMS, J. I. (1968). The ultimate uplift capacity of foundations. *Canadian Geotechnical Journal*, Vol. 5, No. 4, pp. 225-244.

OVERSEN, N. K. (1964). Anchor slabs, calculation methods and model tests. *Bulletin No. 16*, Danish Geotechnical Institute, Copenhagen, Denmark, pp. 1-39.

THOMAS, P. A. and BRAY, J. D. (1999). Capturing Nonspherical Shape of Granular Madia with Disk Clusters. *Journal of Geotechnical and Geoenvironmental Engineering*, Vol. 125, No. 3, pp. 169-178.

TRAUTMANN, C. H. and O'ROURKE, T. D. (1983). Behavior of Pipe in Dry Sand Under Lateral and Uplift Loading. *Geotechnical Engineering Report 83-7*, Cornell University.

TURNER, J. P. and KULHAWY, F. H. (1987). Experimental Analysis of Drilled Shaft Foundations Subjected to Repeated Axial Loads Under Drained Conditions. *Report to Electric Power Research Institute*, Cornell University.

YIMSIRI, S., SOGA, K., YOSHIZAKI, K., DASARI, G. R., and O'ROURKE, T. D. (2004). Lateral and Upward Soil-Pipeline Interactions in Sand for Deep Embedment Conditions. *Journal of Geotechnical and Geoenvironmental Engineering*, ASCE, Vol. 130, No. 8, pp. 830-842.

Table 1 Input parameters for DEM analysis

Parameters	**Values**
Normal contact stiffness of particle, $k_{N,sand}$	From Eqs. (2) or (3)
Tangent contact stiffness of particle, $k_{T,sand}$	$k_{T,sand} = k_{N,sand}$
Normal contact stiffness of pipe, $k_{N,pipe}$	$k_{N,pipe} = k_{N,sand}$
Tangent contact stiffness of pipe, $k_{T,pipe}$	$k_{T,pipe} = k_{N,pipe}$
Normal contact stiffness of wall, $k_{N,wall}$	$k_{N,wall} = k_{N,sand}$
Tangent contact stiffness of wall, $k_{T,wall}$	$k_{T,wall} = 0$
Inter-particle friction angle, ϕ_μ	$\tan \phi_\mu = 0.5$ or 1.0 or 3.0
Pipe surface friction angle, ϕ_{pipe}	$\phi_{pipe} = \phi_\mu/2$
Tank wall surface friction angle, ϕ_{wall}	$\phi_{wall} = 0$
Density of particle, ρ (kg/m^3)	2740
Radius of particle, r	Varies in Regions A, B, C, D, E

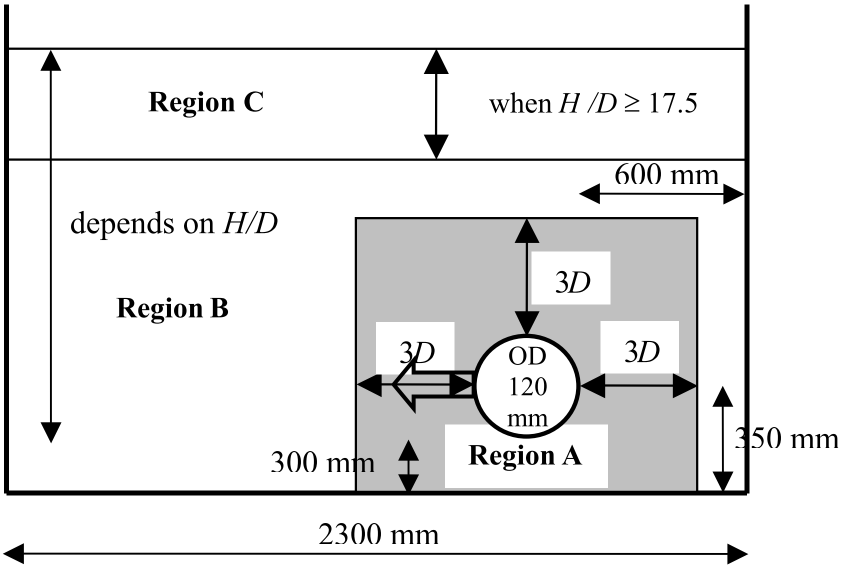

(a) Lateral pipe loading (H/D < 30)

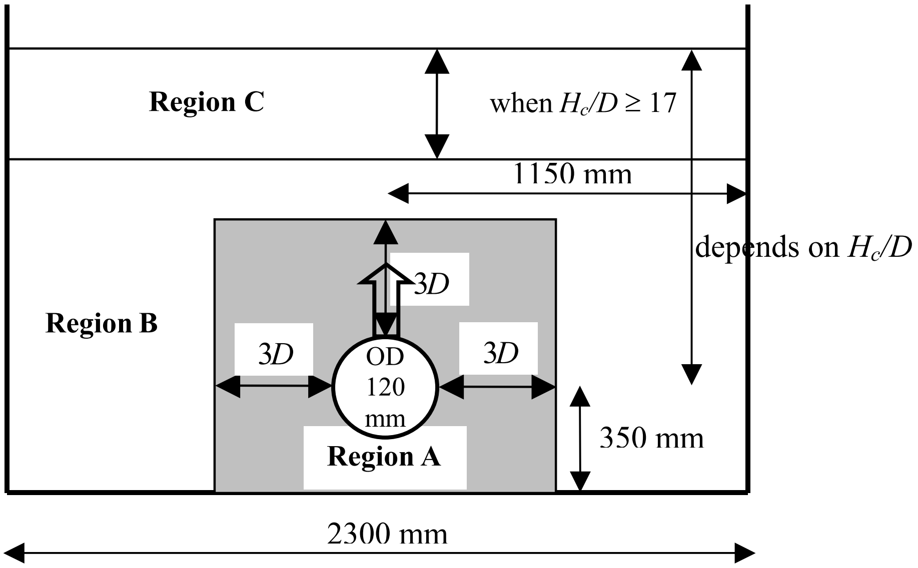

(b) Upward pipe loading ($H_c/D < 30$)

Figure 1 Various regions of the DEM model ($H/D < 30$ and $H_c/D < 30$)

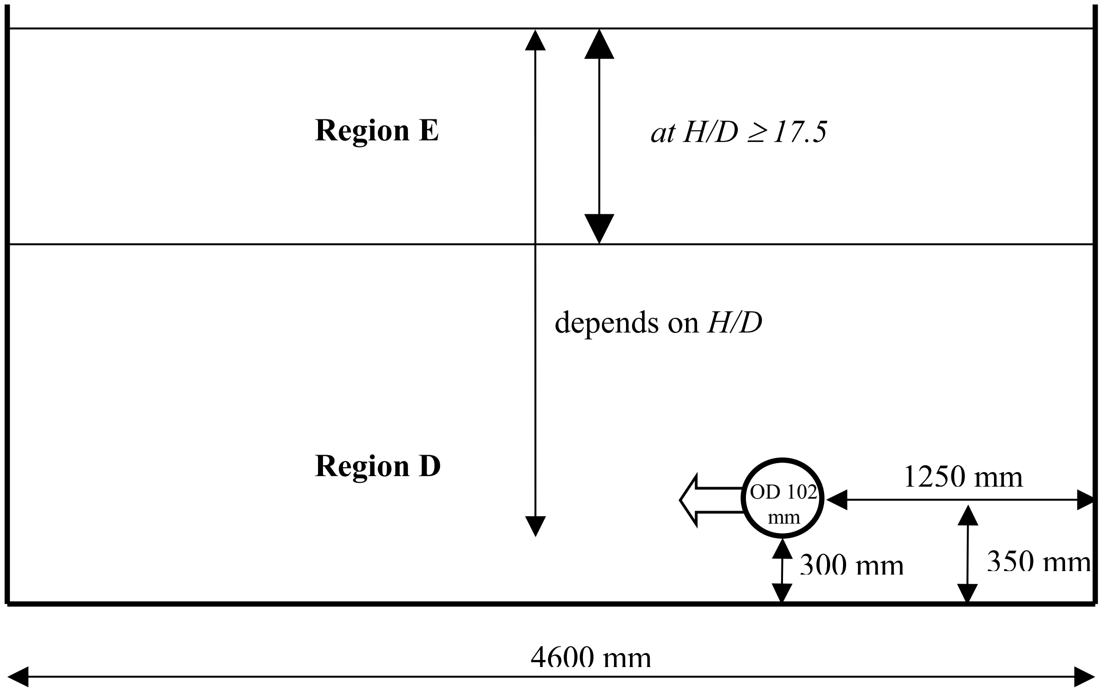

(a) Lateral pipe loading ($H/D \geq 30$)

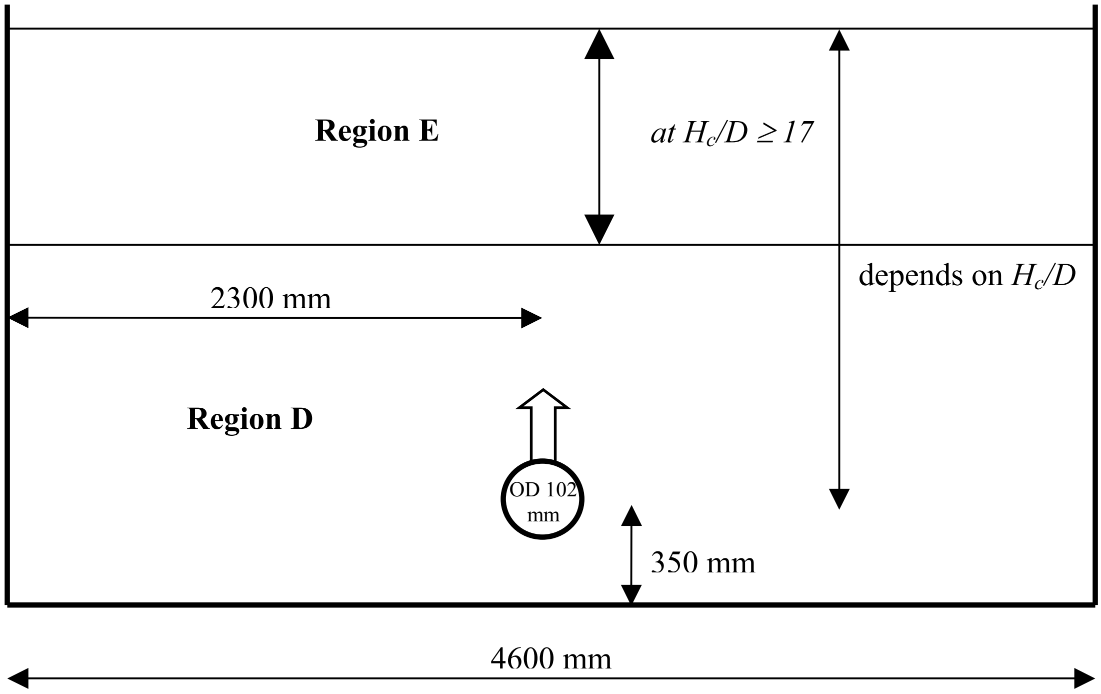

(b) Upward pipe loading ($H_c/D \geq 30$)

Figure 2 Various regions of the DEM model ($H/D \geq 30$ and $H_c/D \geq 30$)

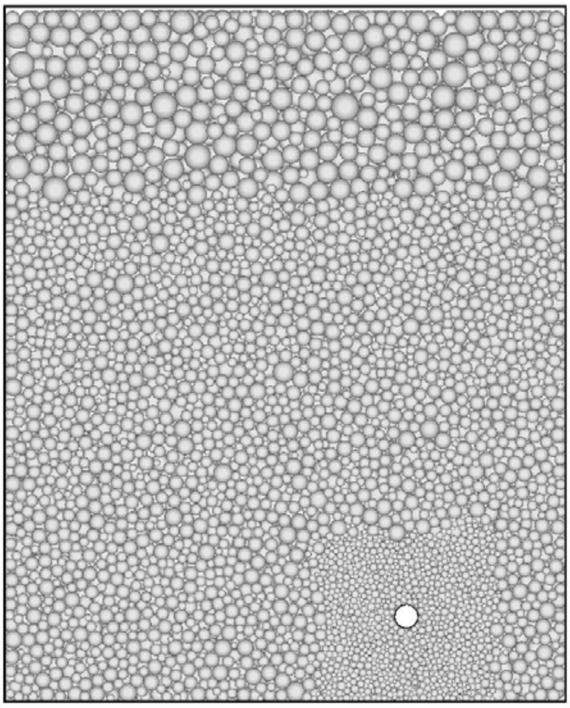

(a) Lateral pipe loading (medium sand, H/D = 25)

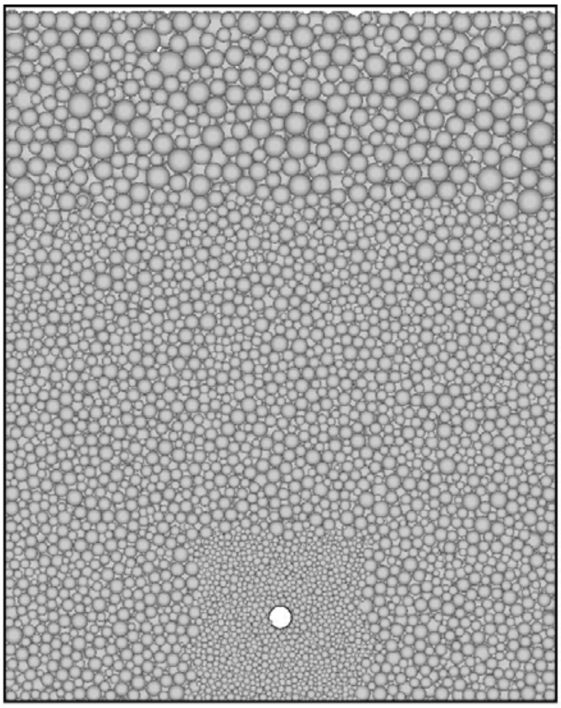

(b) Upward pipe loading (medium sand, $H_c/D = 25$)

Figure 3 Examples of DEM model

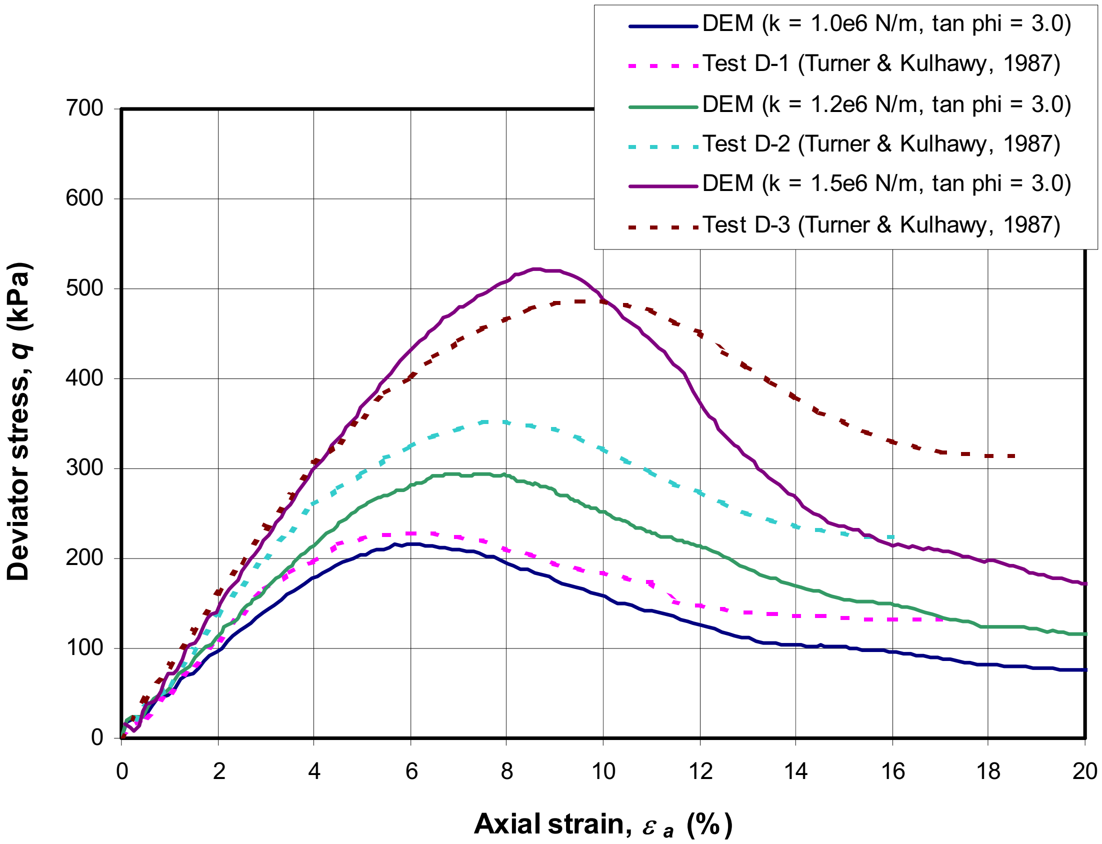

Figure 4 Calibration of DEM results against triaxial test data

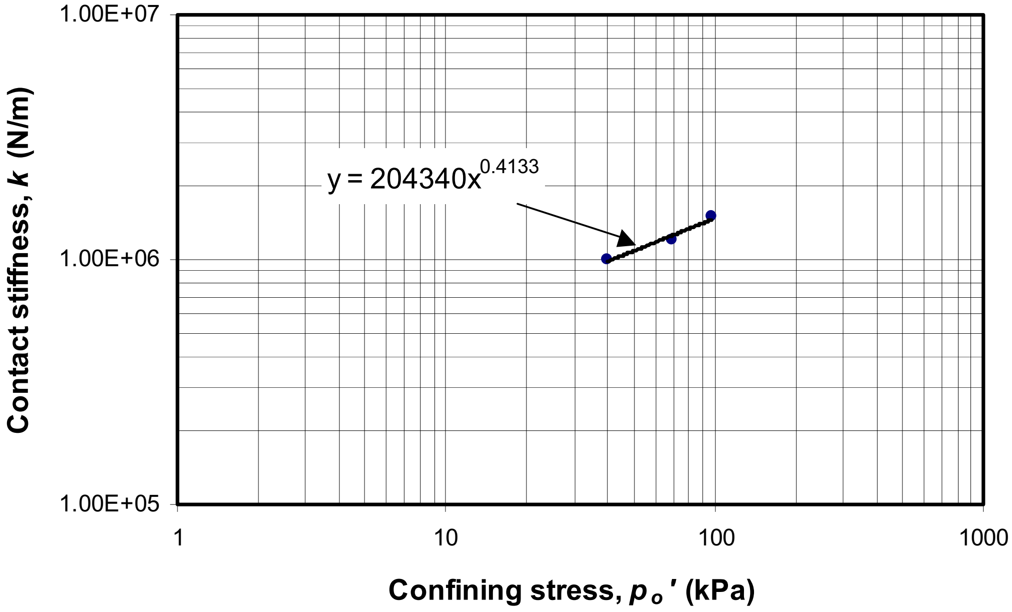

Figure 5 Relationship between contact stiffness and confining stress from triaxial simulation

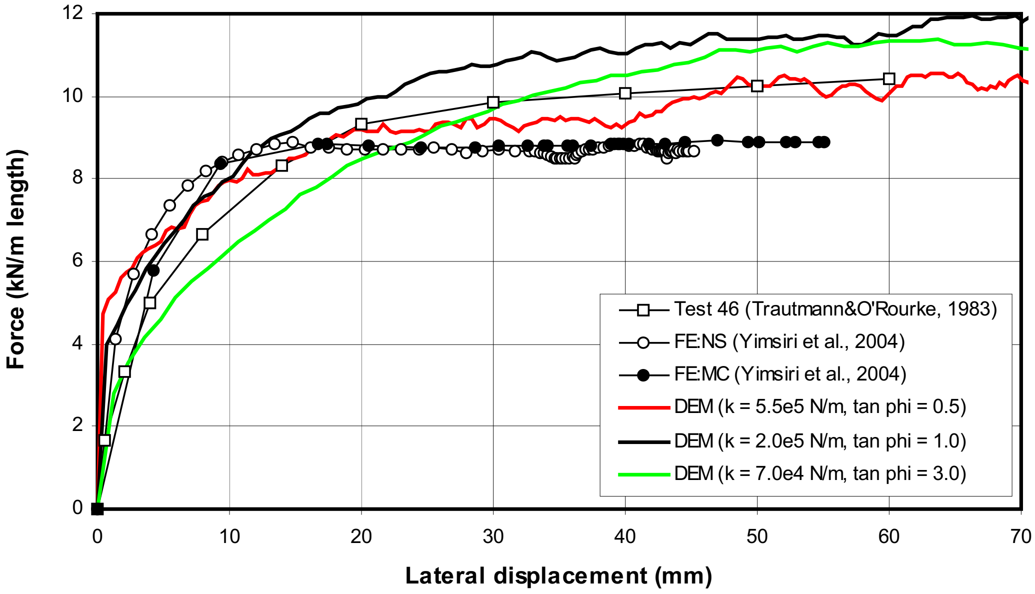

(a) H/D = 6, Medium sand

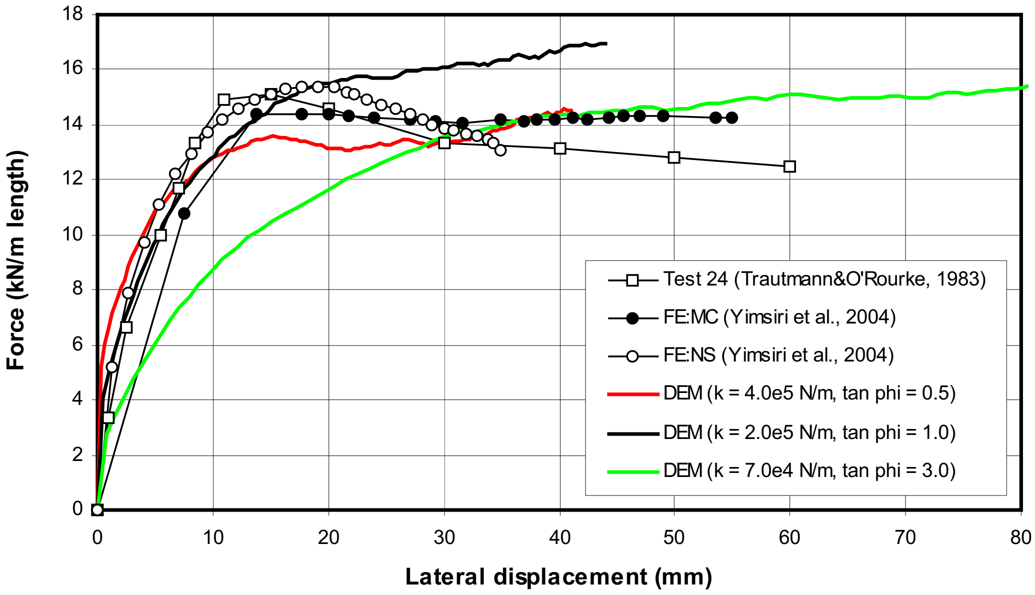

(b) H/D = 6, Dense sand

Figure 6 Force-displacement relationships at shallow embedment depth of lateral pipe loading

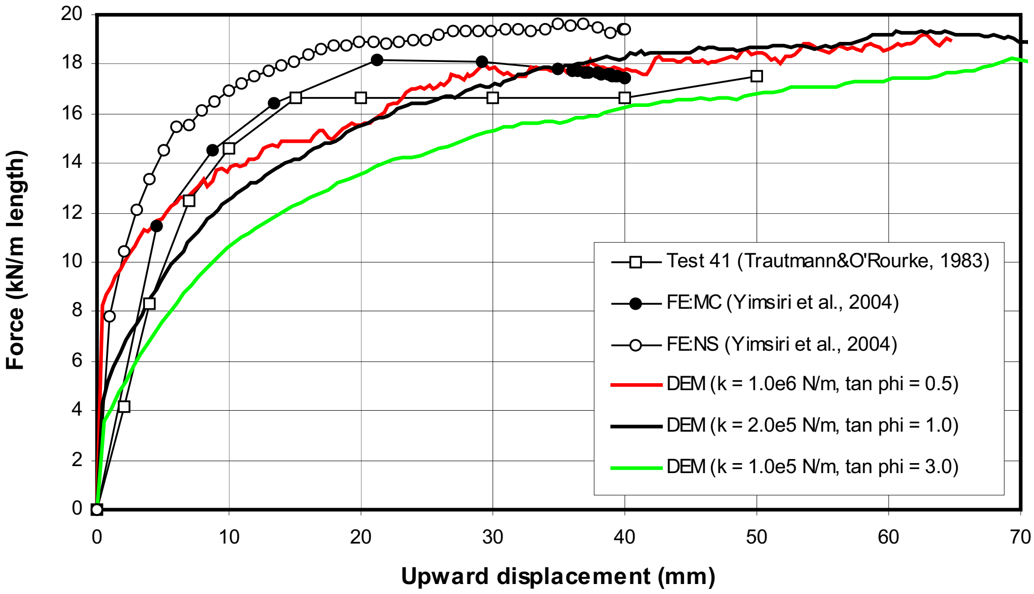

(a) H_c/D = 13, Medium sand

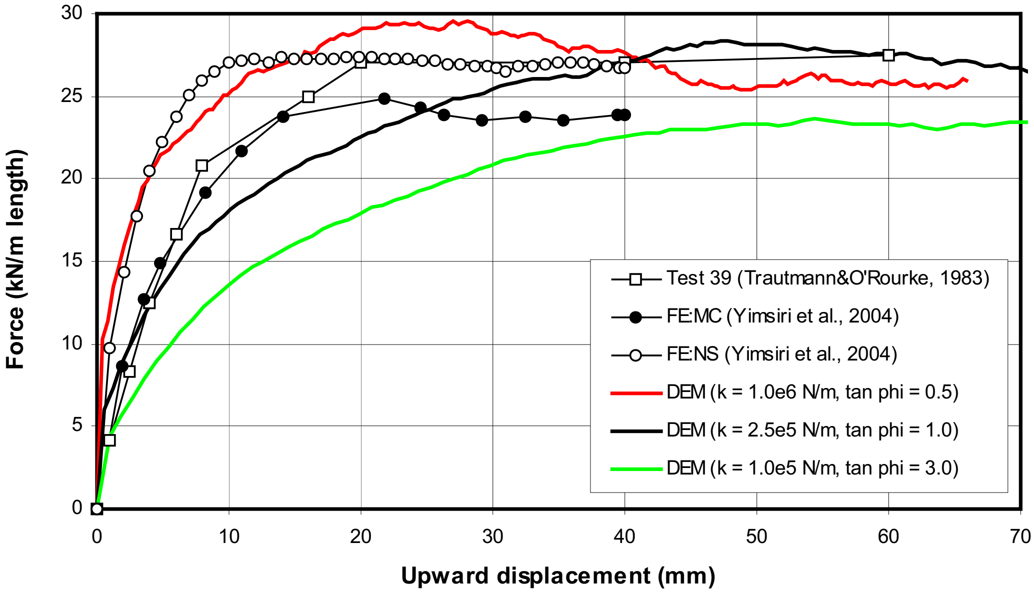

(b) H_c/D = 13, Dense sand

Figure 7 Force-displacement relationships at shallow embedment depth of upward pipe loading

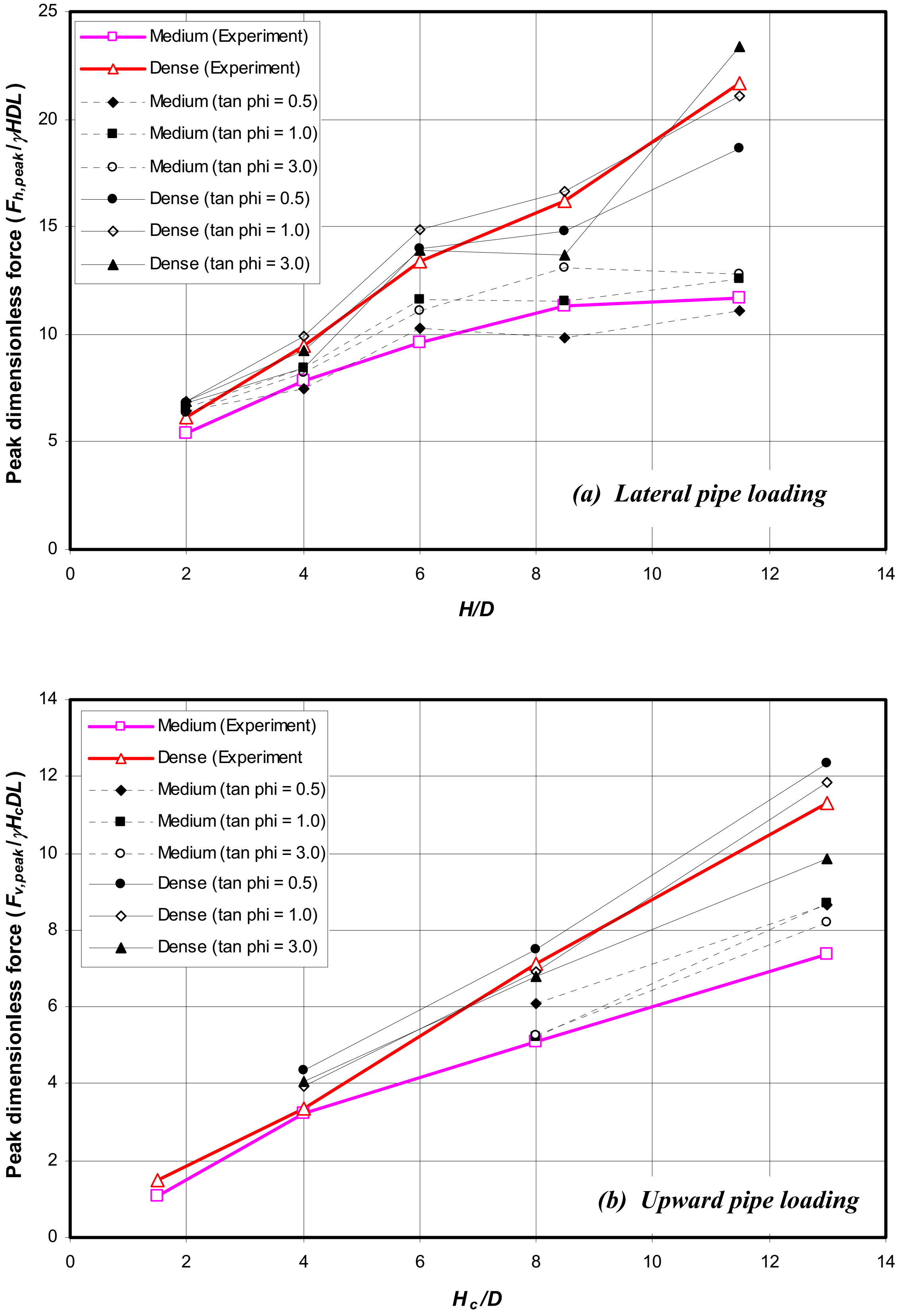

Figure 8 Plots of peak dimensionless force against embedment ratios at deep embedment depth

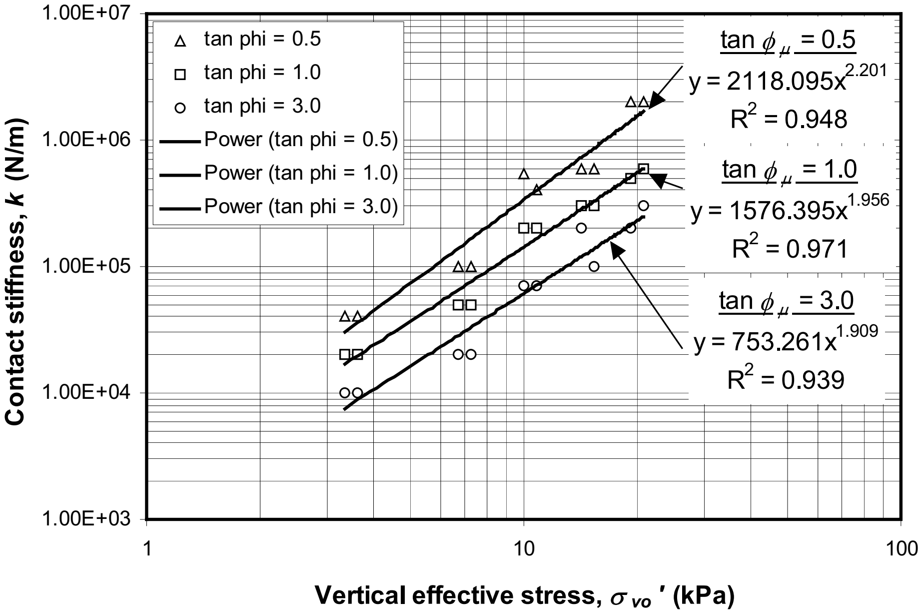

(a) Lateral pipe loading

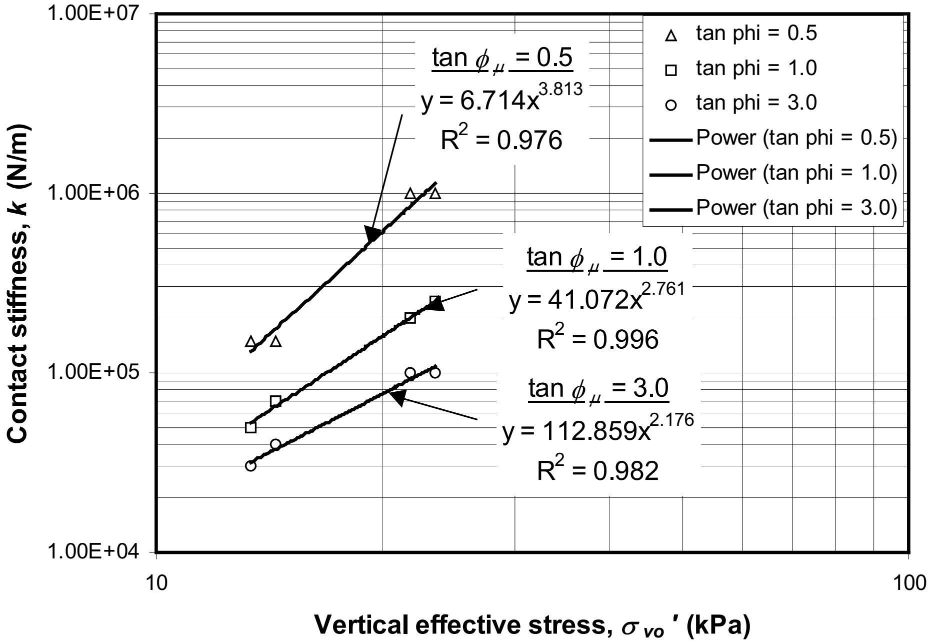

(b) Upward pipe loading

Figure 9 Relationship between contact stiffness and confining stress from pipe loading simulation

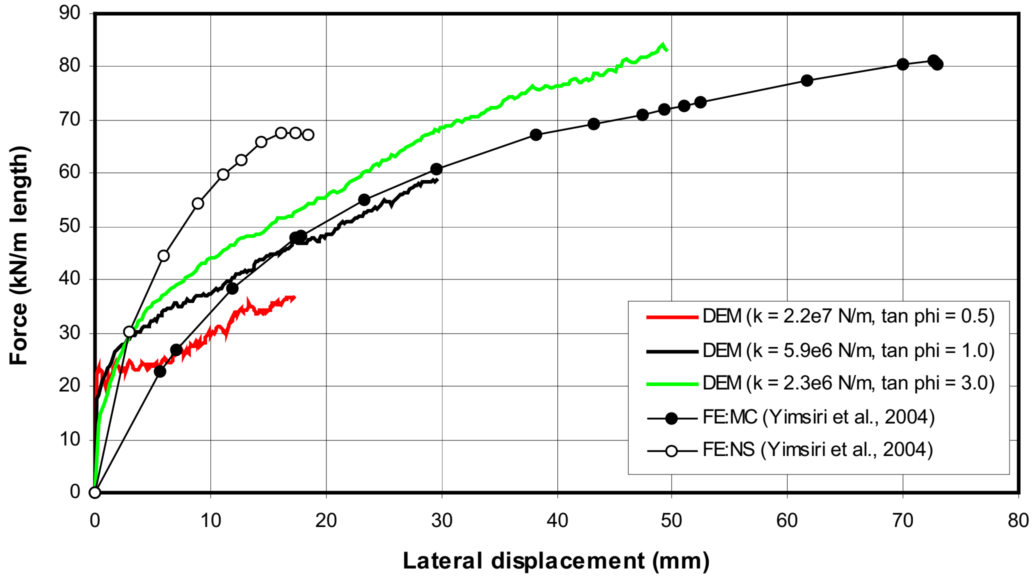

(a) H/D = 40, Medium sand

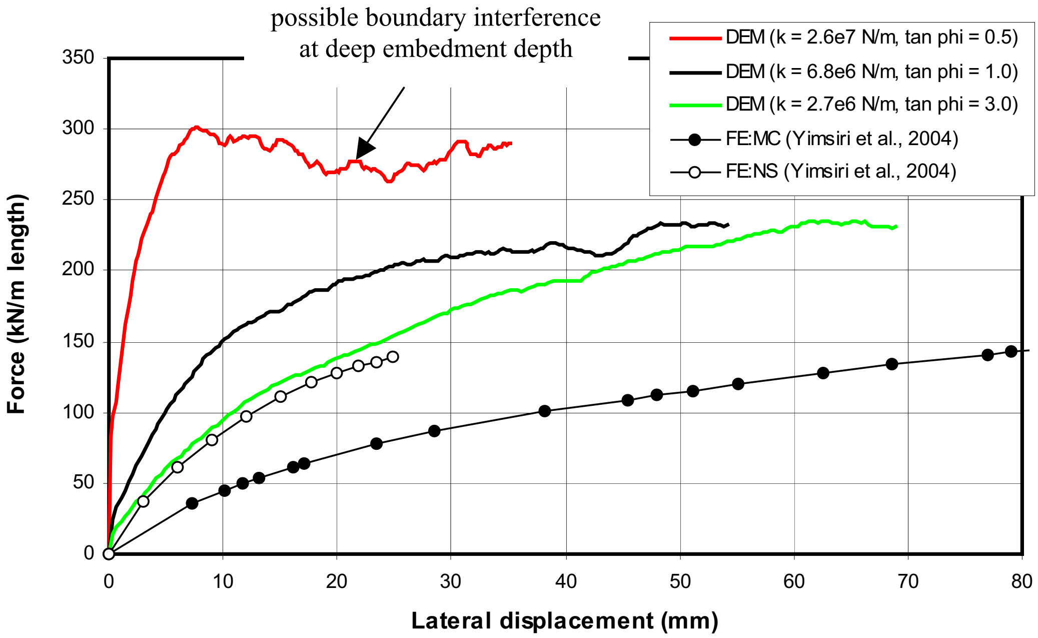

(b) H/D = 40, Dense sand

Figure 10 Force-displacement relationships at deep embedment depth of lateral pipe loading

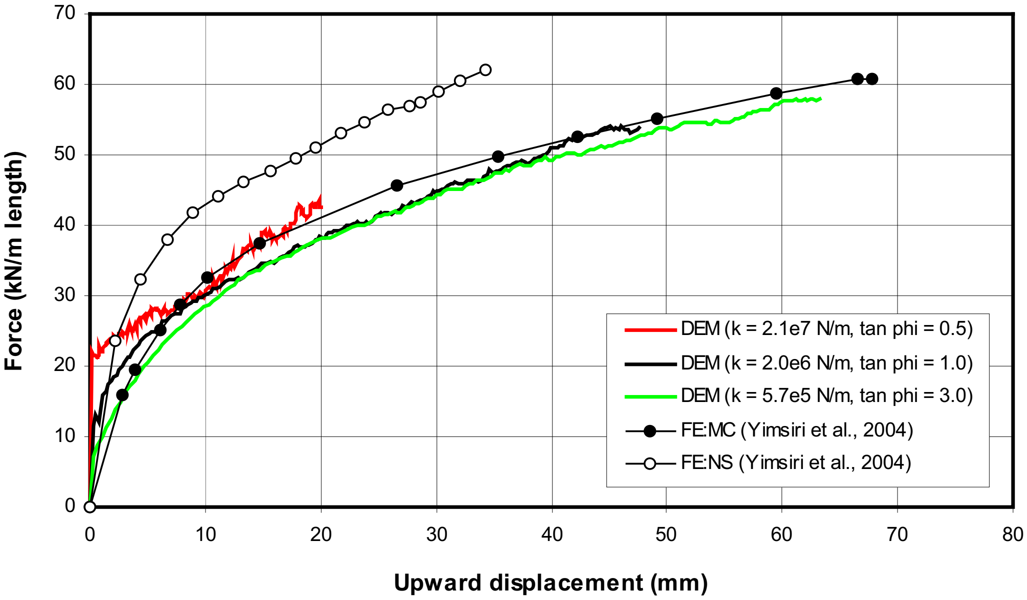

(a) H_c/D = 30, Medium sand

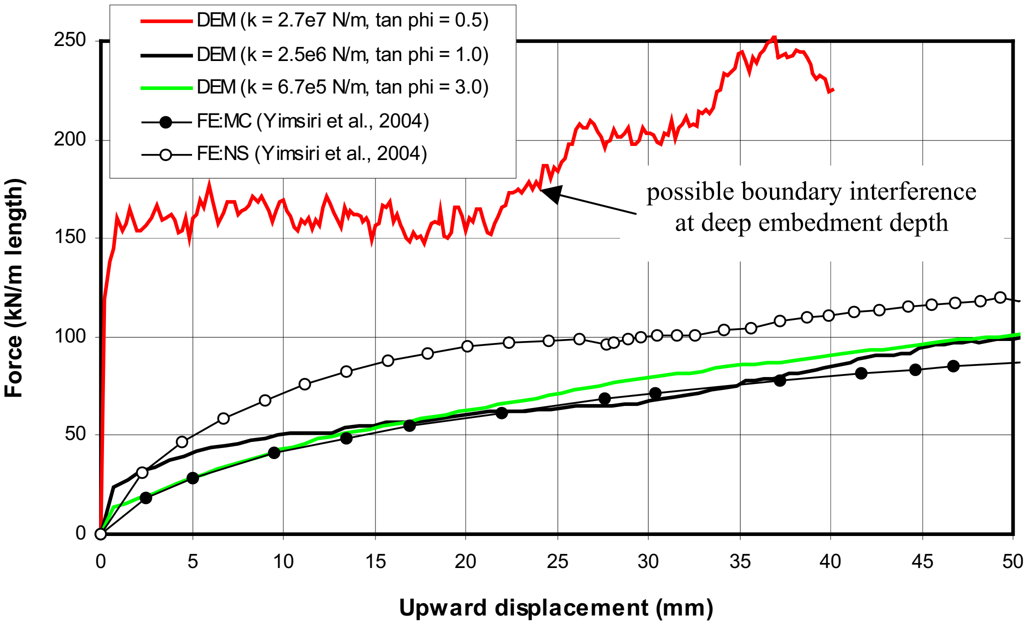

(b) H_c/D = 30, Dense sand

Figure 11 Force-displacement relationships at deep embedment depth of upward pipe loading

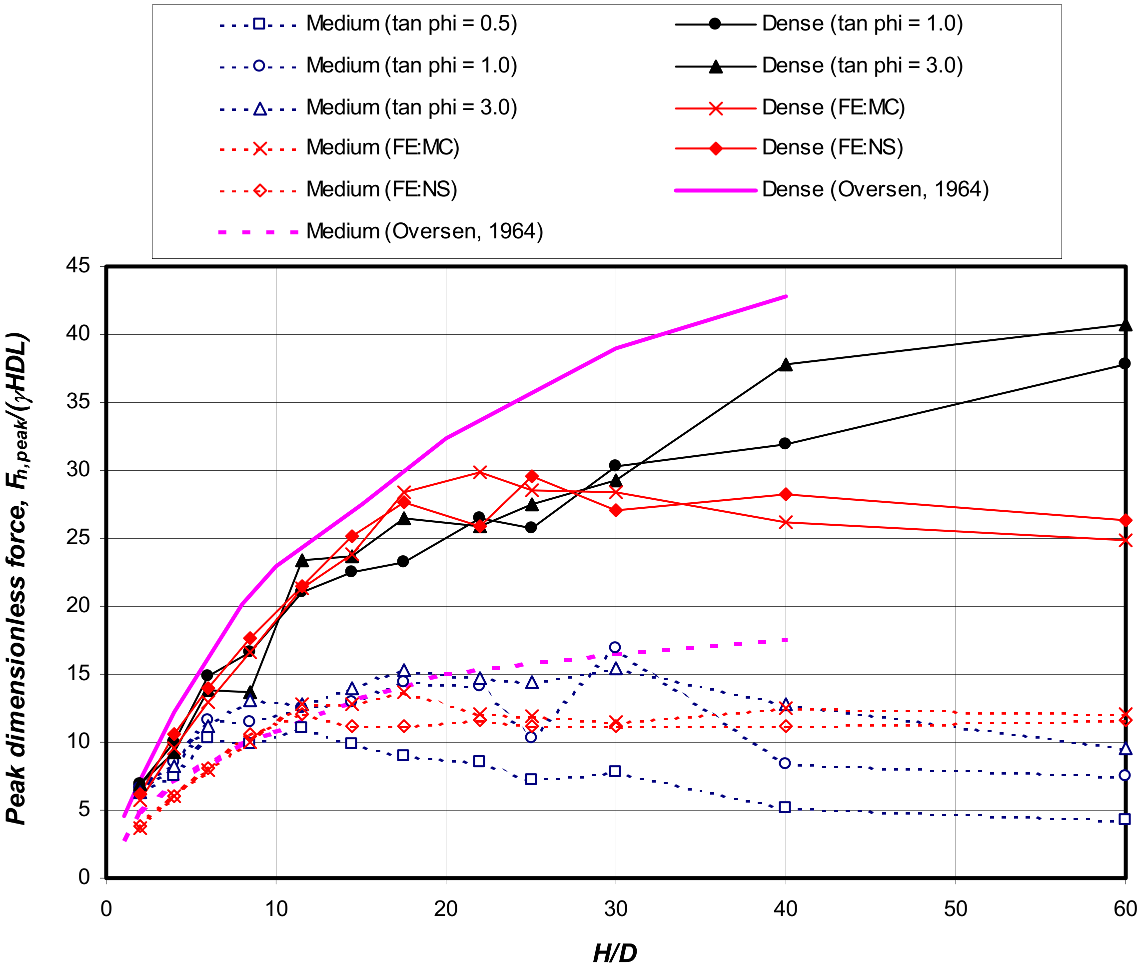

(a) Lateral pipe loading

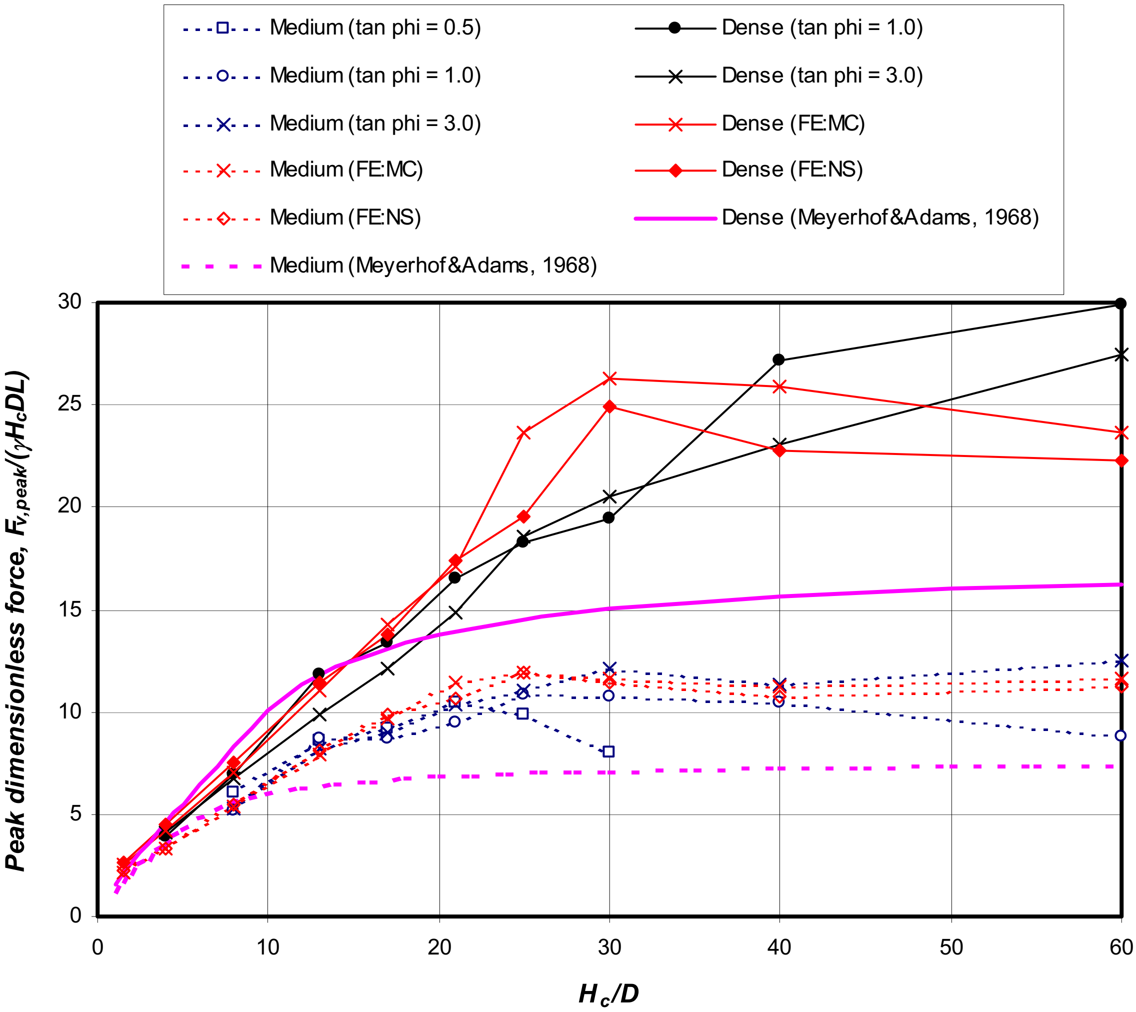

(b) Upward pipe loading

Figure 12 Comparison of peak dimensionless force from DEM, FEM, and analytical solutions at deep embedment depth

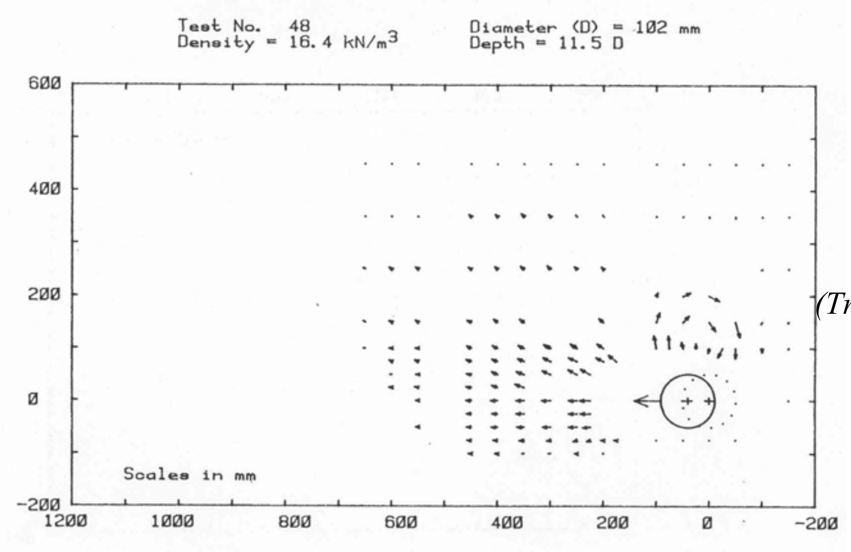

(a) Experimental tank test

(Trautmann & O'Rourke, 1983)

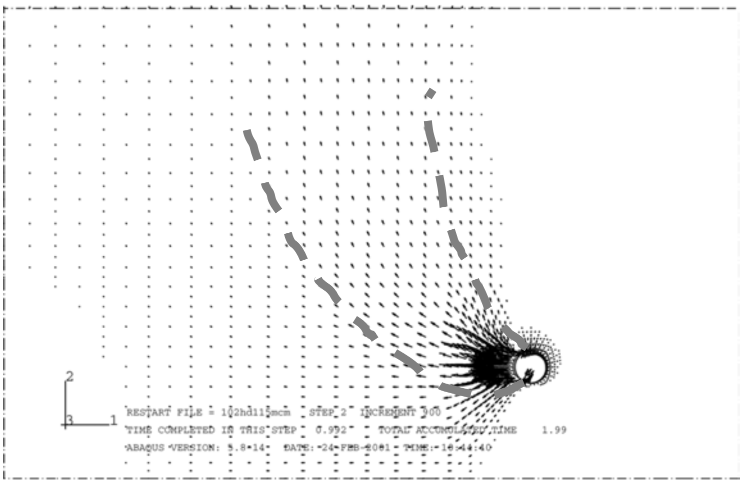

(b) FEM results

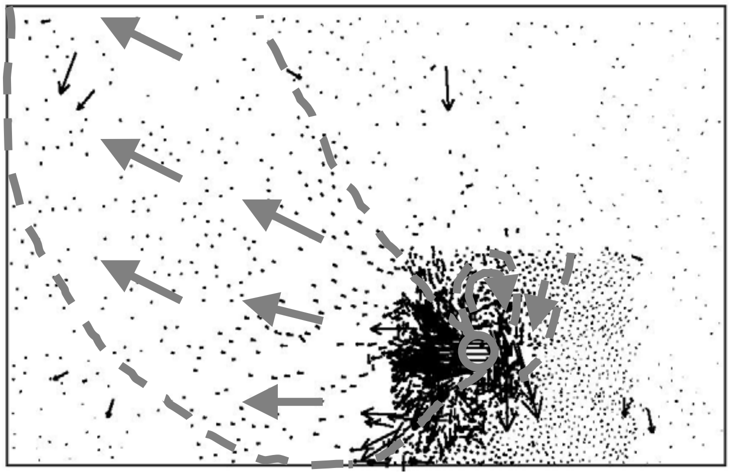

(c) DEM results (tan $\phi_\mu = 3.0$*)*

Figure 13 Comparison of displacement pattern of lateral pipe loading from experimental, FEM and DEM (*H/D* = 11.5, Medium sand)

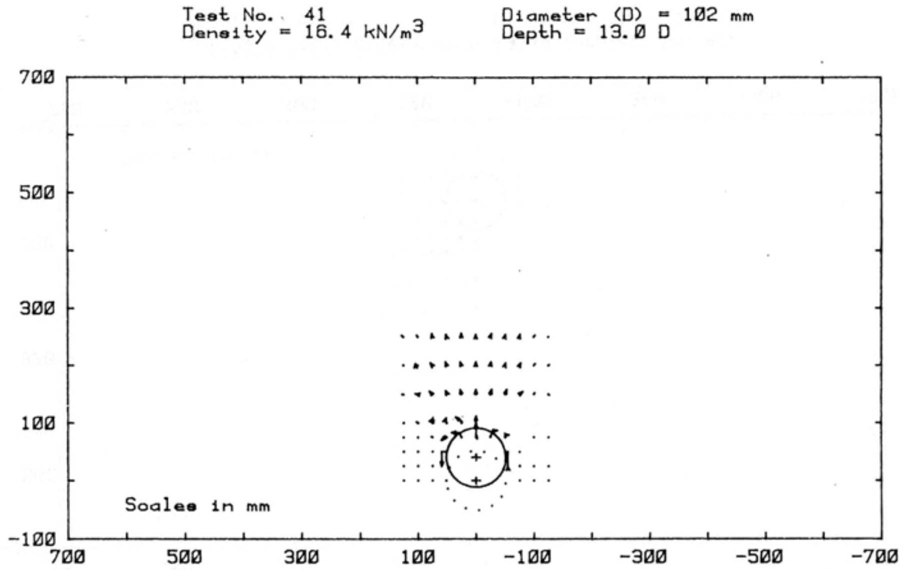

(a) Experimental tank test (Trautmann & O'Rourke, 1983)

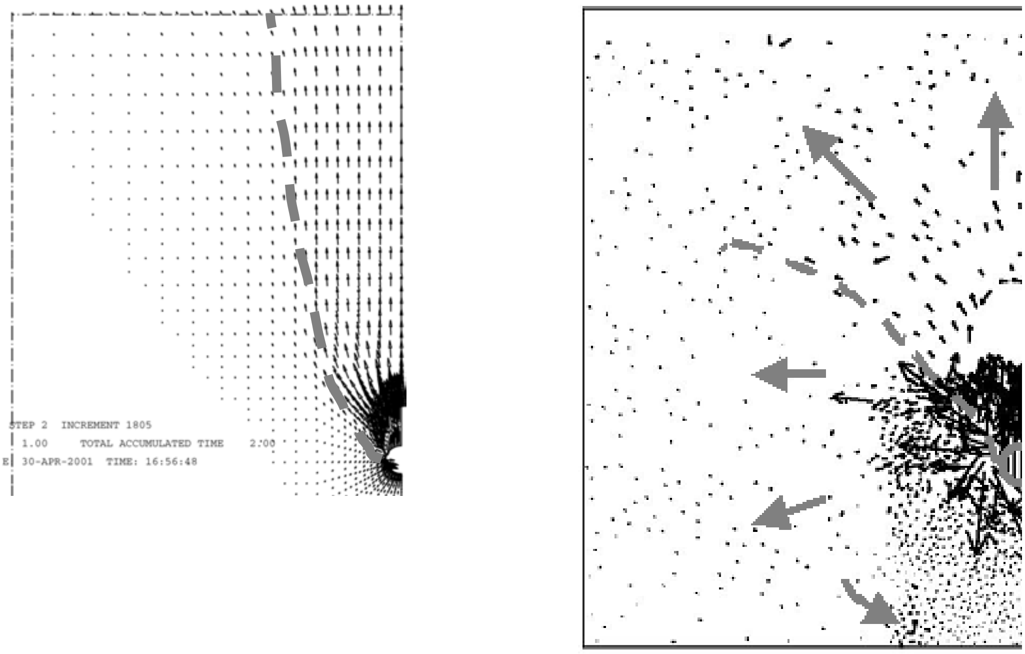

(b) FEM results

(c) DEM results (tan ϕ_μ = 3.0)

Figure 14 Comparison of displacement pattern of upward pipe loading from experiment, FEM and DEM (H_c/D = 13, Medium sand)

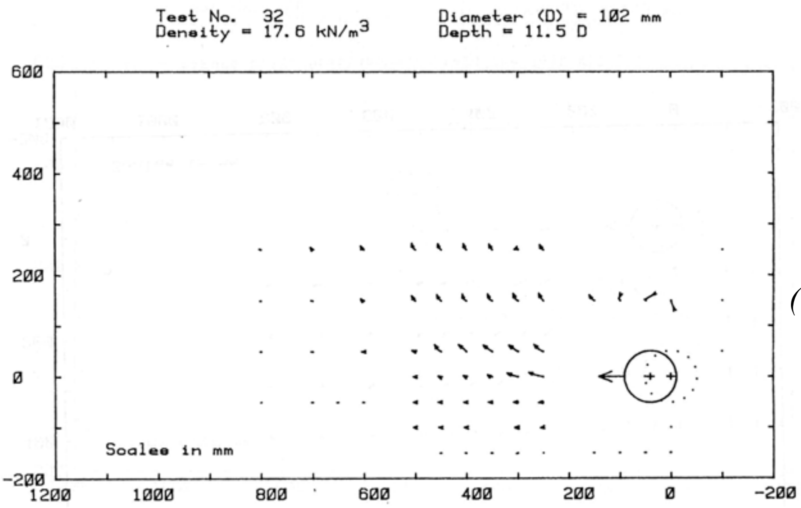

(a) Experimental tank test

(Trautmann & O'Rourke, 1983)

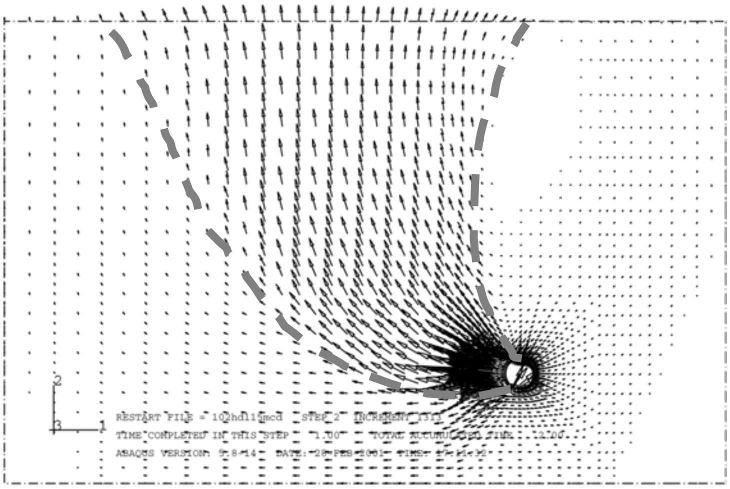

(b) FEM results

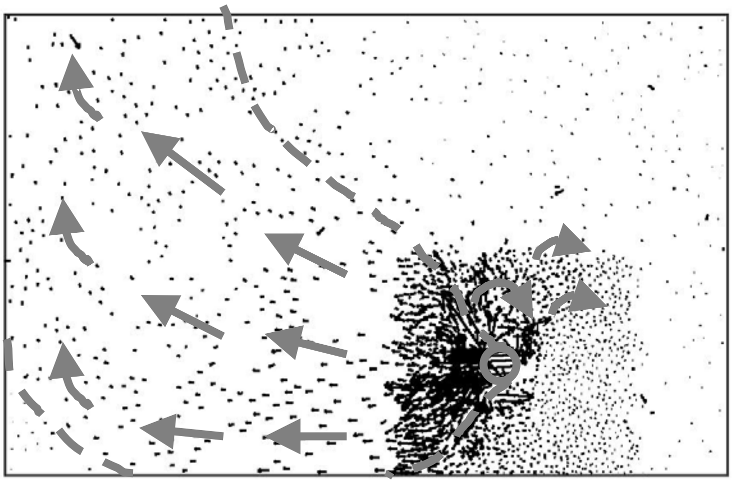

(c) DEM results (tan ϕ_μ = 3.0)

Figure 15 Comparison of displacement pattern of lateral pipe loading from experiment, FEM and DEM (*H/D* = 11.5, Dense sand)

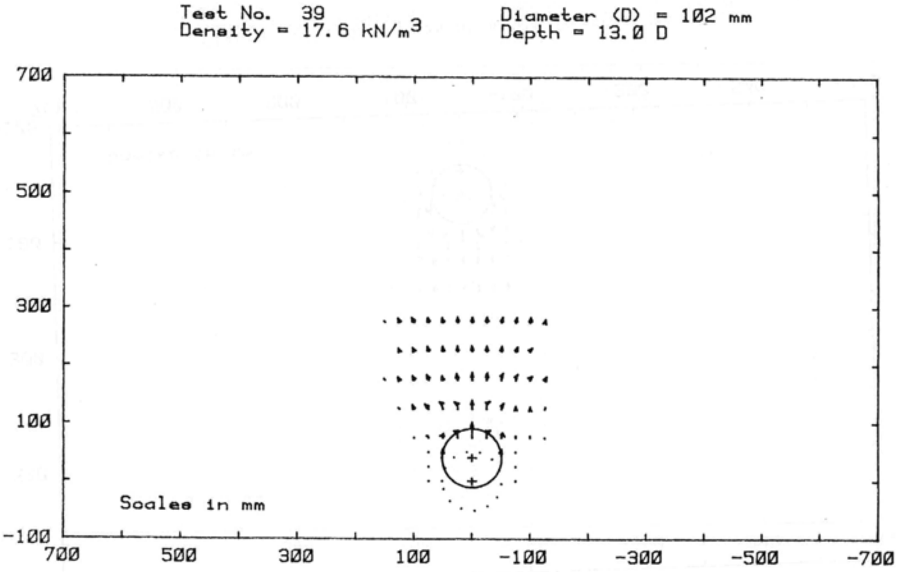

(a) Experimental tank test (Trautmann & O'Rourke, 1983)

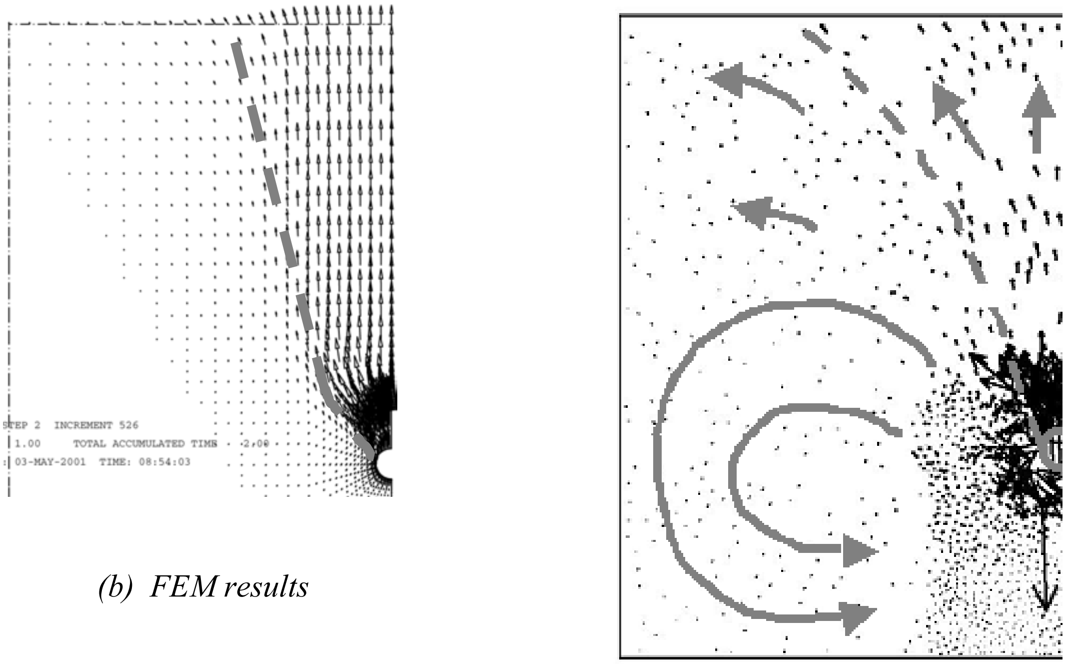

(b) FEM results

(c) DEM results (tan ϕ_μ = 3.0)

Figure 16 Comparison of displacement pattern of upward pipe loading from experiment, FEM and DEM (H_c/D = 13, Dense sand)

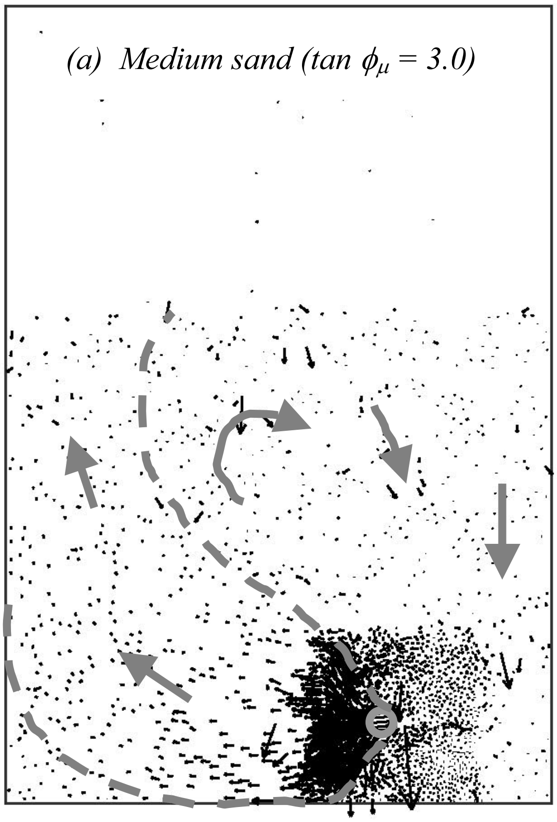

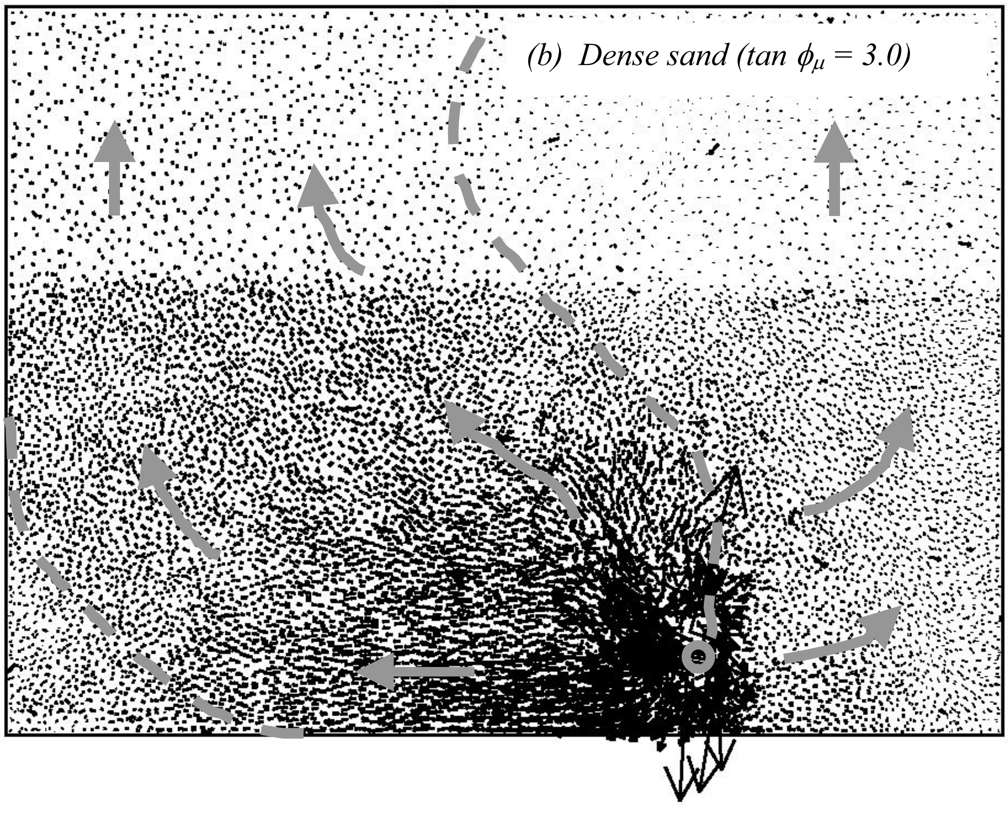

Figure 17 Displacement pattern from DEM of lateral pipe loading (*H*/*D* = 30)

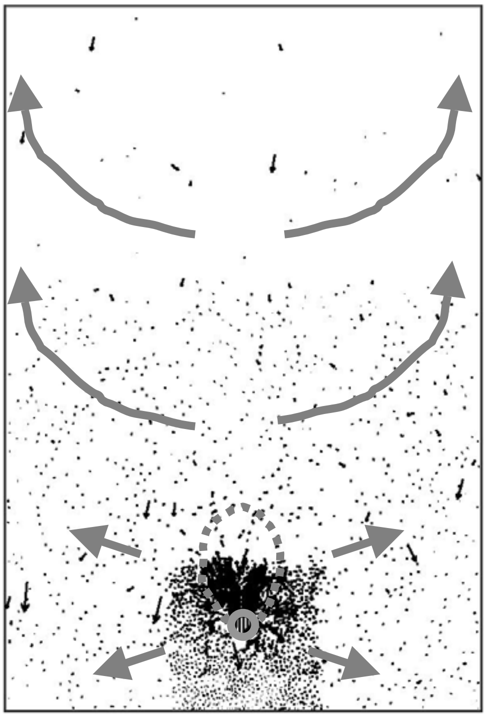

(a) Medium sand (tan $\phi_\mu = 3.0$)

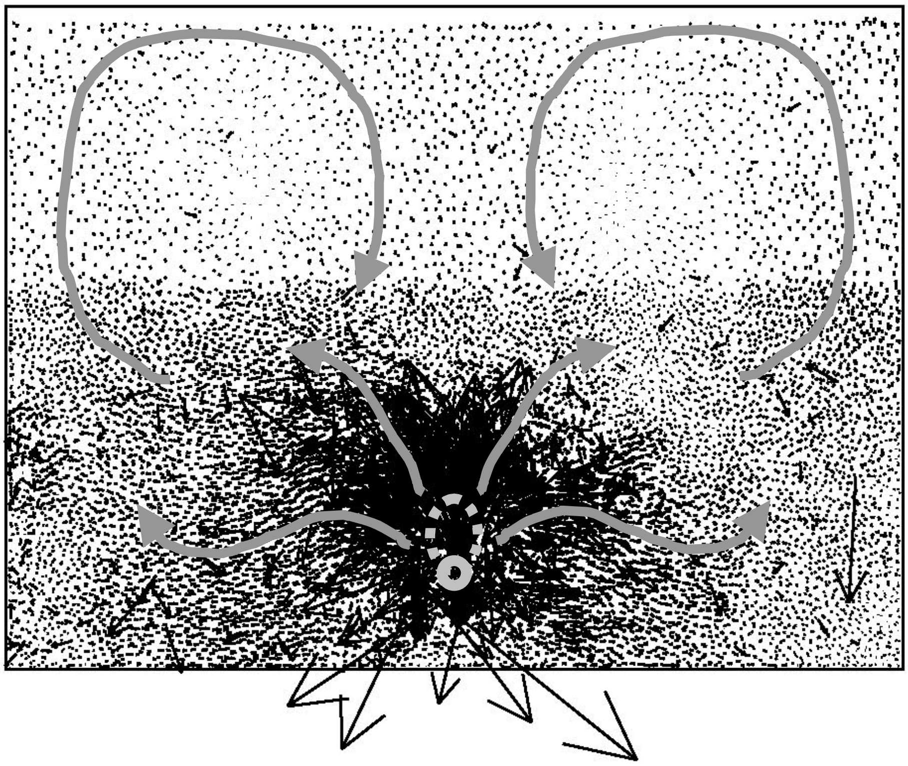

(b) Dense sand (tan $\phi_\mu = 3.0$)

Figure 18 Displacement pattern from DEM of upward pipe loading ($H_c/D = 30$)